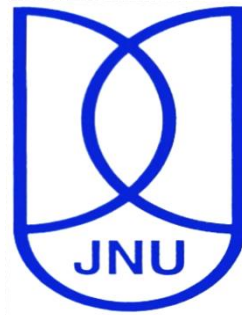


**Size Property Relationship in Low Dimensional
Nanostructures and their Bioactivity: Physical
and Biophysical Aspects**

**Thesis submitted in fulfilment of requirement for the degree of
Doctor of Philosophy**

KISHAN DAS



**School of Physical Sciences
Jawaharlal Nehru University
New Delhi - 110067, India**

July 2018

© 2018 Kishan Das

Jawaharlal Nehru University, New Delhi - 110067, India

निम्न आयामी अत्यणुसंरचना एवं उनकी जैवसक्रियता
में भौतिक तथा जैवभौतिक स्वरूपों में
आकार अनुगामी गुण

डॉक्टर ऑफ फिलॉसफी

की उपाधि के लिए अपेक्षित पूर्ति में निवेदित किया गया शोध प्रबंध

किशन दास



भौतिक विज्ञान संस्थान
जवाहरलाल नेहरू विश्वविद्यालय
नई दिल्ली - ११००६७, भारत

जुलाई २०१८

© २०१८ किशन दास

जवाहरलाल नेहरू विश्वविद्यालय, नई दिल्ली - ११००६७, भारत

Statement of Originality

This thesis is an account of work carried out by the author in the School of Physical Sciences, Jawaharlal Nehru University, New Delhi, India under the supervision of Prof. H. B. Bohidar. Where the work of others has been drawn upon this is duly acknowledged in the text, and a list of references is presented at the end of each chapter. No part of this thesis has been submitted towards the completion of another degree at Jawaharlal Nehru University or elsewhere.



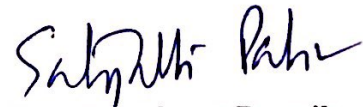
Kishan Das

School of Physical Sciences
Jawaharlal Nehru University
New Delhi-110067, India



Prof. Himadri B. Bohidar

Thesis Supervisor
School of Physical Sciences
Jawaharlal Nehru University
New Delhi-110067, India



Prof. Satyabrata Patnaik

Dean
School of Physical Sciences
Jawaharlal Nehru University
New Delhi-110067, India

मेरी माता जी श्रीमती कमलेश्वरी देवी और
पिता जी श्री सुरेश चन्द्र को उनके
असीम वात्सल्य, प्रोत्साहन
एवं प्रेरणा के लिए
समर्पित...

Acknowledgement

With the blessings of Ishtadev Shri Hanuman ji and Baba Vishwanath Bhagwan, I am going to write this thesis. Working for this thesis has certainly been a long and arduous journey, but it would not have 'been' at all possible were it not for the help and support of a rather special group of people.

I would like to begin by thanking my supervisor 'Guru Ji' Prof. Himadri B. Bohidar for his expert supervision, guidance and support throughout the length of this study. It has been an excellent learning experience working together with him. I wish to thank him also for allowing utmost freedom to carry out all "wild" experiments that came to my mind. He has provided a very conducive ambient for scientific research and has been patient and encouraging throughout. I take this opportunity to wish him lots of success in all his future scientific endeavours.

But everything will be useless if I do not express my gratitude to 'Gurudev' Prof. S.S.N. Murthy under whom I started my life in this field. My thanks are due to him for his critical supervision and constructive suggestions, which helped me improve my analytical aptitude and also for special attention, attentive consideration and encouragement which he gave me in my initial experimental life.

I am also thankful to my grad Acharya Dr. Keshav Chand Sood who motivated me to reach this level.

I gratefully acknowledge the contributions of several people from different research groups, with whom we collaborated in the context of this thesis work. Dr. Rajan Patel, Dr. Paulraj Rajamani and Dr. Ramovatar Meena are such important person.

I would also like to thank all the members of the School of Physical Sciences, JNU for their constant co-operation and attention during my Ph.D. days.

Without the help of technical staff (AIRF, JNU) Mr. Saroj, Dr. Ruchita, Dr. Smita, Dr. Gajender, Dr. Manish, Dr. Manoj, Mr. Ashok, Mr. Sandeep, Dr. Prabhat and Ms. Neetu, I would not have contemplated the wide ranging instrumentation and experiments involved in this work.

I wish to acknowledge the Council of Scientific and Industrial Research, India for my research fellowship.

I thank to Dr. Najmul, Dr. Nidhi, Dr. Jyotsana, Dr. Anshu, Rahul, Irshad (Kashmiri), Pankaj and Priyanka to give me such a great and memorable environment in my days in lab. Special thanks to Manjeet, Pavan (Pauna) and Irshad with whom I always feel 'good'. Irshad and me were always entering and leaving together whether it was Sutlej my hostel or SPS my centre. The new doctor member of my lab Dr. Epsita and Dr. Nidhi are also thanked for their useful discussion of my work. SPS Life would have been definitely boring without the company of Dr. Ambuj, Dr. Firoz, Dr. Vishwapal, Dr. Prasenjeet, Dr. Ashwani, Panchu, Harish, Yogendra, Vikrant, Sunil, Kishor, Umesh (Bon-gaali), Nasir, Arijit Ajit, Ganesh, Jagdeesh, Rahul Singh, Avinash, Neetu, Khemchand, Amit, Lalita, Virendra. JNU life was highly joyful because of some Sutlejits. Shiv Shankar, Wasim Bhai, Xuan Wang, Dr. Arihant, Shauryajeet, Asif Bhai, Saleem Bhai, Sanjeev (Baba) and Shiv Prakash are few whom I remember at the moment. I would like thank to Jagriti (Simpri) for being always there whenever I need along with her enormous patience and love. There are also many friends and seniors, whom I may have not named here but whose support have enabled me to overcome many setbacks. I would like to thank them for their support.

Above everything, this Ph. D would not have been possible without the constant support, encouragement, blessings and good wishes of my family. I would never be able to repay their unconditional support and personal sacrifices, which made it possible for me to achieve this goal. I would like to pay my heartfelt thanks to Mummy, Papa, Gopal (Little B), Rani (Lil sis), Suraj (Chafnu), Riya Di (Mrs. Sanjay), Gudia Di (Mrs. Ajay), Anuj (Allu), Rajesh bhaiya and Dinesh Chacha. And also thanks to my cousin Bhaiyas Rajan, Rahul, Ravish and sweet Bhabhis Nilima, Pooja, Dr. Ena for encouraging me in my life. I feel very blessed to have Komal Jiji, Annapurna (Annu) Jiji and Ragini Jiji.

In the last, special thanks to Lil champs Ashtha (Chundal), Aaditya (Laddu), Snigdha (Ilu), Pia, Kanha, Darshika, Shivam and Ishan for their innocent and enormous love.

Kishan Das

Contents

Chapter 1

Introduction

1.1 Historical Introduction.....	1
1.2 Low Dimensional Nanostructure.....	5
1.2.1 Quantum Dots.....	7
1.2.2 Core/Shell Quantum Dots.....	10
1.3 Low Dimensional Nanostructure synthesis.....	10
1.3.1 Synthesis of Quantum Dots.....	11
1.3.1.1 Physical Methods for Synthesis.....	11
1.3.1.2 Chemical Methods for Synthesis.....	11
1.3.2 Synthesis of Core/shell Quantum Dots.....	12
1.4 Objectives and contributions of this thesis.....	13
1.5 Thesis Organization.....	14
1.6 References.....	15

Chapter 2

Materials and Experimental Techniques

2.1 Materials.....	19
2.1.1 Materials used for Synthesis of Quantum Dots.....	19
2.1.2 Anisotropic Nanoclays: Laponite and Montmorillonite.....	20
2.1.3 Globular Plasma Proteins.....	21
2.1.4 Lysozyme.....	22
2.1.5 Candida albicans.....	22
2.1.6 Cell lines.....	23
2.2 Synthesis Method and Setup.....	23
2.3 Synthesis.....	24
2.3.1 Synthesis of Selenium based QDs in the Organic Phase.....	24
2.3.1.1 Synthesis of Fluorescent CdSe QDs.....	25

2.3.1.2	Synthesis of Highly Fluorescent CdSe /CdS QDs.....	25
2.3.1.3	Synthesis of MnSe QDs in the Organic Phase.....	25
2.3.2	Purification.....	26
2.3.3	Transformation into Hydrophilic by Ligands Exchange.....	26
2.4	Characterization Techniques.....	26
2.4.1	Physical Characterization.....	27
2.4.1.1	Structure Characterization.....	27
2.4.1.2	Property Characterization.....	39
2.4.1.2.1	Optical Property Characterization.....	39
2.4.1.2.2	Magnetic Property Characterization.....	43
2.4.2	Biophysical Characterization: Protein Interactions.....	44
2.5	Bioactivity.....	49
2.5.1	Enzymatic activity.....	49
2.5.2	Antimicrobial activity.....	49
2.5.3	Biocompatibility: <i>in vitro</i> studies.....	50
2.6	References.....	52

Chapter 3

Size Variational Physical and Biophysical Characterization of Synthesized Surfactant Functionalized Quantum Dots

3.1	Introduction.....	55
3.2	Sample Preparation.....	56
3.3	Physical Characterization.....	58
3.3.1	Morphology and Surface Charge	58
3.3.2	Ligand Exchange Conformation.....	63
3.3.3	Crystalline Structure.....	65
3.3.4	Spectroscopic Properties.....	66
3.4	Biophysical Characterization.....	69
3.4.1	BSA-QD Binding.....	69
3.4.2	Effect on Environment of Protein.....	73

3.4.3 Effect on Protein Secondary Structure.....	76
3.5 Size and Coating Dependent Differential Binding.....	78
3.6 Summary.....	79
3.7 References.....	79

Chapter 4

Size Variational Synthesis and Characterization of Cubic MnSe

Nanospheres

4.1 Introduction.....	82
4.2 Size Variational Synthesis of MnSe Nanospheres.....	83
4.2.1 Synthesis of Hydrophobic MnSe Nanospheres.....	83
4.2.2 Filtration.....	84
4.2.3 Ligands Exchange to Hydrophilic State.....	84
4.3 Characterizations.....	84
4.3.1 Effect of Reaction Temperature on Structure.....	84
4.3.2 Size Dependent Optical Properties.....	86
4.3.3 Size Dependent Magnetic Properties.....	88
4.4 Summary.....	93
4.5 References.....	93

Chapter 5

Size Variational Biophysical Interactions of Nanostructures

5.1 Introduction.....	97
5.2 Sample Preparation.....	98
5.3 Protein - Nanoclay Binding.....	99
5.3.1 UV-Vis absorption spectroscopy.....	99
5.3.2 Fluorescence spectroscopy: Binding Constant.....	101
5.3.2.1 Effect on Fluorescence.....	101
5.3.2.2 Fluorescence Quenching and Binding Constant.....	102
5.4 Stoichiometry of Protein-Clay Binding.....	104
5.4.1 Effect on Hydrodynamic Radius.....	104

5.4.2 Effect on Net Surface Charge.....	105
5.4.3 Effect on pH of Proteins.....	105
5.5 Conformational Changes in Protein after Binding.....	106
5.5.1 Effect on Microenvironment around Fluorophores.....	106
5.5.2 Effect on Secondary Structure.....	109
5.5.3 Effect on Fluorescence Lifetime.....	111
5.6 Nanoclay-Protein interaction: Surface Patch binding.....	113
5.7 Summary.....	115
5.8 References.....	116

Chapter 6

Size Variational Quantum Dot -Lysozyme Interaction and Effect on Enzymatic Activity

6.1 Introduction.....	119
6.2 Sample Preparation.....	121
6.3 UV-Vis absorbance: Complex Formation and Binding Constant.....	121
6.3.1 Strength of the Binding Forces.....	123
6.3.2 Nature of the Binding Forces: Thermodynamic Parameters...	124
6.4 Fluorescence Spectroscopy: Quenching and Binding Constant.....	125
6.4.1 Binding Constant and Number of Binding Sites.....	126
6.4.2 Electrostatic Binding Contribution.....	128
6.5 Structural Changes in Lysozyme after Binding.....	131
6.5.1 Effect on Microenvironment around Fluorophores.....	131
6.5.2 Effect on Secondary Structures.....	132
6.6 Enzymatic Activity of Size Dependent QDs-Lysozyme Complex.....	133
6.7 Phenomenology of Differential Binding.....	134
6.8 Summary.....	135
6.9 References.....	136

Chapter 7

Size Variational Synthesis and Antimicrobial Activity of Core/Shell CdSe/CdS Quantum Dots

7.1	Introduction.....	139
7.2	Sample Preparation.....	141
7.2.1	Synthesis of CdSe QDs of Different Size.....	141
7.2.2	Synthesis of CdSe/CdS QDs with varying Shell Thickness..	141
7.3	Physical Characterization.....	142
7.3.1	Structural Characterization.....	142
7.3.2	Surface Charge.....	144
7.3.3	Optical Characterization.....	145
7.3.4	Crystalline Structure.....	147
7.4	Antifungal Activity of Synthesized QDs.....	147
7.5	Summary.....	149
7.6	References.....	150

Chapter 8

Size Variational Cellular Uptake and Cytotoxicity of Quantum Dots

8.1	Introduction.....	153
8.2	Sample Preparation.....	156
8.2.1	Synthesis of CdSe QDs.....	156
8.2.2	Synthesis of CdSe/CdS Core /Shell QDs.....	156
8.3	Physical Characterization.....	156
8.3.1	Structural Characterization.....	156
8.3.2	Surface Charge.....	157
8.3.3	Crystalline Structure.....	158
8.3.4	Optical Characterization.....	159
8.4	Cytotoxicity Analysis for Biocompatibility Screening.....	160
8.5	QDs induced Reactive Oxygen Species Production.....	162
8.6	QDs induced Apoptosis Mechanism.....	163
8.7	Effect of QDs Treatment to Cells on Cellular Morphology.....	166

8.8 Cellular Uptake.....	168
8.9 Summary.....	171
8.10 References.....	172

Chapter 9

Conclusions and Perspectives.....	175
--	------------

9.1 Conclusions.....	176
-----------------------------	------------

9.2 Perspectives.....	178
------------------------------	------------

Appendix 1.....	179
-----------------	-----

Appendix 2.....	181
-----------------	-----

List of Publications.....	182
---------------------------	-----

Chapter 1

Introduction

“ बालाग्रशतभागस्य शतधा कल्पितस्य च ।
भागो जीवः स विज्ञेयः स चानन्त्याय कल्पते ॥ ”

“बाल के अग्रभाग के सौवें के भी सौवें भाग की कल्पना की जाए तो इस तरह के प्रत्येक भाग का ज्ञान प्राप्त कर लेने वाला जीव अनंत की कल्पना कर सकता है।” - श्वेताश्वतर उपनिषद् (५.९)

Imagine the hundredth of the hundredth part of the tip of the hair, then the person who acquires knowledge of each such part can imagine the Ultimate.

1.1 Historical Introduction

To innovate new properties and functions, the manipulation of materials and controlling them at very tiny scale seems like it should be a very complicated and great modern concept. But past artisans and craftsmen controlled matter at nanoscopic scale and used it. We can say that they were working with nanocomposites. These are the mixture of materials in which at least one component is nanoscale particles to enhance the properties of the composite material.

From nearly 2500 BC in India, *Swarna bhasma* (nanocomposite with gold nanoparticles) were used as a therapeutic agent in traditional Ayurvedic treatment for many health disorders including diabetes mellitus, rheumatoid arthritis, bronchial asthma and neurological diseases ^[1]. *Swarna bhasma* could be taken orally mixed with some eatables as well as applied to skin directly. Recently, size-dependent absorption of gold nanoparticles through rat skin and intestine have been confirmed. ^[2]

“Indian craftsmen and artisans used nanotechnology extensively about 2000 years ago to make weapons and long-lasting cave paintings though they were completely unaware that they were practising carbon nano-techniques that are most sought after in the current age.”

- Robert F Curl (Nobel Prize winner in chemistry in 1996)

on the 3rd day of the 7th Science Conclave-2014 at the Indian Institute of Information Technology Allahabad, India.

The above said sentences are related to Ajanta cave paintings in which gold nanoparticles were used and Damascus blades found in Tipu Sultan's sword in which carbon nanotubes were used. In Figure 1.1, one example for each are shown.



Fig. 1.1: Padampani, one of the Ajanta Cave paintings and sword of Tipu Sulatan are shown.

It is also believed that gold nanoparticles were used in Tanjore wall paintings such as Ajanta cave paintings. Examples of one painting is shown in Figure 1.2 ^[3].



Fig. 1.2: Brihadeshwara (Rajarajeshwara) temple wall paintings, Tanjaore is shown.

There are many more famous evidences of ancient creation made up of nanocomposites. For example, the Lycurgus cup that is a dazzling decorative Roman glass chalice of AD

400. The unique thing about that glass is its colour changes that depends on from where light is coming. Due to unique distribution of gold-silver alloyed nanoparticles in this glass, it looks green in reflected light (i.e. illuminated from outside) but glows brilliant red in transmitted light (i.e. it glows from inside) [3].



Fig. 1.3: Lycurgus Cup with reflected and transmitted light is shown.

Azure blue pigment known as Maya Blue that was amazingly resistant to severe weathering and was used extensively since AD 800, in Chichen Itza (one of the city of the Mayan civilization). It is nanocomposite made by white clay in which nanopores were available. And indigo dye that was extracted from vegetable was chemically fused in that nanopores to make a highly stable colouring material. This majestic color cannot be affected by ordinary strength alkalis, acids or chemical solvents. Not even nitric acid can damage it. [3]



Fig. 1.4: A painting of a warrior with Maya blue on the background is shown.

Damascus steel swords were made between AD 300 and AD 1700 in the Middle East. These swords had amazing strength and prodigious sharp cutting edge. And also were

unbreakable. Nanotubes and nanowires like structures were embossed on these steel swords, due to which the properties of these materials got intensified. [3]



Fig. 1.5: Damascus steel swords with pattern of nanowires and nanotubes is shown.

Pottery from across the Renaissance Mediterranean region (1450 – 1600 AD) was often beautified with a dramatic iridescent metallic glaze called lustre. To achieve the gold and red lustre effects, 5 to 100 nanometre sized nanoparticles of silver and copper metal were used. Rather than scattering of light, the nanoparticles' surface cause incident light to bounce off at different wavelengths, giving iridescent effects. [3]



Fig. 1.6: Lustered Armorial Plate, workshop of Giorgio di Andreoli, Italian, Gubbio, AD 1524, is shown.

The craftsmen and artisans who made these materials are they really nanotechnologist? According to Ian Freestone, a famous archaeologist in London, who investigated the Lycurgus cup, they were not. Even after doing all these work on nanoscale, they would be called extremely skilled artisan because they did all these work unknowingly.

the Damascus sword specialist Peter Paufler in Dresden says "*they developed materials by trial and error similar to evolution in biology. They didn't know the processes going on inside the solids.*" [3]

In the American Chemical Society annual meeting on 29th Dec, 1959 in Pasadena, Nobel Laureate Richard P. Feynman delivered a far-sighted talk “There’s Plenty of Room at the Bottom” which predicts immense possibilities opened up by miniaturization. It became one of the great lecture in science of 20th century. The technological perception without violating laws of physics of extreme miniaturization have presented by him many years before the word “chip” was introduced. He presented his visionary ideas about to manipulate and control the things on very tiny scale. Reckoning from existing physical laws, he predicted the technology employing the fundamental hardware of nature (atoms), to make nano arrangements where those forces will have dominant effect which were neglected due to being very weak and that will open up vast kind of possibilities. Lastly he predicted the development of nanorobots (like our biological cells) which does what we want. That should be the future of today’s nanotechnology.

Figure 1.7 shows the today’s world tiniest computer which starts the new era of nanotechnology just as predicted by Feynman.

World’s tiniest ‘computer’ is smaller than a rice grain


Researchers at the University of Michigan in the US have come out with the world’s ‘smallest computer’ — a device measuring just 0.3mm to a side, completely dwarfed by a grain of rice.

Unlike traditional desktops that retain their programs and data with or without a power back-up, these new microdevices lose all prior programming and data as soon as they are switched off.

“We are not sure if they should be called computers. It’s more of a matter of opinion whether they have the minimum functionality required,” said David Blaauw, a professor of electrical and computer engineering, who led the development of the new system. In addition to the RAM and photovoltaics, the new micro-computing device — Michigan Micro Mote — has processors and wireless transmitters and receivers.

As the Motes are far too small to carry conventional radio antennae, they receive and transmit data with visible light. A base station provides light for power and programming, and it receives the data.

The computer can report temperatures in minuscule regions, such as a cluster of cells, with an error of about 0.1 degree Celsius. The system is very flexible and could be reimaged for a variety of purposes. The device can help in oncology research. AGENCIES



MINI-TECH: Motes developed by University of Michigan can help in oncology research

Fig. 1.7: This article is published in “The Times of India” newspaper in India on 24th June 2018.

1.2 Low Dimensional Nanostructures

The material whose size is in nanoscale upto 100 nm at one or more than one dimensions is called low dimensional nanostructures like nanosheets, nanodisk, nanowire and quantum dots etc.

Energy Band Physics: Energy levels in atomic orbital are not continuous but discreet. Many atoms are used to make molecules due to which their atomic orbitals are overlapped to make a new set of orbitals called molecular orbitals like in a coupled oscillator. This new set of orbitals are the same in number as atomic orbitals. To make a molecule of two atoms, two molecular orbitals are produced after annihilating two atomic orbitals, bonding (low energy) called Highest Occupied Molecular Orbital (HOMO) and antibonding (higher energy) called Lowest Unoccupied Molecular Orbitals (LUMO).

Solid is composed of bountiful atoms of the order of 10^{23} due to which the produced molecular orbitals tends to extremely large number. The energy difference between these levels becomes so small that the continuous energy bands are formed by these discrete energy levels as shown in Figure 1.8. However, as many atoms are assembled some energy gap is always remains, called band gaps.

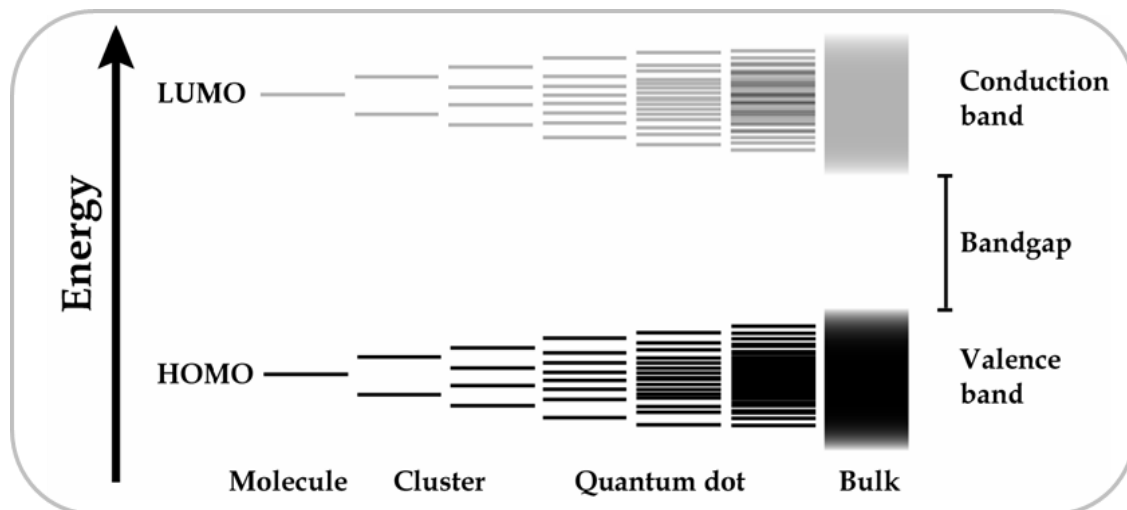


Figure 1.8: The distribution of energy level while forming bulk semiconductor from two-atom molecule with intermediate cases. With increasing the size, energy band gap is reducing.

In bulk material, the position of electrons or holes is not precisely defined but momentum, hence energy, is. In quantum dots, the uncertainty in position decreases so for momentum it is increases due to Heisenberg's uncertainty principle. This increasing window of momentum increases the average momentum hence band gap. This is the qualitatively description of higher energy band gap in quantum dots with respect to their bulk.

1.2.1 Quantum Dots (QDs)

Quantum dots (QDs) are semiconductor nanoparticles with size comparable to the length parameters i.e., exciton Bohr radius a_B and the de Broglie wavelength λ of the quasiparticles (holes, electrons and excitons) hence having strong quantum confinement effect in all 3 dimensions.^[4]

$$a_B = \frac{\hbar^2 \epsilon}{e^2} \left[\frac{1}{m_e^*} + \frac{1}{m_h^*} \right] \quad (1.1)$$

$$\lambda = \frac{h}{p} = \frac{h}{\sqrt{3m_{e(h)}^* k_B T}} \quad (1.2)$$

where \hbar, e, k_B and T have their usual meaning. ϵ is the dielectric constant and $m_{e(h)}^*$ is the effective mass of electron (hole) for that material. For the most familiar semiconductors like CdSe, CdTe and CdS, λ is around 10 nm at room temperature and a_B is also around 10 nm which means quantum confinement are prominent even for a nanoparticle with size 10 - 100 times more than the lattice parameter. With this size in any dimension, nanoparticle can be considered as a macroscopic object but for quasi particles, it should be treated as the quantum box for same dimension and the motion of holes and electrons are confined in that dimension and quantized, giving rise to atomic like discrete (quantized) energy levels as shown in Figure 1.9.

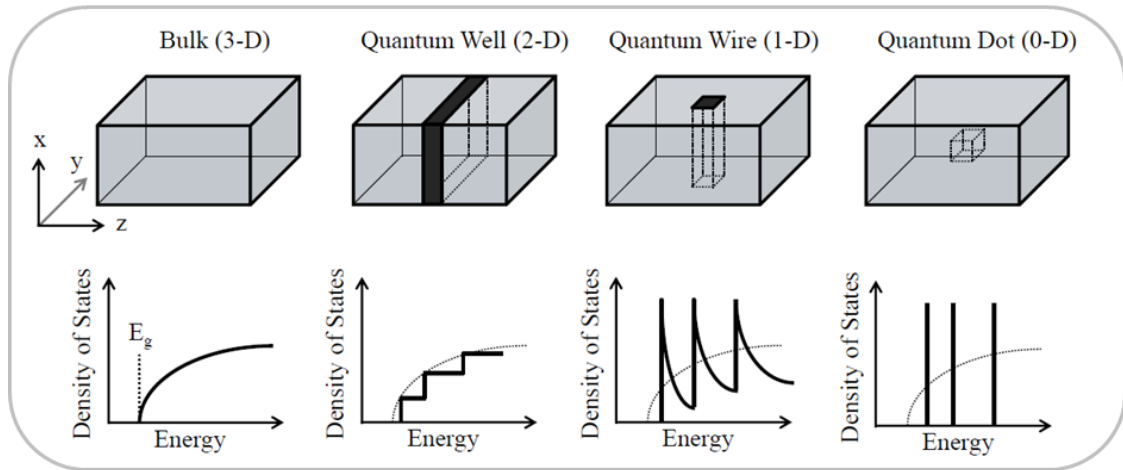


Figure 1.9: Schematic illustration of density of states for particles with spatial degrees of freedom.

The strong confinement of electrons and holes in QDs of radius r_Q , corresponds to a spherical infinite potential at the boundary of the dots.

$$V(r) = \begin{cases} 0, & \text{if } r < r_Q \\ \infty, & \text{if } r \geq r_Q \end{cases} \quad (1.3)$$

The quantized energy levels can be calculated for that is

$$E_n = \frac{\hbar^2 \pi^2}{2 m_{e,h}} \left(\frac{n}{r_Q} \right)^2, n \text{ is integer} \quad (1.4)$$

We see that the energy is quantized and depends on the size of the QDs. As size is decreased, quantized energy levels are increased and separated more. This explains the observed redshift in colour of nanoparticle dispersion with increase in size.

But in this model, Coulombic interaction of electron and hole is not considered. Since the size of QDs is so small that this interaction has some significant value. With considering confinement and Coulombic effect, energy band gap of QDs is^[5]

$$E_Q = E_g + \frac{\hbar^2 \pi^2}{2 r_Q^2} \left[\frac{1}{m_e^*} + \frac{1}{m_h^*} \right] - 1.8 \frac{e^2}{\epsilon r_Q} \quad (1.4)$$

where E_g is the energy band gap of corresponding bulk and constants have their usual meaning.

Properties of Quantum Dots

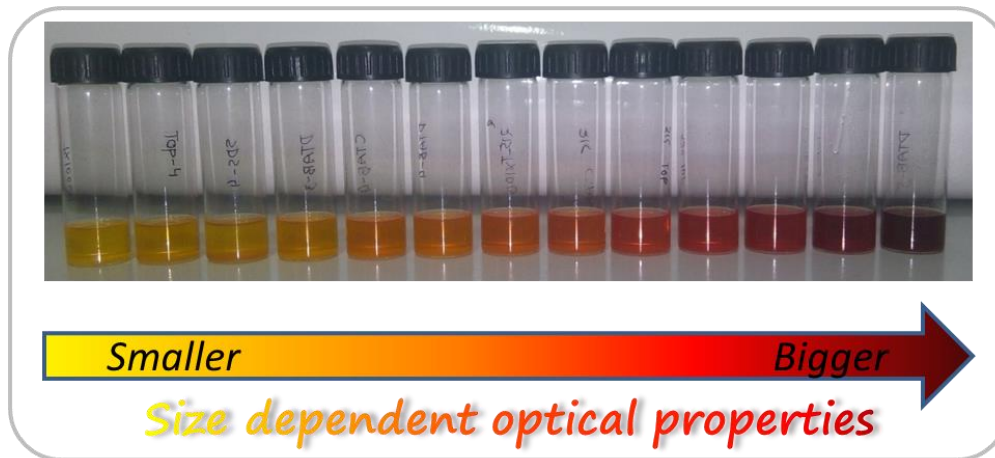


Figure 1.10: Size dependent color (absorbance) of CdSe QDs.

Optical property: Since QDs have atoms like discrete energy levels and band gap, they show optical property (absorption and photoluminescence) and this property is unique in the sense that it is size tunable as we can see from equation 1.4 that the separation of discrete energy levels and band gap of QDs is size dependent. So we can tune the band gap, hence optical property from visible to near infrared region, according to our need by tuning its size.

Magnetic property: Nanocrystals that shows some observable response under an external magnetic field are called magnetic nanocrystals (MNCs). More active surface

spins^[6] are mainly responsible for changes in the magnetic order of the whole particle. The magnetic properties and the coercivity field (H_C) with the Curie constant (C), Weiss constant, blocking temperature^[7] or Néel (T_N) temperatures are different than those of a bulk material^[8,9]. Finite size effects, i.e. quantum confinement of the electrons and single or multi magnetic domains structures, and surface effects, i.e. effects of symmetry-breaking of chemical and physical environment at surface, are dominating to decide the magnetic property of any nanoparticles. Magnetic nanoparticles (MNPs) have immense applications including ultrasensitive sensors^[10], high-density data storage, bioimaging^[11], logic devices^[12] and many more biomedical applications^[13] like hyperthermia i.e. the treatment of certain cancers^[14].

Pure magnetic metal and metal alloys of Fe, Co, and Ni, are very sensitive to air^[15]. Iron based magnetic nanoparticles have some limitations due to their poorly suspension and instability in water and for overcoming to that limitation, one has to coat their surface properly and by that their size goes up and extra work have to be do^[16,17]. Therefore non-iron based magnetic nanoparticles get more attention.

Surface effects: Surface of QDs also have a significant effect on their fundamental properties. Decreasing the particle size is resulting the increase of the surface to volume ratio for it. For the nanocrystals (NCs), this ratio is very high resulting more atoms on the surface as compared to core's atoms. The reduced coordination number and lack of symmetry for surface atoms make them more chemically active and induce extra electronic levels in the band gap, which act as trap centers for electron or hole. These trap centres reduce the fluorescence quantum yield.^[18]

Enhancing fluorescence: Surface traps and defects have very strong effects on the photoluminescence property due to the non-radiative recombinations at defects and traps. It is observed that non radiative emission due to defects even at densities as low as $10^{-7}/\text{nm}^3$ can dominate over fluorescence (radiative emission). Defects can be reduced by enhancing synthesis method and surface traps by appropriate ligand based organic or core shell based inorganic surface passivation.

Applications: So we can say that high surface to volume ratio and quantum confinement in QDs is the basis of their novel physical, chemical and mechanical behaviours with regard to their bulk. Size, shape and crystal structure dependent physical and chemical properties of semiconductor nanocrystals^[19-22] make them unique and give them great attraction for not only fundamental scientific research but technical applications also. Trimming their size and shape make them suitable to use in many applications including

solar cells^[23], photodetectors^[24], electronic devices^[25] and sensors^[26]. After surface passivation, very high fluorescence property create their scope in biomedical applications. Due to broad absorption range, size tunable narrow fluorescence spectra, large extinction coefficient and highly stable to physical and chemical degradation compare to organic dyes make QDs very useful to bio imaging. Magnetic property coupled fluorescence effect can create immense opportunity to apply in diverse fields from physics to biology like like in magneto-optical devices, catalysis, sensing, magnetic resonance imaging, bio imaging as well as therapeutic applications such as hyperthermia (AC magnetic field-assisted cancer therapy) ^[27].

1.2.2 Core/shell Quantum Dots

Advantages: QDs are highly surface sensitive due to higher surface to volume ratio even though organic ligand capping is on their surface. And surface trap states considerably decrease the fluorescence quantum yield. Many studies have shown that the shell structure on core QDs can stabilize and enhance fluorescence quantum yield of core QDs. Coating by larger band gap inorganic shell on QDs not only make surface passivation, but also create potential energy well for the core semiconductor, and thus confining the charge carriers in the core and removing surface trap and defect states hence enhance the fluorescence intensity. And also diminished the degrading environmental factors and make QDs more stable. ^[28-30]

Criteria for shell material: The choice of larger band gap inorganic shelling material on core QDs should be like that there was least lattice mismatch. Similarities between the CdS and CdSe lattices (lattice mismatch is only 4%) and the suitability of their bandgaps for superlattice construction dictated the choice of this semiconductor pair.

During the formation of shell on core there should be homogeneous growth of shell on all QDs without any nucleation of shelling materials. In fact, the shelling precursors should be weakly reactive so that there should be no independent nucleation, but strong enough to elevate the epitaxial formation of shell around the synthesized core QDs.

1.3 Low Dimensional Nanostructure Synthesis

The unique optical properties of semiconductors nanocrystals was discovered by Alexey Ekimov (Russia) in 1980 with synthesizing nanocrystals doped glass matrix ^[31] and by Henglein in 1982 with synthesizing nanocrystal in colloidal solutions.^[32] Following this inventions, the theoretical calculations of semiconductor nanocrystal band gap were first presented by Louis E. Brus in 1984.^[5] In 1988, Mark A. Reed gave the name “quantum

dots” first time, much more linguistically appropriate term than “zero-dimensional semiconductor nanostructures”^[33]. But in 1993, there was a pathbreaking work done by C.B.Murray, David J. Norris, and Moungi G. Bawendi (that has 9,548 citations till now) which details a “hot-injection” synthesis for nearly monodisperse semiconductor colloidal nanocrystallites ^[34] and after this work, scientists started evaluating quantum dots for their research applications not just for only curiosity. CdSe QDs are the most extensively studied colloidal II-VI semiconductor nanoparticles because of their high luminescence quantum yield, wide fluorescent emission spectral ranging from blue to red, narrow emission band gap and advances made in their preparation.

1.3.1 Synthesis of QDs

Synthesis methods of QDs can be conditionally divided into chemical (there must be a chemical reaction for the formation of a substance) and physical ones (there is no chemical change of the substance).

1.3.1.1 Physical Method for Synthesis

Generally it is the process of nucleation and growth of nanoparticles in the vapour form. *Molecular beam epitaxy* method is the one physical method in which atoms or molecules are deposited by their beam on a suitable substrate in ultrahigh vacuum. This method produce ordered highly monodisperse QDs arrays that is the example of self – organization of matter and is best to study the quantum size effects. But it requires highly pure material and very complex apparatus.

1.3.1.2 Chemical Method for Synthesis

There are many chemical methods of synthesis of QDs which are discussed below.

1. Micellar synthesis: It is the method in which particles are synthesised in ‘water in oil’ reverse microemulsions. In this method, intermicellar exchange of reactants cause a chemical reaction, resulting in nucleation and growth of nanoparticles. Since the reverse micelle size can be easily controlled by changing the surfactant and water concentrations, the size of synthesized nanoparticles may vary. However, much more complex mechanism of nanoparticle-formationa in this method is revealed.^[35] The other drawback of this method are very low product formation and nonuniformity in size.

2. Hot Injection Method: It involves one-step reaction, pyrolysis of organometallic precursors. The hot injection technique produces a “nucleation” event, which is a crucial factor for the narrow size distribution of the nanoparticles and these nanoparticles have

high luminescence quantum yield. In this method, we have good control on particle size and can get high crystallinity due to synthesis at high temperature. The use of non-ionic precursors in high-boiling organic solvents is responsible for slowly growing of the nanoparticles at high temperature, which yields well-passivated and defect-free nanocrystals. Separation of the nucleation and growth process, that produces very high monodispersity without any post-synthesis size-selective techniques, is the very important aspect of this method^[36]. But it produce hydrophobic nanoparticles. To make hydrophilic, there are two process we have to follow

- i. Ligand exchange by hydrophilic ones:** The hydrophobic ligands can be exchanged by molecules which are hydrophilic at one end and at the other end hydrophobic that is anchored on the surface of QDs^[37] Mercaptopropionic acid, cysteine, dithiothreitol, 2-aminoethanethiol and dihydrolipoic acid are the some examples of that type of molecules. But by this process, fluorescence quantum yield somewhat decreases.
 - ii. Formation of hydrophilic shell:** The formation of water-soluble shell around the hydrophobic QDs makes them to water soluble but surface defects remain unchanged. This is done by micellization, biopolymeric coating or encapsulating into inorganic (e.g., SiO₂) coating. But by this process, synthesized nanoparticles become very large.
- 3. Refluxing:** This procedure is very simple and requires not so complicated setup but we have less control on synthesis of nanoparticles so they are not so uniform but have good quantum yields even though defects are most probably present.^[38] Crystallinity is also not so good. And this method is also not good for core-shell structure.^[39]
 - 4. Hydrothermal method:** By this method, water-soluble QDs with moderate fluorescence are generally synthesized, which involves autoclave-heating of freshly prepared QDs at very high temperatures over a long period. By high temperature crystallinity become well but it take many steps to get nanoparticles of required size.
 - 5. Microwave-assisted synthesis:** By this procedure, highly pure small QDs can be synthesized in very short time with good uniformity due to very rapid but uniform heating of the whole reaction mixture.^[40]
 - 6. Microreactor synthesis:** This flow microreactor synthesis method is quite new.^[41] In this method through microchannels the reaction mixtures are transferred to a micromixer and passed through different temperature gradient zones. In the hot zone, nucleation starts followed by subsequent growth at lower temperatures zone. Highly monodisperse QDs can be synthesized by this technique.

1.3.2 Synthesis of Core/Shell QDs

A very controlled manner to grow a thin film of molecules, atomic-layer-epitaxy (ALE) is used in the molecular beam epitaxy (MBE) method in which cations and anions beams are opened one by one. By this only one half of the monolayer will grow at one time by cations or anions only. Next beam of complementary ion complete the monolayer structure with uniformity and nearly no defects. Since there is no coexistence of cations and anions in the synthesis chamber, there is no chance of nucleation hence extra or nonuniform structures. And we get only uniform layered structure. Inspired by this process, SILAR (successive ion layer adsorption and reaction) method is developed for colloidal synthesis of core/shell structure. Recently impressive results for growing thin films by this method were found in many literature.^[42,43]

For growing one monolayer of the shell at a time on the core QDs, we have to inject air-stable cationic and anionic precursors alternatively into the reaction mixture of core QDs as like in the molecular beam epitaxy (MBE) method.

The formation of the shell in the form of monolayers can be done by alternating drop by drop injection of air-stable metallic (like cadmium) and chalcogenide (like sulphur) precursors into the pre-synthesized core nanostructures colloidal solutions by hot injection method. This process is one pot synthesis of core/shell nanostructures.^[44]

1.4 Objectives and contributions of this thesis

Synthesis of high-quality CdSe and CdSe/CdS core/shell QDs by hot injection method have been reported but they need so many special conditions like vacuum creation, replacement of dissolved oxygen by nitrogen or other inert gases from the reaction vessel etc. Developing a simple approach to synthesize QDs with high purity, good reproducibility and easy manipulation is extremely desirable. Presence of surfactants in the synthesis of gold nanoparticles gives them different morphology. Can these surfactants do same work for semiconductor QDs? It is also desirable to know the effect of size on magnetic property of magnetic nanoparticles. Since QDs are very useful for biological applications, we should know the interaction of proteins with many sized QDs, non-spherical nanostructures and effect of this size dependent interaction on proteins' activity. Effect of core size and shell thickness on their biocompatibility or cytotoxicity is also very important to know so that we can use these QDs precisely.

In order to address all the above discussed issues and gain greater understanding on size dependent properties of QDs, I plan to synthesize high quality different sized QDs by hot injection method and characterize them. Therefore, the objectives of my thesis are:

- i.** With no special condition, synthesis and characterization of different sized CdSe QDs with and without presence of different type of surfactants and study their biological interactions.
- ii.** Synthesis by simple approach and characterization of different sized MnSe nanospheres.
- iii.** Study of proteins interaction with non-spherical nanostructures.
- iv.** Effect of core size and shell thickness of QDs on their bioactivity.

1.5 Thesis Organization

This thesis have nine parts and organized as follows:

Chapter 1 presents the subject of this thesis and highlights the motivation for this work.

Chapter 2 discusses about materials used and experimental techniques in details.

Chapter 3 introduces and discusses a simple approach to synthesize different sized surfactants functionalized colloidal CdSe QDs by more simple hot injection method and their characterizations with biophysical interactions.

The publication related to this chapter is: Kishan Das et al. "Spectroscopic profile of surfactant functionalized CdSe quantum dots and their interaction with globular plasma protein BSA." *Colloids and Surfaces A: Physicochemical and Engineering Aspects* 506 (2016): 495-506.

Chapter 4 presents synthesis and characterizations of different sized non-iron based, MnSe magnetic nanosphere and discusses their size dependent magnetic property.

The publication related to this chapter is: Kishan Das et al. "Size-dependent magnetic properties of cubic-phase MnSe nanospheres emitting blue-violet fluorescence." *Materials Research Express* 5.5 (2018): 056106.

Chapter 5 discusses surface patch binding induced interaction of anisotropic nanoclays with globular plasma proteins with their conformational changes.

The publication related to this chapter is: Kishan Das et al. "Surface patch binding induced interaction of anisotropic nanoclays with globular plasma proteins." *RSC Advances* 6.106 (2016): 104117-104125.

Chapter 6 explores size variational bioactivity of QDs specifically CdSe QDs-lysozyme interaction and effect on enzymatic activity.

The publication related to this chapter is: Kishan Das et al. "Size-dependent CdSe quantum dot-lysozyme interaction and effect on enzymatic activity." *RSC Advances* 6.52 (2016): 46744-46754.

Chapter 7 describes a simpler route to synthesize CdSe/CdS core/shell QDs with varying core size and shell thickness by one pot synthesis and discusses about their antimicrobial activity.

Chapter 8 explores the effect of shelling on cytotoxicity of CdSe quantum dots.

Chapter 9 concludes and summarizes the main findings of this thesis.

1.6 References

- [1] Sarangdharacharya, In Sarangadhara-Samhita Varanasi, *India: Chaukhambha Orientalia* **2002**.
 - [2] G. Sonavanea, K. Tomoda, A. Sano, H. Ohshima, H. Terada, K. Makino, *Colloids and Surfaces B: Biointerfaces* **2008**, 65, 1.
 - [3] <https://www.theguardian.com/nanotechnology-world/nanotechnology-is-ancient-history>.
 - [4] A. Issac, Photoluminescence intermittency of semiconductor quantum dots in dielectric environments **2006**.
 - [5] L. E. Brus, *J. Chem. Phys.* **1984**, 80, 4403.
 - [6] D. Peddis, M.V. Mansilla, S. Mørup, C. Cannas, A.N.N.A. Musinu, G. Piccaluga, F. D’Orazio, F. Lucari, D. Fiorani, *The Journal of Physical Chemistry B* **2008**, 112, 8507.
 - [7] M.C. Buján-Núñez, N. Fontaiña-Troitiño, C. Vázquez-Vázquez, *J. Non-Cryst. Solids* **2008**, 354, 5222.
 - [8] T.C. Han, M.R. Tsai, C.Y. Wei, *J. Appl. Phys.* **2011**, 109, 07B517.
 - [9] V. Markovich, I. Fita, A. Wisniewski, *Phys. Rev. B* **2010**, 81, 094428.
 - [10] I. Koh, L. Josephson, *Sensors* **2009**, 9, 8130.
 - [11] N. A. Frey, S. Peng, K. Cheng, S. Sun, *Chem. Soc. Rev.* **2009**, 38, 2532.
 - [12] D.A. Allwood, G. Xiong, C.C. Faulkner, *Science* **2005**, 309, 1688.
 - [13] M. Colombo, S. Carregal-Romero, M. F. Casula, *Chem. Soc. Rev.* **2012**, 41, 4306.
-

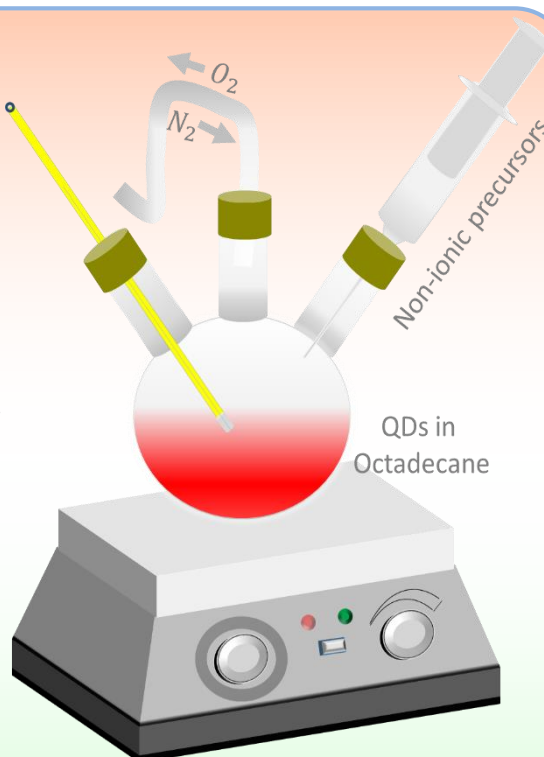
- [14] A.K. Gupta, M. Gupta, *Biomaterials* **2005**, 26, 3995.
- [15] A.-H. Lu, E.L. Salabas, F. Schüth, *Angew. Chem. Int. Ed.* **2007**, 46, 1222.
- [16] K. Woo, J. Hong, J. P. Ahn, *J. Magn. Magn. Mater.* **2005**, 293, 177.
- [17] W. Wu, Q. He, C. Jiang, *Nanoscale Res. Lett.* **2008**, 3, 397.
- [18] Z. Kang, Synthesis, characterization and application of luminescent quantum dots and microcrystalline phosphors. *Diss. Georgia Institute of Technology* **2006**
- [19] R. E. Algra, M. Hocevar, M. A. Verheijen, *Nano Lett.* **2011**, 11, 1690.
- [20] J. S. Hu, L. L. Ren, Y. G. Guo, *Angew. Chem.* **2005**, 117, 1295.
- [21] N. Pinna, K. Weiss, J. Urban, M. P. Pileni, *Adv. Mater.* **2001**, 13, 261.
- [22] J. Zhang, Q. Xu, Z. Feng, M. Li, C. Li, *Angew. Chem. Int. Ed.* **2008**, 47, 1766.
- [23] S.S. Warule, N.S. Chaudhari, B.B. Kale, M.A. More, *CrystEngComm* **2009**, 11, 2776.
- [24] G. Xiao, J. Ning, Z. Liu, *CrystEngComm* **2012**, 14, 2139.
- [25] W. Youn Kim, Y. Cheol Choi, K. S. Kim, *J. Mater. Chem.* **2008**, 18, 4510.
- [26] N. Pinna, G. Neri, M. Antonietti, M. Niederberger, *Angew. Chem. Int. Ed.* **2004**, 43, 4345.
- [27] S. Rittikulsittichai, B. Singhana, W.W. Bryan, *RSC Adv.* **2013**, 3, 7838.
- [28] X. Peng, M. C. Schlamp, A. V. Kadavanich, A. P. Alivisatos, *Journal of the American Chemical Society* **1997**, 119, 7019.
- [29] A. Aharoni, T. Mokari, I. Popov, U. Banin, *Journal of the American Chemical Society* **2006**, 128, 257.
- [30] M. Smith, S. Nie, *Accounts of Chemical Research* **2009**, 43, 190.
- [31] A. I. Ekimov, A. A. Onushchenko, A. V. Tzehomskii, *Sov. Phys. Chem. Glass* **1980**, 6, 511.
- [32] A. Henglein, *Ber. Bunsenges. Phy. Chem.* **1982**, 86, 301.
-

- [33] M.A. Reed, J.N. Randall, R. J. Aggarwal, R. J. Matyi, T. M. Moore, A.E. Wetsel, *Phys. Rev. Lett.* **1988**, *60*, 535.
- [34] C. B. Murray, D. J. Norris, M. G. Bawendi, *J. Am. Chem. Soc.* **1993**, *115*, 8706.
- [35] S A Tovstun, V F Razumov, *Russ. Chem. Bull., Int. Ed.* **2011**, 1203.
- [36] D. M. Donegá, Celso, P. Liljeroth, D. Vanmaekelbergh, *Small* **2005**, *1*, 1152.
- [37] J. Wang, S. Han, D. Ke, R. Wang, *J. Nanomater.* **2012** N129041.
- [38] Y.F. Liu, J.S. Yu, *Journal of Colloid and Interface Science* **2009**, *333*, 690.
- [39] Z. Li, C. Dong, L. Tang, X. Zhu, H. Chen, J. Ren, *Luminescence* **2011**, *26*, 439.
- [40] M. Baghbanzadeh, L. Carbone, P. D. Cozzoli, C. O. Kappe, *Angew. Chem., Int. Ed.* **2011**, *50*, 11312.
- [41] A. J. de Mello, M. Habgood, N. L. Lancaster, T. Welton, R. C. R. Wootton, *Lab Chip* **2004**, *4*, 417.
- [42] M. Ristov, G. Sinadinovski, I. Grozdanov, M. Mitreski, *Thin Solid Films* **1989**, *173*, 53.
- [43] S. Park, B. L. Clark, D. A. Keszler, J. P. Bender, J. F. Wager, T. A. Reynolds, G. S. Herman, *Science* **2002**, *297*, 65.
- [44] J.J. Li, Y.A. Wang, W. Guo, J.C. Keay, T.D. Mishima, M.B. Johnson, X. Peng, *Journal of the American Chemical Society* **2003**, *125*, 12567.

Chapter 2

Materials and Experimental Techniques

Abstract: This chapter discusses the materials and different techniques used to do all the experimental works. Synthesis of QDs were done by hot injection method. Physical characterization techniques were UV-vis absorption spectroscopy, Fluorescence spectroscopy, Zeta potential technique, DLS, XRD, FTIR, TEM, HRTEM & SEAD, TRFS, and PPMS. CD was used to see the changes in secondary structure in proteins. Microtiter plate assay and Broth micro dilution were used for antimicrobial activity. In vitro biocompatibility were done by MTT assay, DCFH-DA assay, TEM, confocal fluorescence microscopy, fluorescence microscopy of JC-1 and western blot analysis.



Pictorial representation of hot injection synthesis of QDs is shown here.

2.1 Materials

Different chemicals for synthesis of quantum dots, synthetic nanostructures i.e. nanoclays, proteins, enzyme, microbe and different cell lines were used to do the experiments related to this thesis.

2.1.1 Materials used for Synthesis of Quantum Dots

The chemicals needed for the synthesis of quantum dots, cadmium oxide CdO, Manganese (II) acetate tetrahydrate ((CH₃COO)₂Mn • 4H₂O) (99%), Se powder (99%), oleic acid (OA, 90%), methanol, hexane, chloroform and acetone were obtained from CDH, India. 1-Octadecene and trioctylphosphine (TOP) were purchased from Sigma Aldrich. 3-mercaptopropionic acid (MPA) was purchased from Fisher Scientific. And all

the reagents were used as received. Methanol, hexane, chloroform, acetone from CDH and deionized water from Organo Biotech Laboratories, India were obtained and used as solvent. For synthesis of surfactant functionalized QDs, following surfactants were used.

Table 2.1: Surfactants used in synthesis process.

S. No.	Ligand	Nature	Structure
1	OA	Hydrophobic	
2	CTAB	Cationic	
3	DTAB	Cationic	
4	SDS	Anionic	
5	TX-100	Neutral	

2.1.2 Anisotropic Nanoclays: Laponite and Montmorillonite

Nanoclays are known to be natural “coin-like” materials (layered mineral silicates) present in the soil (clay fraction) among which montmorillonite (MMT) is naturally occurring clay while Laponite RD[®] is synthetic clay developed by Laporte industries.

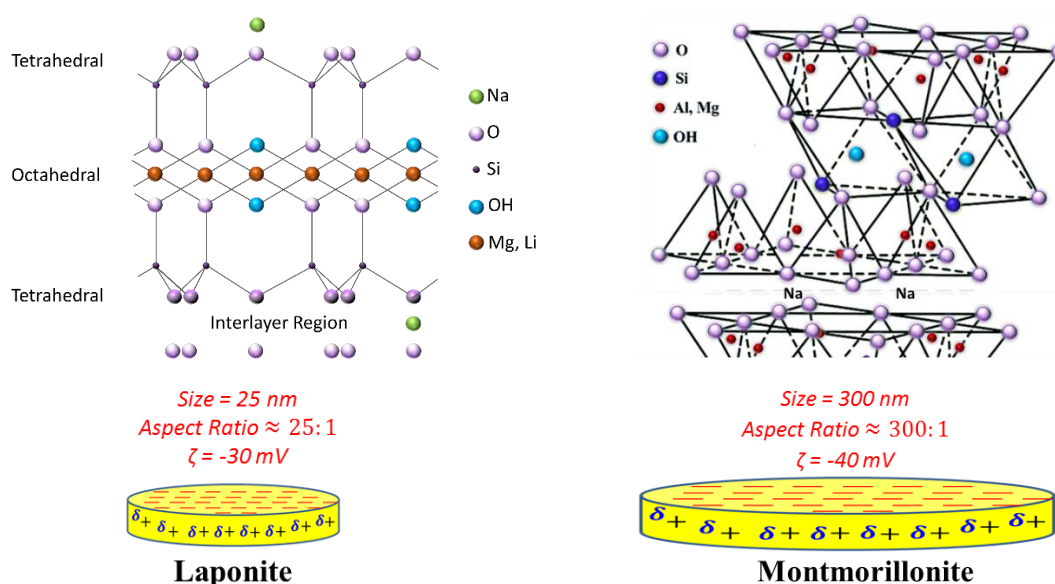


Figure 2.1: The schematic illustrations of nanoclays i.e. Laponite and Na-MMT.

The chemical formula of Laponite is $\text{Na}^{0.7} [(\text{Si}_8\text{Mg}_{5.5}\text{Li}_{0.3}) \text{O}_{20} (\text{OH})_4]^{-0.7}$ and for MMT it is $(\text{Na},\text{Ca})_{0.33}(\text{Al},\text{Mg})_2\text{Si}_4\text{O}_{10}(\text{OH})_2 \cdot n\text{H}_2\text{O}$. In the water-dispersion of nanoclays, released

sodium ions from their faces produce negative charge on it and protonation of the hydroxide group on crystal structure boundary give the fractional positive charge on the rim. The cation exchange capacity of Laponite and MMT are 0.75 and 0.92 mmol g⁻¹ respectively. Both Laponite and MMT have platelet morphology with typical face diameter of 30 and 300 nm, respectively, but both have a common thickness of 1 nm. They are water dispersible, and exhibit zeta potential of -40 and -30 mV, respectively. The faces are negatively charged while the rims possess positive charge. More details on the physical properties of these systems can be obtained from refs [1-2]^[1-2]. Drug molecules can be selectively intercalated into the interlayer galleries of MMT by screened electrostatic interactions because of its excellent swelling property, and relatively high cation exchange capacity.^[3] In addition, nanoclays have found applications in personal care products, painting, and polymer nanocomposites as rheology modifier.

The well characterized nanoclays (in the powdered form) were procured from Southern Clay Products, USA.

2.1.3 Globular Plasma Proteins

The serum albumin proteins used in our study are the most abundant proteins found in the plasma. These three globular plasma proteins namely, bovine serum albumin (BSA), human serum albumin (HSA), and β -lactoglobulin (β -Lg) are the principal carriers for the storage, and transport of endogenous, and exogenous drug molecules.

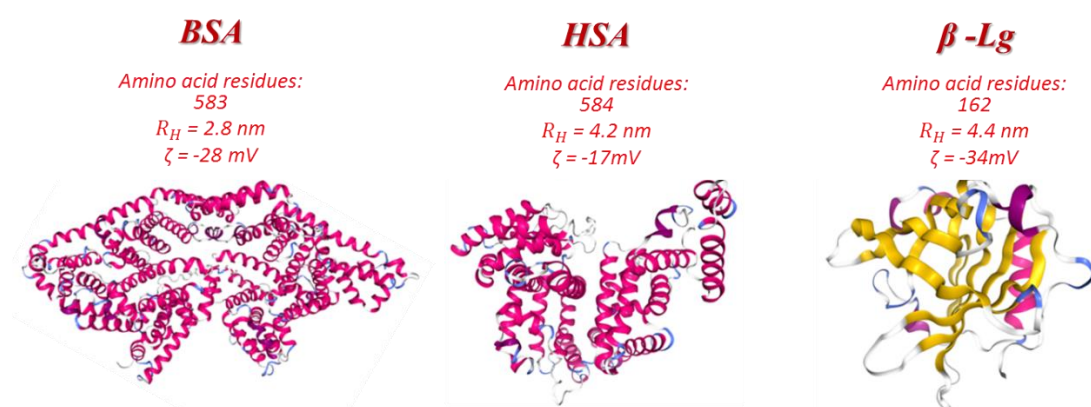


Figure 2.2: The proteins images were taken from the RCSB PDB (www.rcsb.org) and coloured by secondary structure. BSA is most helical and β -Lg is the least.^[4]

In addition, these help in maintaining the osmotic pressure in the circulatory system, function as nutrition carriers, and act as pH buffer. We have given preference to these proteins because of their strong affinity to bind to a variety of inorganic molecules.

Moreover, these stand out as model proteins as most of their physic-chemical properties are well documented in the literature.^[4]

Bovine serum albumin (BSA), β -lactoglobulin (β -Lg) and human serum albumin (HSA) were procured from Sigma-Aldrich chemical company (U.S.A.), which had a purity of > 96%. These were used as received without further purification.

2.1.4 Lysozyme

Lysozyme is small, monomeric, globular bacteriolytic protein of 129 amino acids cross-linked with four disulfide bridges containing six tryptophan, three tyrosine, and four disulphide bonds. Its molecular mass is 14.7 kDa. It has two dominant fluorophores, Trp62 and Trp108. The analysis of the fluorescence properties of these tryptophan residues which depend on their environment provides information of the lysozyme–ligand interaction. The enzyme is often used for lysing bacterial cells such as *Micrococcus lysodeikticus* by hydrolyzing the peptidoglycan present in the cell walls. Therefore *Micrococcus lysodeikticus* is suitable as a lysozyme substrate.

This lysozyme preparation is purified from chicken egg white, crystallized three times, dialyzed, and supplied as a lyophilized powder.

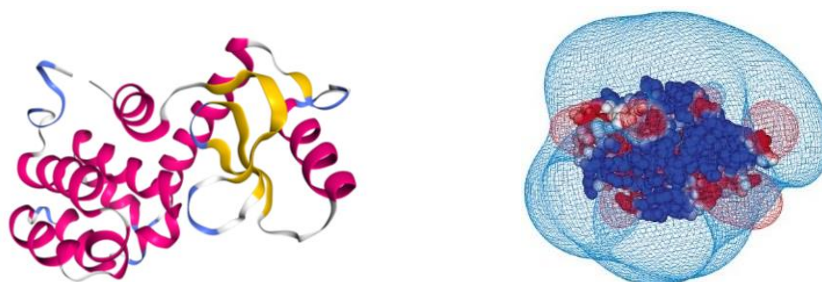


Figure 2.3: The Lysozyme images were taken from the RCSB PDB (www.rcsb.org) and left one is coloured by secondary structure and right one is with surface charge density. Red colour correspond to negative surface charge and blue for positive.

Lysozyme (90%) and *Micrococcus lysodeikticus* and their above discussed specifications were taken from Sigma-Aldrich (Batch no. L6876).

2.1.5 *Candida albicans*

Candida albicans is a shape-changing, pathogenic opportunistic human fungus (yeast) that is normal member in the gastrointestinal tract, mouth and mucous membranes with the other yeasts and bacteria that live there. It is known to cause serious fungal infections ranging from mycoses to severe systemic infections. It is a dimorphic commensal organism that turns pathogenic in individuals with compromised immune system. Most common infection caused by *Candida* includes oro-pharyngeal thrush and vaginal yeast

infections. Though a number of antifungal formulations and drugs are in use against *Candida*, its rapid mutation and drug resistant property poses a major challenge to its antifungal therapy. Additionally, the combination of its complex life cycle, inefficient vaccines and poor efficiency of existing drugs, demands a robust therapy against this opportunistic pathogen.^[5]

In vitro culture of *Candida albicans* CAF2-1 was maintained in YEPD medium (Yeast extract, Peptone, Dextrose). For experimental analysis, the cultures were streaked on YEPD agar medium and allowed to grow by incubating the plates at 37°C for 16 hours. The cultures were then stored at 4°C for further use.

2.1.6 Cell lines

A cell line is consisting of cells, pertaining from particular tissue, with identical genetic composition and it will grow indefinitely under appropriate physiological conditions. It is the representative of the specific biological system from which it is isolated.

Cell lines have achieved an important place in the study of physiology and pathology. It allows the examination of staging changes in cell structure, biology, and genetic makeup under controlled environment. It allows to investigate the structural, biological and genetical modifications in the cell in every step under controlled conditions.

HeLa cell line is a cervical cancer cell line, MCF-7 is a breast cancer cell line and HEK-293 is derived from normal human embryonic kidney cells.

Cells were obtained from National Center for Cell Science, Pune, India. These cells were cultured at 37° C temperature in the presence of 5% CO₂ in DMEM (Dulbecco's Modified Eagle's Medium) additional supplemented with 100 µg/ml streptomycin, 100 U/ml penicillin and 10% FCS (Fetal calf serum)

2.2 Synthesis Method and Setup

Quantum dots were synthesized by well-established hot injection method.^[6] There are so many methods to synthesized nanoparticles or quantum dots but the hot injection technique is based on a “nucleation” event due to which highly uniform size QDs are produced and these nanoparticles have high luminescence quantum yield. In this method, we have good control on particle size and can get high crystallinity due to synthesis in high temperature. The use of non-ionic precursors in high-boiling organic solvents is responsible for the slow growth of the nanoparticles at high temperature, which yields well-passivated and defect-free nanocrystals. Separation of the nucleation and growth process, that produces very high monodispersity without any post-synthesis size-

selective techniques, is the next important aspect of this method [7]. The schematic air-free synthesis set up is shown in Figure 2.4. All synthesization have done by this set up.

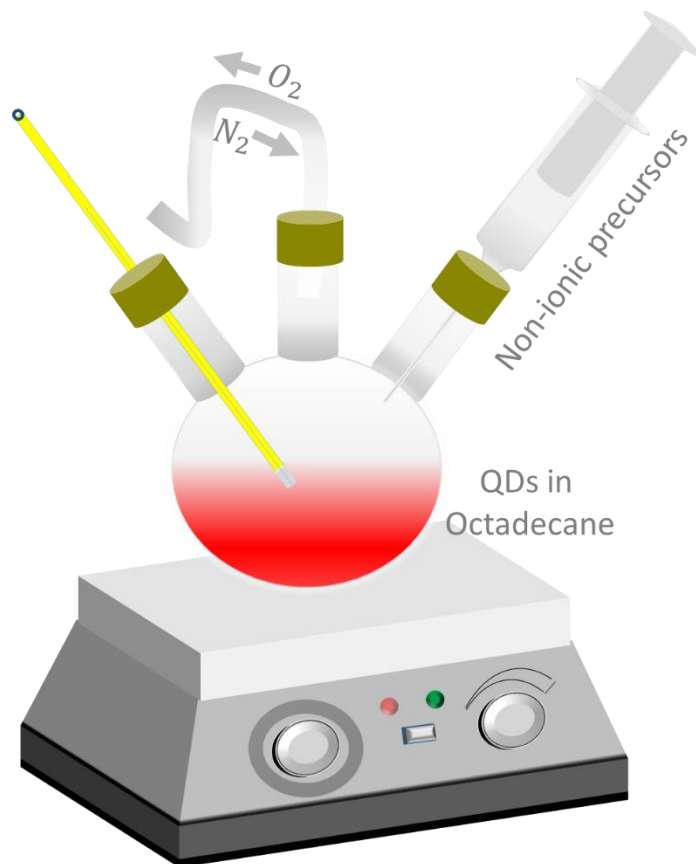


Figure 2.4: Schematic diagram of the air-free synthesis setup for synthesizing QDs.

2.3 Synthesis

By the above discussed hot injection method, different sized quantum dots without and with shells were synthesized. After filtering unreacted precursors, excess organic ligands and by-products, these QDs were converted into hydrophilic from hydrophobic by ligand exchange process. All processes are explained in the following sections.

2.3.1 Synthesis of Selenium based QDs in the Organic Phase

QDs of different size with oleic acid capping were synthesized by the hot injection method using non-ionic precursors in the synthesis setup at constant temperature.

Se precursor was freshly prepared by mixing 80 mg of Se (weighted by highly calibrated weighing machine) and 2 ml of trioctylphosphine (TOP) drawn by calibrated micro-syringe from its sealed bottle in 3 ml of 1-octadecene (ODE) (90%) in an opaque flask that was clamped on a hot plate kept at a temperature of 60⁰ C. The solution was stirred for about 30 min. This stock solution was stored at room temperature (25⁰C) in same air light bottle.

2.3.1.1 Synthesis of Fluorescent CdSe QDs

Cd precursor was made by adding 26 mg of CdO to a 25 ml round-bottom flask containing 0.6 ml of oleic acid and 10 ml of octadecene. The flask was heated gradually and maintained to the fix temperature above 200⁰C. When the solution turned colourless due to the formation of cadmium oleate, 1 ml of previously prepared selenium solution premixed with ligand was injected swiftly into that hot cadmium solution. The physical size and conformation of the products depend on reaction time and temperature. Therefore, timing began when the selenium solution was added to the reaction vessel. The structures were grown until the required size was achieved (growth period after nucleation was the key parameter) which took less than 15 min. Samples were removed from hot plate and stored in glass vials.

2.3.1.2 Synthesis of Highly Fluorescent CdSe /CdS QDs

To make the cadmium precursor for the synthesis of core-shell structures, a solution of CdO (78 mg), OA (1.8 ml), and ODE (3.2 ml) was heated to 290 ⁰C and stirred till it turned colourless, cooled it to ≤ 100 ⁰C and stored.

Sulphur precursor was prepared by mixing 19 mg of S and 1 ml of trioctylphosphine (TOP) in 4 ml of 1-octadecene (ODE) (90%) in an opaque flask and was heated at temperature 60⁰ C and stirred till it turned colourless. This stock solution was stored at room temperature (25⁰C) in same air tight bottle. Both solution was then added drop-wise by equal volume into the previously prepared reaction solution that contained CdSe QDs of the desired size, onto which had to be coated and the reaction temperature was kept below the synthesis temperature. Shell thickness depends on the added volume of precursors used for making the shell so we have to add as much volume as the thickness is required.

2.3.1.3 Synthesis of MnSe QDs in the Organic Phase

Mn precursor was prepared by adding 13 mg of $(CH_3COO)_2Mn \cdot 4H_2O$ to a 25 ml round-bottom borosilicate flask containing 0.6 ml of oleic acid (OA) and 10 ml of octadecene. This mixture was heated up to fix temperature above 200⁰C. After dissolution of manganese (II) acetate tetrahydrate, 1 ml of Se precursor is swiftly injected in this hot Mn solution and the solution was allowed to vigourously stirred for 10 minutes. After that it was left to cool down naturally. With varying the temperature we can make different size of QDs.

2.3.2 Purification

For filtering unreacted precursors, excess ligands and by-products, cooled reacted samples in hexane was mixed in extraction solvent (an equal volume mixture of $CHCl_3 / CH_3OH$) and then extracted from it. This process was repeated thrice. The unreacted precursors and excess OA were extracted into the CH_3OH (methanol) layer and only QDs remained in the ODE / hexanes layer. All samples were isolated using methanol and excess acetone. After centrifuging for 10 min at 10 000 rpm and the products were collected.

2.3.3 Transformation into Hydrophilic by Ligands Exchange

For making water-soluble, these QDs were transformed from hydrophobic into hydrophilic phase, 5 ml of OA capped QDs were dispersed in 25 ml of chloroform to which 2 ml of a basic methanolic solution (pH~10) of MPA (~1.5 times of metal atom) with 2.5 ml of DI water was added. After stirring, the MPA capped QDs were transferred into the water phase. By centrifugation and decantation, excess MPA was removed from aqueous dispersion of QDs. This aqueous dispersion was further used for experiments.

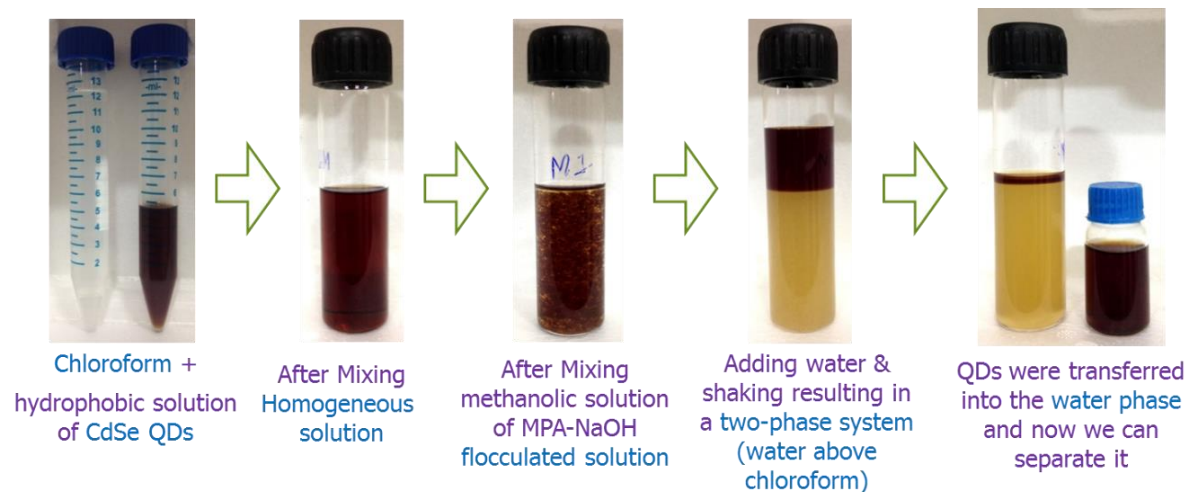


Figure 2.5: Making water soluble from oil soluble by legend exchange process.

2.4 Characterization Techniques

Electromagnetic radiation is one of the best probes for getting the information about the structure and dynamics of the matter. The scattering of light from any matter gives the idea about its shape, size and internal details. The absorption of microwave, infrared (IR), visible (vis) and ultraviolet (UV) radiation has offered detailed understanding about rotational, vibrational, and electronic energy levels of molecules.

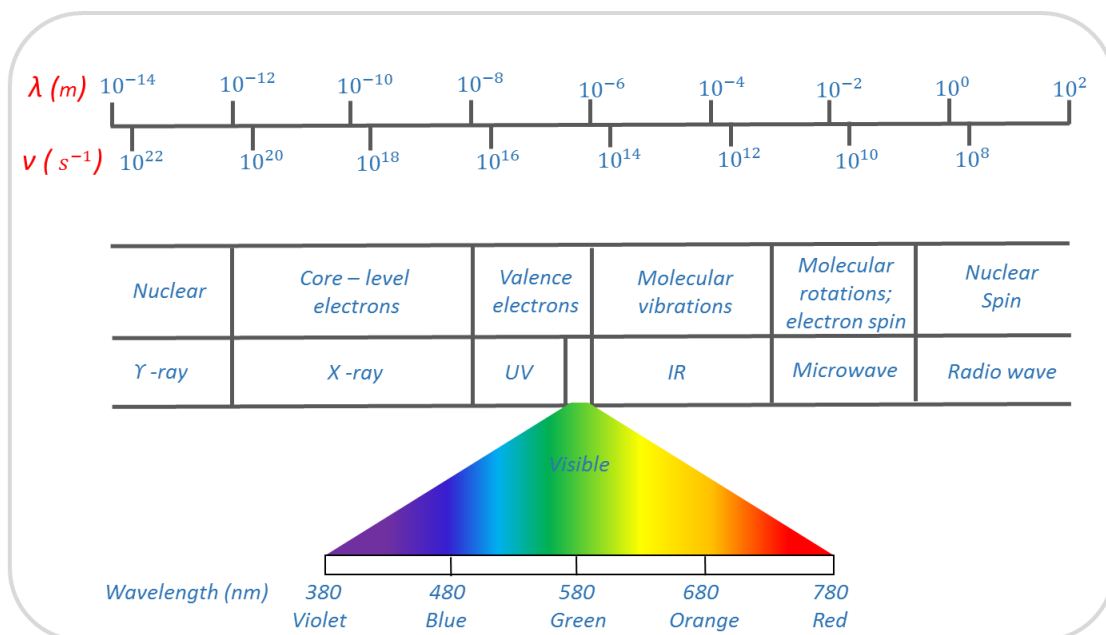


Figure 2.6: Making water soluble from oil soluble by legend exchange process.

Quantum mechanical explanation is that when photons incident on a molecule they scatter either elastically (Rayleigh scattering) or inelastically (Raman scattering). In inelastic scattering, their frequency shifts corresponding to the translational, rotational, vibrational and electronic transitions.

Classical explanation is that when light incidents on matter, the electric field of the light induces an oscillation of same frequency in the electron cloud of the molecules. The oscillation (accelerated motion) of these charge particles behave as secondary sources of light and radiate electromagnetic waves as any accelerated charge does. The frequency shifts, the angular distribution, the polarization and the intensity of the scattered light depend on the size, shape and the molecular interactions in the scattering material.

So we have used different techniques based on the above principle to describe the properties of synthesized QDs.

2.4.1 Physical Characterization

To determine structure-property relationship, all structural characterizations were systematically done.

2.4.1.1 Structure Characterization

Structure characterization were transmission electron microscopy (to measure the accurate size, size dispersity), high resolution transmission electron microscopy and selected area electron diffraction (to see and measure the crystallinity of NPs and QDs), X-ray diffraction (for getting crystal structure and crystallite size), dynamic light

scattering (to measure the hydrodynamic size and for study the dynamics in water), Fourier transform infra-red spectroscopy (to confirm the binding and coating) and Zeta potential technique (to confirm the capping by measuring surface charge).

I: Transmission Electron Microscopy (TEM)

To see any objects, our probe's size should be comparable to the size of that object but not more than that otherwise we cannot see it clearly. So to examine and viewing the nanoscopic material with great resolution, the maximum size of the probe should be nanoscopic. Since the minimum wavelength of visible light is 0.4 micrometre, we can see only microscopic things with it. So to examine and viewing the nanoscopic material with great resolution, that is the work of TEM, nanoscopic probe will be needed. And that is highly energetic electrons with very short de Broglie wavelengths (10,000 times shorter than that of visible light). The de Broglie wavelength, λ of electron (mass m_e and charge e) accelerated by voltage, 'V' in free space is given by-

$$\lambda = \frac{h}{p} = \frac{h}{\sqrt{2m_e eV}} = \sqrt{\frac{h^2/2m_e e}{V}} \Rightarrow \lambda(nm) = \frac{1.505}{\sqrt{V(volts)}} \quad (2.1)$$

But in matter, mass of electron (m_e) is replaced by its effective mass, 'm' in that matter and its de Broglie wavelength will be

$$\lambda = \frac{h}{\sqrt{2meV}} = \sqrt{\frac{h^2/2m_e e}{m_r V}} \Rightarrow \lambda(nm) = \frac{1.505}{\sqrt{m_r V(volts)}} \quad (2.2)$$

where $m_r = m/m_e$ is the effective mass ratio. With the help of equation 2.2, we can calculate the resolution limit of electron probe that is on the order of 0.01 nm.

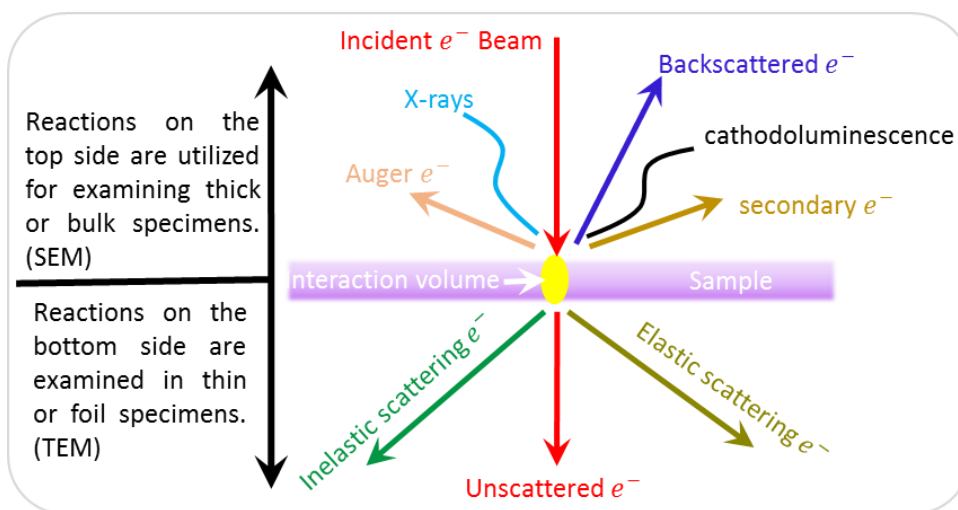


Figure 2.7: Various type of phenomena which take place after interaction of electron with matter.

Energetic electron interacts with matter and produce different types of radiations and electrons as shown in Figure 2.7.

In TEM, highly energetic electrons beam are made to pass through the very thin sample loaded on carbon coated copper grid and the image is formed on the fluorescent screen or captured by CCD camera, either by using the transmitted beam or by using the diffracted beam.

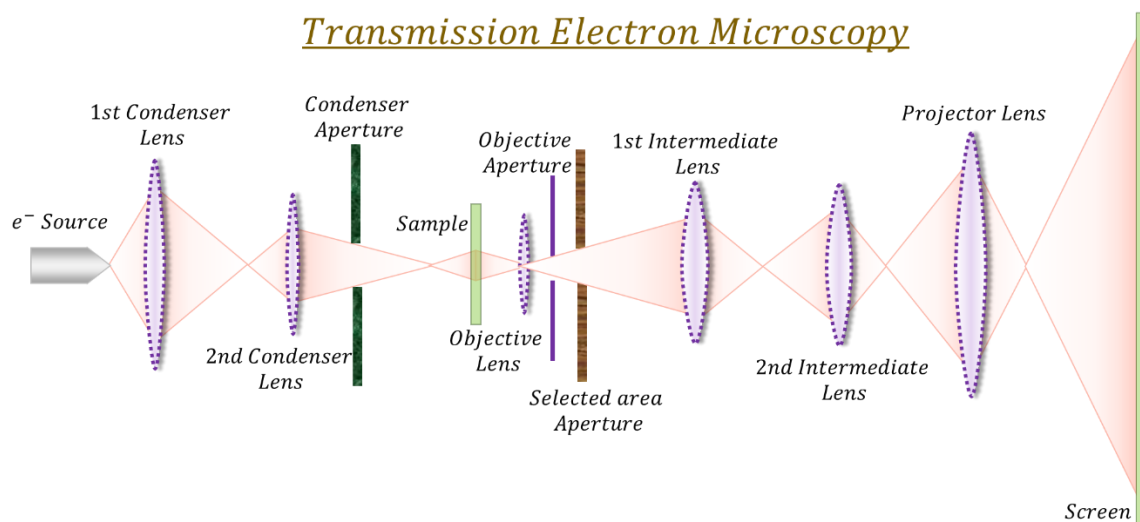


Figure 2.8: The schematic diagram for the working of TEM. All lenses are electromagnetic lenses.

By this technique we can get topographical (the surface features like softness, transmissivity etc.), morphological, compositional and crystalline nature of any material.

The working of TEM shown in Figure 2.8.

The study about size, shape and size distribution of the nanoparticles were done by JEOL 2100F TEM in which electrons were accelerated by 200 kV. Carbon-coated copper grid with 300 mesh size is used to hold the sample for imaging. Images were analysed by Image J software to get the above said information. Typical TEM, HRTEM image with SAED pattern are shown in Figure 2.9.

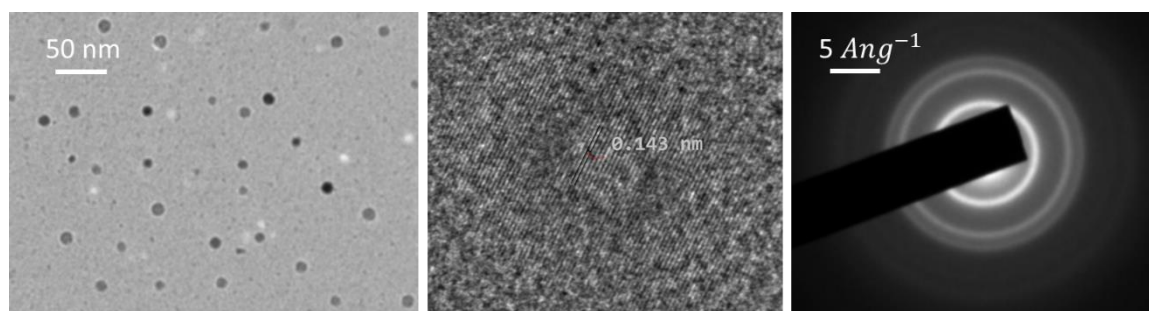


Figure 2.9: The Typical TEM, HRTEM image with SAED pattern are shown.

II: X-ray Diffraction (XRD)

Since X-rays have wavelengths of the order of 0.01 to 10 nm, they can be used to analyse lattice parameters (atomic size ~ 0.1 nm) after making their interaction with matter. When X-rays impinge upon an atom, they elastically scatter and interfere with each other and produce a pattern. This pattern, called Bragg diffraction, is the basis of diffraction analysis.

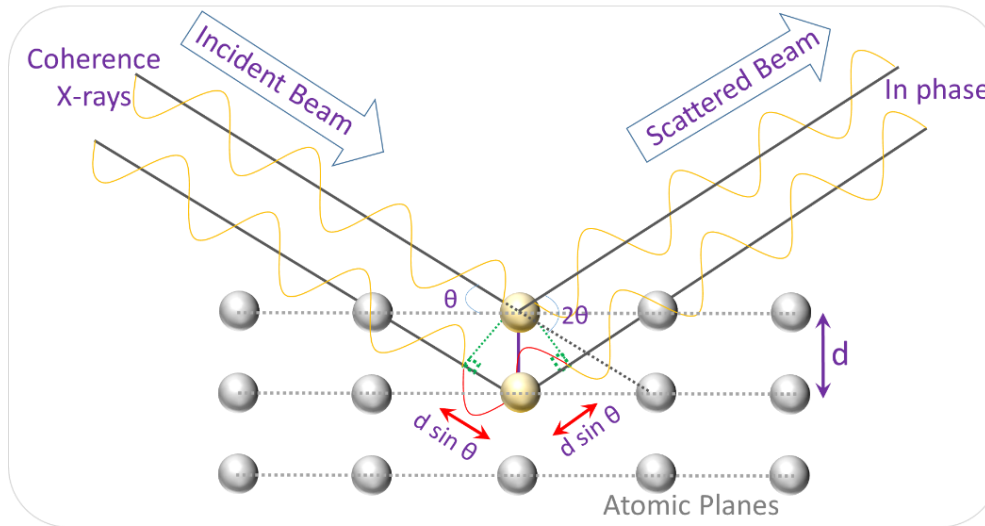


Figure 2.10: The schematic representation of the Bragg's equation is shown.

For getting maxima (peak) i.e. constructive interference, scattered beam should be in phase. And from above diagram, we get the condition for in phase scattered beam that is

$$n\lambda = 2d \sin \theta \quad (2.3)$$

It is clear that the powder diffraction peak position depends on lattice spacing and peak intensity on number of scattering lattice point. But peak broadening comes from mainly two factors, crystallite size and inhomogeneous microstrain.

Take the derivative of equation 2.3 with varying 'd' and 'theta' keeping 'lambda' constant –

$$\lambda = 2 \Delta d \cos \theta \Delta \theta \quad (2.4)$$

Positive value of ' $\Delta\theta$ ' is taken. $\Delta\theta$ is the half width of the XRD peak and Δd is the thickness of the crystal. If the Gaussian peak is considered rather than triangular peak, a prefactor of 0.91 should be added. Now the crystallite size, 't' is calculated as (Debye-Scherrer formula) ^[8]

$$t = \Delta d = \frac{0.91 \lambda}{\beta_L \cos \theta} \quad (2.5)$$

where $\beta_L (= 2 \Delta\theta)$ is the full width at half maxima of the XRD peak.

The contribution of microstrain's broadening is

$$\beta_{MS} = C \varepsilon \tan \theta \quad (2.6)$$

where $c (=4)$ is constant for spherical NPs and ε is strain. So the total broadening is

$$\beta = \beta_L + \beta_{MS} = \frac{0.91 \lambda}{t \cos \theta} + \frac{4 \varepsilon \sin \theta}{\cos \theta} \Rightarrow \beta \cos \theta = \frac{0.91 \lambda}{t} + 4 \varepsilon \sin \theta \quad (2.7)$$

By the equation 2.7 (Williamson-Hall Plot) we can calculate crystallite size and microstrain of any nanoparticles from its XRD peak.

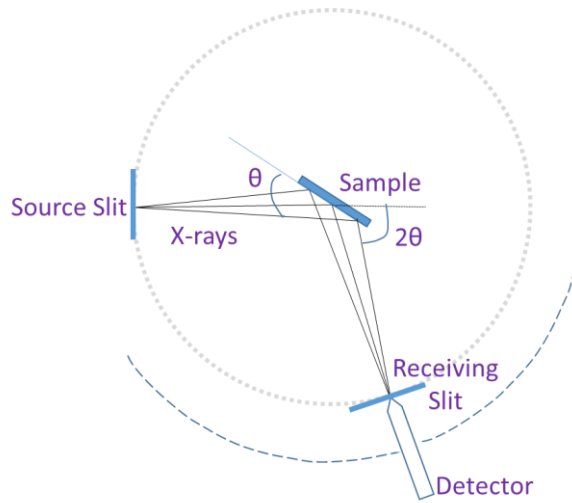


Figure 2.11: The schematic diagram for XRD- arrangement is shown.

In XRD experiment, the X-rays source and detector are movable on a circular path and sample holder is at its centre. The sample surface is always at angle θ and detector at angle 2θ to the incident X-rays. Divergent X-rays incident on the sample surface at different points and after diffracting they converge on detector. This arrangement is called parafocusing. This arrangement gives best result i.e. intensity, peak position and angular resolution. The arrangement of XRD is shown in Figure 2.11. By XRD technique, crystalline phase and orientation can be identified and structural parameter can be determined.

X-Ray diffraction (XRD) investigations were carried out on the Rigaku D/Max 2200 powder X-ray diffractometer that is fully automated and equipped with a Bragg-Brentano focusing geometry in the 2θ range from 10 - 100° and use Cu- $K\alpha$ radiation ($\lambda=1.5406 \text{ \AA}$).

III: Dynamic Light Scattering (DLS)

It is a technique to measure the size distribution or polydispersity and mean hydrodynamic size (d_H) of particles typically in the submicron region in colloidal

suspension. It uses an auto-correlation technique to measure and process the temporal fluctuations (with time) of Rayleigh scattered light (by particles), which gives diffusivity (D) hence size using the Stokes-Einstein relation.

Brownian motion: It is the stochastic motion of the particles under the fluctuated concentration gradient in the colloidal solution. It depends not only on the size and shape of the particles but also on the temperature and viscosity of the solution. During the measurement, temperature should be stable. If not, temperature gradient will cause biased movements which gives wrong size interpretation.

Particle size can be calculated from the translational diffusion coefficient (D) using the Stokes-Einstein Equation:

$$d_H = \frac{k_B T}{3\pi\eta D} \quad (2.8)$$

Where η is the solvent viscosity, T is temperature (in K) and k_B is Boltzmann constant.

Hydrodynamic Size: The diameter or size of the apparent sphere that has the same translational diffusivity as the actual particle is called hydrodynamic size of that particle.

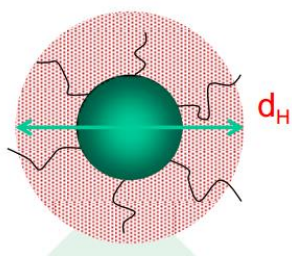


Figure 2.12: The hydrodynamic size of a spherical particle is shown.

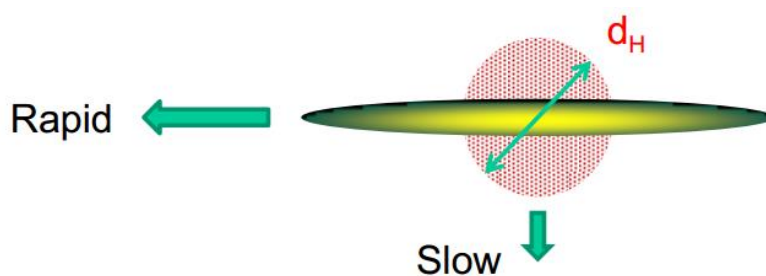


Figure 2.13: The hydrodynamic size of a non-spherical particle showing different diffusivity in different direction

Cause of Fluctuations: Let us imagine the particles that are freezed in their positions in the solution. They behave like ‘slits’ create interference patterns when illuminated by laser light. Scattered lights in phase interfere constructively making bright spot (speckle). These pattern will be stationary due to stationary slits.

Therefore for the randomly moving particles, the moving interference pattern is observed where the position of each bright spot is seen to be in constant motion, creating flickering. This fluctuation in intensity is directly depends on the Brownian motion hence size of the particle as shown in Figure 2.14.

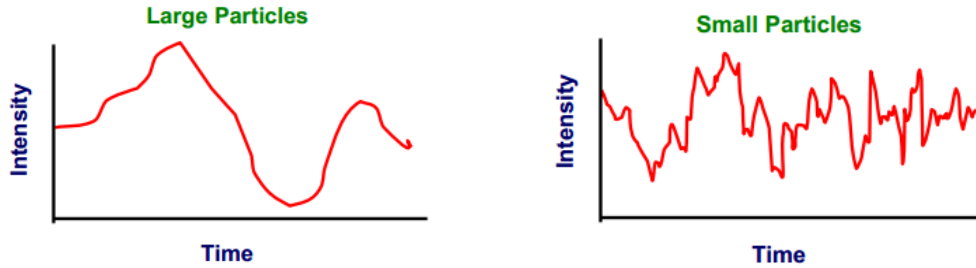


Figure 2.14: The intensity fluctuations arising from the Brownian motion of the particles in a colloidal dispersion.

It is impossible to know the movement of each particles from the “Flickering”. Instead, we can get the correlation between the motion of the each particles as shown in Figure 2.15.

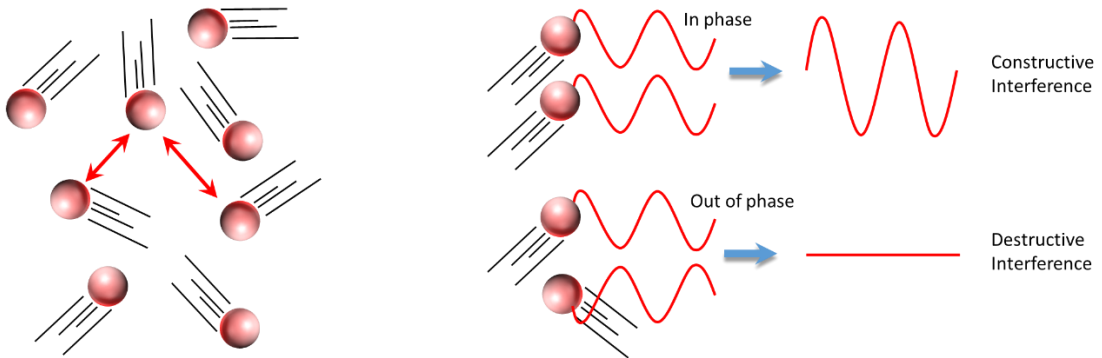


Figure 2.15: The intensity correlation of the motion of particles causes fluctuations in intensity patterns.

The normalized field (electric) auto correlation function, $g_1(\tau)$ is

$$g_1(\tau) = \frac{\langle \mathbf{E}^*(t) | \mathbf{E}(t + \tau) \rangle}{\langle \mathbf{E}^*(t) | \mathbf{E}(t) \rangle} = \exp(-Dq^2\tau) \quad (2.9)$$

where D is the diffusivity, τ is time and q is scattering wave vector.

The gaussian random processes is based on the principle that the two correlation function are related by the Seigert relationship. Since the scattering light is the same process, the directly measured intensity correlation function and the required electric field correlation function (recall: this is what the particles are doing) can also be equated by the Seigert relationship. Therefore normalized intensity correlation function, $g_2(\tau)$ is

$$\begin{aligned}
 g_2(\tau) &= \frac{\langle I^*(0) | I(\tau) \rangle}{\langle I^*(0) | I(0) \rangle} = \frac{\langle E_0^* E_0 | E_\tau E_\tau^* \rangle}{I^2} \\
 &= \frac{\langle E_0^* | E_0 \rangle \langle E_\tau | E_\tau^* \rangle + \langle E_0^* | E_\tau \rangle \langle E_0 | E_\tau^* \rangle + \langle E_0^* | E_\tau^* \rangle \langle E_0 | E_\tau \rangle}{I^2} \\
 &= \frac{I^2 + I^2 |g_1(\tau)|^2 + 0}{I^2} = 1 + |g_1(\tau)|^2
 \end{aligned}$$

But in general -

$$g_2(\tau) = B[1 + \beta |g_1(\tau)|^2] = B[1 + \beta \exp(-2Dq^2\tau)] \quad (2.10)$$

Where ‘B’ is baseline (background intensity at $\tau = \infty$). The coherence factor β is depends on the detector area, the optical alignment and the scattering properties of the system. Typically, values of 0.9–1 can be achieved. Conventionally the detector aperture is adjusted so that $\beta \sim 1$, i.e., only one coherence area (speckle) is measured.

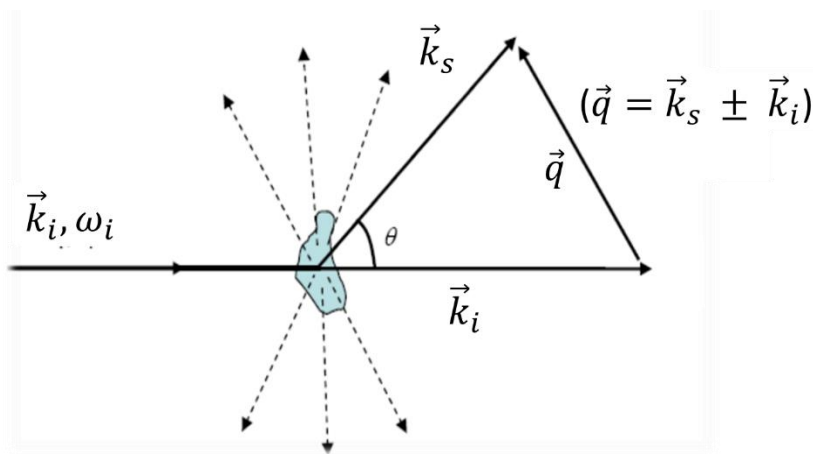


Figure 2.16: The scattering wave vectors having relations with each other are geometrically shown here.

The scattering wave vector, q can be calculated by

$$|q| = |K_i - K_s| = [K_i^2 + K_s^2 - 2K_i K_s \cos \theta]^{\frac{1}{2}} \quad (2.11)$$

Since

$$|K_i| = |K_s| = \frac{2\pi}{\lambda} = \frac{2\pi\eta}{\lambda_0} \quad (2.12)$$

Where η is the refractive index and λ_0 is the wavelength of the incident beam.

Therefore

$$|q| = \frac{4\pi\eta}{\lambda_0} \sin \frac{\theta}{2} \quad (2.13)$$

Decay of correlation function depends on the size of the moving particles. Diffusion is inversely proportional to the size of the particles. Therefore the correlation function decays at a slower rate for larger particles.

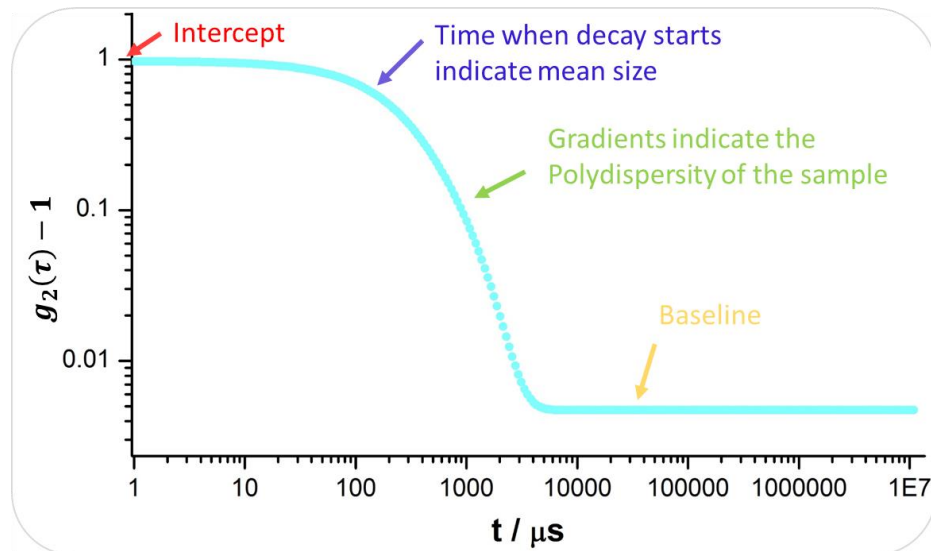


Figure 2.17: The correlogram from a measurement by DLS.

The starting and decaying time of the correlation have the information about the average size of the particles in the colloidal solution. The steepness the correlation curve tells us about the dispersity of the particles present in the sample. The steeper correlation curve means narrow size distribution of the particles.

Experimental Set-up: The setup used in DLS experiment is shown below.

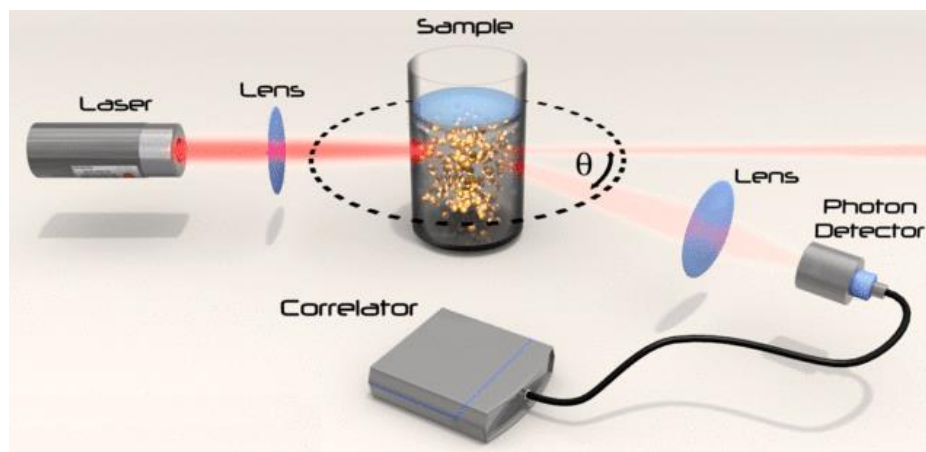


Figure 2.18: The schematic presentation of the DLS experiment, taken from photocor.

The intensity of unpolarised light can be resolve into parallel, I_{\parallel} and perpendicular I_{\perp} components. In Rayleigh scattering, these components have the following relations

$$I_{\parallel} = I_{0\parallel} k^4 \alpha^2 / r^2 \quad (2.14)$$

$$I_{\perp} = I_{0\perp} k^4 \alpha^2 \cos^2 \theta / r^2 \quad (2.15)$$

Where $k (= 2\pi/\lambda)$ is wave vector, α is polarizability, r is the distance of detector from scatterer and θ is the scattering angle. We see that the scattered light at 90° has no perpendicular component i.e. unpolarised incident light produce polarized light in Rayleigh scattering at 90° . If we want to make scattered light polarize to make pattern from unpolarised incident light, we have to take the measurement at 90° .

DLS experiments were performed by Photocor Instruments, USA at a scattering angle of $\theta = 90^\circ$. This instrument is equipped with a 35 mW linearly polarized He : Ne laser wavelength of $\lambda = 632.8$ nm. The CONTIN regression software was used to analyse the measured intensity autocorrelation functions to get the size distribution of the particles in the sample.

IV: Fourier Transform Infrared Spectroscopy (FT-IR)

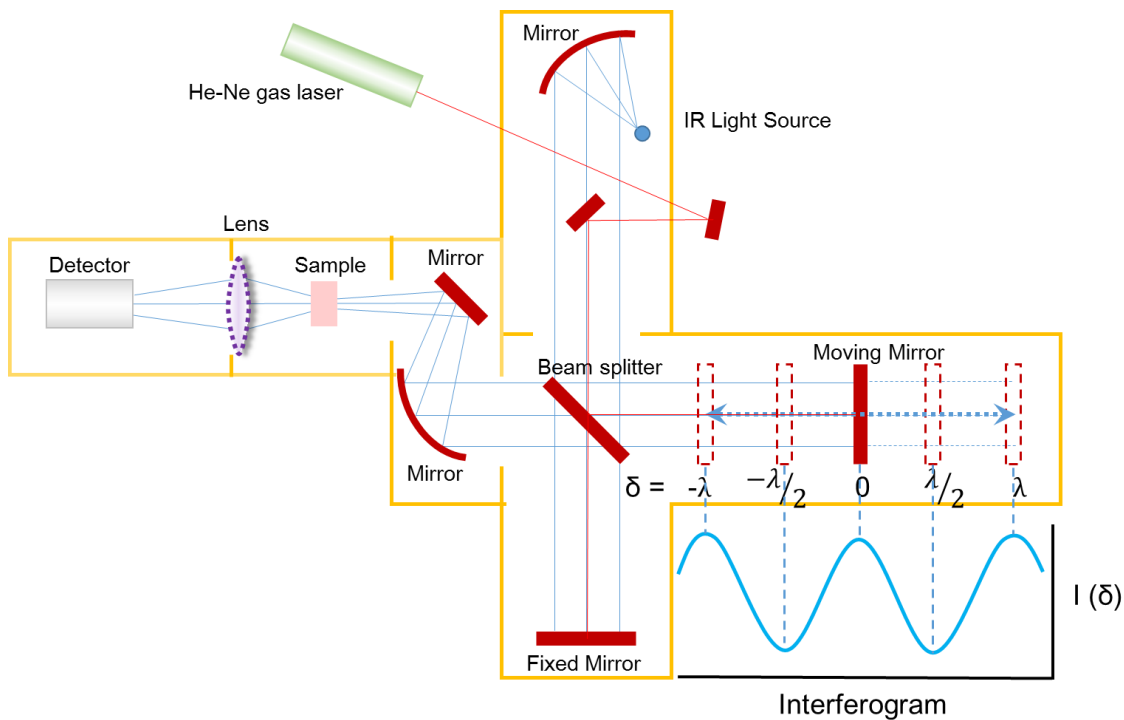


Figure 2.19: The schematic diagram and working of a FT-IR spectroscopy.

It is a vibrational spectroscopic method, to determine the presence of specific functional groups within a compound, in which the absorption of the infrared radiation by asymmetric molecular vibrations is measured by first obtaining an interferogram of a sample signal using an interferometer, then performs a Fourier transform on the interferogram to obtain the spectrum. Since the vibrational energy levels are unique to each molecule, the IR spectrum provide a “fingerprint” of a particular molecule.

Symmetric (or in-phase) vibrations and non-polar groups are most easily studied by Raman while asymmetric (or out-of-phase) vibrations and polar groups are most easily studied by IR.

As seen in the Figure 2.19, FT-IR spectroscopy contains Michelson interferometer which gives single cosine wave (with wavelength λ) of intensity (interferogram) due to constant longitudinal oscillation of moving mirror with the only condition that the light source emits the monochromatic light with same wavelength λ . The Fourier transform of this sinusoidal interferogram will give rise to a single band with a characteristic frequency and intensity of the monochromatic source.

But actually the light source is polychromator so the interferogram will superimposition of all the different cosine functions corresponding to all of the wavelengths and of the intensities in the source as seen in Figure 2.20.

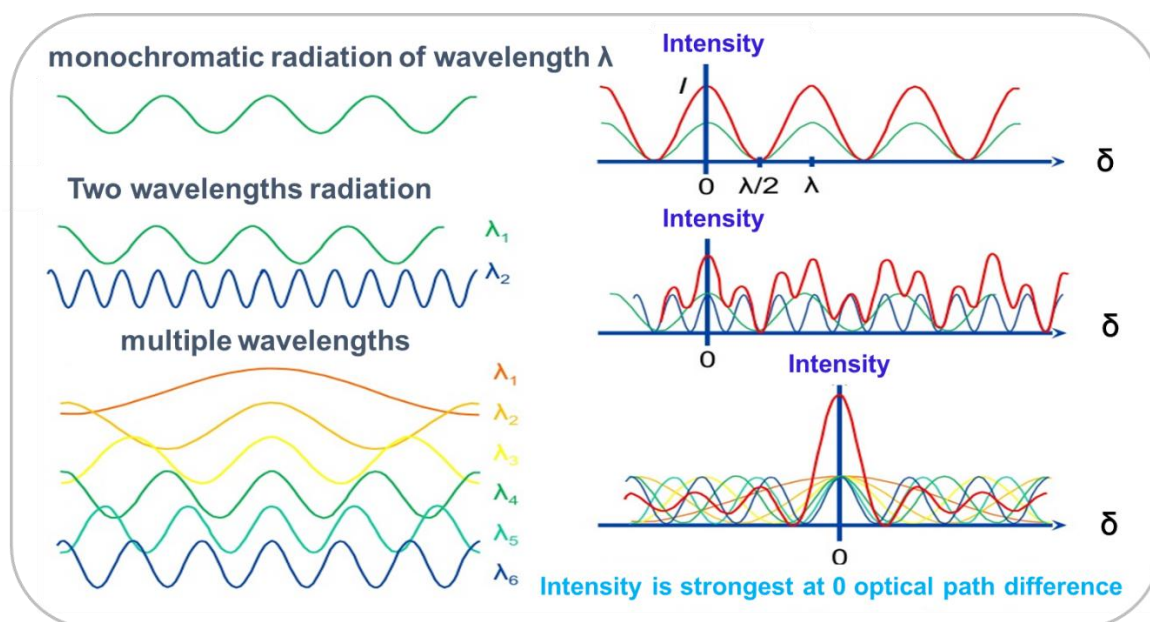


Figure 2.20: The schematic diagram of light interference of multiple wavelengths (interferogram) is shown.

Only at zero path difference will all the wavelengths be in-phase. Thus, the resulting interferogram in FT-IR spectra have a very strong center-burst and rapidly damped

intensity in the wings. And the fast Fourier transform of this spectra deconvolute it and gives the full spectrum.

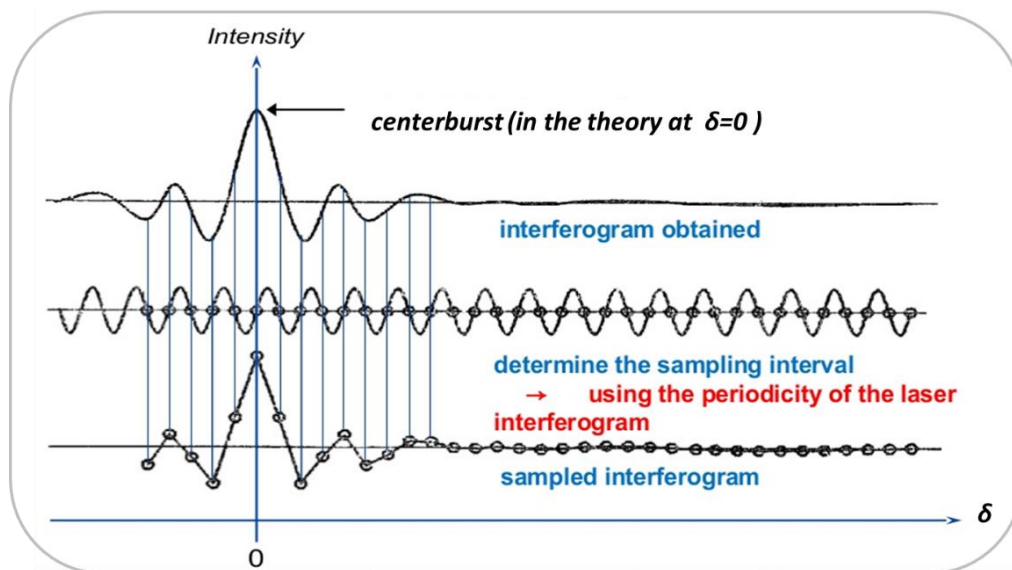


Figure 2.21: The role of laser, whose wavelength is the step of moving mirror, in FT-IR is shown.

Digilab (Varian) FTS 7000 FT-IR Spectrophotometer with UMA 600 Microscope is used to confirm the coating on QDs by identifying the functional groups of coating material in this thesis work.

V. Zeta Potential Technique

The charged particles in colloidal solution have electrical double layer on it. The electric potential on the boundary of the double layer is called zeta potential (ζ).

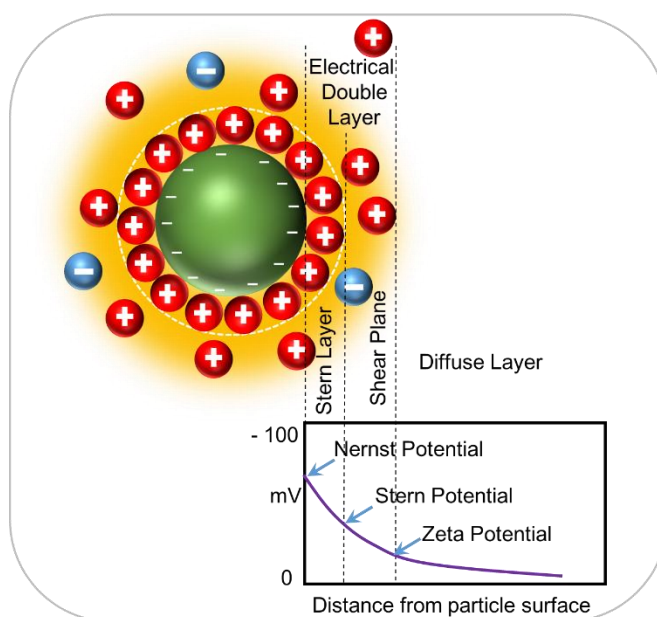


Figure 2.22: The schematic of an electrical double layer around a negatively charged particle with different potentials is shown.

Since double layer also moves with particle, the dynamics of the particle mostly depend on zeta potential. ζ can not be measure directly but can be calculated by its electrokinetics. ζ of dispersion is measured by electrophoresis in which charged particles move under an applied electric field. Electrophoretic mobility (velocity per unit electric field) of the particles can be measured by directly observing individual particles using a microscope and timing their transit across a graticule. And then ζ for non-interacting spherical particles in a solution can be calculated by the equation ^[9]

$$\zeta = 4\pi(\sigma / \varepsilon \kappa) \quad (2.16)$$

$$\zeta = 4\pi(\mu \eta / \varepsilon) \quad (2.17)$$

where μ is the electrophoretic mobility, η is solvent viscosity, σ is the surface charge density of the particle, ε is solvent dielectric constant and κ is Debye-Hückel parameter of the solution. In this thesis work, Cascade Microtech / ZEECOM ZC-2000 was used to measure ζ .

2.4.1.2 Property Characterization

The synthesized QDs have very different property from their bulk from optical to magnetic. To illustrate these properties, different techniques was used which describes in below sections.

2.4.1.2.1 Optical Property Characterization

If the nanoparticles have the unique optical properties like absorption and fluorescence, It means it is due to quantum confinement of charge carriers hence they are QDs. Optical properties characterization techniques were UV-vis absorption spectroscopy (to confirm the synthesis of nanoparticles (NPs) and for estimation of size, monodispersity and concentration), Fluorescence spectroscopy (to confirm the quantum confinement and for measuring fluorescence) and TRFS (for measuring fluorescence lifetime to calculate relative quantum yield),

I: UV-vis Absorption Spectroscopy

In UV-vis spectral region, electronic transitions of atoms and molecules are taking place. The peak in absorption spectra tells us about the energy of excited state. Absorbance is directly related to concentration of sample according to Beer-Lambert law

$$I = I_0 e^{-A} \Rightarrow A = \ln(I_0/I) = \varepsilon c L \quad (2.18)$$

where A is the measured absorbance, I_0 is the intensity of the monochromatic incident light, I is the intensity of transmitted light from sample, L is the sample thickness or path length, and c the concentration of the absorber. ϵ is molar extinction coefficient and a constant for each absorber and wavelength.

Quantum dots have very unique optical properties due to quantum confinement in all three dimensions. The absorption profile of quantum dots has information about size, concentration and particle size distribution. For CdSe QDs of size between 2 to 8 nm, the relations are ^[10]

$$D(\text{nm}) = 59.60816 - 0.54736 \lambda + 1.8873 * 10^{-3} \lambda^2 - 2.85743 * 10^{-6} \lambda^3 + 1.62974 * 10^{-9} \lambda^4 \quad (2.19)$$

$$\epsilon_{1S}(\text{M}^{-1}\text{cm}^{-1}) = 155.507 + 6.67054 * 10^{13} \exp\left(-\frac{E_{1S}}{0.10551}\right) \quad (2.20)$$

$$[\text{CdSe}](\text{M}) = \frac{\text{Abs}}{l(\text{cm})\epsilon_{1S}(\text{M}^{-1}\text{cm}^{-1})} \frac{\Delta E_{1S \text{ HWHM}}(\text{eV})}{0.06} \quad (2.21)$$

Where D is the diameter of QD, λ is first absorption peak, ϵ_{1S} is molar extinction coefficient for first transition, E_{1S} is the energy corresponds to first peak, $[\text{CdSe}]$ is concentration of QDs and $\Delta E_{1S \text{ HWHM}}$ is the half-width-half-maximum of the first absorption peak on the low energy side.

The working of this spectroscope as follow-

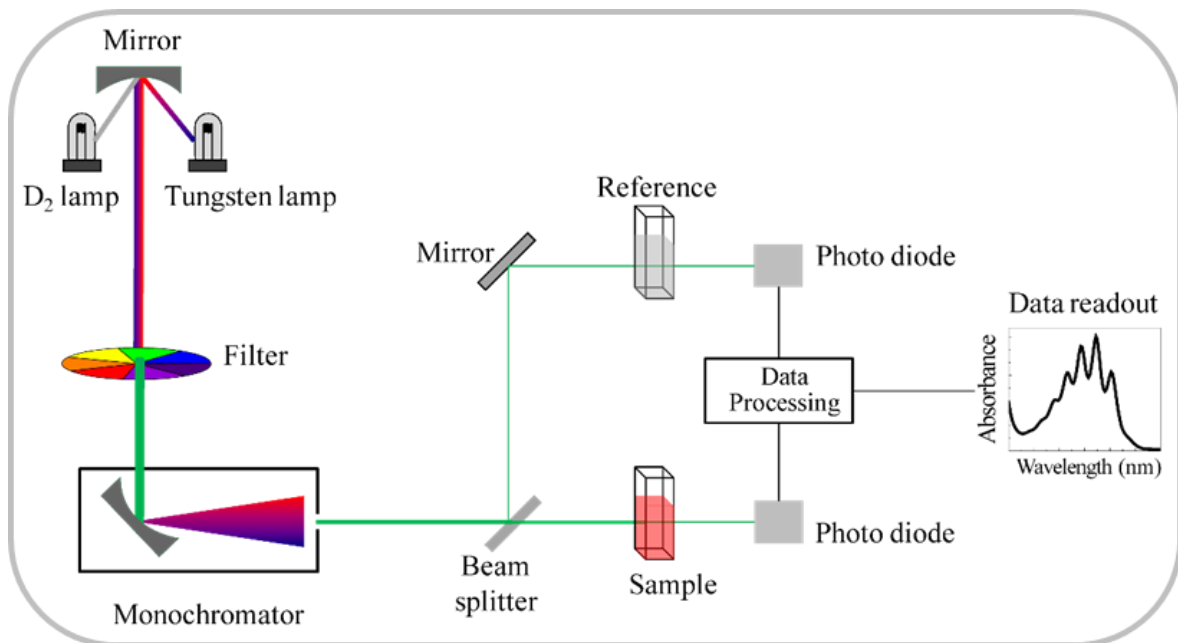


Figure 2.23: The working of UV-vis spectroscope.

UV-Visible absorption spectra were obtained using the Agilent Cary 60 UV-Vis spectrophotometer. These were recorded on samples placed in quartz cuvettes (1 cm, path length), using water or hexane as a reference solvent.

II: Fluorescence Spectroscopy

Cold body emission (from electronically excited state) is called luminescence whereas hot body emission is called **incandescence**. After excited by infrared, visible or UV light, the emission is called **photoluminescence**. **Fluorescence** is the emission from excited singlet state to ground state that does not require change in spin orientation (more common of relaxation) whereas **phosphorescence** is the emission from a triplet excited state to a ground state in which electron requires change in spin orientation. Emissive rates of fluorescence are several orders of magnitude faster than that of phosphorescence. The red-shifting of λ_{max} of fluorescence spectrum compared to the excitation wavelength is called **Stokes shift** and due to the **Franck-Condon rule** which says that vibronic transitions are also occurs during an electronic transition if there are significant overlapping of the vibrational wave functions.

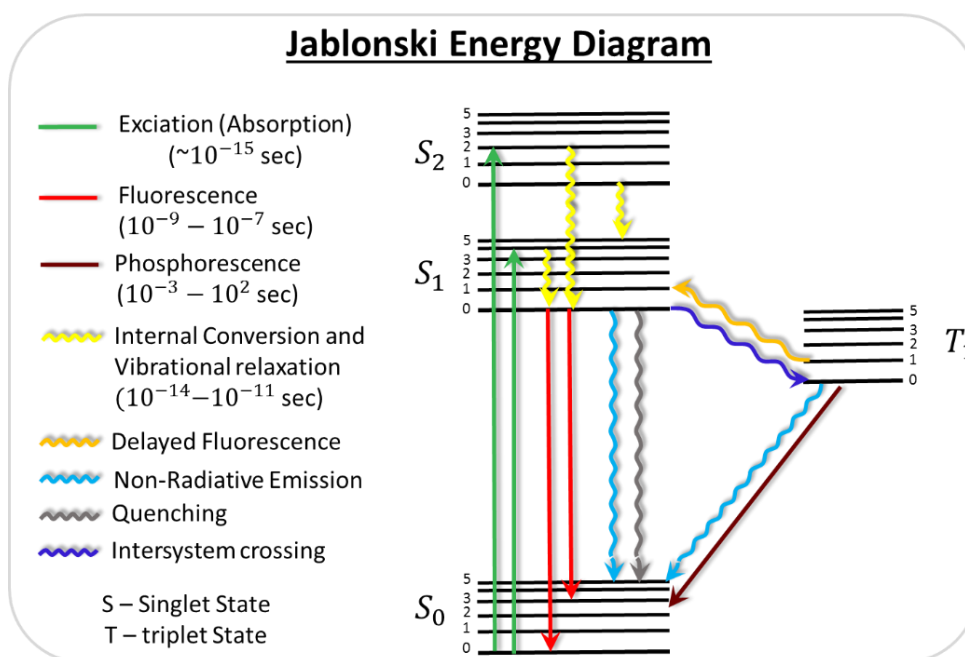


Figure 2.24: The electronic transitions with their life time is shown.

Quantum yield of fluorescence is defined as the ratio of the number of emitted photon to the number of absorbed photon. In practice, it is measured by comparative measurements of fluorescence intensity or lifetime with reference compound of known quantum yield keeping same absorbance.

The image below shows about working mechanism of this spectroscope.

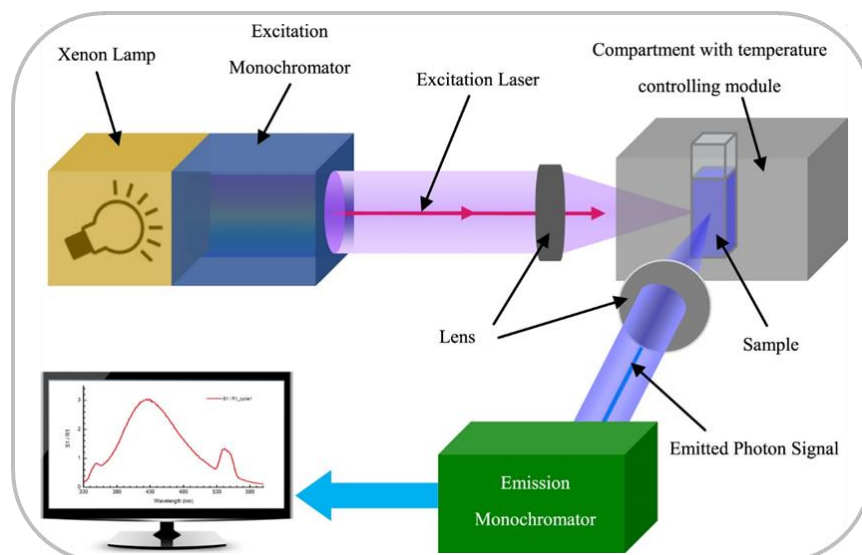


Figure 2.25: The working of fluorescence spectroscopy.

There are two types of fluorescence measurement – steady state and time-resolved fluorescence spectroscopy measurements.

Steady State Fluorescence Spectroscopy is observed with a continuous beam of light and the obtained spectrum shows intensity versus wavelength. Whereas recording the fluorescence spectrum of a fluorophore excited by a laser pulse (\ll decay time) with time is called time-resolved fluorescence spectroscopy (TRFS).

Time-correlated single photon counting (TCSPC) is the technique used to measure TRFS. In TCSPC, fluorophores are excited by a large number of laser pulses with such low intensity that the probability of getting one photon with one pulse is very low and get a distribution of time differences between pulse and emitted photon that corresponds to the fluorescence lifetime.

The steady state fluorescence measurements were performed using a Varian Cary eclipse fluorescence spectrophotometer with a spectral range of 190 to 1000 nm. The lifetime decay measurements were performed using a time-correlated single photon counting setup (FL920, Edinburgh Instrument) at constant excitation and emission wavelengths. The measured data was least-squares fitted to the two-exponential decay functions given by

$$F(t) = a_0 + a_1 \exp\left(-\frac{t}{\tau_1}\right) + a_2 \exp\left(-\frac{t}{\tau_2}\right) \quad (2.22)$$

where a_0 defines the time-shift between the instrumental response function and the sample under study. Relaxation times are given by τ_1 and τ_2 of the characteristic excited states. The fitting accuracy should be $\chi^2 \geq 0.95$ for good analysis. In this framework, the average time constant is given by

$$\langle \tau \rangle = \sum_i a_i \tau_i \quad (2.23)$$

2.4.1.2.2 Magnetic Property Characterization

The magnetic measurements were performed using vibrating sample magnetometer (PPMS, Cryogenic Ltd.) with varying magnetic field and temperature.

A vibrating sample magnetometer (VSM) indirectly measured the magnetization of a sample by vibrating the magnetized sample near a detection (pickup) coil and synchronously detecting the voltage induced which depends on the amplitude and frequency of vibration, external magnetic field and the magnetization of sample. With proper manipulation, we can deduce the value for magnetization from emf.

The changing magnetic flux will induce a voltage in a pickup coil is the basis of this instrument. The induced voltage is:

$$V = \left(\frac{d\Phi}{dt}\right) = \left(\frac{d\Phi}{dz}\right)\left(\frac{dz}{dt}\right) \quad (2.24)$$

Φ is the magnetic flux enclosed by the pickup coil, z is the vertical position of the sample with respect to the coil, and t is time.

For a sample that is oscillating with sinusoidal manner with amplitude A and frequency ν , the voltage is based on the following equation:

$$V = 2\pi f C m A \sin(2\pi \nu t) \quad (2.25)$$

where C is a coupling constant and m is the DC magnetic moment of the sample.

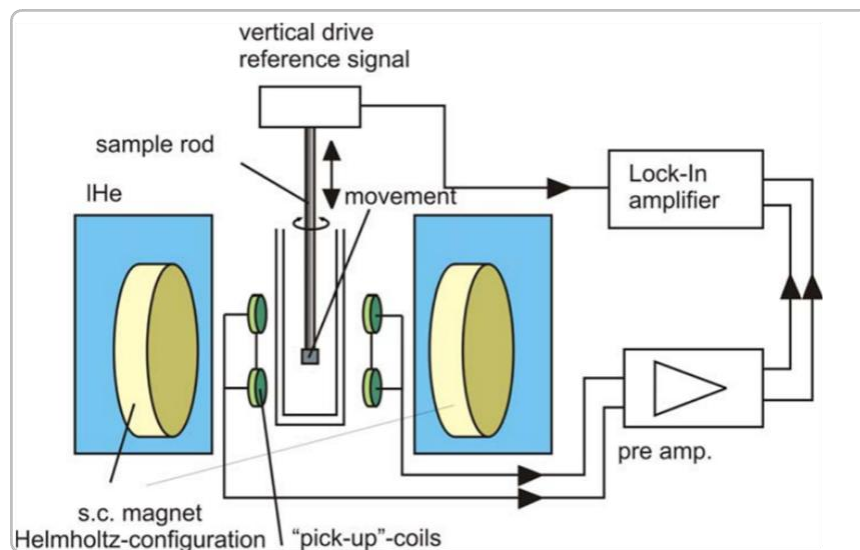


Figure 2.26: The schematic working of a VSM is shown.

2.4.2 Biophysical Characterization: Protein Interactions

UV-vis Absorption and fluorescence spectroscopy measurements were used to evaluate the binding mechanism. CD was used to see the changes in secondary structure in proteins during binding with NPs and QDs. Details of techniques are following.

I: UV-Vis Absorbance: Complex Formation and Binding Constant

UV-visible absorption spectroscopy has been extensively used in the past to explore the change in physical structure, and to identify the complexation between ligands and protein molecules^[11].

I (a): Strength of the Binding Forces

To determine binding parameters, absorption spectra are expressed according to double reciprocal equation^[12]

$$\frac{A_0}{A - A_0} = \frac{\epsilon_P}{\epsilon_{com}} + \frac{\epsilon_P}{\epsilon_{com}} \frac{1}{K_b} \frac{1}{[QD]} \quad (2.26)$$

where A_0 and A are the absorbance of protien in the absence and presence of QDs at 280 nm. $[QD]$ is the analytical concentration of QDs. ϵ_P and ϵ_{com} are the molar extinction coefficients of protien and protien-QDs complex respectively at 280 nm. K_b is the binding constant.

I (b): Nature of the Binding Forces: Thermodynamic Parameters

Secondary force interaction, such as hydrophobic forces, hydrogen bonding, van der Waals forces and Coulombic interactions govern binding between ligands and biomolecules^[13]. Thermodynamic parameters like the enthalpy and entropy are indicators of the existence of non-covalent forces. For instance, enthalpy (ΔH), and the entropy change (ΔS) may provide information about nature of binding forces. Ojha and Das^[14] have categorized interactions based on these parameters. As per their proposition, when $\Delta H < 0$ and $\Delta S < 0$, the responsible forces of interactions are hydrogen bond and van der Waals interactions. Hydrophobic interactions are of consequence in the binding if $\Delta H > 0$ and $\Delta S > 0$. The free energy change (ΔG) is estimated from the following relationship as

$$\Delta G = -RT \ln K = \Delta H - T\Delta S \quad (2.27)$$

where K is the binding constant at the corresponding temperature, R is the universal gas constant and T is the experimental temperature in absolute scale. The values of enthalpy (ΔH), and the entropy change (ΔS) were determined from the fitting curve as described by equation 2.27.

II: Fluorescence Spectroscopy: Quenching and Binding Constant

Fluorescence spectroscopy measurements yield considerable information about the binding mechanism in general. Parameters like the binding constant, number of binding sites, and intermolecular distances are parameters easily accessible from this spectroscopy data^[15].

Reduction of the fluorescence intensity is called fluorescence quenching. When the excited state of fluorophore deactivated upon contact with the quencher is called **collisional quenching** whereas quenching by forming non fluorescent complex with quencher is called **static quenching**.

The quenching mechanism was analysed using the following Stern–Volmer equation^[16]

$$\frac{F_0}{F} = 1 + K_{SV}[Q]^n = 1 + K_q\tau_0[Q]^n \quad (2.28)$$

$$\log\left(\frac{F_0}{F} - 1\right) = \log K_{SV} + n \log [Q] \quad (2.29)$$

where F_0 and F are the fluorescence intensities without and with quencher Q , K_{SV} and n are the Stern–Volmer quenching constant and number of binding sites, respectively, $[Q]$ is the concentration of quencher, K_q is the quenching rate constant of biomolecular reaction and τ_0 is the average lifetime of molecules in the absence of Q .

The binding constant ‘ K_{SV} ’ and number of binding sites ‘ n ’ was determined from the intercept and slope of least square fitted straight line to the data points as described by equation 2.29. When all fluorophores are equally accessible to quenchers, the linear Stern–Volmer plot will be resulted. The basic difference between static and dynamic quenching is tabled below.

Table 2.2: The nature of static and dynamic quenching.

	Static quenching	Dynamic quenching
τ_0/τ	1	F_0/F
Slope with temperature	Falls	Rises
Absorption Spectra	Change	Not change

We can deduce the similar information of fluorescence quenching from TRFS also.

III: Conformational Changes after Complex Formation

The interaction of proteins with QDs may induce conformational changes in their secondary structure, due to hydrophobic binding, which may change the surrounding of its fluorefores hence synchronous fluorescence intensity. CD was used to see the changes in secondary structure in proteins.

III (a): Circular Dichroism (CD)

Circular dichroism (CD) spectroscopy is a special type of absorption spectroscopy that measures the difference in absorbance of right- and left-circularly polarized light by the sample. This difference, called circular dichroism occurs when the sample contains at least one chiral chromophore. And this type of sample is called optically active material. The difference in refractive index for right- and left-circularly polarized light in the sample is called circular birefringence.

The plane polarized light is the superimposition of right- and left-circularly polarized light of equal amplitude. When it enters the optical active material, the light coming outside will be right (or left)-elliptically polarized due to higher absorbance (i.e. higher decrease in amplitude) of left (or right)-circularly polarized light than that of other one.

And when it enters in a medium with circular birefringence, the light coming outside is also the plane polarized but at different angle due to difference in velocity (i.e. refractive index) of right- and left-circularly polarized light.

In reality, birefringence and dichroism exist together in any material for any certain wavelength of light. So the light coming outside has the effect of both phenomena as seen in Figure 2.27.

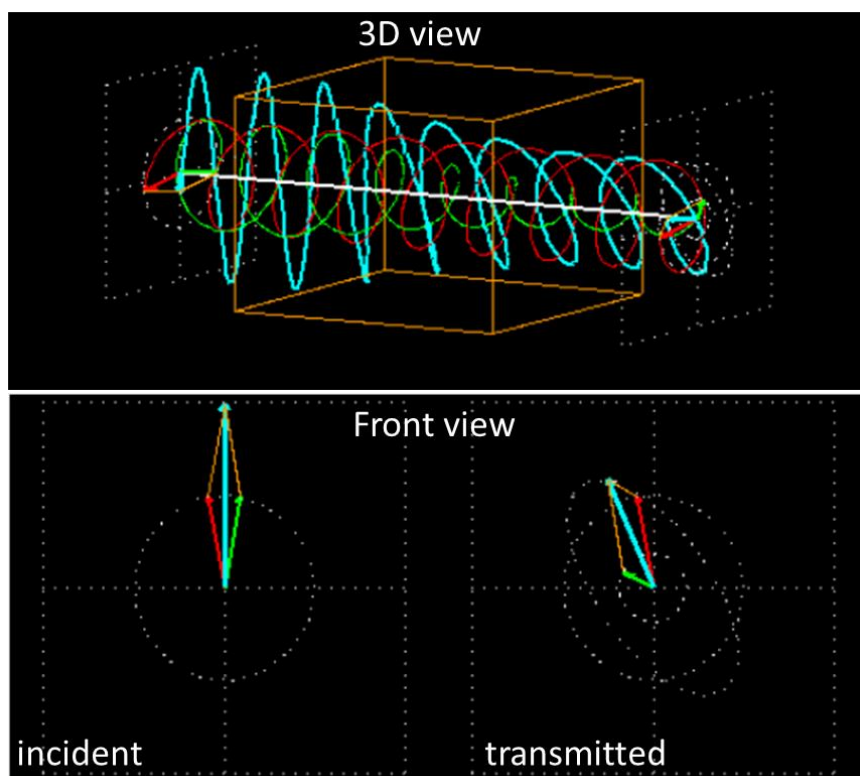


Figure 2.27: The incident plane-polarized wave in a medium with both circular dichroism and circular birefringence with the transmitted elliptically polarized light rotated at different angle is shown.

The optical activity of bio-macromolecules provides information about its structural properties. CD spectra from 260 to 180 nm can be analysed for different secondary structure like α -helix, β -sheets, β -turns, random coils and others present in proteins.^[17] Ellipticity of these secondary structures in pure form are shown in Figure 2.28.

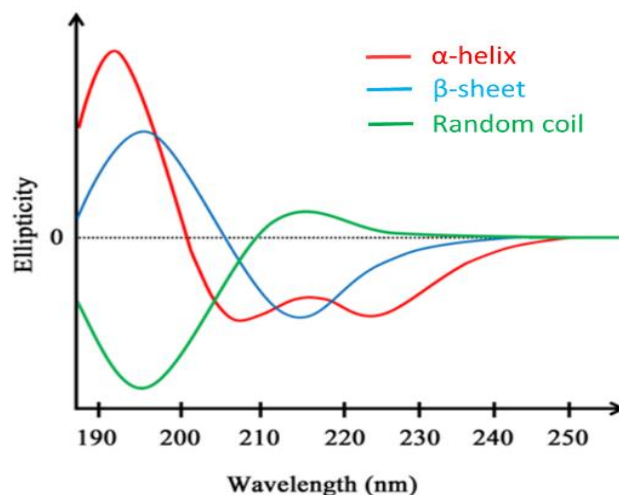


Figure 2.28: The CD spectra of protein secondary structures are shown.

Band and transition related information of these secondary structures are tabulated in table 2.3.

Table 2.3: The band position and related transitions in protein secondary structures.

	-ve band (nm)	Related transition	+ve band (nm)	Related transition
α-helix	222	$n \rightarrow \pi^*$	192 (strong)	$\pi \rightarrow \pi^*$
	208	$\pi \rightarrow \pi^*$		
β-sheet	216-218	$n \rightarrow \pi^*$	195	$\pi \rightarrow \pi^*$
β-turn	225 (weak)	$n \rightarrow \pi^*$	200-205 (strong)	$\pi \rightarrow \pi^*$
	180-190 (strong)	$\pi \rightarrow \pi^*$		
Random coil	< 200 (strong)	$\pi \rightarrow \pi^*$	218 (weak)	$n \rightarrow \pi^*$

Optical rotation, ' ϕ ' and ellipticity, θ can be determined from equations given below.

$$\phi(deg) = 180 l(n_L - n_R)/\lambda \quad (2.30)$$

$$\theta(deg) = 2.303 (A_L - A_R) 180/4\pi = 33.0 \Delta A \quad (2.31)$$

where l is the sample length.

To compare results of different samples it is necessary to consider molarity. Molar rotation and molar ellipticity are

$$[\theta](deg.\frac{cm^2}{desimol}) = M \phi / 100 c l \quad (2.32)$$

$$[\theta](deg.\frac{cm^2}{desimol}) = M \theta / 100 c l \quad (2.33)$$

where M is the molecular weight, concentration, c is in g/cm³ and sample length, l is in decimetre. Helix content of the proteins could be determined from the equation given by

$$\% \alpha - helix = \frac{[-[\theta]at\ negative\ band - 4000]100}{(33000 - 4000)} \quad (2.34)$$

Circular dichroism (CD) experiments were done using Applied Photophysics Chirascan instrument (USA) with wavelength range from 200 to 280 nm. Below 200 nm, CD data is not much reliable to analyse the secondary structures of the proteins. Helicity % was calculated by CDNN software.

III (b): Synchronous Fluorescence Quenching

Synchronous fluorescence spectroscopy happens to be a sensitive technique to explore the alteration in the molecular environment of fluorophore residues.^[18]

Synchronous fluorescence is a standard technique for the simultaneous determination of multi-component samples without any pre-treatment.^[19,20] One of the major advantages of this technique is, the analysis can be carried out directly under ambient conditions.

Selection of wavelength interval is a major experimental parameter, when synchronous fluorescence technique is used. For $\Delta\lambda = 15$ nm scan, the peaks revealed good peak shape with a synchronous scanning between $\lambda_{exc} = 230-360$ nm, and $\lambda_{em} = 245-375$ nm. This selected spectral region had 130 distinct wavelength values for each sample.

Spectral bandwidth reduction combined with spectral simplification, and perturbation effect noticed in synchronous spectra offer signature information on Tyr and Trp residues, when the $\Delta\lambda$ was fixed at 15 and 60 nm, respectively.^[21] Positional synchronous maxima of these residues are usually manifested on binding, and this yields information about changes in polarity around these fluorophores, and thus on their proximity to the ligand concerned.^[22]

2.5 Bioactivity

The effect of QDs- enzyme interaction on the enzymatic activity, antimicrobial activity of QDs and their biocompatibility were studied in this thesis. Different techniques were used like UV-vis spectroscopy for enzymatic activity by spectrophotometric turbidity

assay, microtiter plate assay and Broth micro dilution (to determine MIC) for antifungal activity. In vitro biocompatibility were done by MTT assay (for cytotoxicity), DCFH-DA assay (for oxidative stress assessment), TEM (for cellular morphological changes), confocal fluorescence microscopy (for cellular uptake of QDs), fluorescence microscopy of JC-1 (Analysis of mitochondrial membrane potential), and western blot analysis (for protein regulation assessment). Details of these techniques are given below.

2.5.1 Enzymatic activity

In spectrophotometric turbidity assay, the normalized reading of optical density (OD), at 450 nm, of micrococcus lysodeikticus was used to indicate the activity of lysozyme. As we add the lysozyme-QD complex, the OD at 450 nm is changed due to die out of bacteria, micrococcus lysodeikticus.

All data were fitted with exponential decaying with $R^2 > 0.99$ to find out the time taken by complex to decrease the OD by $1/e$ times and compare this time with the time taken by only lysozyme.

2.5.2 Antifungal activity

The antimicrobial activity of synthesized QDs was performed by microtiter plate assay and minimum inhibitory concentration (MIC) was determined. Broth micro dilution for determining MIC was performed as follows. *Candida albican* culture was grown for 16 hours in YEPD (Yeast extract, Peptone, Dextrose) plates to obtain single colonies. Prior to the experimental analysis, the primary culture was resuspended in 0.9% NaCl solution so as to obtain an optical density of 0.1 at 600 nm. The resuspended culture (OD ~ 0.1) was then diluted 100 times in fresh YEPD medium. 100 μ l of the diluted cell suspension was added to the wells of 96-well plate, that contained equal volumes of medium (100 μ l/well) and the respective QDs in different dilutions. Control set with the YEPD media and cells without nanoparticle was also run simultaneously. The 96 well plates were then incubated at 30 °C for 48 h. After the endpoint the reading was taken at OD₆₂₀ in a microplate reader. MIC₈₀ and percentage of inhibition was then determined. Separate sets of experiments were conducted for the three sets of nanoparticle formulations. All experiments were performed in duplicates for reproducibility.

2.5.3 In vitro Biocompatibility

(a). **Cytotoxicity Assay:** The cytotoxicity of QDs was evaluated by MTT assay.^[23] Comparative cytotoxicity of QDs on the cell lines was assessed. Known number of cells

per well were incubated in 100 μ l of Iscove's modified Dulbecco's medium supplemented with 100 μ g/ml streptomycin, 100 U/ml penicillin and 10% FCS (Fetal calf serum) at 37° C temperature and 5% CO₂ for 24 h and 48 h. After that old media is replaced with fresh media containing various concentrations of QDs and incubated. Four hours prior to completion of incubation, 20 μ l of 5 mg/ml of MTT (3-(4,5-dimethylthiazol-2-yl)-2,5-diphenyl tetrazolium bromide) was added to each well. Then media was removed and 200 μ l of DMSO was added and it was incubated further for 10 minute at room temperature. Absorbance was taken at 570 nm in ELISA reader. The % of cytotoxicity was calculated using following equation

$$\% \text{ Cytotoxicity} = \frac{\text{Absorbance of treated sample}}{\text{Absorbance of Control (untreated) samples}} \times 100 \quad (2.33)$$

All measurements were performed in triplicates.

(b). Measurement of intracellular reactive oxygen species (ROS) level: Intracellular ROS induced by QDs was detected by using 2', 7'Dichlorofluorescein-diacetate (DCFH-DA) staining. Cells were seeded at density of 5×10^5 in 6-plated well and incubated overnight at 37°C temperature and 5% CO₂. After that, cells were treated with fresh media containing different concentrations of QDs for 12h. After that, cells were washed twice with PBS. Cell were stained with 40 μ M DCFH-DA at 37°C for 30 min, lysed in alkaline solution and washed with PBS. Fluorescence intensity was measured using 485 excitation and 520 nm emission filters using a fluorimeter (RF-5301 PC Shimadzu spectrofluorometer, Nakagyo-ku, Kyoto, Japan).^[23]

(c). Electron paramagnetic resonance (EPR) spectroscopy: EPR measurements of free radicals were carried out in a Bruker EMX Micro X spectrometer according to the modified protocol.^[24] The following conditions were used for the measurements: Sweep width, 200.83; modulation amplitude, 4.0 G; microwave power, 16 mW; temperature, 298 K; conversion time, 40 ms; and time constant, 163.84 ms. The treated cells were suspended in 100mM DMPO. Sample were loaded in sealed quartz capillary tubes and transferred to the EPR cavity to obtain spectra. For each sample, 2D spectrum was recorded by Bruker e-Scan EPR. Spectrometer Quantitation of EPR spectra and baseline correction was done using Bruker WinEPR Data Processing software.

(d). Microscopic analysis: To analyze the effects of QDs on cellular morphological, cells were collected after 12 h treatment of QDs by trypsinization (0.05 % trypsinase).

Cells were prefixed with 2.5 % gluteraldehyde for 30 min, post-fixed with 1 % osmic acid prepared in 0.1 M PBS, dehydrated in graded ethanol, embedded in Epon 812 mixture and cut into ultrathin sections (70-80 nm) by an Ultramicrotome (Leica Ultracut—UCT). The cells were observed under a transmission electron microscope (JEOL-JEM-2100F) at 200 kV after staining with uranyl acetate.^[23]

(e). Cellular Uptake: The cells were treated with various concentrations of QDs and incubated for 12 h at 37 °C, in 5% CO₂. After treatment cells were washed with 0.1 M phosphate buffer saline and trypsinized by 0.05 % trypsinase and dissolved in 1 ml of 0.1 M phosphate buffer saline. Imaging has been done under bright field, UV (405 nm) and blue (488 nm), excitation using Olympus Fluo View TM FV1000 laser scanning confocal microscope and measured the fluorescence intensity under blue (488 nm) excitation wavelength.^[23]

(f). Analysis of mitochondrial membrane potential (MMP): The MMP was measured by JC-1 (Fluorochrome-5,5',6,6'-tetrachloro-1,1',3,3'-tetraethylbenzimidazol-carbocyanine iodide), has been extensively used to study the loss of the mitochondrial membrane potential.^[25] For this, cells were grown in 6-well plate and treated with same concentration of QDs. After 12 h treatment cells were washed with PBS and stained with 2 µg/ml of JC-1 dye and incubated at 37°C in dark for 30 min. Then cells were washed with PBS and images were captured with Nikon Eclipse 90i Epi fluorescence upright microscope equipped with Nikon DXM 1200 digital camera and viewed at 20x magnifications. The quantitative measurement of mitochondrial membrane potential was done through fluorometer. At the end of exposure cells were then incubated with the mitochondrial-membrane-permeable dye JC-1 (10 µg/ml in PBS) for 20 min at 37°C, after that cells were harvested and washed with phosphate buffer saline. The fluorescence intensity was measured at 530/590 nm.

(g). Protein extraction and western blot analysis: The equal numbers of cells were seeded in 60mm plate and after 80% of confluency, cells were treated with fixed concentration of QDs for 12h. At the end of treatment, cells were harvested by trypsinization and washed with ice-cold PBS. After that whole cell protein suspension was prepared in RIPA buffer containing 1x protease inhibitors (G-Bioscience, India). Protein content was measured by Bradford assay. The proteins were separated in 8% SDS-PAGE gel and transferred to nitrocellulose membrane. The membrane was blocked

using 5% BSA in PBS and probed with primary antibodies of p53, Bax, bcl-2 and caspase-3 followed by incubation with secondary antibody anti-mice Ig-G. The densitometry analysis of protein band was performed by Image Analysis Software (Thermo Fisher Scientific, MA, USA) and β -actin was used as internal control.^[25]

(h). Cytochrome C in cytosolic fraction: For isolation of cytosolic fraction, cells were trypsinized after 12 h of treatment and washed in PBS and resuspended into 500 μ L fractionation buffer (Buffer HEPES (pH7.4) 20mM, KCl10mM, MgCl₂ 2 mM, EDTA 1mM, EGTA 1 mM , DTT 1mM Protease Inhibitors Cocktail- 50 μ L/10 ml buffer) and incubated for 15 min on ice. Cells suspension was passed through a 27 gauge needle (1 mL syringe) 10 to 15 times and then kept on ice for further 20 min and further centrifuged at 3,000 rpm for 5 min. Supernatant was collected and again centrifuged at 8,000 rpm for 5 min. Pellet was discarded and supernatant was used to analysis the expression of cyochrome-c in cytosolic fraction. The extracted protein was separated in 8% SDS-PAGE gel for western blotting analysis as mentioned protocol above.^[25]

All the materials and methods discussed above were used for the fulfillment of the goal of this thesis.

2.6 References

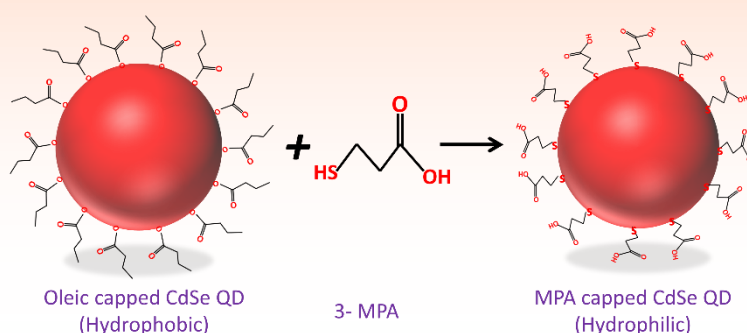
- [1] H. V. Olphen, *Willey and Sons: New York* **1997**.
- [2] Laponite Technical Bulletin *Laponite Industries Limited*, LI04/90/A **1990**.
- [3] R. K. Pujala, H. B. Bohidar, *Soft Matter*. **2012**, 8, 6120.
- [4] G. Serrien, G. Geeraerts, L. Ghosh, P. Joos, *Colloids and Surfaces* **1992**, 68, 219.
- [5] R. A. Calderone, W. A. Fonzi, *Trends in microbiology* **2001**, 9, 327.
- [6] Z. A. Peng, X. Peng, *J. Am. Chem. Soc.* **2001**, 123, 183.
- [7] D. M. Donegá, Celso, P. Liljeroth, D. Vanmaekelbergh, *Small* **2005**, 1.12, 1152.
- [8] B. D. Cullity, *Addison-Wesley*. **1978**, 102.
- [9] H. Ohshima, *Adv. Colloid Interface Sci.* **1995**, 62, 189.
- [10] J. Jasieniak, L. Smith, J. V. Embden, P. Mulvaney, M. Califano, *The Journal of Physical Chemistry C* **2009**, 113, 19468.

- [11] X. Pan, R. Liu, P. Qin, L. Wang, X. Zhao, *J. Lumin.* **2010**, *130*, 611
- [12] J. K. Maurya, M. U. H. Mir, U. K. Singh, N. Maurya, N. Dohare, S. Patel, A. Ali, R. Patel, *Biopolymers* **2015**, *103*, 406.
- [13] Z. Chi, R. Liu, H. Zhang, *Biomacromolecules* **2010**, *11*, 2454.
- [14] B. Ojha, G. Das, *J. Phys. Chem. B* **2010**, *114*, 3979.
- [15] Y. Shu, M. Liu, S. Chen, X. Chen, J. Wang, *J. Phys. Chem. B* **2011**, *115*, 12306.
- [16] Y. P. Wang, Y. Wei, C. Dong, *J. Photochem. Photobiol. Chem.* **2006**, *177*, 6.
- [17] Y. H. Chen, J. T. Yang, H. M. Martinez, *Biochemistry (Mosc.)* **1972**, *11*, 4120.
- [18] J. Q. Lu, F. Jin, T.-Q. Sun, X.-W. Zhou, *Int. J. Biol. Macromol.* **2007**, *40*, 299.
- [19] M. del Olmo, C. Díez, A. Molina, I. de Orbe, J. L. Vilchez, *Anal. Chim. Acta* **1996**, *335*, 23.
- [20] A. Espinosa-Mansilla, A. Muñoz de la Peña, F. Salinas, D. González Gómez, *Talanta* **2004**, *62*, 853.
- [21] J. Fan, X. Chen, Y. Wang, C. Fan, Z. Shang, *J. Zhejiang Univ. Sci. B* **2006**, *7*, 452.
- [22] G. Zhang, N. Zhao, L. Wang, *J. Lumin.* **2011**, *131*, 880.
- [23] R. Meena, S. Kumar, U. S. Gaharwar, P. Rajamani, *Biomedicine & Pharmacotherapy* **2017**, *94*, 944.
- [24] S. Kaur, S. Sundaram, R. Meena, P. Rajamani, *ROS.* **2018**, *5*, 134.
- [25] R. Khanam, R. Kumar, I. I. Hejazi, S. Shahabuddin, R. Meena, V. Jayant, P. Kumar, A. R. Bhat, F. Athar, *Apoptosis* **2018**, *1*, 19.

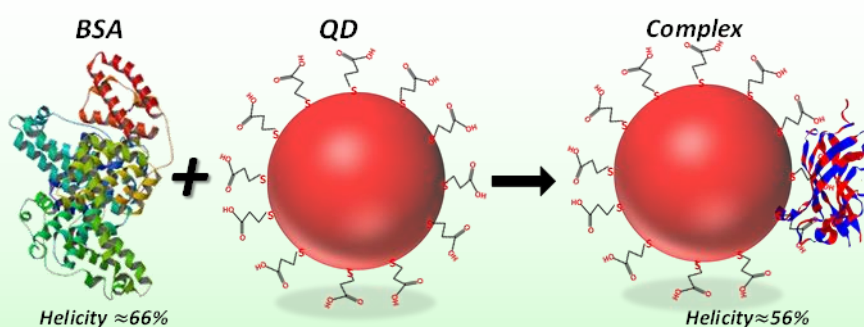
Chapter 3

Size Variational Physical and Biophysical Characterization of Synthesized Surfactant Functionalized Quantum Dots

Abstract: This chapter discusses the physical and biophysical characterization of different sized CdSe Quantum Dots which were synthesized in the presence of different surfactants using hot-injection method.



Pictorial representation of legend exchange in QDs is shown here.



Pictorial representation of protein-QDs complex formation is shown here.

3.1 Introduction

To enhance QDs optical and energy transport properties, the synthesis and processing conditions must be optimized. These nanomaterials have generated strong interest in fundamental research due to their applications in diverse areas. It has been already established, both experimentally and theoretically, that their spectroscopic profiles vary both with composition, and morphology.^[1-5] These features are understood in the context of solid-state electron-in-quantum-well models in the effective mass approximation.^[6] The drawback lies in their applicability which is limited to relatively large structures. For smaller structures, the electronic transitions are normally understood by the other

reported approaches.^[1,2,7] In order to overcome the low quantum efficiency, appropriate surface passivation of QDs is required for application purposes. Various surface modification protocols (inorganic and organic including polymer capping, surface grafting, and ligand exchange) have displayed passivation of the surface defects hence enhancing their quantum yield.^[8-10] In addition, preparation of inorganic wide bandgap shells have been normally used. Formation of wide-bandgap inorganic shells must be taken into account to resolve problems related to lattice mismatch, and variation of core dimension that lead to peak broadening.

The surface state problems (related to low PL efficiency) cannot be completely solved by shelling quantum dots via ligand exchange process.^[11] In such synthesis conditions, the surface ligands cannot be cleared completely, because these are required for maintaining solubility. The impact and physical understanding of these ligands (surfactant coatings) on the spectroscopic properties of QDs is poorly understood. *Wuister et al* have observed the thiol capping of ligands acting as hole-acceptor in the case of CdSe quantum dots which induced quenching in luminescence.^[12] In the present work, we have systematically assessed the impact of four surface active ligands on the physical, and spectroscopic properties of CdSe quantum dots having two distinct size groups of approximately 2.5 and 3.5 nm. It is clearly established that particular surfactant coating of QDs facilitated the quantum yield enhancement by inhibiting agglomeration. Differential biophysical characterization were done with model plasma protein BSA.

3.2 Sample Preparation

Quantum Dot Synthesis: The protocol used for the preparation of the QDs of different size and coating is same as described in Chapter 2 with only some modification in selenium precursor.

A stock solution of Se precursor was prepared by adding 30 mg of Se to 5 ml of 1-octadecene (ODE) (90%) in a 10 ml round-bottom flask that was clamped on a hot plate. A calibrated micro-syringe was used to draw 0.4 ml of trioctylphosphine (TOP) from its Sure-Seal bottle, and added to the reaction flask. The solution was stirred for about 15 min. It was warmed to allow for the faster dissolution of Se powder. Now, Se stock solution was mixed with the different surfactant ligands as described in Chapter 2 (0.05 mM in 1 ml of Se stock sol) in separate vial and again stirred for 1 hour. This stock solution was stored at room temperature (25 °C) in air tight container, and these five solutions were Se precursor for five preparations.

Cd precursor was made by adding 13 mg of CdO to a 25 ml round-bottom flask with 0.6

ml of oleic acid and 10 ml of octadecene. The flask was heated gradually to the fix temperature (200⁰C for size group QD₁ and 230 ⁰C for size group QD₂) and 1 ml of previously prepared selenium solution premixed with ligand was added to the hot cadmium solution. The physical size and conformation of the products depend on reaction time and temperature. Therefore, timing began when the selenium solution was added to the reaction vessel. Samples were removed from hot plate after 100 s. For getting rid of unreacted precursors and by-products, extraction process was done for cooled samples and ligand exchange process also done for making hydrophilic as described in Chapter 2. By the above mentioned protocol, we prepared the hydrophilic CdSe QDs with five different types of ligand capping: OA (oleic acid), CTAB (Cyltrimethylammonium bromide), DTAB (Dodecyltrimethylammonium bromide), SDS (Sodium dodecyl sulphate) and TX-100 (4-Octylphenol polyethoxylate). It may be noted that OA capped QDs are also referred to as bare QDs in this report and the surfactant coated QDs do contain OA as the first layer of capping.^[13] The fluorescence signature of these particles is clearly shown in Figure 3.1.

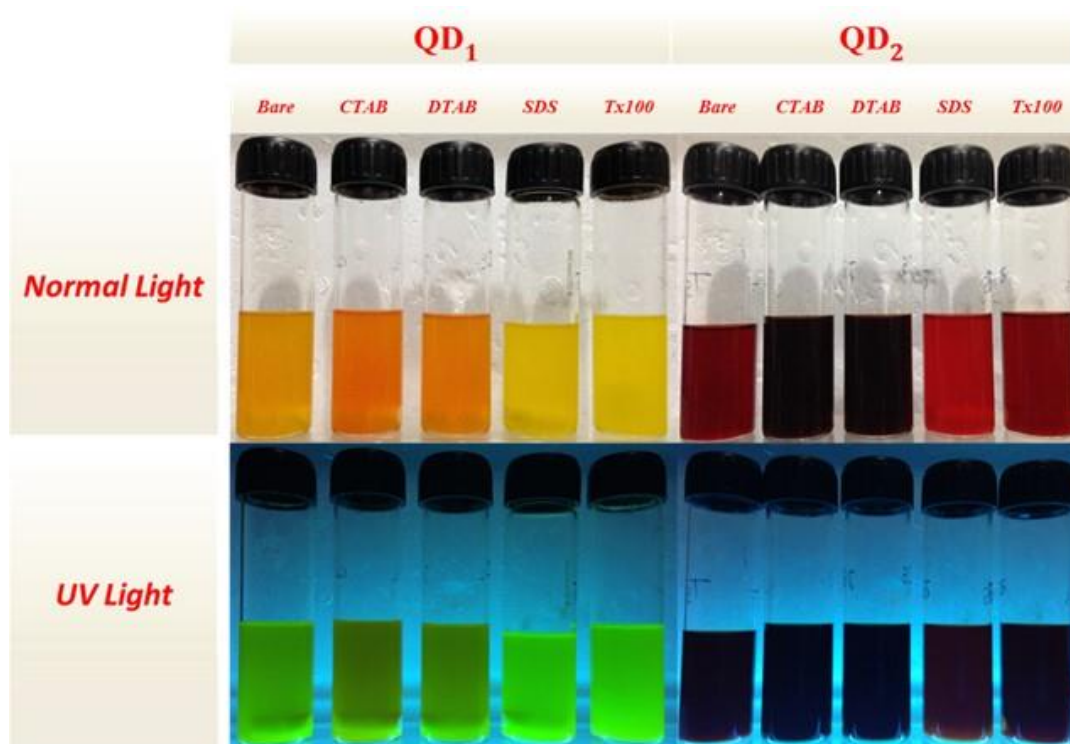


Figure 3.1: CdSe quantum dots of two groups of size stabilized with different types of ligands under bright light (Top) and UV illumination (Bottom). QD₁ and QD₂ refer to the 2.5 and 3.5 nm size group QDs.

Protein solution: The aqueous protein solutions were prepared at a fixed concentration of 0.01% (w/v) by dissolving the required amount of protein powder in deionized water

at 25⁰C under stirring for ~1 hr, and the pH of the solutions were ~ 5.5±0.5, which produced homogeneous and optically clear solutions. Stock solutions were stored in sterilized air tight borosilicate glass bottles for future use.

3.3 Physical Characterization

3.3.1 Morphology and Surface Charge as function of Surfactant Capping

The particle size, size distribution and cluster morphology were probed by both Transmission Electron Microscopy (TEM) and Dynamic Light Scattering (DLS) techniques. Table 3.1 compares the mean cluster / particle size obtained from both the techniques. The difference in the two sizes is expected because of the change in the hydration state of QDs in DLS. More specifically, TEM probed the dried particles while the DLS measured the size of the hydrated structures. Consequently, DLS provided better estimate of mean cluster size with hydration layer. The TEM data could provide two important pieces of information. First, the synthesis method was validated for consistency (CdSe core size ~ 2.5 and 3.5 nm) independent of the choice of capping ligand (Figure 3.2 & 3.3 and Table 3.1). Second, the TEM data allowed us to observe drastic change in the structure of agglomerated quantum dots as function of temperature for a fixed reaction time, which is discussed in details in the following section.

Table 3.1: Comparison of average core size and cluster size obtained from TEM and DLS measurements. Fractal dimensions for CdSe-CTAB QDs having different core size (2.5 nm and 3.5 nm) is also listed.

Surface Ligand	Cluster Morphology	Cluster Size TEM/ nm	Size UV-Vis / nm	Size DLS/ nm	Core Size TEM/ nm	Fractal Dimension
Bare/TOP	Dispersed	-	3.4	6.0 ±0.7	3.5±0.3	-
			2.4	3.7 ±0.4	2.5±0.2	-
CTAB (Cationic)	Tetrapod	42.0±5.0	3.7	81± 9.0	3.8±0.4	1.48
			7.0±3.0	2.5	17.0± 2.0	2.5±0.2
DTAB (Cationic)	Spherical	43.0±5.0	3.7	48.0±6.0	3.8±0.4	-
			18±5.0	2.4	21.0±3.0	2.5±0.3
SDS (Anionic)	Network	-	3.2	78.0±16.0	3.5±0.6	-
			2.3	10.0±1.0	2.3±0.3	-
TX-100 (Anionic)	Dispersed	-	3.1	9.2±0.8	3.2±0.2	-
			2.2	3.4±0.3	2.3±0.3	-

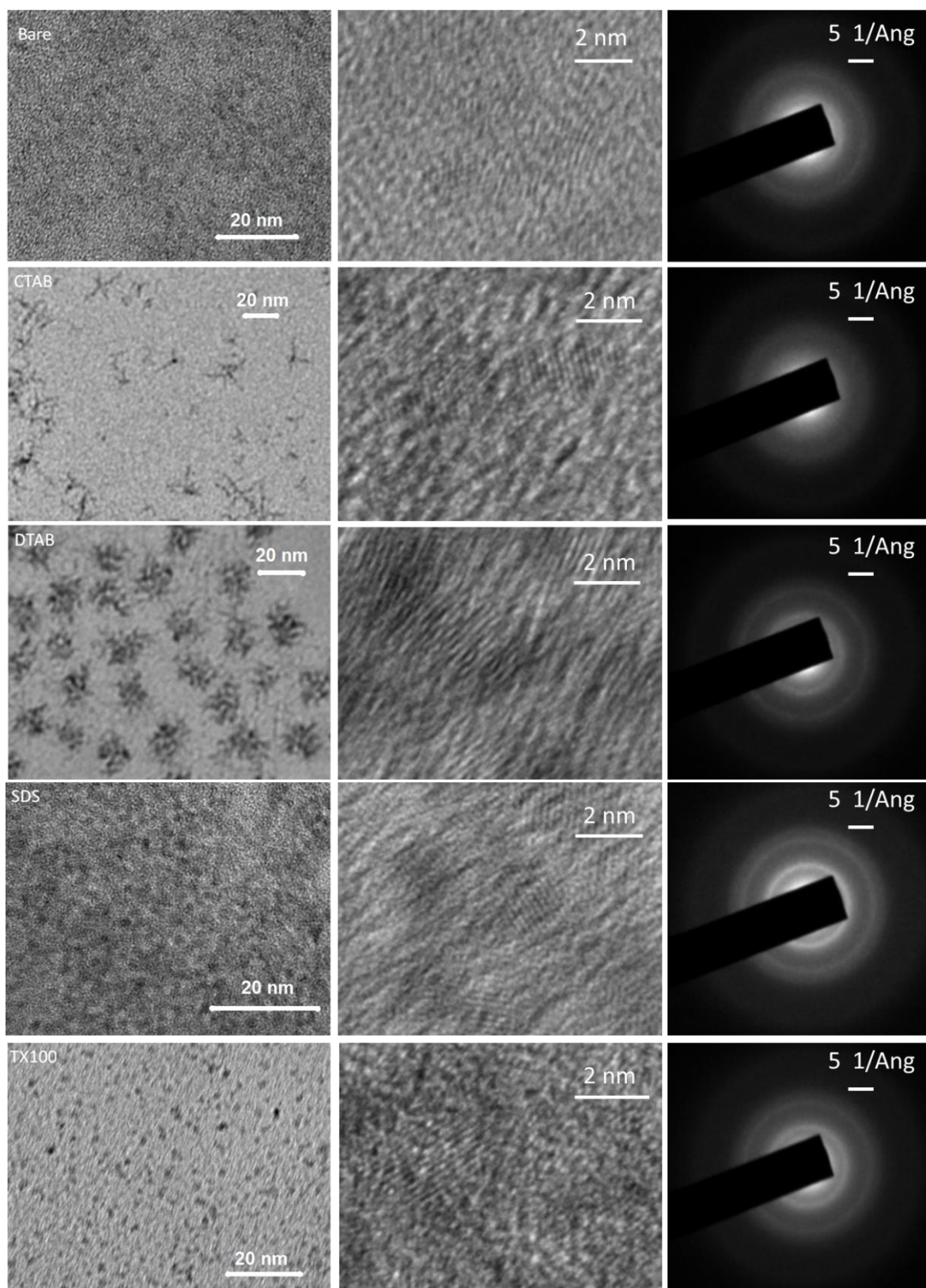


Figure 3.2: TEM, HRTEM images and SAED pattern of CdSe QDs of first size group (core ≈ 2.5 nm) without and with different surfactant capping.

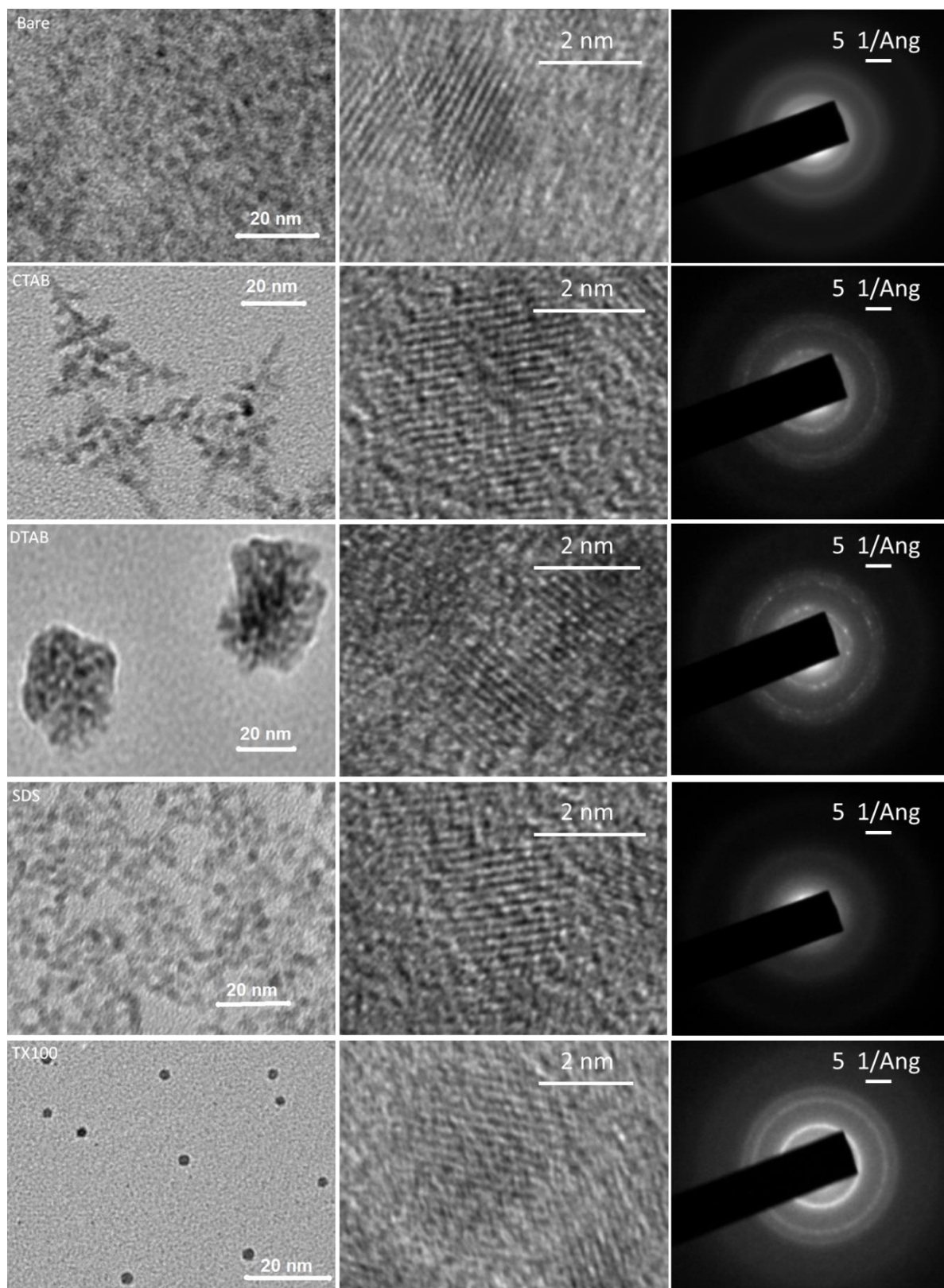


Figure 3.3: TEM, HRTEM images and SAED pattern of CdSe QDs of second size group (core ≈ 3.5 nm) without and with different surfactants.

The particle diameters D (in nm) of quantum dots were estimated from the first absorption maxima of the UV–visible absorption spectra using the expression 2.19.

As discussed earlier, it was possible to control the size of the CdSe core by controlling the temperature of the reaction mixture. Systematic physical characterization was performed to evaluate the size of core quantum dots which are listed in Table 3.1. Two distinct core sizes (2.5 and 3.5 nm) could be obtained with our approach. The zeta potential graph for QDs with these two size are presented in Figure 3.4 (b) which reveals that the highest negative surface charge was observed for bare QDs (-64 ± 4 and -52 ± 3 mV for 3.5 and 2.5 nm core size particles, respectively) and lowest negative charge was observed for the cationic ligand DTAB (-35 ± 4 and -24 ± 3 mV for 3.5 and 2.5 nm core size particles, respectively). It is to be noted that surface modification did not change the polarity of the coated QDs regardless of the use of cationic, anionic or neutral ligands. The smaller quantum dots (core size ≈ 2.5 nm) had greater surface charge density.

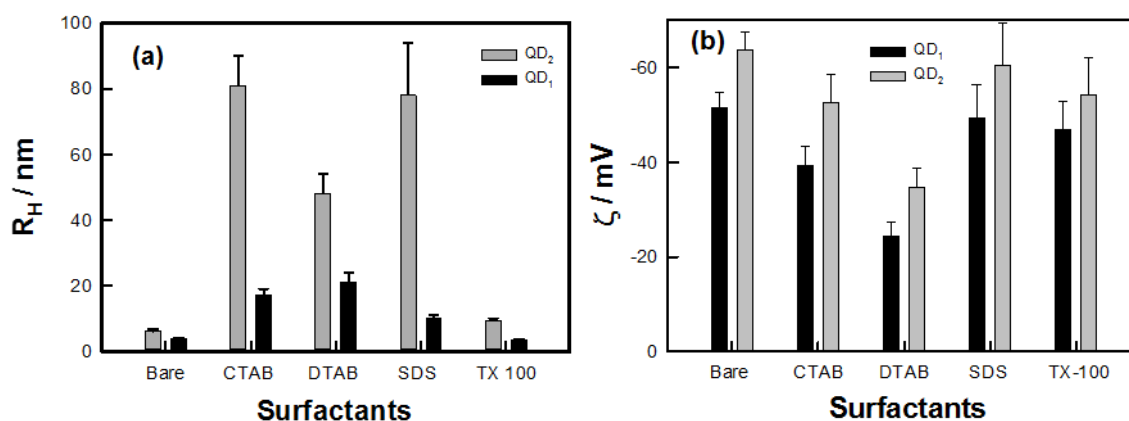


Figure 3.4: (a) Plot of average hydrodynamic radius R_h and (b) zeta potential of QDs capped with different ligands. Two different samples of CdSe QDs are compared in these diagrams.

In addition to changing the zeta potential, variation in the type of surface ligand drastically changed the morphology, and aspect ratio of QD clusters. Figures 3.2 and 3.3 present TEM micrographs for CdSe QDs capped with four different surfactants. Although we expected the actual cluster shape in solution to be different than that observed by TEM, the TEM data revealed that the choice of ligand leads to drastically different QD cluster size and morphology strongly suggesting surface controlled agglomeration. We first compare the Figures 3.2 and 3.3, which compares agglomeration for QDs made at different temperatures in the presence of CTAB, DTAB and SDS ligands. The clusters observed with CTAB have a tripod shape, though it is unclear if the tripod is three-dimensional or planar. Clusters emerging in the presence of DTAB showed a nearly spherical cluster shape without well-defined symmetry. Clusters emerging in the presence of SDS showed a network-like morphology. Although, the existence of these network-like morphology was not confirmed by DLS results.

In each case, the characteristic cluster morphology evolved with increasing temperature. From Figures 3.2 and 3.3, one can compare the cluster size and morphology of QDs prepared in the presence of CTAB ligands with increasing the temperature from 200 to 230 °C. The rapid initial nucleation, and subsequent growth of tripod structures in octadecene solvent was followed by a significant branching in the tripod shape with increasing temperature. The tripod arms were observed to lengthen from ≈ 10 to 20 nm over this temperature. The simultaneous spreading of the tripod branches during the reaction was attributed to selective growth following diffusion controlled aggregation mechanism. Figures 3.2 and 3.3 show the TEM pictures for QDs with DTAB ligand with increasing temperature from 200 to 230 °C. A cluster structure of the QDs with very well defined boundary was observed with cluster size increasing from ≈ 15 to 25 nm in diameter. QDs synthesized in the presence of SDS ligands are depicted in Figures 3.2 and 3.3, where network-like clusters can be easily seen. In case of OA and TX-100, we could see spherical quantum dots.

SAED is the diffraction pattern obtained in the reverse space of the lattice planes. If selected area aperture selects numerous, randomly-oriented nanocrystals or polycrystals, SADP consists of rings sampling all possible diffracting planes that is in our case as shown in Figure 3.5. But HRTEM show good crystalline quality i.e. there is no polycrystal. So it confirms that there are numerous, randomly-oriented nanocrystals i.e. nanosized quantum dots. And calculation shows that the structure is Zinc blende [14]. Table 3.2 provide a list of various crystal parameters.

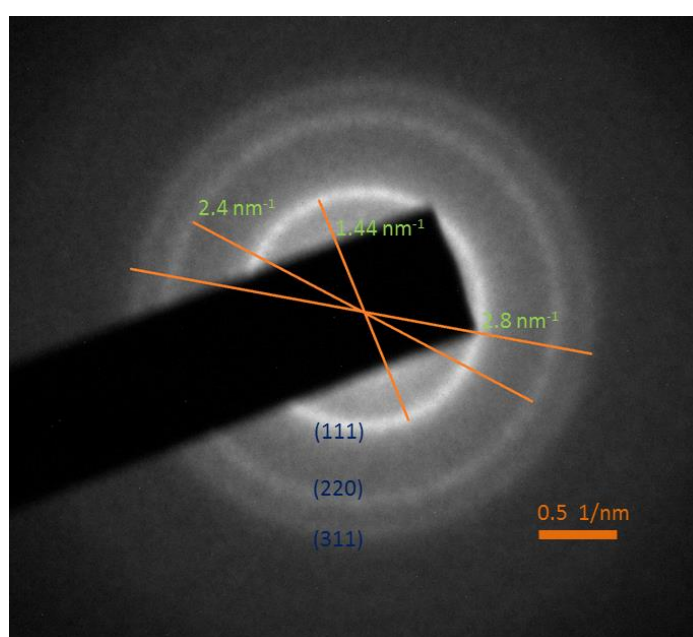


Figure 3.5: SADP of Tx-100 coated CdSe QDs of second size group (core ≈ 3.5 nm).

Table 3.2: Different crystal parameters are listed.

Diameter of rings (nm^{-1})	Diameter of rings (nm)	Radius of rings (d-spacing) (nm)	Lattice Parameter (nm)	Corresponding lattice plane
1.44	0.694	0.347	0.60	(111)
2.40	0.417	0.209	0.59	(220)
2.80	0.357	0.179	0.59	(311)

The unique morphologies of clusters obtained from synthesis with CTAB capping ligands could be further quantified by analysing the fractal dimension of the observed structures. The fractal dimension allowed us to assess the degree of structural complexity by evaluating how fast the characteristic size increased or decreased. Objects with non-integer dimension are called fractals and their dimensionality is called the fractal dimensionality ^[15]. TEM images of CdSe-CTAB clusters were analysed using the software FRACTAL3 because these structures had a self-similar appearance (Figure 3.6). The evaluated fractal dimensions are listed in Table 3.1.

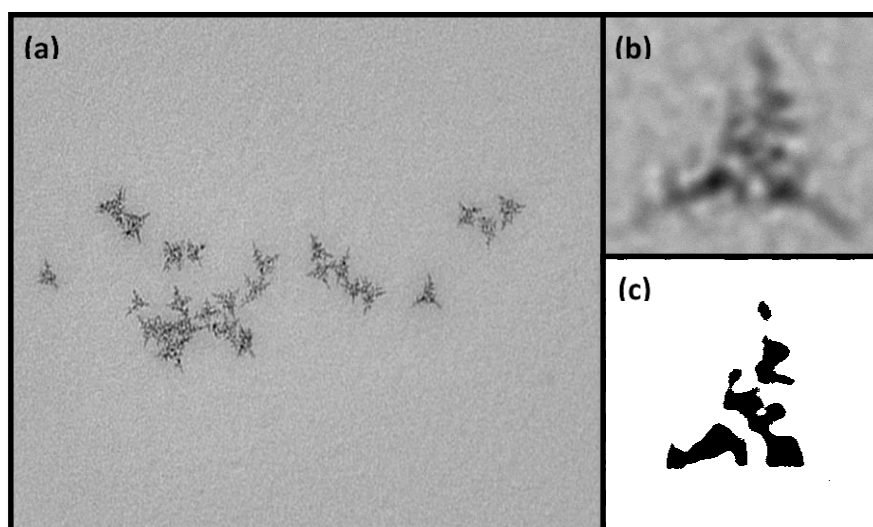


Figure 3.6: (a) TEM image of CdSe-CTAB (core diameter 3.5 nm), (b) cropped TEM image of CdSe-CTAB (core diameter 3.5 nm), (c) Median image used by the software to analyse the fractal dimensions discussed in details at appendix 1.

3.3.2 Ligand Exchange Conformation by FT-IR

The surface functionalization of CdSe QDs capped with oleic acid and 3-MPA were comparative analyzed by the FTIR spectra that is depicted in Figure 3.7. This FTIR spectra shows the existence of Cd-Se ($\sim 699 \text{ cm}^{-1}$) bonding with long alkane chains. Presence of CH_3 (bending at 1466 cm^{-1} , symmetrical stretching at 2872 cm^{-1} and asymmetrical stretching at 2970 cm^{-1}) and $-\text{C}=\text{C}-$ stretching (2076 cm^{-1}) confirms the

capping of oleic acid, forming a carboxylate structure (-COO-) with CdSe QDs. As we can see in the FTIR spectra that the absence of -SH stretching (2564 cm^{-1}) and the presence of the characteristic -COOH peak (1712 cm^{-1} for -C=O stretching in carboxyl group) confirming the bind formation between MPA and Cd sites through the thiol groups ^[16].

Table 3.3: Assignment of the bands in the FT-IR spectrum of OA-CdSe QDs and MPA-CdSe QDs.

OA capped CdSe QDs (cm^{-1})	MPA capped CdSe QDs (cm^{-1})	Assignment
699	699	Cd – Se bond
	920	-OH bending
	1013-1109	-C-O-C vibration
	1318	C-H scissoring mode bending
	1413	-CH ₂ - scissoring mode bending
1466		C-CH ₃ asymmetrical bending
	1712	-C=O stretching in carboxyl group
2076		-C=C- stretching
2872		Symmetrical Stretch -CH ₃
2970		Asymmetrical Stretch -CH ₃
	2830	Symmetrical Stretch -CH ₂
	2928	Asymmetrical Stretch -CH ₂

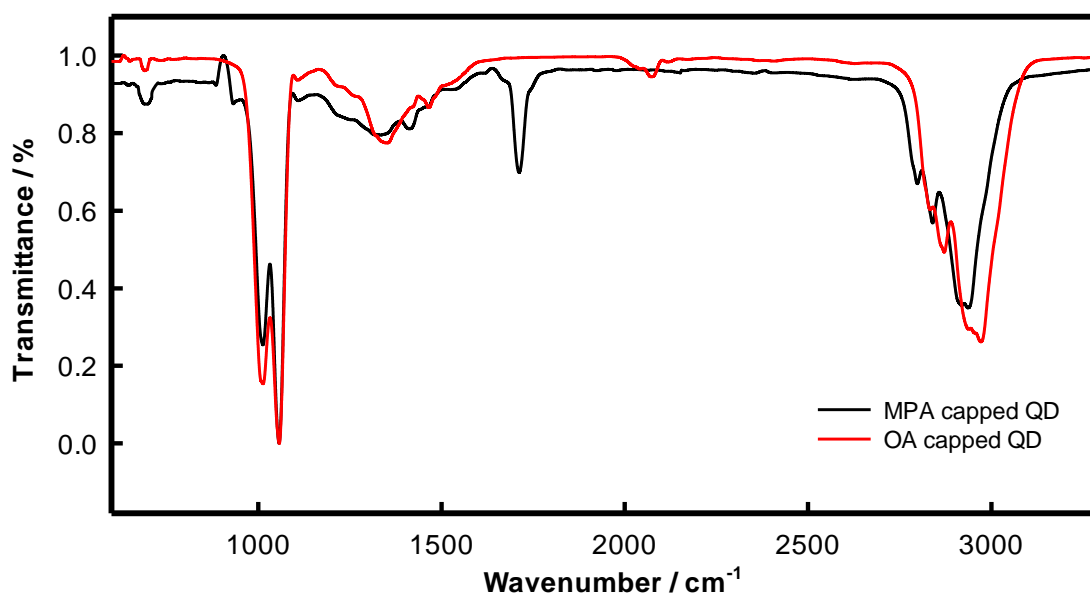


Figure 3.7: FT-IR spectra of CdSe QDs with oleic acid (OA) and 3-mercaptopropenoic acid (MPA) capping.

The FT-IR spectra of different surfactant functionalized oleic acid capped CdSe QDs is shown in Figure 3.8 that clearly shows the outermost capping of oleic acid around all type of surfactants functionalized QDs.

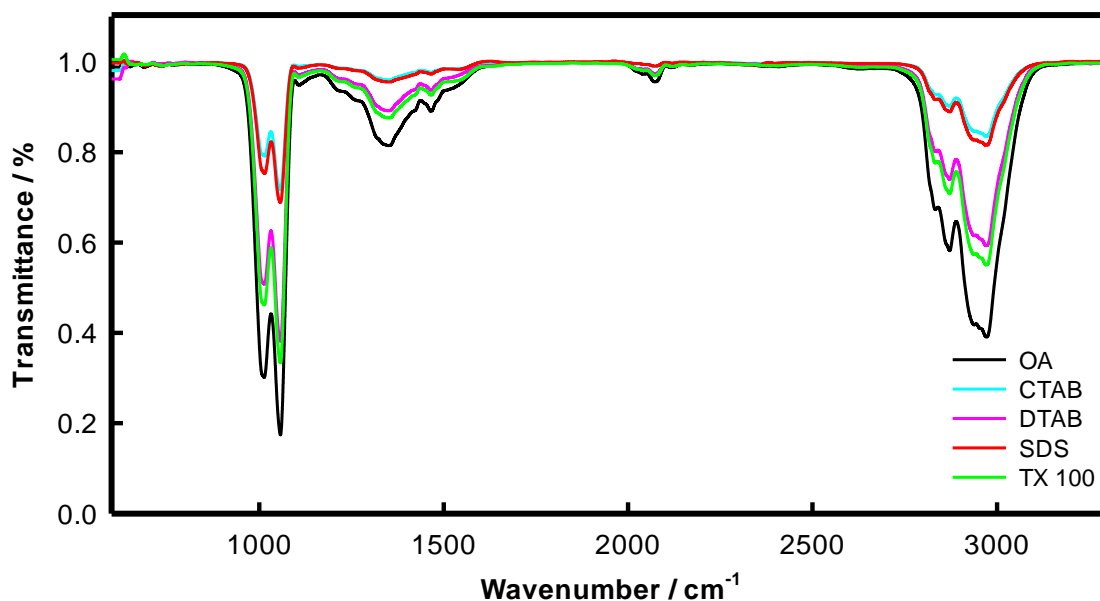


Figure 3.8: FT-IR spectra of surfactant functionalized oleic acid capped CdSe QDs.

3.3.3 Crystalline Structure

To see the crystallographic features, XRD of MPA coated CdSe QDs for both QDs groups have been done. The XRD pattern analysis revealed the crystallographic planes, phase and crystallite size of the NCs.

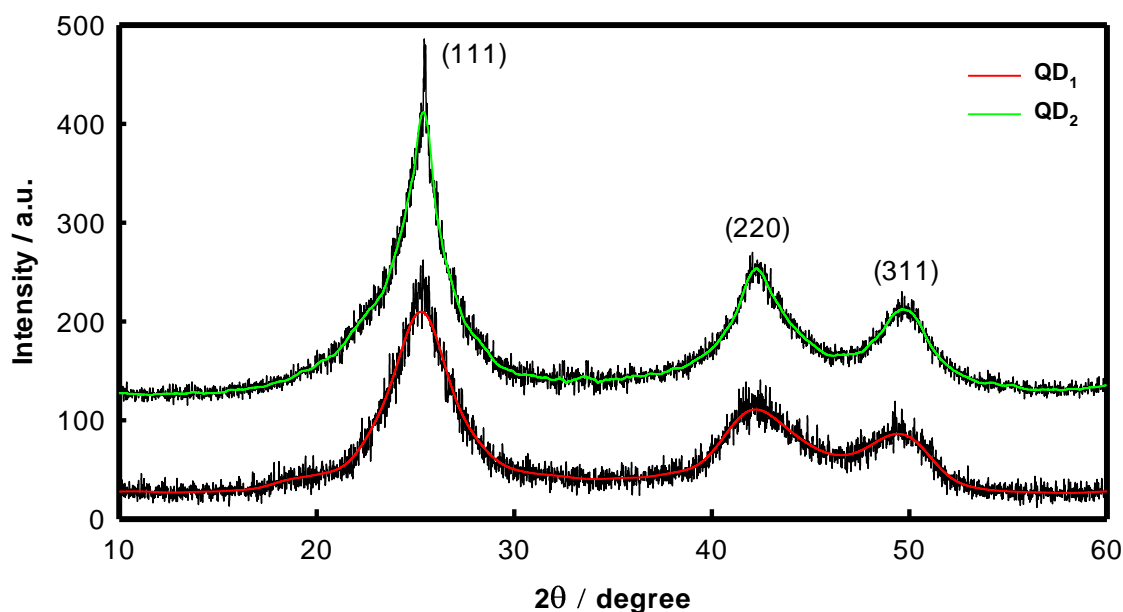


Figure 3.9: XRD pattern with plain indexed of MPA capped CdSe QDs of both groups (QD₁~2.5 nm and QD₂~ 3.5 nm).

The diffraction peaks are shown in Figure 3.9 located at 3 distinct angles given by $2\theta =$

25.35⁰, 42.15⁰ and 49.45⁰ could be correlated to the diffraction planes of (111), (220) and (311) of the lattice corresponding to the known cubic crystal structure of CdSe. The broad peaks implied that they are nanocrystals with nano sized crystallinity. No other peaks were observed i.e. impurities were not present. Next step was to get more information about the NC structure, the other parameters were calculated described in section 2.4.1.1 (II) of Chapter 2 and tabulated in Table 3.4.

The diffraction peaks showed progressive narrowing when going from group QD₁ to group QD₂, indicating an increase in crystal size because overall size of NCs was increasing.

Table 3.4: Crystallite parameters of MPA capped CdSe QDs of both groups.

	Plane (hkl)	2θ (degree)	FWHM (degree)	d-spacing (nm)	Lattice vector a (nm)	Crystallite size (nm)	Strain × 10 ⁻²	Mean size (nm)
QD ₁	(111)	25.40	3.8	0.35	0.607	2.2	7.43	2.1
	(220)	42.2	4.2	0.21		2.1	4.77	
	(311)	49.5	4.4	0.18		2.0	4.17	
QD ₂	(111)	25.30	2.6	0.35	0.607	3.3	5.03	3.2
	(220)	42.1	2.9	0.21		3.1	3.29	
	(311)	49.4	2.9	0.18		3.2	2.75	

3.3.4 Spectroscopic Properties

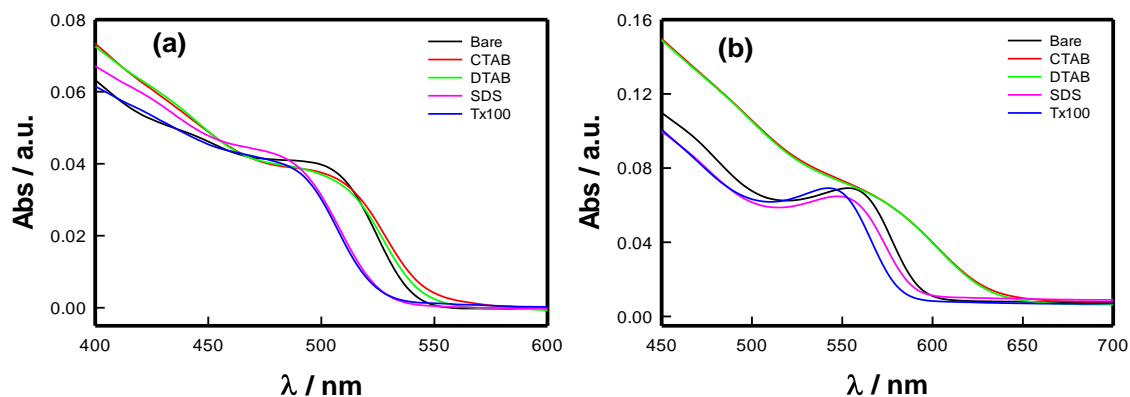


Figure 3.10: Absorbance Spectra of quantum dots with core diameter of (a) 2.5 nm and (b) 3.5 nm with four different ligands.

The absorbance and steady state photoluminescence (PL) measurement data were used to probe the effect of surface ligands on the spectroscopic properties of these colloidal nanoparticles. Figure 3.10 shows the absorbance, and the fluorescence spectra of quantum dots synthesized with the four surfactant ligands.

As the reaction temperature, and time were kept constant, the size of the CdSe core, was found to be independent of the choice of capping ligand (Table 3.1), and thus any changes in the absorption or luminescence spectra can be attributed mainly to the choice of capping ligand, and not to the change in the particle size induced by nucleation or growth rate. For QDs synthesized with SDS, TX-100, the absorbance was observed to blue shift, and for QDs synthesized with CTAB and DTAB, the absorbance was observed to red shift relative to QDs synthesized without any surfactant (Figure 3.10).

We postulate that the changing surface charge alters the effective confining potential, but this cannot be conclusively established with the data presently available. This data suggest that changing the surface functionalization changes the surface charge, and hence provides a pathway for manipulating the optical properties of QDs, in our case the shift in the absorption wavelength was in the window of approximately 15 nm.

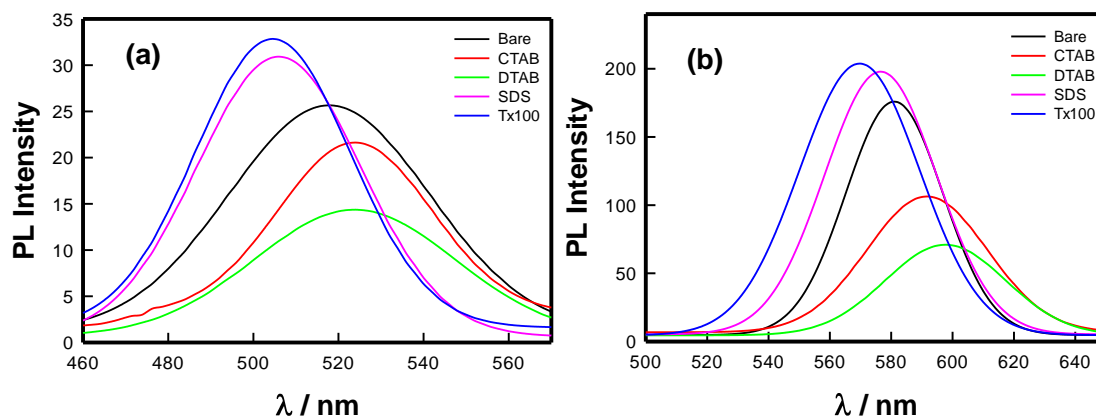


Figure 3.11: Comparison of Photoluminescence (PL) emission measurements for CdSe quantum dots with core diameter (a) 2.5 nm and (b) 3.5 nm with different surface ligands.

As is shown in Figure 3.11, the functionalization with ligands (surfactants) resulted in a substantial change in the PL emission intensity relative to QDs functionalized with only OA. The highest enhancement in fluorescence can be seen in TX-100 functionalized QDs then in SDS functionalized QDs, whereas CTAB and DTAB surface ligands caused loss in PL w.r.t. QDs functionalized with only OA. It is possibly due to cluster structure and well boundary of the coated quantum dots. Only CTAB and DTAB functionalized QDs have cluster structure so there is loss in PL. DTAB functionalized QDs have better boundary and more loss in PL than CTAB functionalized QDs. The peak wavelength

corresponding to absorption and emission spectra of all these surfactant coated QDs are listed in Table 3.5.

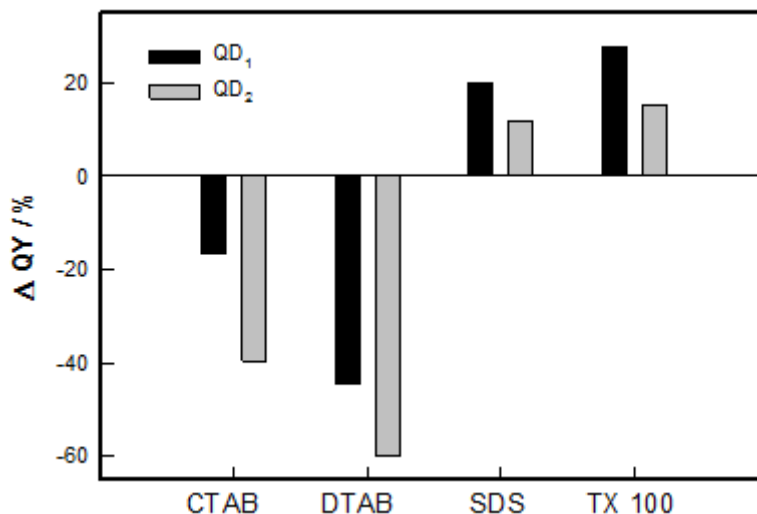


Figure 3.12: Plot showing change in quantum yield (%) for CdSe QDs coated with different surface ligands *w.r.t.* OA coated QDs. Data in black and grey represent QD core diameters of 2.5 and 3.5 nm respectively.

Table 3.5: Comparison of absorption peaks, emission peaks and quantum yield for different surface functionalized CdSe QDs. CdSe QDs with two different core diameters (2.5 and 3.5 nm) are compared in this table.

		No Surfactant	CTAB	DTAB	SDS	TX-100
QD ₁	λ_{Abs} (nm)	498.0	505.0	502.0	486.0	483.0
	λ_{Emi} (nm)	518.0	524.0	522.0	506.0	502.0
	ΔQY (%)		-16.5	-44.4	20.0	27.8
QD ₂	λ_{Abs} (nm)	558.0	571	572.0	552.0	547.0
	λ_{Emi} (nm)	580.0	591	594.0	575.0	569.0
	ΔQY (%)		-39.5	-59.9	11.9	15.2

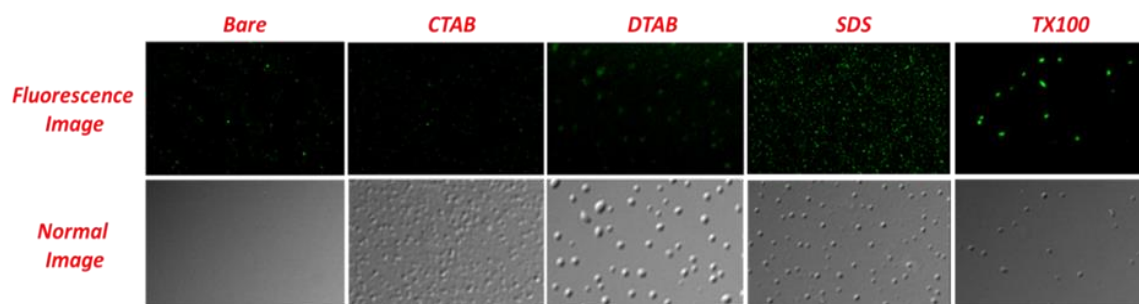


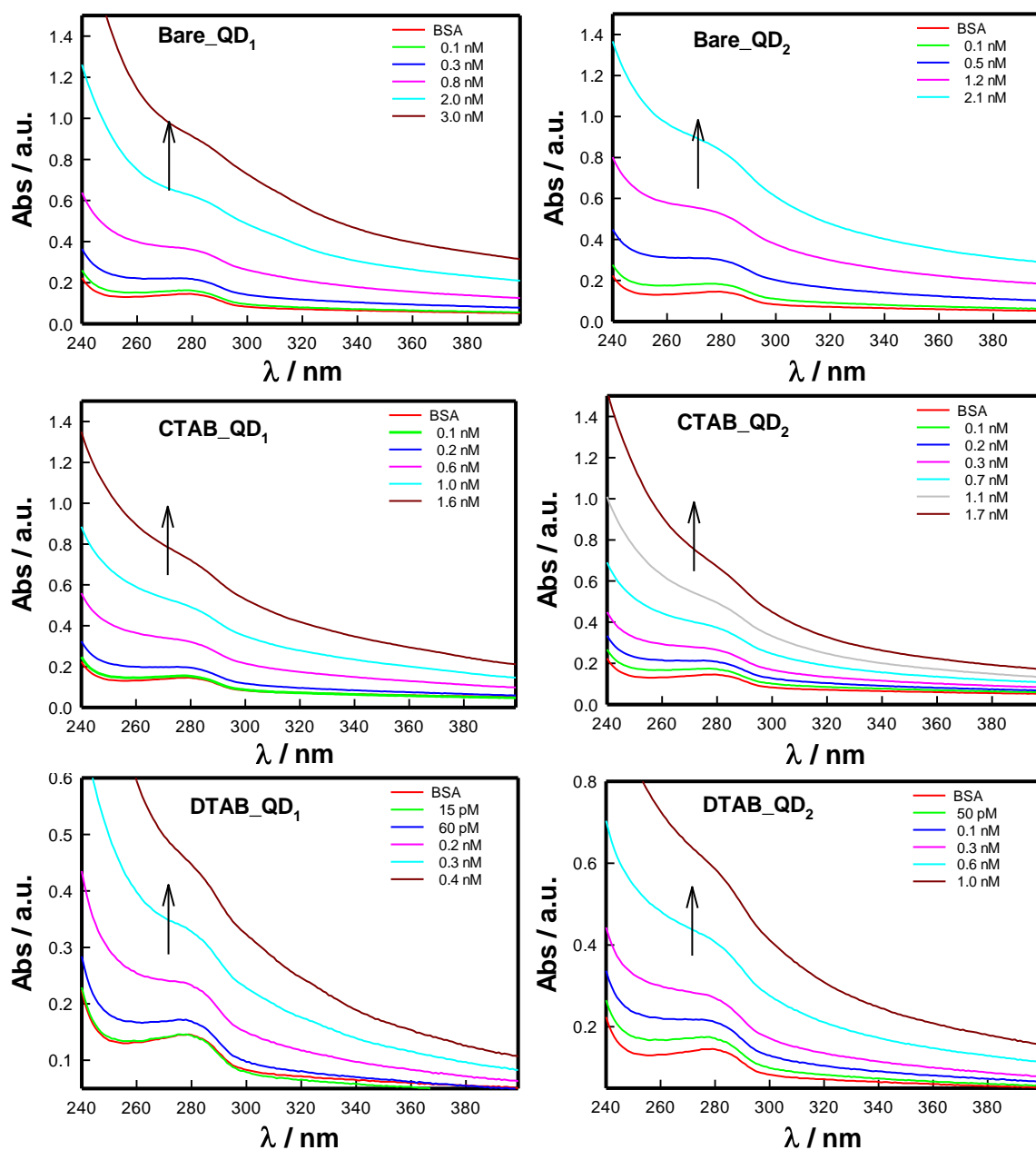
Figure 3.13: Confocal images of smaller QDs without surfactant coating (Bare) and with surfactant (CTAB, DTAB, SDS and TX-100) coating.

The confocal imaging clearly indicates that the fluorescence intensity order: TX100 > SDS > Bare > CTAB > DTAB. This visual observation was consistent with the results obtained from fluorescence spectroscopy data.

3.4 Biophysical Characterization

3.4.1 BSA-QD Binding

UV-Vis absorption spectroscopy can be used to locate the onset of complex formation, and to establish the binding profile. Absorption spectra of BSA showed an absorption band centered at $\lambda = 280$ nm, which can be attributed to the presence of Tyrosine (Tyr) and Tryptophan (Trp) amino acids. Figure 3.14 illustrates the absorbance spectra of BSA as function of concentration of two size groups of QDs (2.5 and 3.5 nm).



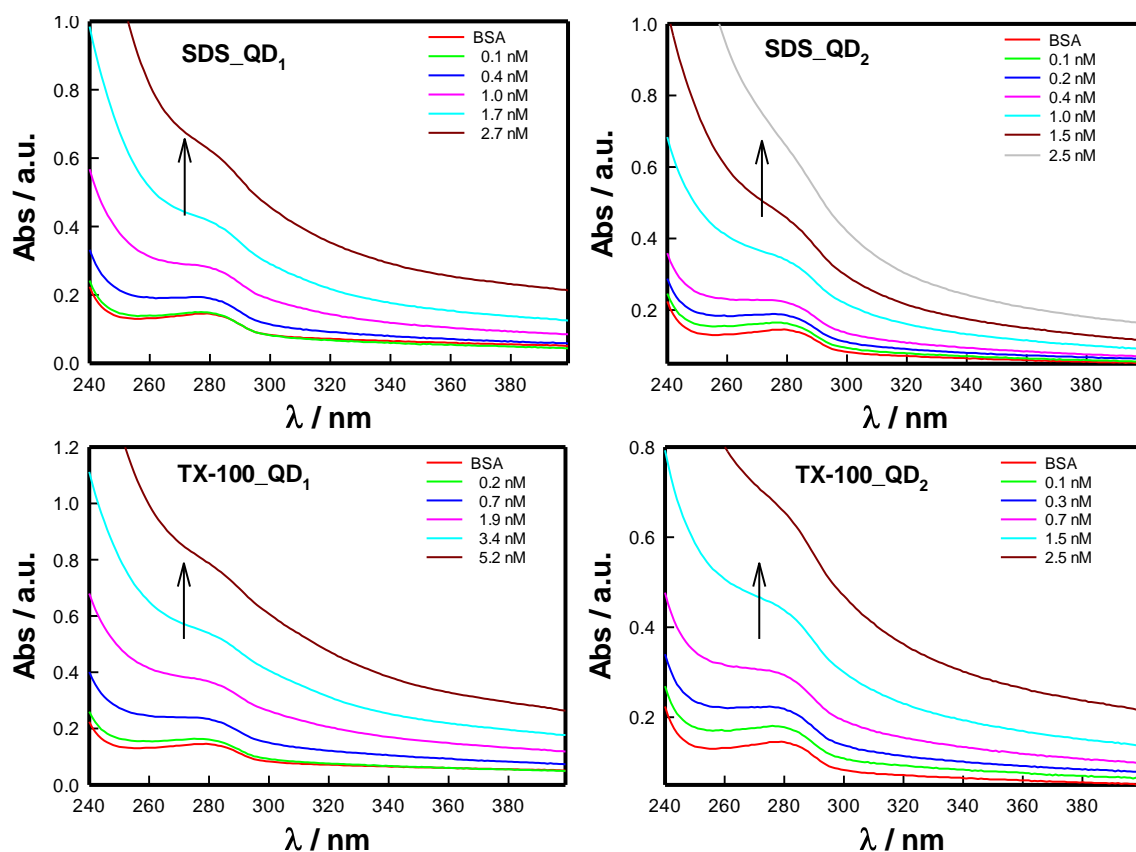


Figure 3.14: Absorbance spectra of protein BSA (1.5 μ M) in the absence and presence of QD₁ and QD₂ functionalized with surfactants CTAB, DTAB, SDS, TX100 and without any surfactant (Bare).

When the QD content was increased, the absorbance increased linearly regardless of the QD size and surfactant type indicating BSA-QD complex formation (Figure 3.15).

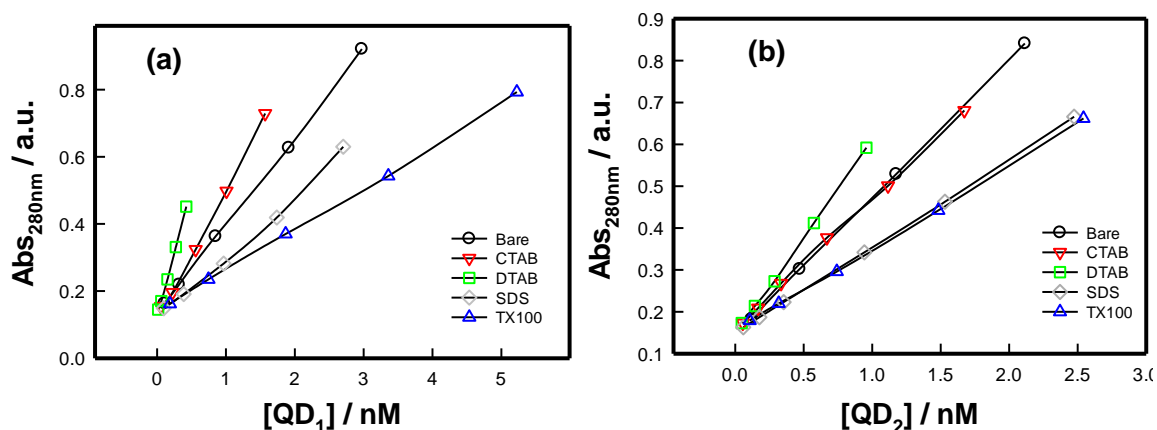
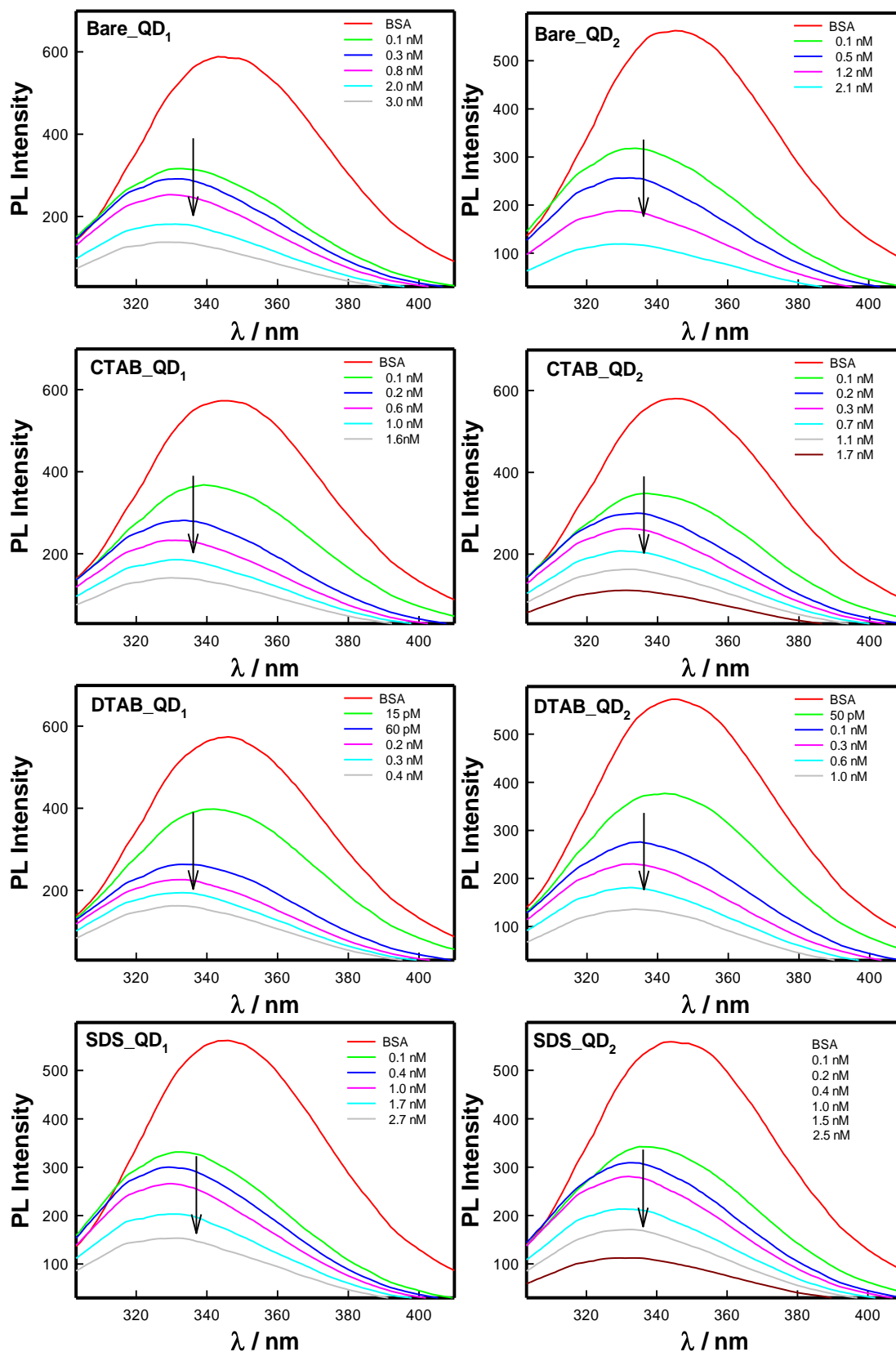


Fig. 3.15: Absorbance at $\lambda = 280$ nm of protein BSA (1.5 μ M) in the absence and presence of (a) QD₁ (2.5 nm), and (b) QD₂ (3.5 nm) nanoparticles capped with different surfactants. Notice the linear dependence.

In the next step, titration of protein solution with quantum dot dispersions was carried out where fluorescence quenching was observed at 350 nm, which is depicted in Figure 3.16. The maximum emission wavelength of protein (donor) is nearly 350 nm, which is

higher than the excitation wavelength of QDs (acceptor). So when we add QDs in aqueous solution of protein, emission intensity of proteins is used to excite the QDs and the non-radiative loss in fluorescence spectra (quenching) of proteins is occurred.



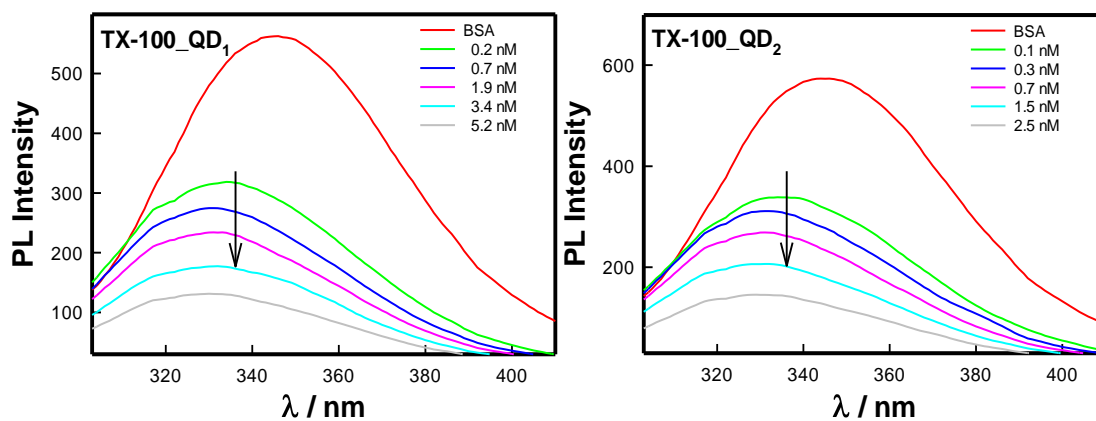


Figure 3.16: Emission spectra of protein BSA (1.5 μ M) in the absence and presence of QD₁ and QD₂ functionalized with surfactants CTAB, DTAB, SDSTX100 and without any surfactant (Bare).

The quantitative degree of quenching of (intrinsic) fluorescence of BSA upon binding to quantum dots was analysed by equation 2.29 of Chapter 2.

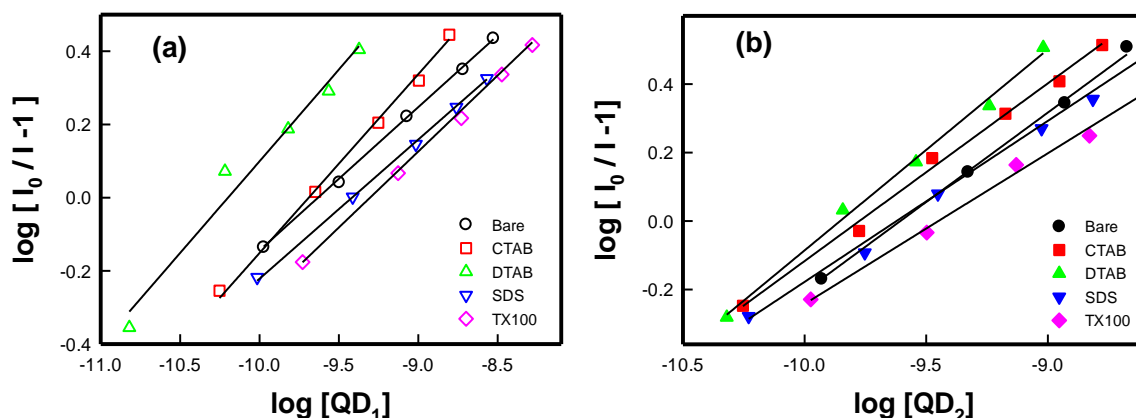


Figure 3.17: Double log plot shown for proteins BSA (1.5 μ M) as function of concentration of (a) QD₁ and (b) QD₂ uncoated and coated with different surfactants. Solid lines are fitting to eqn. (2.29) of Chapter 2.

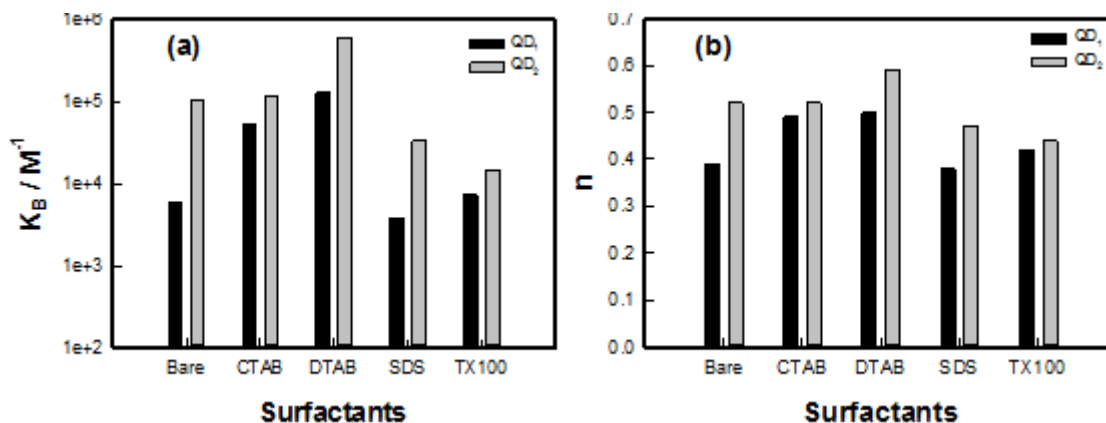


Figure 3.18: (a) Binding constant K_B and (b) number of occupied binding sites, n , shown for both size group of QDs coated with different surfactants.

The fluorescence lifetime of protein fluorophore τ_0 needs to be determined from time-resolved fluorescence spectroscopy data. Realize that K_{SV} is related to quenching rate constant through the relation $k_q = K_{SV}/\tau_0$ which is typically on the order of $10^{13} - 10^{14} \text{ M}^{-1}\text{s}^{-1}$ [17]. The normalized intensity parameter, $\log [I_0/I-1]$ is plotted as function of concentration of quencher, which is shown in Figure 3.17, in a typical data analysis procedure. One can determine the value of binding constant, and number of occupied binding sites, n from intercept, and slope of such a plot. These values are tabulated in Table 3.6.

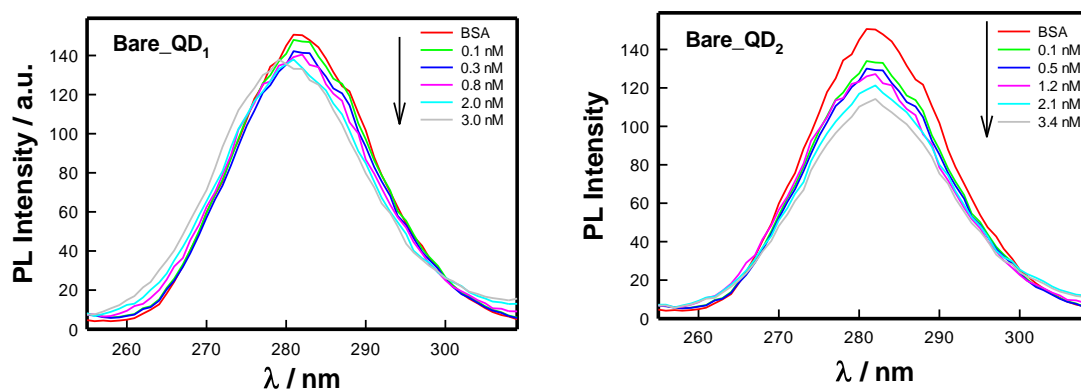
Table 3.6: Binding constant K_B , number of occupied binding sites n and fluorescence quenching constant K_q of various BSA-QD samples. QD₁ and QD₂ refer to 2.5 and 3.5 nm core sized particles.

Capping	$K_B / \times 10^3 \text{ M}^{-1}$		n		$K_q / \times 10^{-6} \text{ M}^{-1}\text{s}^{-1}$	
	BSA-QD ₁	BSA-QD ₂	BSA-QD ₁	BSA-QD ₂	BSA-QD ₁	BSA-QD ₂
Bare	5.9	104.0	0.39	0.52	24.0	426.0
CTAB	54.0	118.0	0.49	0.52	221.0	483.0
DTAB	130.0	608.0	0.50	0.59	533.0	2492.0
SDS	3.8	33.0	0.38	0.47	15.0	135.0
TX100	7.3	14.0	0.42	0.44	29.0	57.0

Several conclusions could be derived from these observations pertaining to BSA-QD binding: (i) the binding affinity followed $QD_1 < QD_2$, (ii) the average number of the (active) binding sites available on BSA was $\approx 0.5 \pm 0.1$ and (iii) the fluorescence quenching followed $QD_1 < QD_2$.

3.4.2 Effect on Environment of Protein: Synchronous Fluorescence Spectra

Synchronous fluorescence spectra obtained from these samples are shown in Figure 3.19 (quenching in Tyr with QD₁ and QD₂), and Figure 3.20 (quenching in Trp with QD₁ and QD₂).



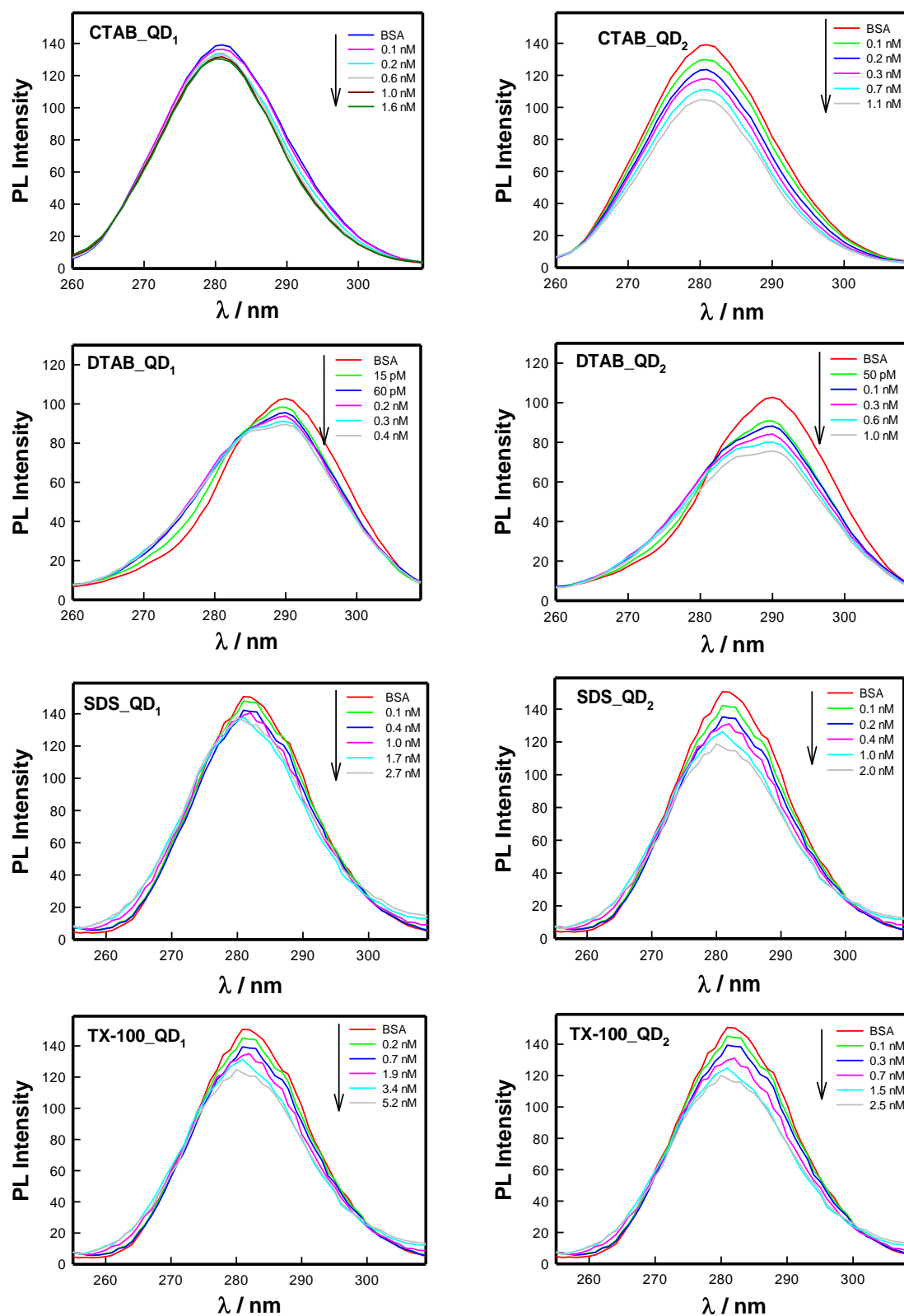
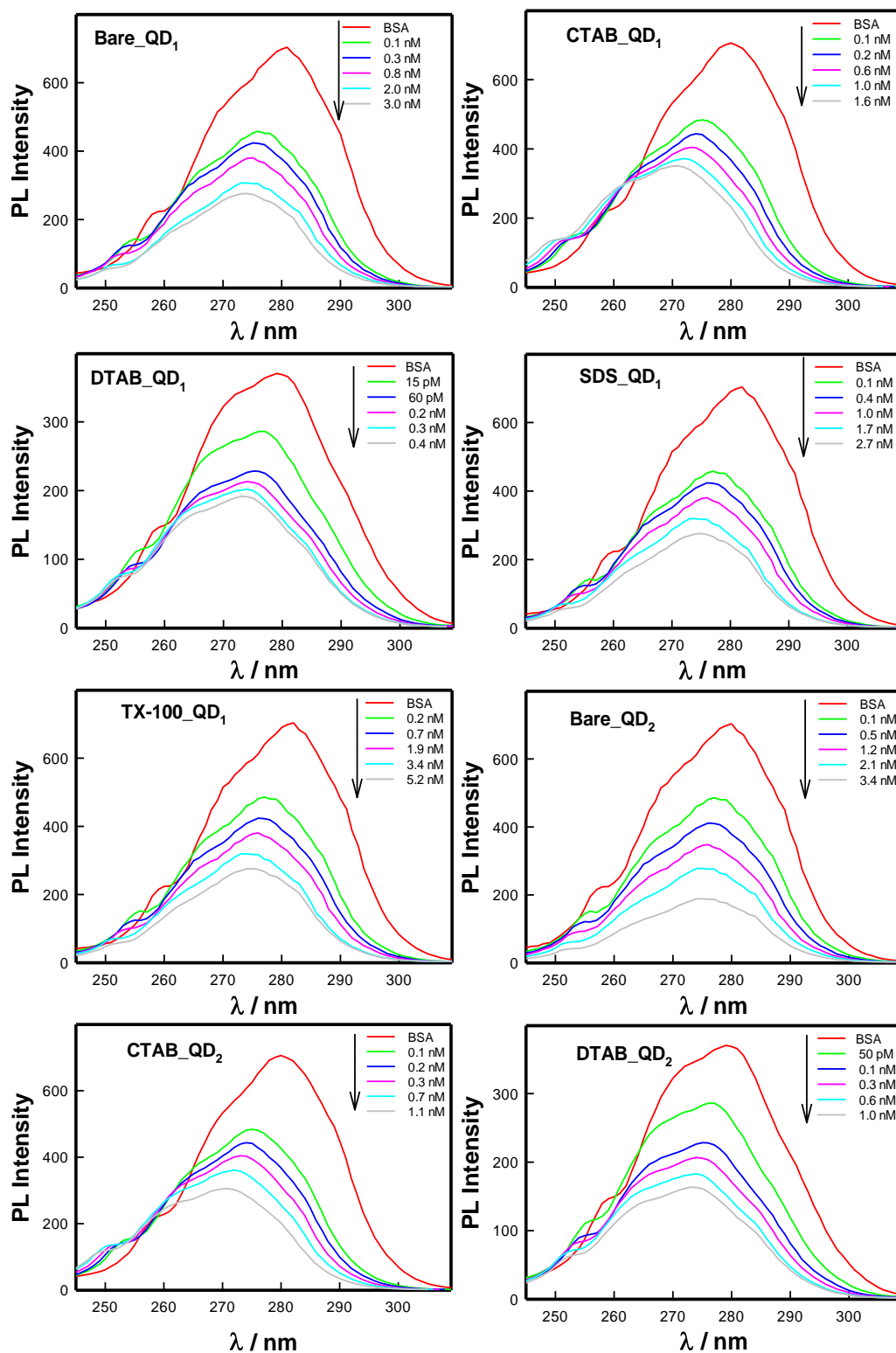


Figure 3.19: The synchronous fluorescence spectra at $\Delta\lambda=15$ nm (Tyrosine) of proteins BSA ($1.5\mu\text{M}$) in the absence and presence of QD₁ and QD₂ of uncoated and coated with different surfactants.

This data clearly inferred that increase in the concentration of quantum dots caused the fluorescence of Trp to decrease which was more than that of Tyr (Fig. 13). This implied

that quantum dots quenched the intrinsic fluorescence (due to the presence of Trp residues) of BSA. In addition, we noticed blue shift in maximum emission wavelength. Thus, the presence of quantum dots changed the microenvironment in the vicinity of the Trp residue, which resulted in the changes in the conformation of the protein concerned [18].



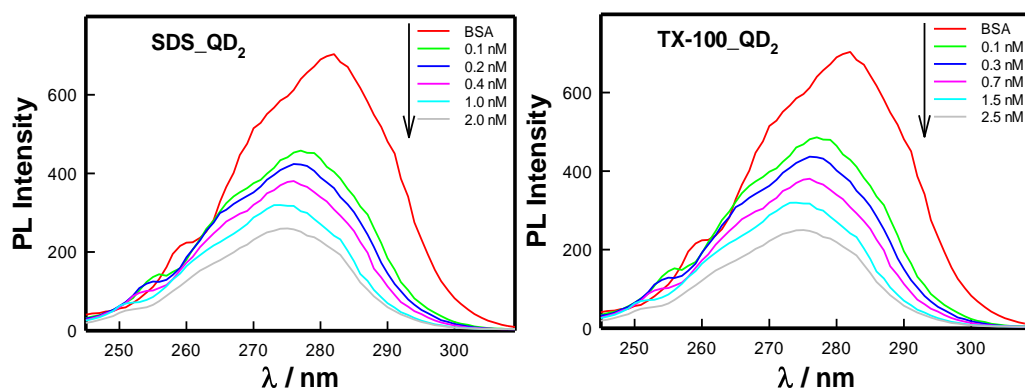


Figure 3.20: The synchronous fluorescence spectra at $\Delta\lambda=60$ nm (Tryptophan) of proteins BSA ($1.5\mu\text{M}$) in the absence and presence of QD_1 and QD_2 of uncoated and coated with different surfactants.

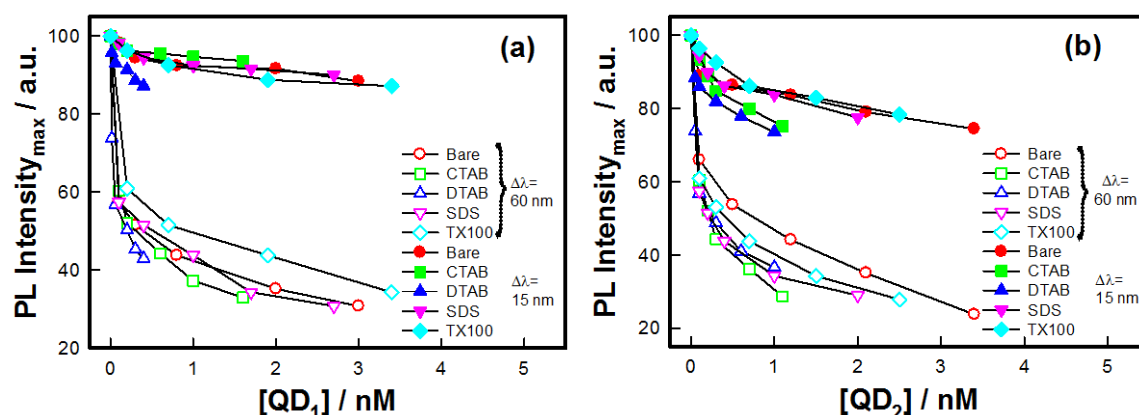
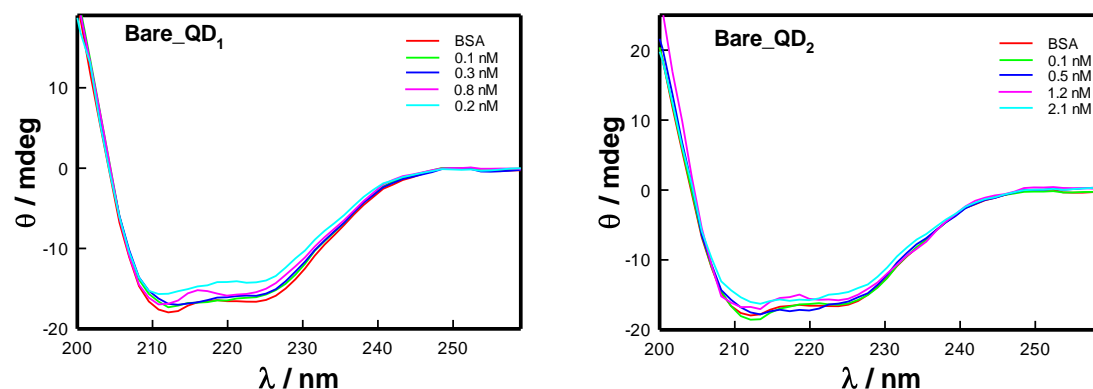


Figure 3.21: Peak intensity of synchronous fluorescence spectra for $\Delta\lambda=60\text{nm}$ (Trp), and $\Delta\lambda=15$ nm (Tyr) of BSA versus concentrations of (a) QD_1 (2.5 nm) and (b) QD_2 (3.5 nm) nanoparticles coated with different surfactants. Solid lines are guide to the eye.

3.4.3 Effect on Protein Secondary Structure

Protein-QD interaction can cause conformational changes in the native state of the protein at secondary structure level. CD spectra obtained from BSA and the same of their quantum dot bound complexes are shown in Figure 3.22. The BSA-QD complexes revealed signature peaks (two negative doublet peaks) arising from α -helix content (of proteins) became shallower. Therefore, it is concluded that the helix content of BSA



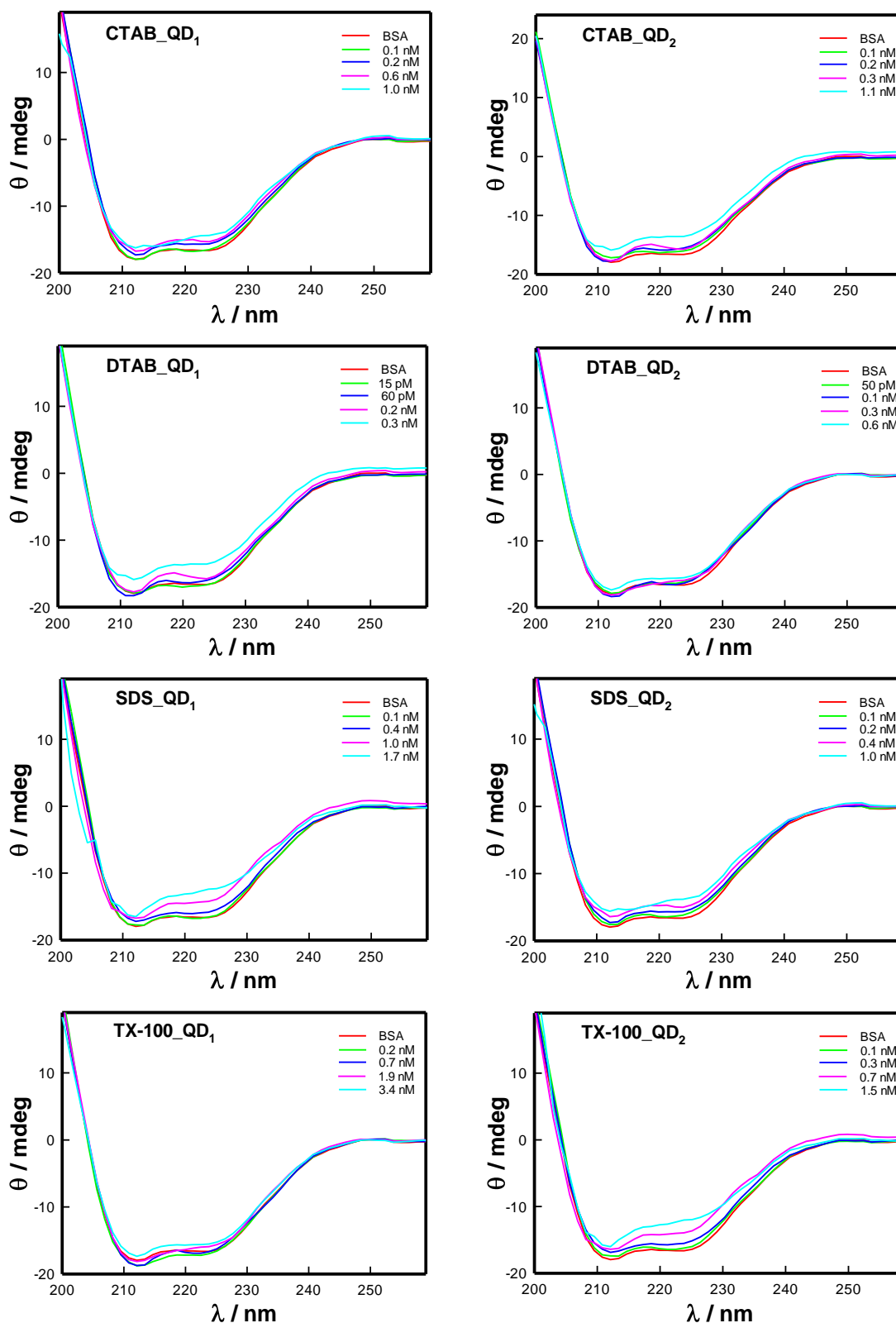


Figure 3.22: The CD spectra of protein BSA ($1.5\mu\text{M}$) in the absence and presence of QD₁ and QD₂ of uncoated and coated with different surfactants.

continuously decreased inferring strong associative interaction with quantum dots of both size [44-47]. As shown in our results, QDs coated with different surfactants have caused same amount of conformational changes in the BSA as in the case of QDs

without surfactant coating (Circular Dichroism result). And all types of QDs have same outer MPA coating (Zeta potential's result). So we can say that the QD-BSA interaction was mediated mainly through this outer coating neither due to the interactions of CdSe QD core nor surfactant coating (inner layer) on QDs with amino acids of the protein. The changes in helicity of protein can be the results of the size, surface charge and shape of outer surfaces of QDs.

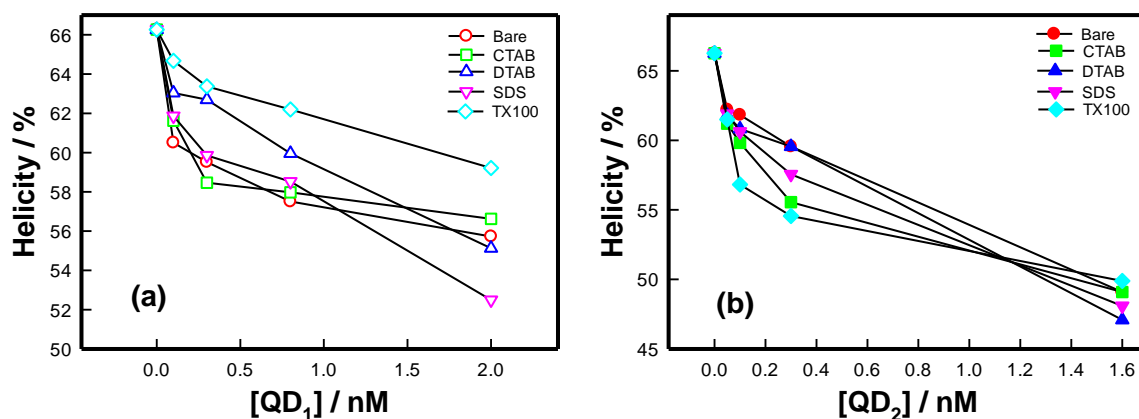


Figure 3.23: Variation of secondary structure (helicity) of proteins BSA (1.5 μM) on the concentration of (a) QD₁ (2.5 nm) and (b) QD₂ (3.5 nm) of coated with different surfactants. Note the drastic loss in the secondary structure of BSA due to its binding with bigger size quantum dot (3.5 nm).

Typically, the helix content of the proteins can be determined from the equation 2.31 of Chapter 2. The CD data was utilized in equation 2.31 to evaluate the helix content which is depicted in Figure 3.23.

3.5 Size and Coating Dependent Differential Binding

It is imperative to discuss the size and coating dependent differential binding observed in this work. We have dealt with quantum dots of size 2.5 and 3.5 nm. BSA has an apparent hydrodynamic size of 3.5 nm. The zeta potential of both type of QDs was close to within 10% for any given surfactant (see Fig. 4). Thus, their charge density was almost identical. However, the surface area of bigger size QD was atleast 6 times larger than its smaller competitor. Therefore, bigger size QD group would exhibit enhanced binding compared to smaller quantum dots purely from geometric considerations. Thus, the differential binding must arise from the BSA surface charge density anisotropy, difference in ligand surface area, size and coating present on the QDs. BSA dissolved in water has pH ~ 5.5 hence overall surface charge is approximately -10 mV [19]. So quantum dots having less negative surface charge density would permit the proteins to adsorb more onto their surfaces which would again be biased towards bigger size QDs

and DTAB coated QDs. Intuitively, it can be argued that increase in favourable interaction first causes the water molecules bound to BSA to redistribute, and dehydrate the loci of contacts. These effects will finally quench the intrinsic fluorescence of protein and give the hydrophobic environment to it. In addition, this would destroy the secondary structure of protein concerned.

3.6 Summary

We have reproducibly demonstrated considerable enhancement of photoluminescence quantum yield in the core of CdSe QDs with particular (anionic) surface ligands through the passivation of surface states. We observed that the quantum yield of CdSe QDs was enhanced selectively when functionalized with TX-100 and SDS ligands. Incremental change in quantum yield was observed in surfactant coated QDs due to the inhibition of aggregation process. The enhancement in quantum yield was found to be maximum for TX-100, and maximum quenched for DTAB with respect to bare (coated with OA) particles. The ability to use surface ligands to control the passivation of surface states and non-radiative energy loss pathways can prescribe a route to enhancement of photocurrent enabling tailored design of nanocrystal-based light emitting and photovoltaic devices with improved efficiency. When used in vivo, these nanoparticles are immediately exposed to plasma proteins which motivated our second part of this work. It was noticed that the binding had QD size selectivity and this caused loss in the secondary structure of the plasma protein BSA. Clearly, more work in this topic needs to be done to develop better understanding of the nanoparticles-protein interaction.

3.7 References

- [1] P. E. Lippens, M. Lannoo, *Phys. Rev. B: Condens. Matter*, **1990**, *41*, 6079.
- [2] L. W. Wang, A. Zunger, *Phys. Rev. B: Condens. Matter* 1996, *53*, 9579.
- [3] W. W. Yu, L. Qu, W. Guo, X. Peng, *Chem. Mater.* **2003**, *15*, 2854.
- [4] R. Xie, U. Kolb, J. Li, T. Basche, A. Mews, *J. Am. Chem. Soc.* **2005**, *127*, 7480.
- [5] R. W. Meulenberg, J. R. I. Lee, A. Wolcott, J. Z. Zhang, L. J. Terminello, T. V. Buuren, *ACS Nano* **2009**, *3*, 325.
- [6] Y. Fu, T.T. Han, H. A gren, L. Lin, P. Chen, Y. Liu, G.Q. Tang, J. Wu, Y. Yue, N. Dai, *Appl. Phys. Lett.* **2007**, *90*, 173102-1-3.

- [7] J. Jiang, B. Gao, T.T. Han, Y. Fu, *Appl. Phys. Lett.* **2009**, *94*, 092110-1-3.
- [8] W. T. Al-Jamal, K. T. Al-Jamal, P. H. Bomans, P. M. Frederik, K. Kostarelos, *Small* **2008**, *4*, 1406.
- [9] H. W. Park, D. H. Kim, *Journal of Nanomaterials - Special issue on Photoluminescence Properties of Nanoparticles* **2012**, *1*, 1.
- [10] X. Ji, J. Zheng, J. Xu, V. K. Rastogi, T. C. Cheng, J. J. De Frank, R. M. Leblanc, *J. Phys. Chem. B*, **2005**, *109*, 3793.
- [11] H. Shen, H. Yuan, J. Z. Niu, S. Xu, C. Zhou, L. Ma, L. S. Li, *Nanotechnology* **2011**, *22*, 375602-1-11.
- [12] S. F. Wuister, C. M. Donega, A. Meijerink, *J. Phys. Chem. B* **2004**, *108*, 17393.
- [13] W. W. Yu, Y. A. Wang, X. Peng, *Chemistry of Materials* **2003**, *15*, 4300.
- [14] I.A. Mir, K. Das, K. Rawat, H.B. Bohidar, *Colloid Surface A*. **2016**, *494*, 162.
- [15] B.B. Mandelbrot, *Freeman, San Francisco, USA*, **1982**.
- [16] Wang, C., Gao, X., Ma, Q., Su, X., *Journal of Materials Chemistry* **2009**, *19*, 7016.
- [17] M. Tachiya, *J. Chem. Phys.* **1982**, *76*, 340.
- [18] G. Zhang, N. Zhao, L. Wang, *J. Lumin.* **2011**, *131*, 880.
- [19] K. Rawat, H. B. Bohidar, *The Journal of Physical Chemistry B* **2012**, *116*, 11065.

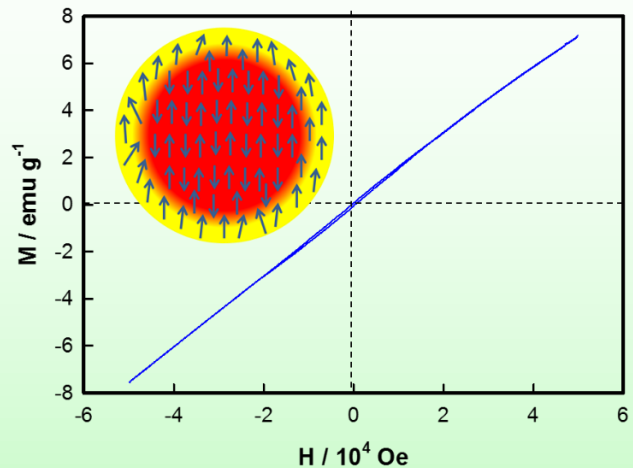
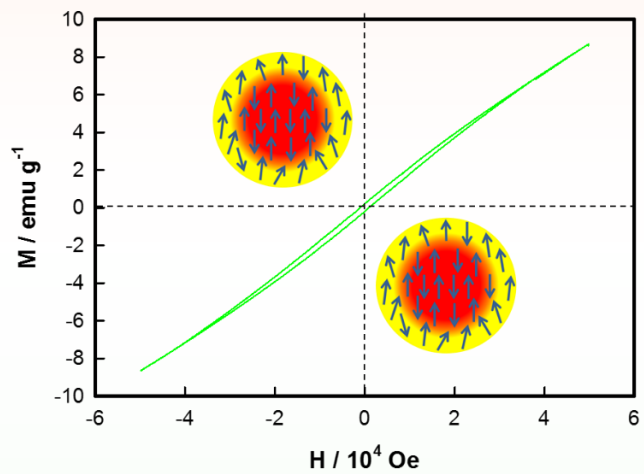
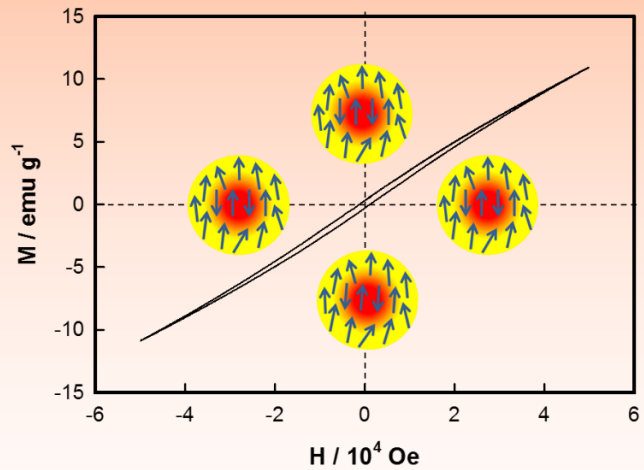
Chapter 4

Size Variational Synthesis and Characterization of Cubic MnSe Nanospheres

Abstract: This chapter discusses the facile controlled synthesis of non-iron based highly crystalline cubic phase MnSe antiferromagnetic nanospheres of different sizes in organic phase by hot injection method without need for special conditions.

Effect of the reaction temperature on size, optical and magnetic properties has been presented and discussed.

Pictorial representation of hysteresis loop caused by surface spins of MnSe nanospheres of different sizes is shown here.



4.1 Introduction

Nanocrystals that show observable response under an external magnetic field are called magnetic nanocrystals (MNCs). Decreasing the particle size results in the increase in the surface to volume ratio. For the nanocrystals (NCs), this ratio is very high resulting in more atoms on the surface as compared to the core. The reduced coordination number and lack of symmetry of surface spins ^[1] are mainly responsible for changes observed in the magnetic order in the particle. The magnetic properties and the coercivity field (H_C) ^[2] with the Curie constant (C), Weiss constant, blocking temperature ^[3] or freezing (T_F) temperatures are significantly different than those of the bulk material ^[4,5]. Finite size effects ^[2], i.e. quantum confinement of the electrons and single or multi magnetic domains structures, and surface effects, i.e. effects of symmetry-breaking of chemical and physical environment at surface, are dominating factors that decide the magnetic property of these nanoparticles. Magnetic nanoparticles (MNPs) have found applications in ultrasensitive sensors ^[6], high-density data storage, bioimaging ^[7], logic devices ^[8] and bio-nanomedicine ^[9] like hyperthermia i.e. the treatment of certain cancers ^[10,11]. Thus the combination of magnetic with fluorescence properties can enhance the physical and biological application potential of any nanomaterial.

Pure magnetic metals and alloys of Fe, Co, and Ni are very sensitive to ambient condition ^[12]. Iron based magnetic nanoparticles have some limitations due to their poor aqueous suspension properties and for overcoming these limitations, one may have to coat their surface properly. This alters the surface chemistry of the nanoparticle as well as its size ^[13,14]. Therefore non-iron based magnetic nanoparticles are getting more attention in the recent past, because of their multifunctionality.

Transition metal chalcogenides attracted much attention due to their interesting magnetic, optical, and transport properties. Especially, crystal structure resultant magneto-optical property ^[15] makes manganese selenide (MnSe) special. It has three crystal structures: metastable ZB ^[16], WZ ^[15] and most stable RS ^[17]. RS-MnSe has unique antiferromagnetic ordering with large magnetic moment (theoretically^[18] and experimentally ^[19]) and size tuned band gaps that span the ultraviolet to visible range of electromagnetic spectrum ^[15,20]. With these dual properties, this material can be used in many applications such as in the design of multi-colour LEDs, diluted magnetic semiconductors, short-wavelength magneto-optical and optoelectronic devices. Moreover MnSe NCs are used to fabricate dilute magnetic nanoparticles, rechargeable battery electrodes ^[21], solar cells, gas sensors

and electrochromic devices. Recently, it has been predicted that using MnSe in heterostructures of magnetic insulator/ topological insulator is best to realize topological magneto-electric effect [22]. If we compare toxicity of MnSe with most commonly used CdSe semiconductor quantum dots, UV light create photolytic dissolution of highly fluorescent Cd-based semiconductor nanoparticles that results in the generation of free radicals in the form of toxic Cd ion [23] because of the use of cadmium ion precursor which is a soft Lewis acid [24]. Mn ion precursor is relatively harder one compared to Cd ion precursor so it is less reactive to the surrounding that results in lower photo bleaching, which makes it more biocompatible [25]. It has been reported that the cubic phase crystal structure is the most stable morphology of MnSe and many studies have been done on the synthesis, and on the evolution of properties of RS-MnSe [26–28]. However, there have been no reports on facile hot injection synthesis of highly crystalline and monodispersed spherical cubic-phase MnSe nanoparticles, which constitutes one of the main objectives of the work. Further, study of their size dependent spectroscopic and magnetic properties was undertaken which is discussed in this chapter. Considering the importance of non-iron based fluorescent magnetic nanoparticles in the evolving arena of nanotechnology, the relevance of the present work can be hardly stressed.

4.2 Size Variational Synthesis of MnSe Nanospheres

MnSe nanocrystals of different size with oleic acid capping are synthesized by the hot injection method described by Das et al [29]. This method offers many advantages, like narrow particle-size distribution of the product, good shape control and high yield over another synthesis methods.

4.2.1 Synthesis of Hydrophobic MnSe Nanospheres

Briefly, Se precursor was freshly prepared by mixing 60 mg of Se and 1 ml of trioctylphosphine (TOP) drawn by calibrated micro-syringe from its sealed bottle in 5 ml of 1-octadecene (ODE) (90%) in a opaque flask that was clamped on a hot plate maintained at temperature of 60⁰ C. The solution was stirred for about 30 min. This stock solution was stored at room temperature (25⁰C) in the same air tight bottle.

Mn precursor was prepared by adding 13 mg of (CH₃COO)₂Mn • 4H₂O to a 25 ml round-bottom borosilicate flask containing 0.6 ml of oleic acid (OA) and 10 ml of octadecene. This mixture was heated to different temperatures ranging from 200⁰ to 280⁰C in equal intervals of 40⁰C each for 30 minutes to prepare 3 different size of nanocrystals. After dissolution of manganese (II) acetate tetrahydrate, 1 ml of Se precursor was swiftly

injected into this hot Mn solution and the solution was allowed to vigorously stir for 10 min. After that it was left to cool naturally to room temperature 25⁰ C.

4.2.2 Filtration

For filtering unreacted precursors and by-products, the cooled sample in hexane was mixed in the extraction solvent (an equal volume mixture of CHCl₃ / CH₃OH) and then the aliquot was extracted from it. This process was repeated thrice. The unreacted precursors and excess OA were extracted into the CH₃OH (methanol) layer and only nanoparticles were remained in the ODE / hexanes layer. All samples were isolated using methanol and excess acetone, followed by centrifugation for 10 min at 10 000 rpm and the aliquots collected at the bottom.

By the abovementioned protocol, we prepared the hydrophobic MnSe NCs with three different sizes. It may be noted that OA capped QDs were hydrophobic^[29] and these were used for their physical characterization.

4.2.3 Ligands Exchange to Hydrophilic State

For making water-soluble, these nanocrystals were converted from hydrophobic to hydrophilic phase, 10 ml of OA capped nanoparticle dispersion was dispersed in 25 ml of chloroform to which 2 ml of a basic methanolic solution (pH~10) of MPA (~1.5 times of Mn atom) with 2.5 ml of DI water was added. After stirring, the MPA capped nanoparticles were transferred into the water phase. By centrifugation and decantation, excess MPA was removed from aqueous dispersion of nanoparticles. This aqueous dispersion were used for biological applications.

4.3 Characterizations

Effect of reaction temperature on structure, size dependent physical and magnetic properties were systematically characterized for their validation.

4.3.1 Effect of Reaction Temperature on Structure

Reaction temperature intensively affected the growth hence size of the nanospheres if we keep the other parameters fixed. Above the temperature of 190 ⁰C, as we injected the Se precursor in Mn precursor, the solution colour changed that indicated the beginning of nucleation process and with time the particles grow to bigger size. As we increase the reaction temperature the growth process becomes faster resulting in bigger size of the nanoparticles. The TEM images of MnSe nanoparticles synthesized at different

temperatures (sample 1 at 200 °C, sample 2 at 240 °C and sample 3 at 280 °C; reaction time ~ 10 min) are shown in Figure 4.1.

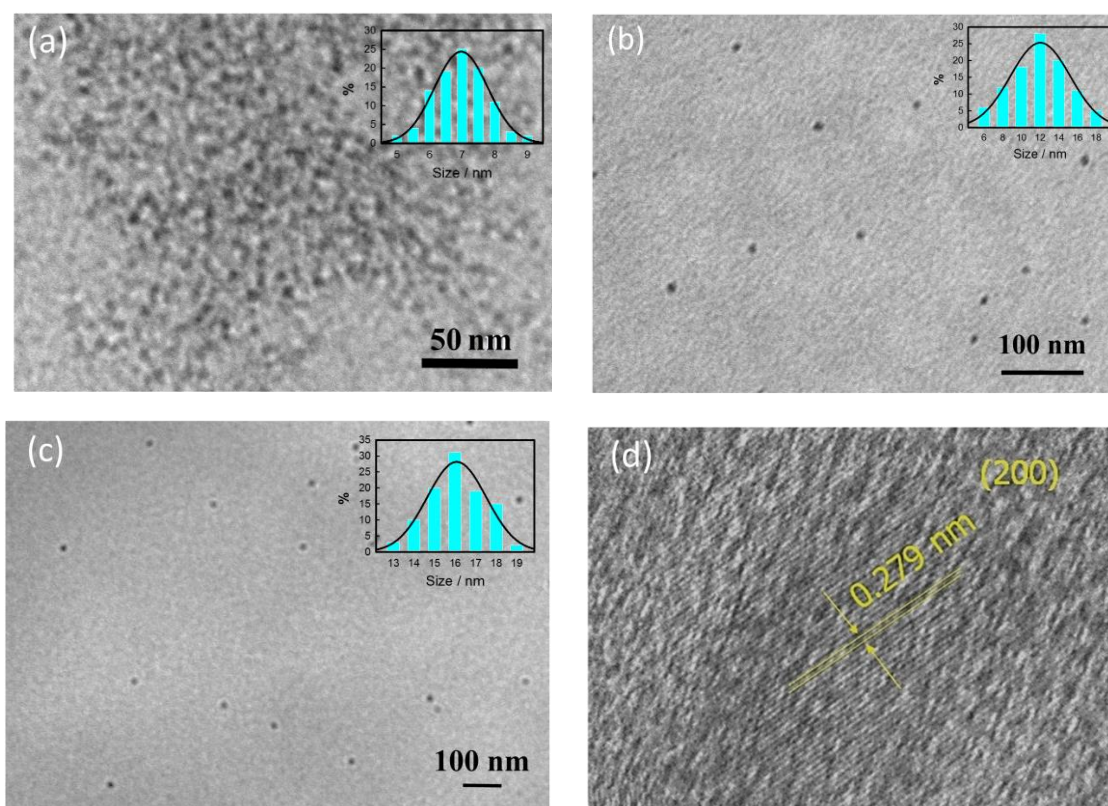


Figure 4.1. TEM images with size-distribution histogram (in inset) of MnSe NCs: (a) sample 1 ~ 7 nm, (b) sample 2 ~ 12 nm and (c) sample 3 ~ 16 nm. (d) HRTEM image of MnSe NCs of sample 3.

TEM images shown in Figure 4.1 were statistically analysed by Image J software and respective histograms are graphed. These histograms are fairly good fitted by Gaussian peak distribution where mean of peak gives the average particle size. The mean size obtained were (7 ± 1) , (12 ± 4) and (16 ± 1.5) nm for samples 1, 2 and 3, respectively. As shown in Figure 4.1, the shapes of nanoparticles were very uniform and spherical in nature. High resolution TEM image shows crystal lattice fringes with d-spacing of 0.276 nm that corresponds to dominant (200) crystallographic planes of the cubic lattice of MnSe. This image confirms the cubic crystalline nature of synthesized nanoparticles.

To see the crystallographic features, XRD for all samples were done. The XRD pattern analysis revealed the crystallographic planes, phase and crystallite size of the NCs. The diffraction peaks are shown in Figure 4.2 located at 6 distinct angles given by $2\theta = 27.5^\circ$, 31.8° , 45.5° , 56.7° , 66.4° and 75.4° could be correlated to the diffraction planes of (111), (200), (220), (222), (400) and (420) of the lattice corresponding to the known cubic crystal structure of MnSe^[30]. The highly intense and sharp peaks implied that crystallinity was

very high in these samples. No characteristic peaks for other phase of MnSe such as ZB or WZ phases and other impurities were observed. Next step was to get more information about the NC structure, the crystallite size for spherical nanoparticles which was calculated using the Debye–Scherrer formula ^[31]

$$D = \frac{0.9 \lambda}{[\beta \cos \theta]} \quad (4.1)$$

where D is the diameter of the crystalline domain, 0.9 is a factor for spherical crystal, λ is the X-ray wavelength ($\lambda = 1.5406 \text{ \AA}$ for Cu K α line), β (radians) is the full width at half maximum of the diffraction peak, and θ (angle) is the position of diffraction peak. The crystallite size obtained was 5.4 nm for sample 1, 9.6 nm for sample 2 and 14.5 nm for sample 3. The diffraction peaks showed progressive narrowing when going from sample (1) to (3), indicating an increase in crystal size because overall size of NCs was increasing. The size calculated by XRD is near about 23, 20 and 9% less than the size obtained by TEM analysis for samples 1, 2 and 3, respectively. This shows that the synthesized nanoparticles were nearly in single crystalline phase that was cubic. XRD data showed much similarity with HRTEM analysis because (200) crystallographic planes were highly dominant in both cases.

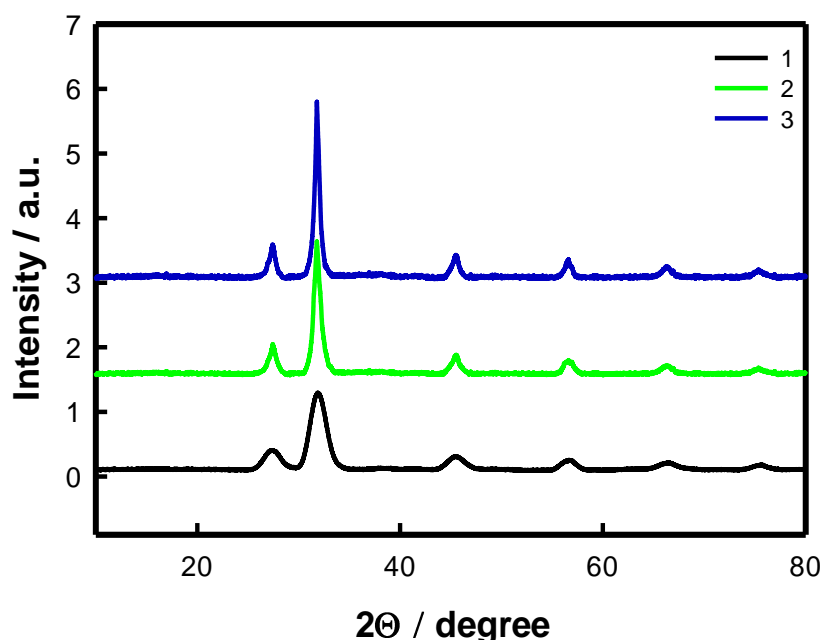


Figure 4.2. X-ray diffractograms of MnSe NCs of size: (1) 7 nm, (2) 12 nm and (3) 16 nm.

4.3.2 Size Dependent Optical Properties

The absorbance and steady state photoluminescence (PL) measurement data were used to

probe the effect of size on the spectroscopic properties of these colloidal magnetic nanocrystals. Figure 4.3 shows the absorbance, and the fluorescence spectra of these NCs.

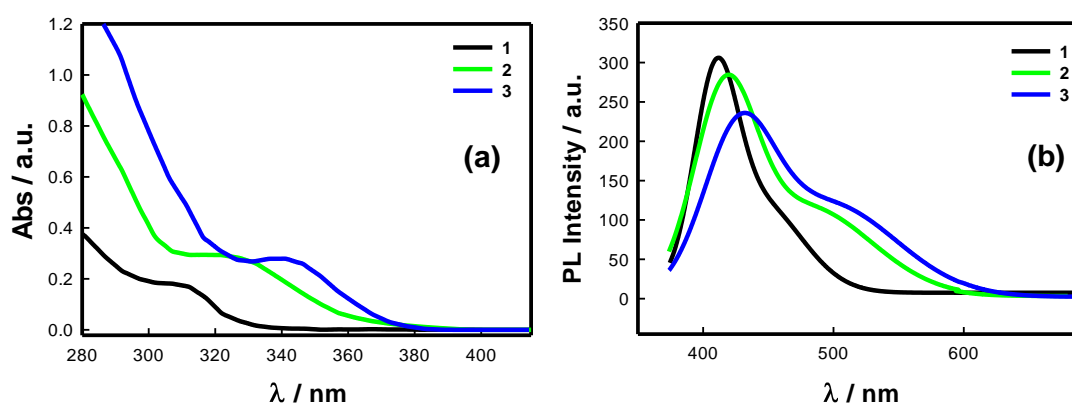
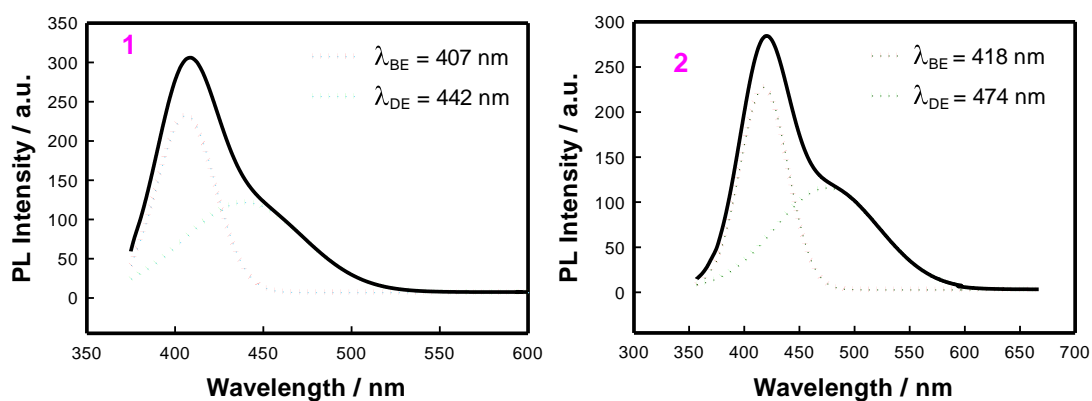


Figure 4.3. (a) Absorbance and (b) emission Spectra ($\lambda_{Exc}=300$ nm) of MnSe NCs: (1) 7 nm, (2) 12 nm and (3) 16 nm.

Figure 4.3 shows the effect of reaction temperature hence size of nanocrystals on the UV-visible and fluorescence spectra of oleic acid (OA) capped MnSe NCs. We can easily observe from this Figure that the prominent first absorption edge and fluorescent peak are red-shifted with particle size and the shift was from 311 to 344 nm for absorption, and from 411 to 432 nm (mainly blue light) for emission (Table 4.1). Energy corresponding to the absorption edge of the largest size particle was 3.61 eV (~ 344 nm) which was blue shifted by 1.11 eV with respect to the bulk value of cubic phase MnSe (~ 2.5 eV), but was red-shifted by 0.11 eV w.r.t. the bulk value of WZ phase MnSe (~ 3.5 eV). That implied effective quantum confinement of the charge carriers in the NCs if the crystal phase was cubic.

The emission spectra can be seen as composition of more than one peak because they are not symmetric in nature so we had to deconvolute each spectra to find out positions and intensities contributed by the components peaks.



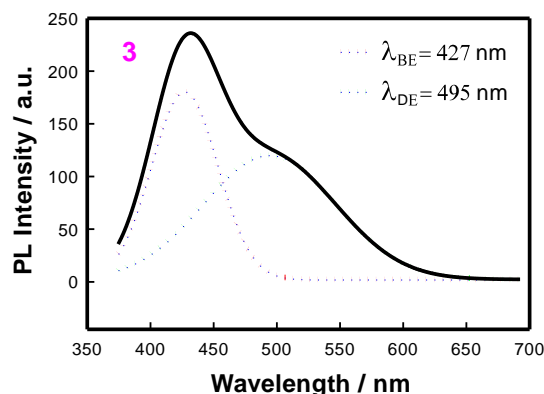


Figure 4.4. The deconvoluted fluorescence spectra of all 3 MnSe NCs: (1) 7 nm, (2) 12 nm and (3) 16 nm, samples.

The deconvolution of the raw spectra are shown in Figure 4.4. Each spectra revealed super imposition of two peaks: first was the narrow peak that arose from near band edge emission (λ_{BE}) and second was the broad peak that corresponded to the defect related emission (λ_{DE}) [20]. The peak positions, intensities and ratio of two emissions (I_{BE} / I_{DE}) are listed in Table 4.1. Intensity of near band emission (I_{BE}) decreased with size, but intensity of defect related emission (I_{DE}) was found to increase with particle size. That could be due to improper surface passivation. Therefore with proper surface passivation one would be able to get symmetric and narrow emission peak mainly in blue light range.

4.3.3 Size Dependent Magnetic Properties

To explore the size dependent magnetic properties, the temperature and field dependence of magnetization of the MnSe NCs were measured.

The temperature dependency of magnetization can be observed from the FC (Field Cooled) and ZFC (Zero Field Cooled) curve shown in Figure 4.5. In FC conditions, first we cooled the samples to 2 K under the applied field of 500 G and then measured the magnetization response with increasing temperature up to 300 K under an applied magnetic field of 500 G. And under the ZFC conditions, the protocol was the same except during the cooling there was no applied magnetic field.

The FC and ZFC curves diverge maximally at the lowest temperature (2K) for all samples. And the two magnetization curves meet at the magnetic irreversible or freezing temperature (T_F) where ZFC magnetization value is the highest. With increasing temperature, FC magnetization decreases whereas ZFC magnetization increases below the freezing temperature (T_F). Above freezing temperature (T_F) to room temperature (300 K) both curves show identical nature of magnetization.

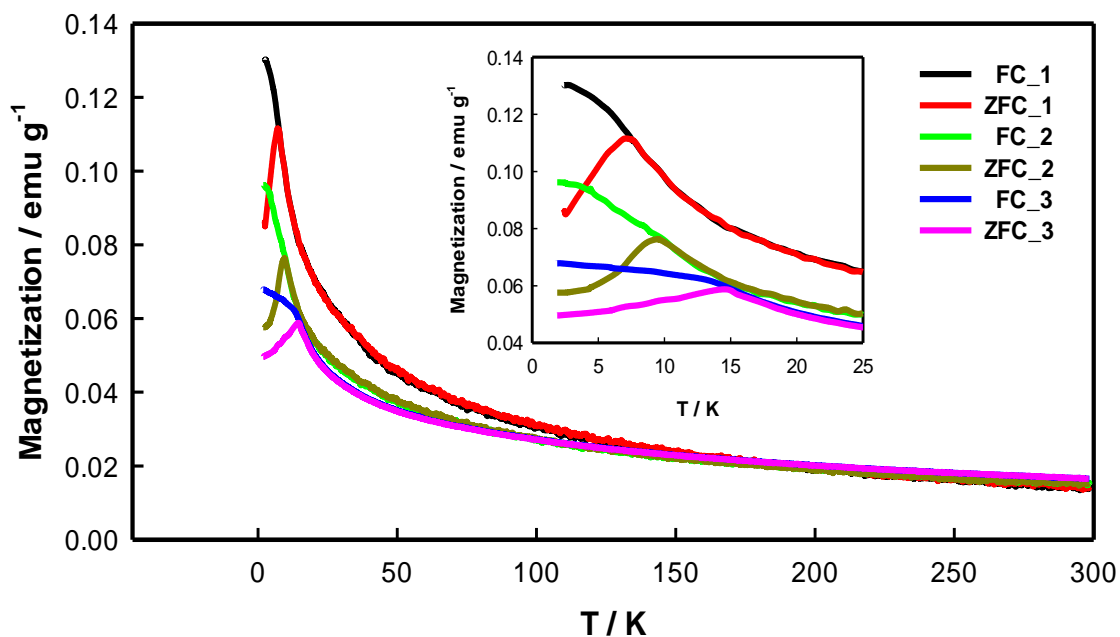


Figure 4.5. Temperature dependence of magnetization of the MnSe NCs: (1) 7 nm, (2) 12 nm and (3) 16 nm, measured under the DC field of 500 G following the FC and ZFC protocol. Variation in T_N with size is clearly seen.

The monotonically decreasing of the magnetization above T_F where spins are free to follow thermal fluctuations, shows the coexistence of paramagnetic and anti-ferromagnetic ordering with different degrees. Uniformity in size could be the reason for sharp and pronounced peak in each ZFC curve. In ZFC condition, below T_N where thermal fluctuations are weak with decreasing temperature and magnetic ordering was found to increase. So the magnetization was decreasing due to increasing antiferromagnetic ordering with decreasing temperature. And under the FC condition, below T_F the magnetization increased with decreasing temperature due to the freezing process of surface spin-glass layer^[1] along the external field direction. Spin-glass like behaviour can be seen due to the surface effect which is the inhomogeneity in surrounding of surface spins whereas spins in core have homogenous surrounding. The surface effects could drastically influence the magnetic response of the nanoparticles, especially at lower temperatures where thermal disturbance is minimum.

The field dependence of magnetization at 2 K can be seen as clear hysteresis loops for all the NCs (Figure 4.6). The loops indicate that the samples had weak ferromagnetism, which are found in nanostructured antiferromagnetic materials as a result of the surface spins. And high field magnetization nature shows that these NCs were very far from being saturated even at 50 kOe.

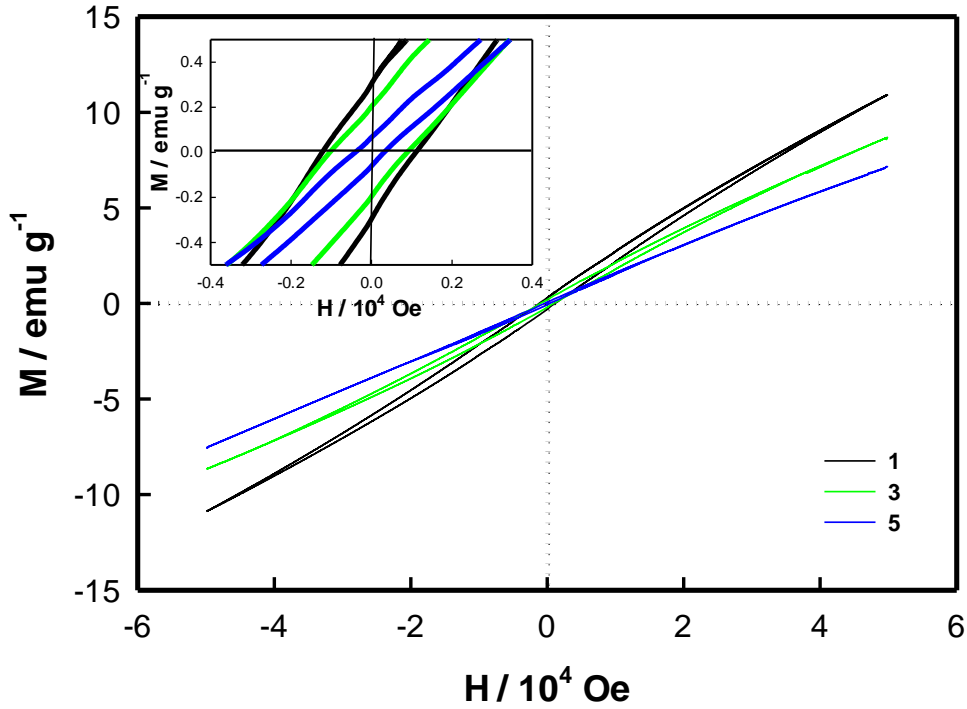


Figure 4.6. Field dependent magnetization at temperature 2 K of MnSe NCs: (1) 7 nm, (2) 12 nm and (3) 16 nm, samples show hysteresis loop. The inset shows the region around the zero field.

Effect of increasing the size of NCs on their magnetic properties can be seen as mainly shifting of the freezing temperature (T_F) to higher temperature and decrease in the magnetization value because ferromagnetism due to the surface spins becoming stronger for NCs with higher surface area (i.e. smaller size). All measured magnetic parameters for MnSe NCs are listed in Table 4.1.

The inverse susceptibility (χ^{-1}) (calculated from the FC curve) as function of temperature is plotted in Figure 4.7 and the data was fitted linearly in the higher temperature range ($T > T_F$) according to the suitably arranged modified Curie-Weiss (CW) equation^[32] given by

$$\chi(T) = \frac{M(T)}{H} = \chi_o + \frac{C}{(T - \theta_p)} \Rightarrow (\chi - \chi_o)^{-1} = \frac{T}{C} - \frac{\theta_p}{C} \quad (4.2)$$

Where χ_o is the temperature independent susceptibility, C is Curie constant and θ_p is Curie temperature. The sign of θ_p tells us about nature of magnetic behaviour. θ_p is positive for ferromagnet and negative for antiferromagnet systems.

The negative sign of θ_p confirms the antiferromagnetic behaviour. Increasing $|\theta_p|$ values indicate the increase in the antiferromagnetic behaviour with size.

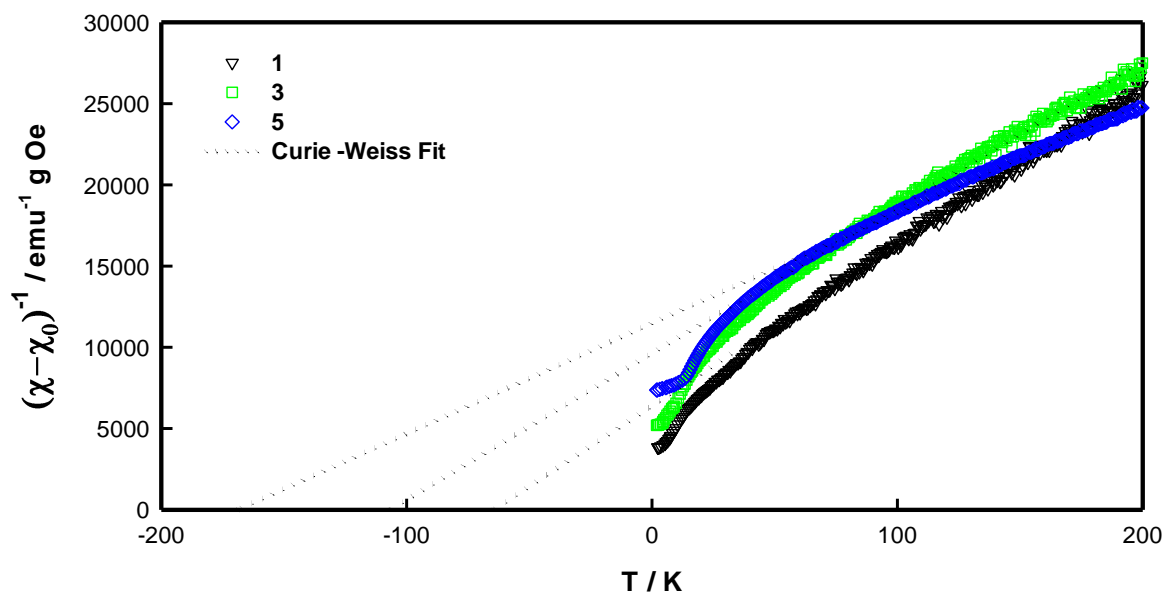


Figure 4.7. Inverse susceptibility vs temperature graph of MnSe NCs: (1) 7 nm, (2) 12 nm and (3) 16 nm, with linear fitting in higher temperature regime according to modified Curie-Weiss law. Extrapolations of fitting lines towards negative axis of temperature scale are only for graphical calculations of Curie temperature.

The magnetic state of NCs can be examined from the Arrott plot (M^2 vs H/M). The linear fitting at higher field regime gives an intercept at M^2 axis. If this intercept is positive, it implies that the spontaneous magnetization (FM ordering) is present in system (NCs).

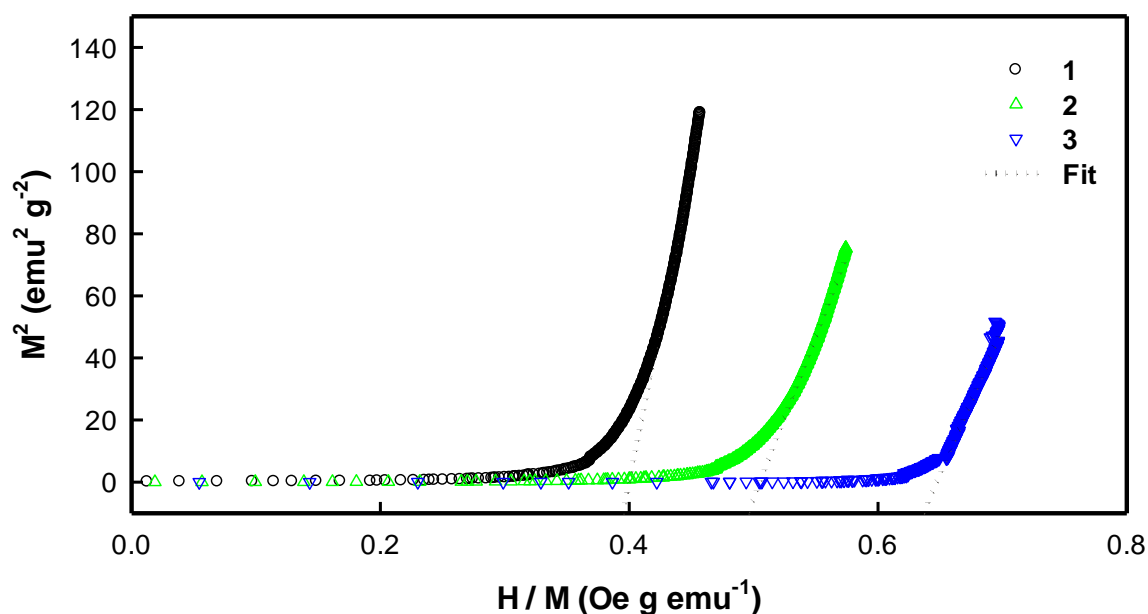


Figure 4.8. Arrott plot of magnetization at 2 K of MnSe NCs: (1) 7 nm, (2) 12 nm and (3) 16 nm samples, is shown and fitted linearly at higher temperature range.

Banerjee's criterion tells that positive slope of Arrott plot indicates second order magnetic phase transition whereas negative slope refers to first order phase transition [33]. As is

shown in Figure 4.8 the positive slopes intercept at negative M^2 axis, emphasized the absence of FM ordering that implied that the loops are made by only surface effect and second order phase transition was taking place.

Table 4.1. All physical and magnetic parameter for 3 samples of synthesized MnSe NCs are listed.

Sample	1	2	3
reaction temperature / °C	200	240	280
size / nm	(7±1)	(12±4)	(16±1.5)
λ_{Abs} / nm	311	327	344
λ_{Emi} / nm	411	419	432
λ_{BE} / nm	407	418	427
λ_{DE} / nm	442	474	495
I_{BE} / I_{DE}	1.90	1.98	1.51
crystallite size / nm	5.4	9.6	14.5
crystallite size / relative %	77	80	91
freezing temperature , T_F / K	7.3	9.4	14.7
coercivity, H_C / G	1243	1034	419
remanence, M_r / emu g ⁻¹	0.329	0.222	0.770
$\chi_o / 10^{-5}$ emu g ⁻¹ Oe ⁻¹	2.84	3.04	3.30
θ_p / K	-64	-106	-169
C / emu K g ⁻¹ Oe ⁻¹	0.010	0.011	0.015

Thus we see that smaller size particles show higher magnetization value and larger hysteresis loop at very low temperature (2 K) as weak ferromagnetism, caused by surface spins, are getting stronger with higher surface area (i.e. more surface spins). The schematic diagrams is shown in Figure 4.9.

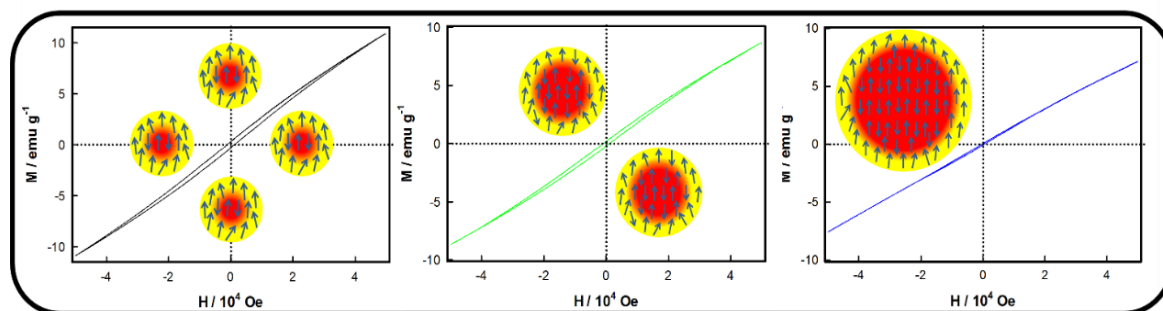


Figure 4.9. The schematic diagram of hysteresis loop caused by surface spins of MnSe nanosphere is shown.

4.4 Summary

In this chapter, a facile controlled synthesis of non-iron based cubic phase MnSe magnetic nanocrystals with well-defined spherical shape of different size (7-16 nm) by hot injection method without need for special conditions is presented. The results clearly indicate that the size and its polydispersity could be easily controlled by controlling the reaction temperature. The highly crystalline synthesized nanoparticles showed blue-violet fluorescence emission and were antiferromagnet in nature. The observed size dependent weak ferromagnetism, resulting hysteresis loop in antiferromagnet was attributed to the surface spins. Surface effects that were dominant in smaller size, gave weak ferromagnetism to antiferromagnet nanocrystals. Therefore hysteresis loops are more pronounced in smaller size NCs. Strengthening of antiferromagnetism with increasing size could be the reason for increasing the freezing temperature and Curie constant and decreasing the coercivity and remanence values.

4.5 References

- [1] D. Peddis, M. V. Mansilla, S. Mørup, C. Cannas, A. Musinu, G. Piccaluga, F. D.Orazio, F. Lucari, D. Fiorani, *J. Phys. Chem. B* **2008**, *112*, 8507.
- [2] R. Masrour, A. Jabar, *Phys. Stat. Mech. It's Appl.* **2018**, *497*, 211.
- [3] M. C. Bujan-Nunez, N. Fontaina-Troitino, C. Vazquez-Vazquez, M. A. Lopez-Quintela, Y. Pineiro, D. Serantes, D. Baldomir, J. Rivas, *J. Non-Cryst. Solids* **2008**, *354*, 5222.
- [4] T. C. Han, M. R. Tsai, C. Y. Wei, *J. Appl. Phys.* **2011**, *109*.

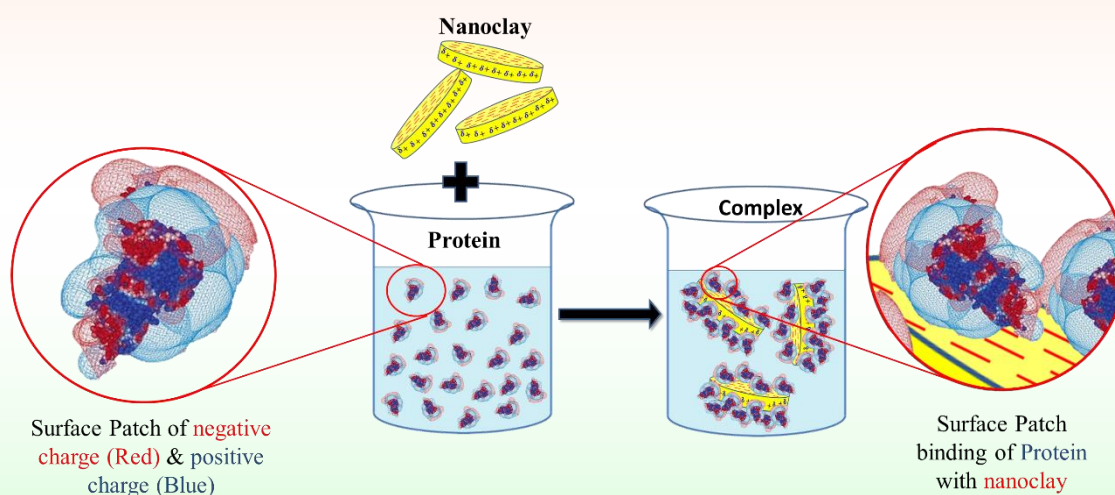
- [5] V. Markovich, I. Fita, A. Wisniewski, D. Mogilyansky, R. Puzniak, L. Titelman, C. Martin, G. Gorodetsky, *Phys. Rev. B* **2010**, *81*.
- [6] I. Koh, L. Josephson, *Sensors*, **2009**, *9*, 8130.
- [7] A. Frey N, S .Peng, K .Cheng , S .Sun, *Chem. Soc. Rev.*, **2009**, *38*, 2532.
- [8] D. A. Allwood, G. Xiong, C. C. Faulkner, D. Atkinson, D. Petit, R. P. Cowburn, *Science*, **2005**, *309*, 1688.
- [9] M. Colombo, S .Carregal-Romero, M .F. Casula, L .Gutiérrez, M. P. Morales, I. B. Böhm, J .T. Heverhagen, D. Prospero, W. J. Parak, *Chem. Soc. Rev.* **2012**, *41*, 4306.
- [10] A. K. Gupta, M. Gupta, *Biomaterials*, **2005**, *26*, 3995.
- [11] S. Rittikulsittichai, B .Singhana, W. W. Bryan, S. Sarangi, A. C. Jamison, A. Brazdeikis, T. R. Lee, *RSC Adv.*, **2013**, *3*, 7838.
- [12] A. H. Lu, E. L. Salabas, F .Schuth, *Angew. Chem. Int.* **2007**, *46*, 1222.
- [13] K. Woo, J. Hong, J. P. Ahn, *J. Magn. Magn. Mater.* **2005**, *293*, 177.
- [14] W. Wu, Q. He, C. Jiang, *Nanoscale Res. Lett.*, **2008**, *3*, 397.
- [15] I. T. Sines, R. Misra, P. Schiffer, R. E. Schaak, *Angew. Chem. Int.*, **2010**, *49*, 4638.
- [16] R. M. Murray, B. C. Forbes, R. D. Heyding, *J. Chem.*, **1972**, *50*, 4059.
- [17] H. J. Chun, J. Y. Lee, D. S. Kim, S. W. Yoon, J. H. Kang, J .Park, *J. Phys. Chem.* **2007**, *111*, 519.
- [18] R .Masrour, E. K. Hlil, M. Hamedoun, A. Benyoussef, O. Mounkachi, H. El. Moussaoui, *J. Magn. Magn. Mater.* **2014**, *361*, 197.
- [19] R. J. Pollard, V. H. McCann, J. B. Ward, *J. Phys. C Solid State Phys.*, **1983**, *16*, 345.
- [20] R. Sarma, Q. Das, A. Hussain, A. Ramteke, A. Choudhury, D. Mohanta, *Nanotechnology*, **2014**, *25*, 275101.
- [21] N. Li, Y. Zhang, H. Zhao, Z. Liu, X. Zhang, Y. Du *Inorg .Chem.*, **2016**, *55*, 2765.
-

- [22] W. Luo, X. L. Qi, *Phys. Rev.*, **2013**, 87, 085431.
- [23] Y. Xing, J. Rao, *Cancer Biomark.*, **2008**, 4, 307.
- [24] R. G. Pearson, *J. Am. Chem. Soc.*, **1963**, 85, 3533.
- [25] D. Zhu, X. Jiang, C. Zhao, X. Sun, J. Zhang, J.J. Zhu, *Chem. Commun.*, **2010**, 46, 5226.
- [26] X. Liu, J. Ma, P. Peng, W. Zheng, *J. Cryst. Growth* **2009**, 311, 1359.
- [27] T. Qin, J. Lu, S. Wei, P. Qi, Y. Peng, Z. Yang, Y. Qian, *Inorg. Chem. Commun.* **2002**, 5, 369.
- [28] L. Wang, L. Chen, T. Luo, K. Bao, Y. Qian, *Solid State Commun.* **2006**, 138, 72.
- [29] K. Das, S. Sanwlani, K. Rawat, C. R. Haughn, M. F. Doty, H. B. Bohidar, *Colloids Surf. Physicochem. Eng. Asp.* **2016**, 506, 495.
- [30] M. Wu, Y. Xiong, N. Jiang, M. Ning, Q. Chen, *J. Cryst. Growth*, **2004**, 262, 567.
- [31] U. Holzwarth, N. Gibson, *Nat. Nanotechnol.* **2011**, 6, 534.
- [32] H. Kumar, A. K. Pramanik, *J. Magn. Magn. Mater.* **2016**, 409, 20.
- [33] S. K. Banerjee, *Phys. Lett.*, **1964**, 12, 16.

Chapter 5

Size Variational Biophysical Interactions of Nanostructures

Abstract: This chapter discusses the morphology dependent electrostatic interaction of anisotropic nanoclays with globular plasma proteins through surface patch binding. Binding parameters, properties of protein-nanoclay complex and structural changes in proteins after binding have been presented and discussed.



Pictorial representation of the protein-nanoclay complexation is shown.

5.1 Introduction

Nanoparticles of various morphology and surface charge distribution may enter our human body mainly through the respiratory tract because of the extensive use of nanomaterials in personal care products, textiles and clothing, building materials, paper and pulp industry etc. Investigations, in particular, of protein–nanomaterial interaction are important in pharmaceutical and biomedical applications. Recall that when nanomaterials encounter cellular environment, they immediately interact with intracellular proteins, which may transmit distress signals due to their altered secondary structure conformation. This perturbed signalling transduction in cells may give rise to cytotoxicity, and various biochemical disorder.

There is dearth of such studies evaluating the interaction of physically anisotropic platelets with biological systems at the molecular level. In particular, the interaction of polypeptides, proteins, polynucleic acids with nanoparticles of different morphology remains a very poorly probed and understood domain of research. Anisotropic nanomaterials have the advantage of offering heterogeneous binding sites to ligands which make these materials polyfunctional, and hence, such materials are darlings of nanoscientists. However, it is not always easy to synthesize uniformly dispersed anisotropic nanomaterials with sufficient confidence and reproducibility. Therefore, it is imperative to use model nanosize materials that befit the requirement. Here comes the relevance of nanoclay platelets such as Laponite RD[®] and MMT both of which are anisotropic in their physical morphology, and surface charge distribution.^[1-3]

In spite of the wide spread use of these anisotropic nanosize materials as fillers and benign additives in products that we use in our daily life, there has been a scarcity of reports on their impact on the native protein structure, arising from their binding to important biomolecules. A pertinent question arises here: how does the nanoclay affect the protein activity? Herein, we address this issue through a series of controlled experiments and observations using Laponite and MMT as model anisotropic nanomaterials. Different proteins have different surface charge anisotropy and hence it is expected that they will interact differently with specific nanomaterials. Herein, the importance of surface patch binding (SPB) comes into picture where associative interactions occur even when the two partners have similar net charge.^[4] SPB interactions are important in biology. Due to the fewer number of experimental studies reported in the literature on plasma protein-anisotropic nanomaterials, to date, our knowledge of interaction between these two moieties remains poorly understood. This, in particular, has motivated the present work.

5.2 Sample Preparation

Bovine serum albumin (BSA), β -lactoglobulin (β -Lg) and human serum albumin (HSA) were procured from Sigma-Aldrich chemical company (U.S.A.), which had a purity of > 96%. These were used as received without further purification. The aqueous protein solutions were prepared at a fixed concentration of 0.01% (w/v) by dissolving a given amount of protein powder in deionized water at 25⁰C under stirring for ~1 hr, and the pH of the solutions were ~ 5.5 \pm 0.5, which produced homogeneous and optically clear solutions. The stock solutions were stored in sterilized air tight borosilicate glass bottles

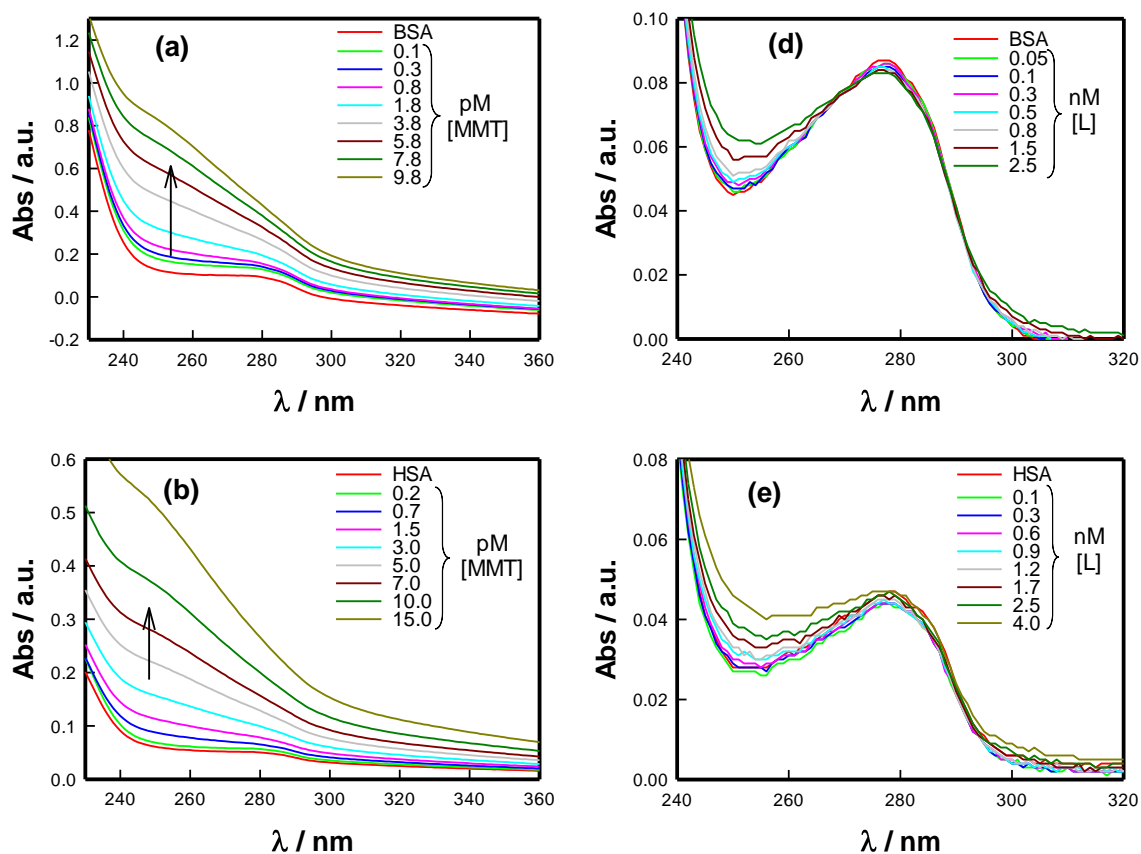
for future use. The well characterized nanoclays (in the powdered form) were procured from Southern Clay Products, USA. Powdered Laponite® (L) and Na-MMT were weighed in required amount and then distilled water was added to it to make up for the required concentration of 0.05% (w/v). This dispersion was made homogeneous using a magnetic stirrer. After 2 and 4 hours of stirring a clear solution of Laponite and MMT were obtained (with $\text{pH} = 9.0 \pm 0.5$) that were stored in airtight borosilicate glass bottles at room temperature. These stock solutions were used for experiments.

5.3 Protein - Nanoclay Binding

Proteins are highly amorphous as far as their surface charge, and surface hydrophobicity distributions are concerned. The protein hydrophobicity is an important parameter that often governs its secondary structure, and its binding affinity to various types of ligands. UV-Vis absorption and fluorescence spectroscopy offer a facile and rapid method to establish the binding profile, and locate onset of complex formation.^[5]

5.3.1 UV-Vis absorption spectroscopy

The absorption spectra of the proteins clearly show absorption bands located at $\lambda = 280$ nm, originating from the presence of tryptophan (Trp) and tyrosine (Tyr) residues.



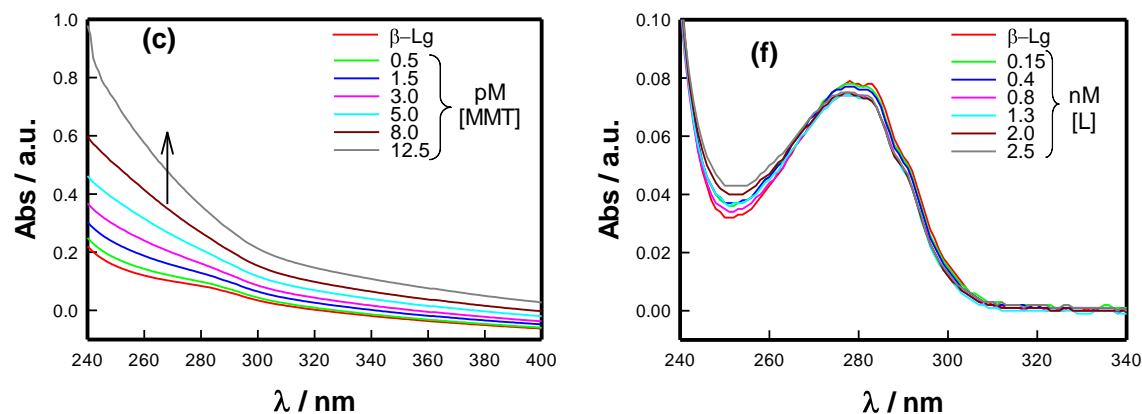


Figure 5.1: Absorbance spectra of proteins, (a) BSA (1.5 μ M), (b) HSA (1.5 μ M), (c) β -Lg (5.5 μ M) in the absence and presence of MMT and (d) BSA (1.5 μ M), (e) HSA (1.5 μ M), (f) β -Lg (5.5 μ M) in the absence and presence of Laponite.

In Figures 5.1 (a) to (f), we showed the absorbance spectra of the various proteins (BSA, HSA, β -Lg) with varying concentration of nanoclays. It can be clearly observed that there was significant change in the absorbance peak positions and these got shifted from 280 to 260 nm (blue shift) for protein – MMT and observable change in absorption intensity at 260 nm for protein – Laponite but there were no changes in absorption at peak position, 280 nm, which can be attributed to the formation of protein-clay complexes. A strong absorption band (\approx 290 nm, π - π^* transition) was noticed in all proteins. When the clay platelets were added, the absorbance pattern was noticeably different from that of pristine protein, and clay dispersions.

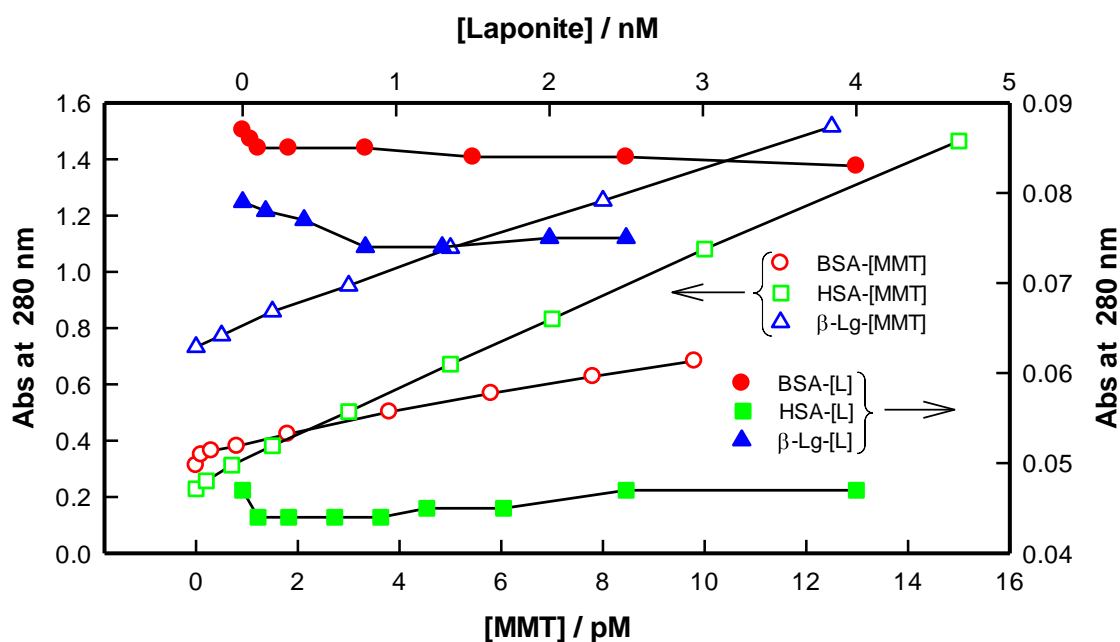


Figure 5.2: Absorbance at $\lambda=280$ nm of proteins, BSA (1.5 μ M), HSA (1.5 μ M), and β -Lg (5.5 μ M) in the absence and presence of MMT and Laponite.

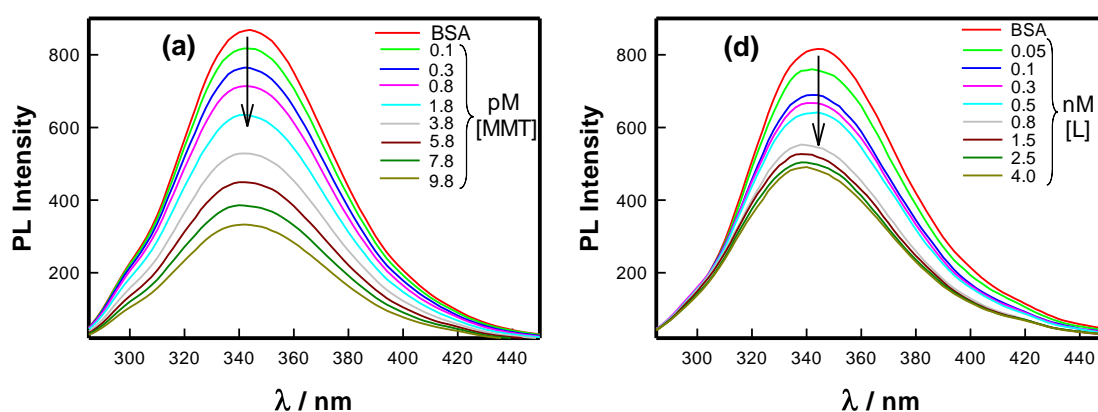
The conformational changes manifested by the difference in the spectral profile at 290 nm may arise from the alteration of polypeptide's micro-environment.^[6,7] It is to be noted that there was not much difference in the Laponite - protein binding while selective interaction of proteins with MMT prevailed (Figure 5.2). The aggressive binding noticed in the case of MMT can be attributed to the larger surface area of this particular clay. Since typical radius of MMT platelet surface is about 10-times larger than that of Laponite, one MMT platelets offers ($2\pi r_{MMT}^2/2\pi r_L^2 = 300^2/30^2 = 100$) typically ~ 100 times more surface for binding leading to higher absorbance, the data presented in Figure 5.2 is justified.

5.3.2 Fluorescence spectroscopy: Binding Constant

Bovine serum albumin (BSA) protein has two Tryptophan residues at positions namely, Trp-134 (more solvent exposed) and Trp-212 residue (not solvent exposed). Human serum albumin (HSA) has a single tryptophan residue at position namely, Trp-214. Trp-134 exists only in BSA and Trp-212 of BSA behaves the same as Trp-214 of HAS due to their homologous nature^[8]. In bovine beta-lactoglobulin (β -Lg) has two tryptophan-residue at position 19 and 61. Out of which Trp-19 would be indispensable for its structure and function such as maintaining the molecular structure and biological activity.^[9] Trp 19 located in the first strand of the β -sheet (β A) is buried whereas Trp 61 is solvent exposed. These Trp-residues are responsible for the intrinsic fluorescence of these serum proteins.

5.3.2.1 Effect on Fluorescence

During the nanoclay interaction, in some cases, fluorescence peak intensity is quenched and that is possible when the environment around Trp opens up to polar environment (i.e. water) but the resulting state still contains some non-native structure, which gives rise to incomplete protection of amide protons and to the nonpolar environment of the



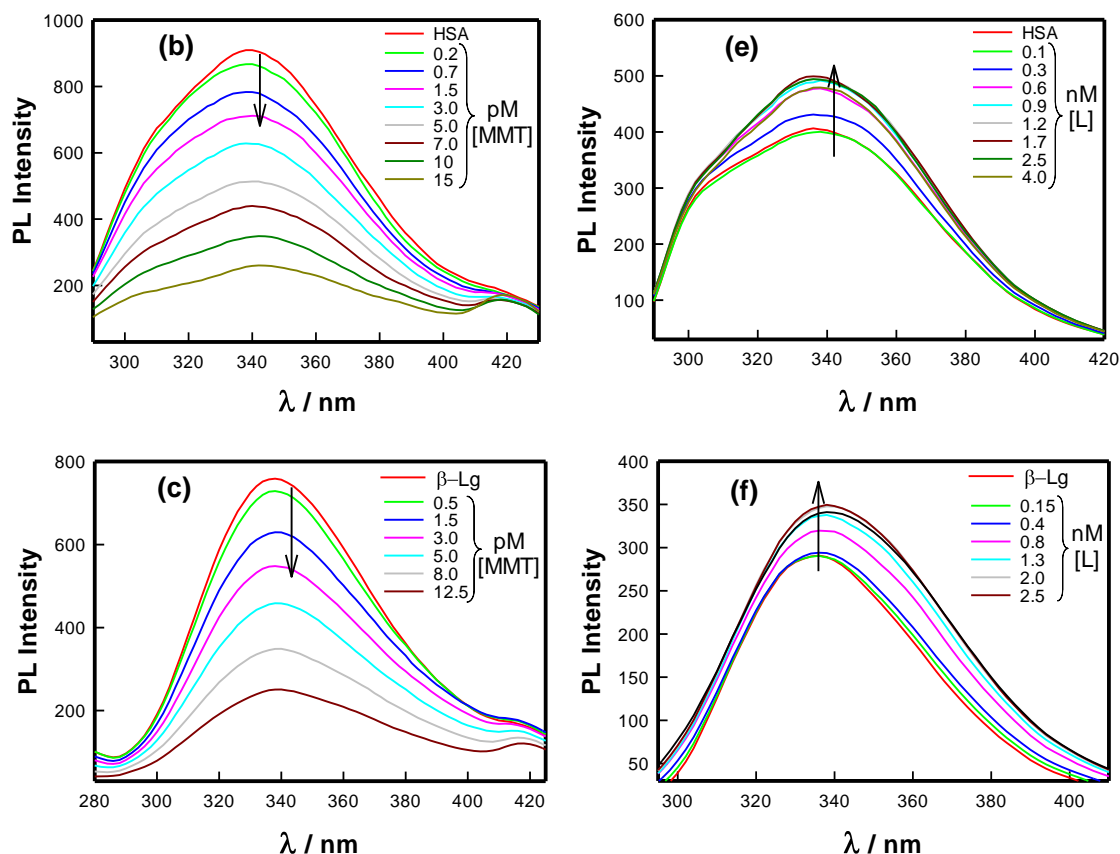


Figure 5.3: Emission spectra of proteins, (a) BSA (1.5 μ M), (b) HSA (1.5 μ M), (c) β -Lg (5.5 μ M) in the absence and presence of MMT and (d) BSA (1.5 μ M), (e) HSA (1.5 μ M), (f) β -Lg (5.5 μ M) in the absence and presence of Laponite.

Trp residues. The enhancement in Trp fluorescence can be due to is attributed to formation of a partially helical compact state at higher pH.^[10] β -Lg is stable at low pH than the neutral pH. One of the factors preventing the use of neutral or alkaline pH conditions is the low reversibility of the unfolded state.^[11] These results confirmed that the nanoclays do affect the local environment of Trp residues.

5.3.2.2 Fluorescence Quenching and Binding Constant

The degree of quenching of intrinsic fluorescence of proteins upon binding to clay platelets could be analyzed in the framework of modified Stern-Volmer equation given by^[12]

$$\frac{F_0}{F_0 - F} = \frac{1}{f_a K_a [Q]} + \frac{1}{f_a} \quad (5.1)$$

Where F_0 is the initial fluorescence intensity, and F is the intensity in the presence of quenching agent 'Q'. f_a is the fraction of accessible fluorephores of proteins. Here, $[Q]$ is the molar concentration of quencher, and K_a is the effective quenching rate constant for the accessible fluorephores.

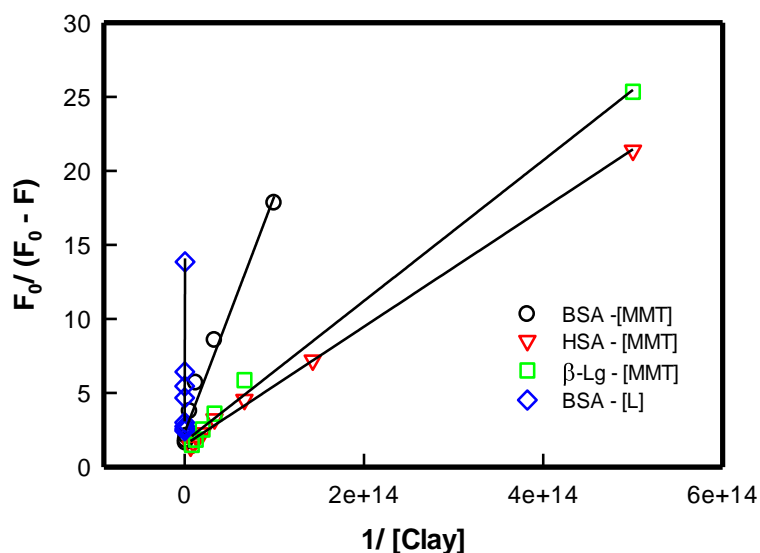


Figure 5.4: The modified Stern-Volmer plot shown for various proteins {BSA ($1.5\mu\text{M}$), HSA ($1.5\mu\text{M}$) and $\beta\text{-Lg}$ ($5.5\mu\text{M}$)} as function of concentration of clay.

The parameter, $\{F_0 / (F_0 - F)\}$ is plotted against reciprocal of the quencher concentration, which is shown in Figure 5.4. And all data are linear fitted with Chi-square ≥ 0.97 . The quenching constant K_a was estimated by dividing intercept by the slope of linear fitted plot. Our data revealed that protein-clay complexes had higher quenching rate constant K_a . This higher values obtained here suggest that the quenching of tryptophan fluorescence occurred due to specific interaction of protein with nanoclays. This proved that the quenching was static in nature arising from the specifics of complexation between protein and the platelets.

Table 5.1: Binding constant K_a , and fraction of accessible fluorophore of proteins, f_a , of various proteins-clay samples.

Samples	f_a	$K_a(\text{l M}^{-1})$	χ^2
BSA-MMT	0.43 ± 0.15	$(1.46 \pm 0.63) * 10^{13}$	0.98
$\beta\text{-Lg}$ -MMT	0.58 ± 0.18	$(4 \pm 1) * 10^{13}$	0.99
HSA-MMT	0.67 ± 0.08	$(4.14 \pm 0.61) * 10^{13}$	0.99
BSA-L	0.33 ± 0.09	$(1.36 \pm 0.47) * 10^{11}$	0.97

Several conclusions can be made from these observations as far as protein-MMT binding is concerned: (i) the binding affinity followed $\text{BSA} < \beta\text{-Lg} < \text{HSA}$, (ii) number of the accessible fluorophore available on these proteins was different for different nanoclay, and (iii) fluorescence quenching followed $\text{BSA} < \beta\text{-Lg} < \text{HSA}$. Thus, the binding was highly specific to the proteins concerned.

An increase in fluorescence rather than quenching for Laponite interaction with HSA and $\beta\text{-Lg}$ are shown in Figures 5.3 (e) and (f). We can argue that this happens due to

unfolding of those proteins hence more fluorophores are exposed and intensity is increased. There may be other reasons for this. Since, these could not be described through Stern-Volmer equation, it was not possible to determine binding constants for these samples.

Since our fluorescence data could not be fitted linearly, we adopted modified Stern-Volmer equation for fitting. This equation is appropriate for those systems that have fraction of sites accessible for interaction instead of all sites. The binding constant obtained depends much more on nature of clays, but very less on nature of proteins. The binding constant of proteins with any clay followed the trend of pI value of proteins concerned that is HSA > β -Lg > BSA. Since, the pI values of HSA and β -Lg are nearly equal so was their binding constant values. So, we can say that the differential binding owes its origin to protein surface charge, and not protein surface charge anisotropy, and the difference in surface area of the platelets.

5.4 Stoichiometry of Protein-Clay Binding

The exact adsorbed amount of proteins per platelet was not accessible. Thus, we made an attempt to correlate the various physical parameters of the protein-clay complexes, such as the apparent hydrodynamic radius R_h , zeta potential ζ , and solution pH which may yield the missing information.^[13]

5.4.1 Effect on Hydrodynamic Radius

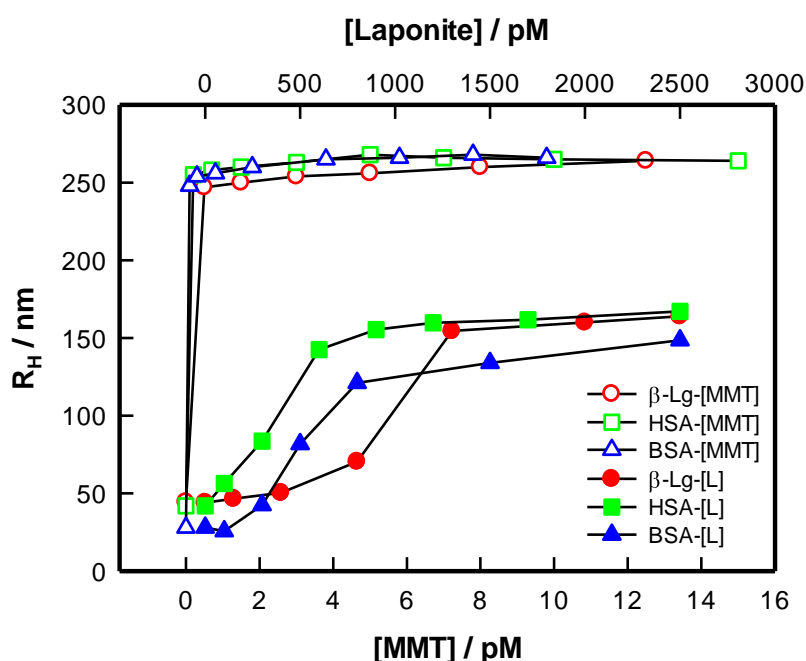


Figure 5.5: Variation of hydrodynamic radius (R_h) of proteins (BSA ($1.5\mu\text{M}$), HSA ($1.5\mu\text{M}$) and β -Lg ($5.5\mu\text{M}$)) with and without clays.

Figure 5.5 shows increase in R_h upon binding of clay platelets to the protein surface. This data indicates that proteins were adsorbed on the clay platelets, which produced saturation binding.

5.4.2 Effect on Net Surface Charge

The zeta potential measurements were carried out as a function of clay concentration. The positive surface charge on protein molecule was neutralized by addition of nanoclays platelets (net negatively charged). As depicted in Figure 5.6, the surface charge of protein (3.5 ± 0.5 mV) decreased to -50 ± 5 mV upon binding to clay platelets, and further addition of clay did not induce more changes.

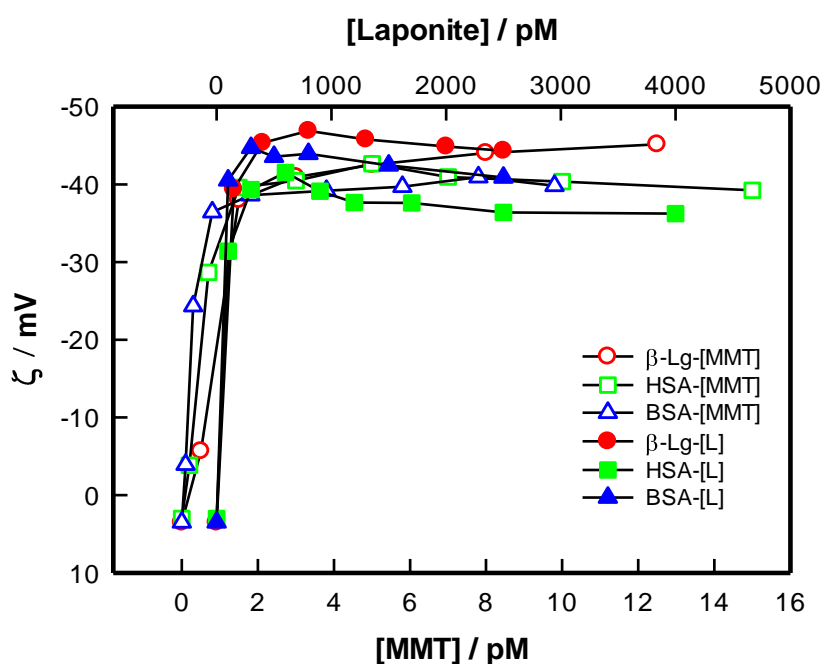


Figure 5.6: Variation of zeta potential of proteins (BSA ($1.5 \mu\text{M}$), HSA ($1.5 \mu\text{M}$) and β -Lg ($5.5 \mu\text{M}$)) with, and without clays.

5.4.3 Effect on pH of Proteins

The corresponding changes in the pH are shown in Figure 5.7. The fact that the zeta potential remains constant beyond a binding saturation limit implied that the proteins were stabilized by both charge-compensation, and steric effects in the bound state. The pH of MMT-protein dispersions increased from 4.5 to 7.0 ± 0.5 and 4.5 to 8.5 ± 0.5 in case of Laponite. At $\text{pH} > 6$, proteins and nanoclays have electrostatic repulsion due to same polarity (both are negatively charged), but they still interact which is due to surface patch binding phenomenon.^[4] In this mechanism, proteins bind to polymers/colloids having similar net charge, often called “binding on the wrong side of pH”. Numerous realization

of this has been documented in the literature.^[4] The protein surface charge anisotropy has direct implication on such surface patch binding. Thus, the nanoclay-protein interaction is surface charge anisotropy dependent.

The net surface charge of proteins in the experimental condition ($\text{pH} > \text{pI}$) is negative. Due to lesser surface charge density nanoclay (MMT) binds more effectively to it because repulsive electrostatic interactions are weaker compared to the higher surface charge density nanoclay (Laponite), and this binding is facilitated by surface patch binding. This is adequately observed from Figures 5.7 and 5.10.

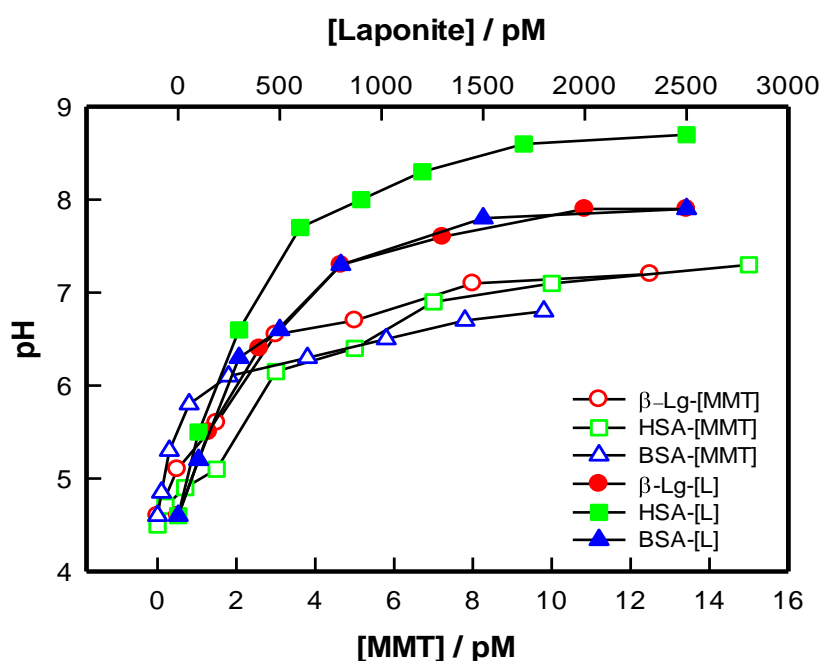


Figure 5.7: Variation of pH of proteins (BSA (1.5 μM), HSA (1.5 μM) and β -Lg (5.5 μM)) with, and without clays.

5.5 Conformational Changes in Protein after Binding

The interaction of a protein with platelets may induce conformational changes in their secondary structure, due to surface patch binding, which may change the surrounding of fluorophores of proteins hence synchronous fluorescence intensity and lifetime of fluorescence.

5.5.1 Effect on Microenvironment around Fluorophores

Synchronous fluorescence measurements provides the information about conformational changes in proteins. To avoid different perturbing effects in measurement of the very minute changes in micro environment of protein's fluorophores with high sensitivity is possible only with synchronous fluorescence spectroscopy. Spectral bandwidth reduction and spectral simplification advantages of this method.^[13]

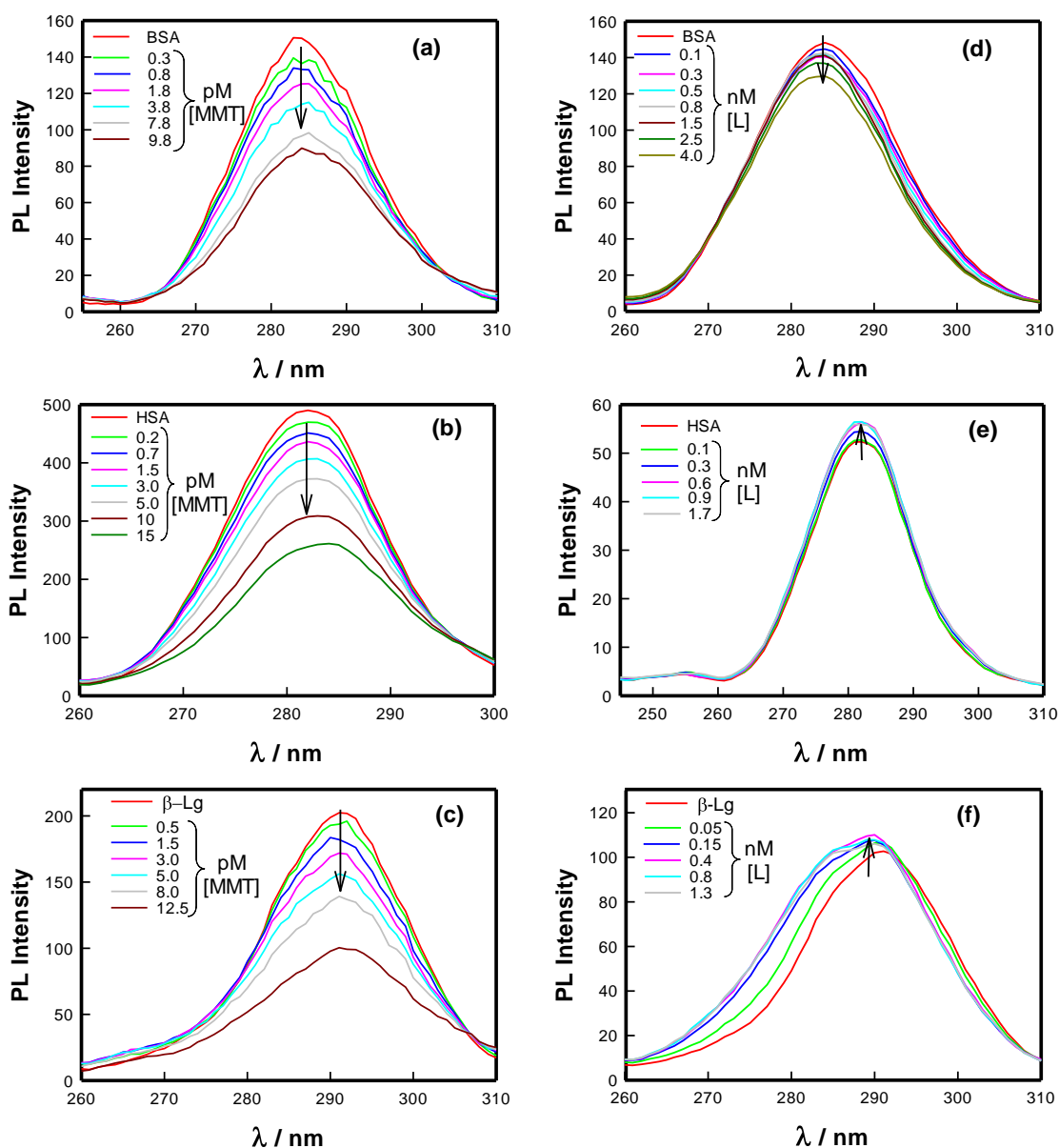
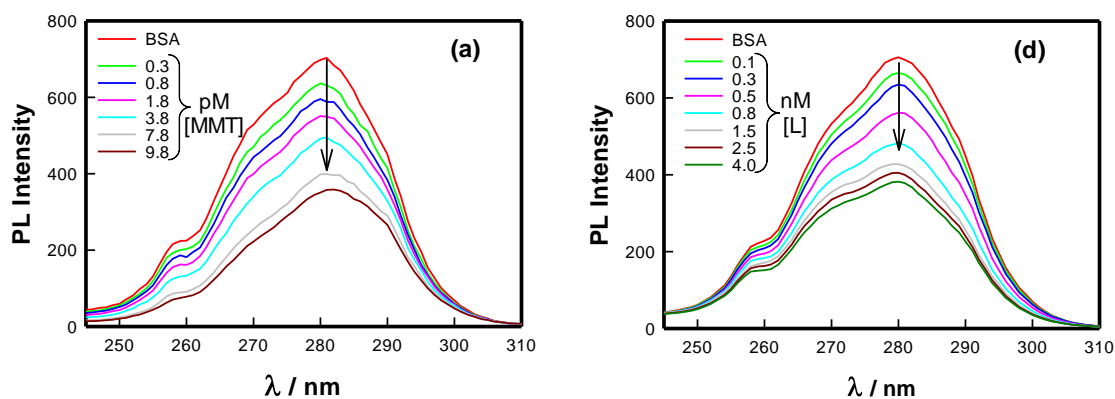


Figure 5.8: The synchronous fluorescence spectra at $\Delta\lambda=15$ nm (Tyrosine) of proteins, (a) BSA (1.5 μ M), (b) HSA (1.5 μ M), (c) β -Lg (5.5 μ M) in the absence and presence of MMT and (d) BSA (1.5 μ M), (e) HSA (1.5 μ M), (f) β -Lg (5.5 μ M) in the absence and presence of Laponite.



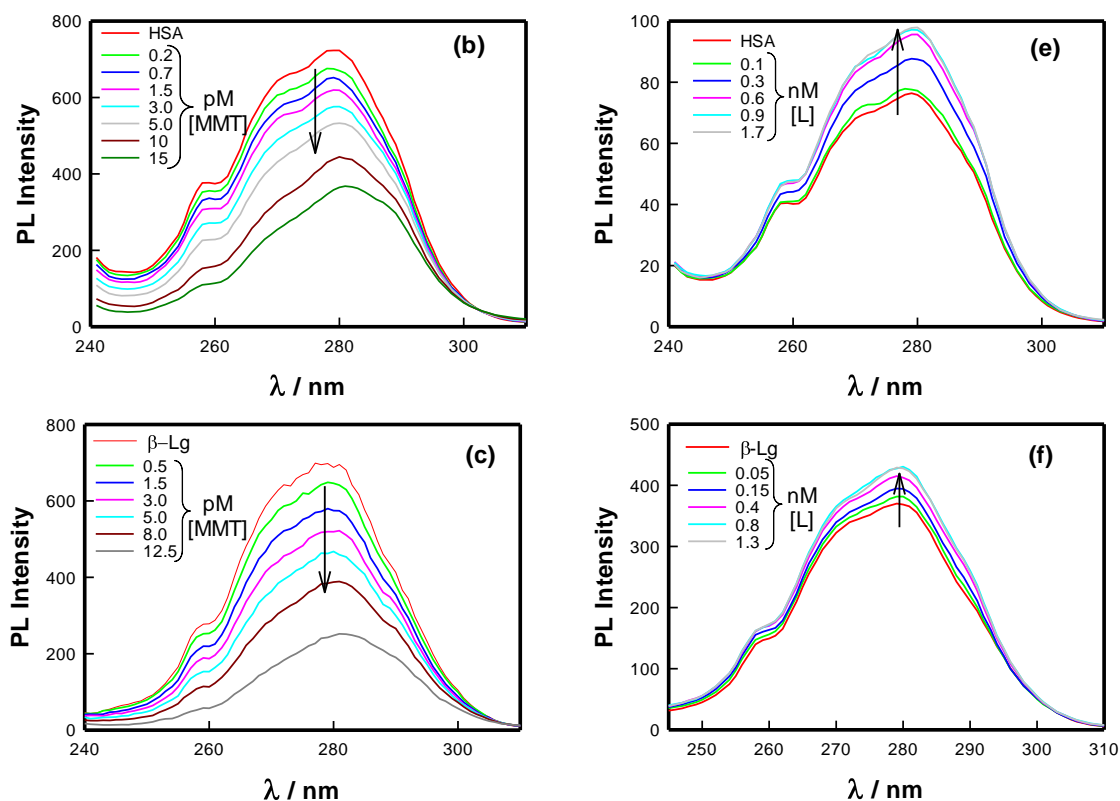
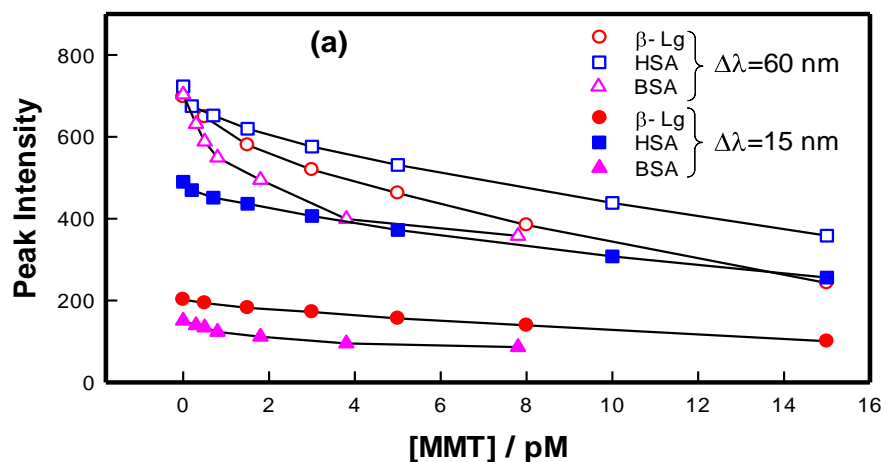


Figure 5.9: The synchronous fluorescence spectra at $\Delta\lambda=60$ nm (Tryptophan) of proteins, (a) BSA (1.5 μ M), (b) HSA (1.5 μ M), (c) β -Lg (5.5 μ M) in the absence and presence of MMT and (d) BSA (1.5 μ M), (e) HSA (1.5 μ M), (f) β -Lg (5.5 μ M) in the absence and presence of Laponite.

Peak positional wavelength and intensity of emission spectra of the protein's fluorophores depends on the surrounding polarity i.e. hydrophobicity or hydrophilicity, and binding strength. Any shifting of peak position or intensity meant the changes of polarity or binding. Such spectra can offer characteristic information on the Tyr and Trp residues of polypeptides when the $\Delta\lambda$ between emission and excitation wavelength were fixed at 15 nm and 60 nm, respectively.^[14]



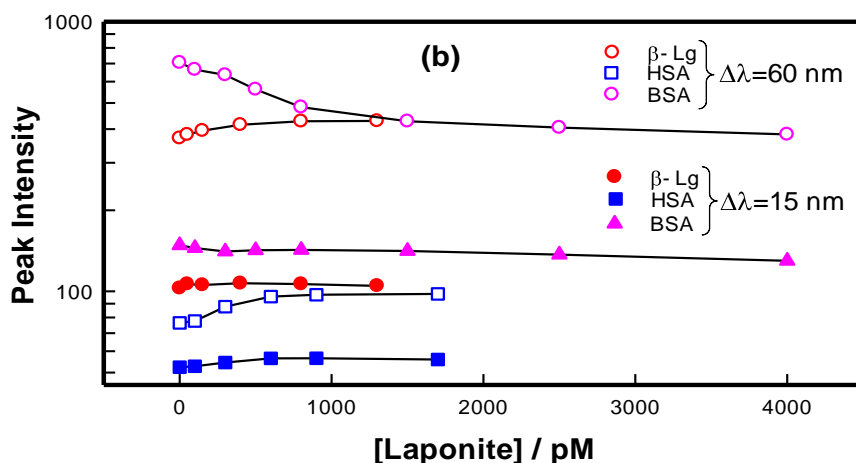


Figure 5.10: Peak intensity of synchronous fluorescence spectra for $\Delta\lambda=60$ nm (Tryptophan) and $\Delta\lambda=15$ nm (Tyrosine) versus wavelength plot of various proteins in the absence and presence of various concentrations of (a) MMT and (b) Laponite.

Synchronous fluorescence spectra of these samples are shown in Figure 5.8 for tyrosine and figure 5.9 for tryptophan. This data indicated that increase in the concentration of clay caused the fluorescence of Trp to decrease more than that of Tyr (Figure 5.10) which clearly implied that clay platelets bound more with Trp residues of proteins. In addition, a minor red shift in maximum emission wavelength of proteins interacted with MMT only was noted when $\Delta\lambda$ was fixed at 60 nm only. It meant that the presence of MMT made hydrophilic environment in the proximity of the Trp residue only, causing changes in the conformation of proteins. But for other cases in this study, there was not any significant changes on binding.

5.5.2 Effect on Secondary Structure

CD spectra of native proteins, and the same of their clay bound complexes are depicted in Figure 5.11. It was noted that when these platelets were added to proteins, the characteristic signature peaks (two negative double humped peaks) arising from α -helix content (of proteins) became deeper. Thus, the helix content of BSA decreased implying strong associative interaction between platelets and the protein molecule.^[15] The CD result is normally given in terms of average residue ellipticity ($\text{deg cm}^2 \text{dmol}^{-1}$) given by $[\theta]$. Helix content of the proteins could be determined from the equation 2.34 of Chapter 2.

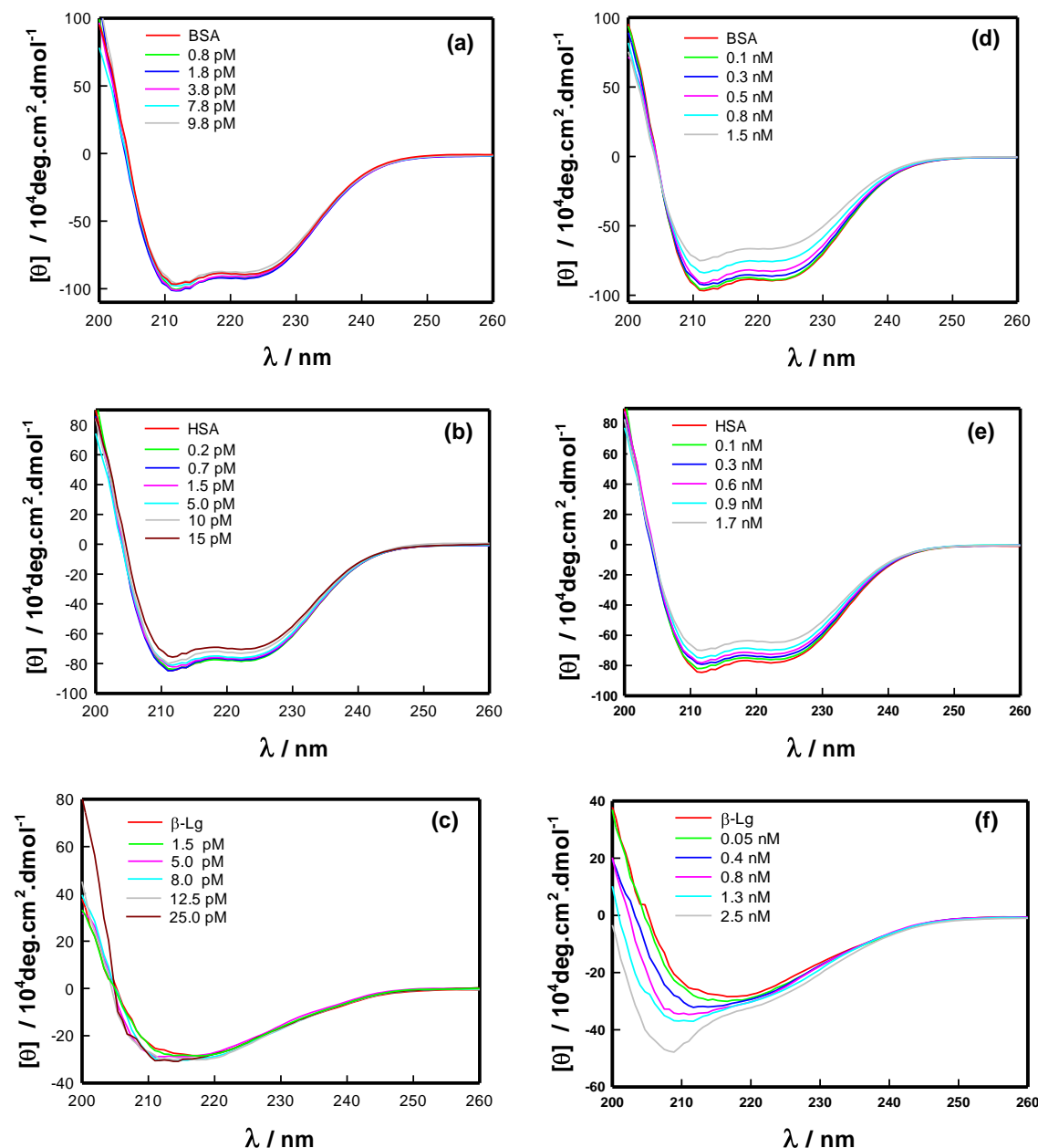


Figure 5.11: CD spectra of proteins, (a) BSA (1.5 μ M), (b) HSA (1.5 μ M), (c) β -Lg (5.5 μ M) in the absence and presence of MMT and (d) BSA (1.5 μ M), (e) HSA (1.5 μ M), (f) β -Lg (5.5 μ M) in the absence and presence of Laponite.

The CD data was used in eq. (5.2) to ascertain the helix content which is shown in Figure 5.12. Some of the salient features observed were: (i) protein molecules lost 50% of their helix content when these were bound to clay platelets, and (ii) saturation binding occurred when clay concentration was 4 pM. Note the drastic change in secondary structure due to complexation of proteins with clay platelets. In case of β -Lg we noticed a rise in helicity on binding with both Laponite and MMT. β -Lg has more planer part than helical part in water (pH = 7) and when clay is mixed in that solution, pH is

increased causing conformational changes in it that facilitated increase in helical part. It will be improper to stretch this conclusion further.

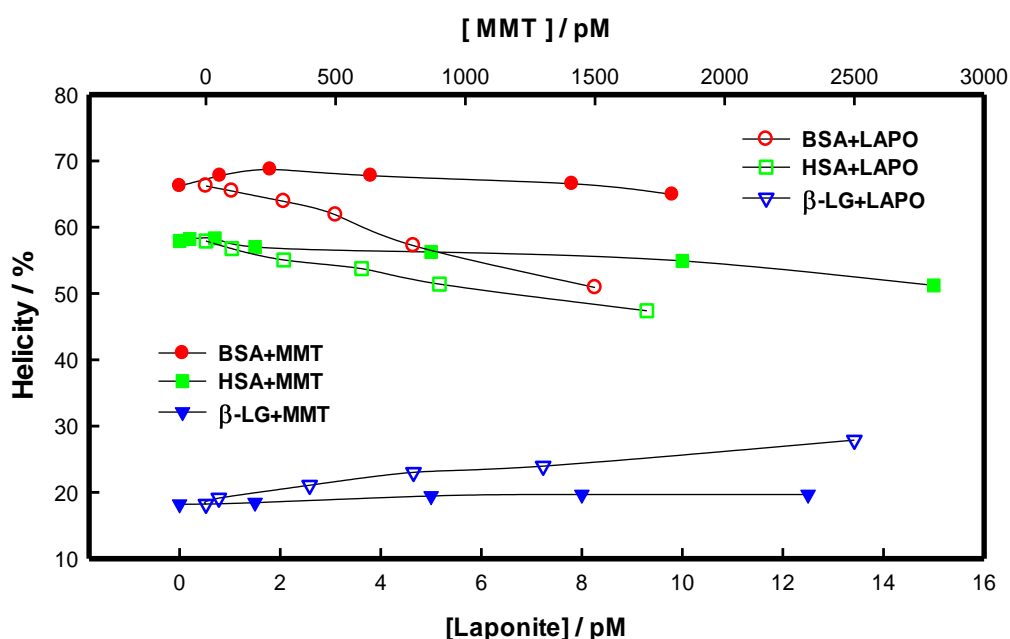
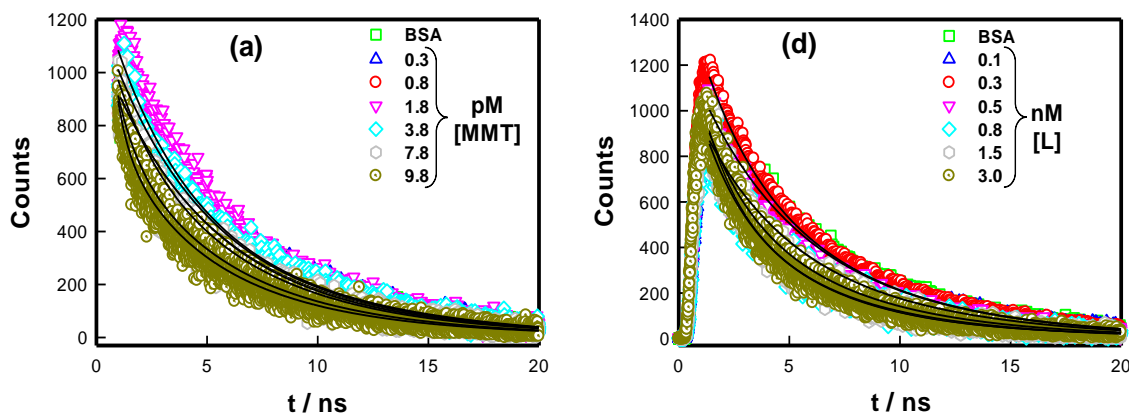


Figure 5.12: Dependence of secondary structure (helicity) of proteins [BSA ($1.5\mu\text{M}$), β -Lg ($5.5\mu\text{M}$) and HSA ($1.5\mu\text{M}$)] on the clay concentration.

5.5.3 Effect on Fluorescence Lifetime

The time resolved data, obtained from TCSPC experiments (excitation and emission at 405 and 350 nm), are depicted in Figures 5.13. All the decay profiles were least-squares fitted to a two-exponential decay function given by eq. 2.22 and 2.23 of Chapter 2.

The interaction of proteins with clay affected the exciton lifetime considerably (Figure 5.14). The decay time systematically decreased with increase in the content of complexes in every case for MMT containing samples. This was also true for Laponite-BSA samples. However, for Laponite-HSA or β -Lg samples, we observed an increase in the fluorescence life time.



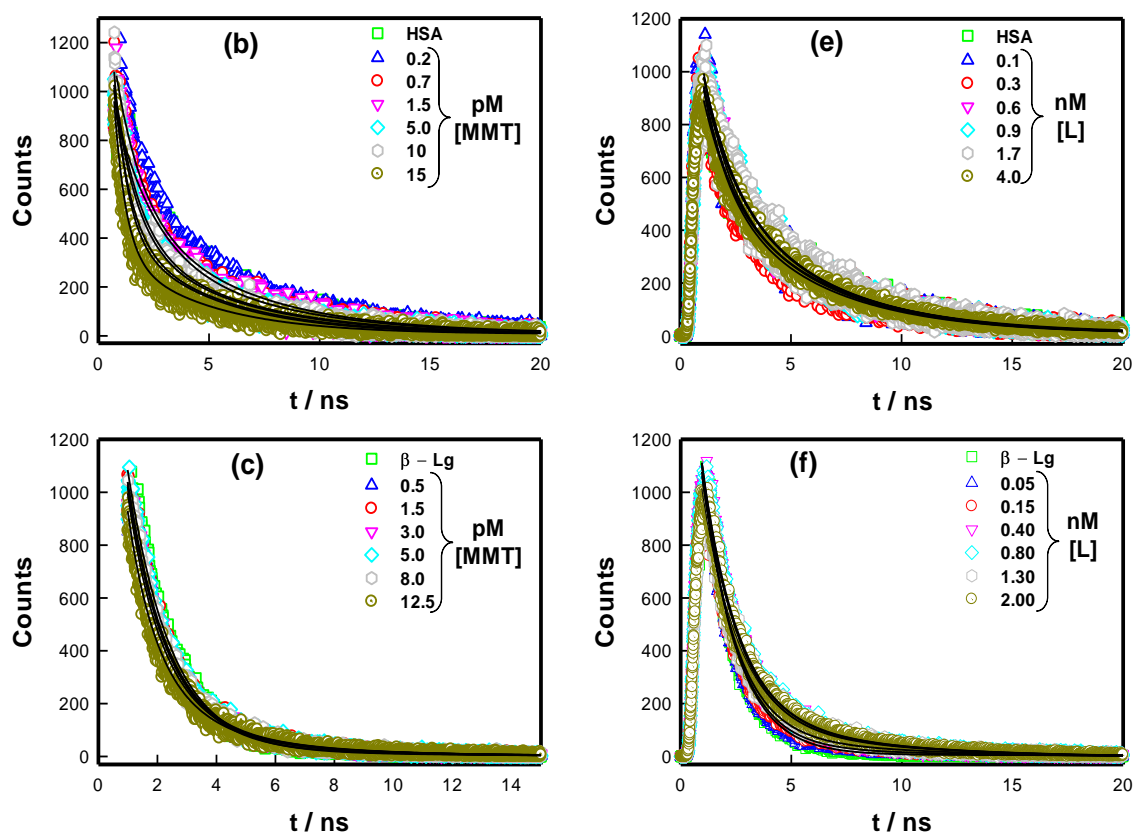
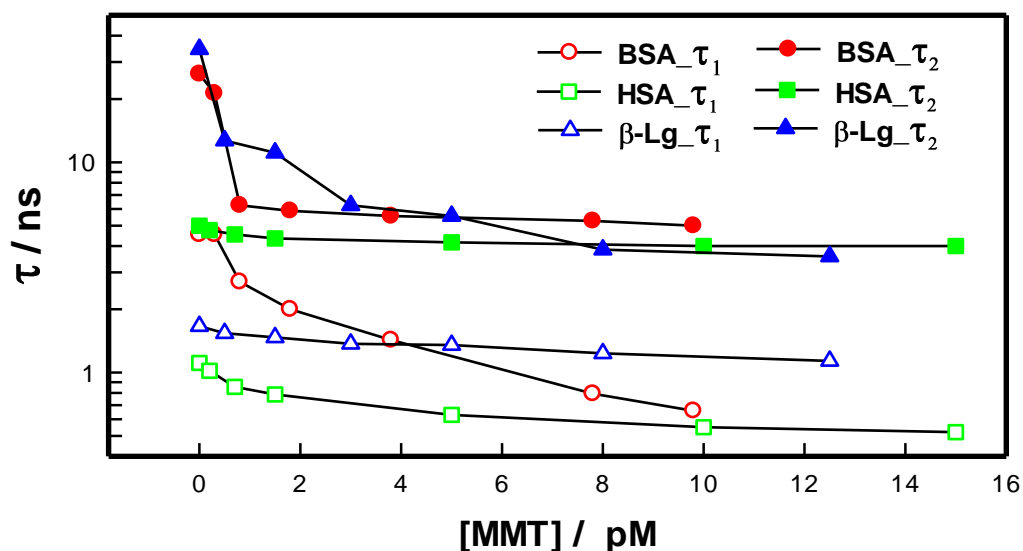


Figure 5.13: Time resolved fluorescence spectra of (a) BSA (1.5 μ M), (b) HSA (1.5 μ M), (c) β -Lg (5.5 μ M) in the absence and presence of MMT and (d) BSA (1.5 μ M), (e) HSA (1.5 μ M), (f) β -Lg (5.5 μ M) in the absence and presence of Laponite recorded at room temperature (Excitation Wavelength = 290nm (LED)).

In the case of BSA, the first and second decay time reduced by $\sim 20\%$ when the protein concentration was less than 4.05 μ M. It showed plateau value for higher concentrations. HSA exhibited shorter decay time compared to BSA in the low protein concentration samples (<4 pM). Thus, it can be argued that binding of platelets to HSA and β -Lg molecules was similar a large degree in comparison to the BSA samples.



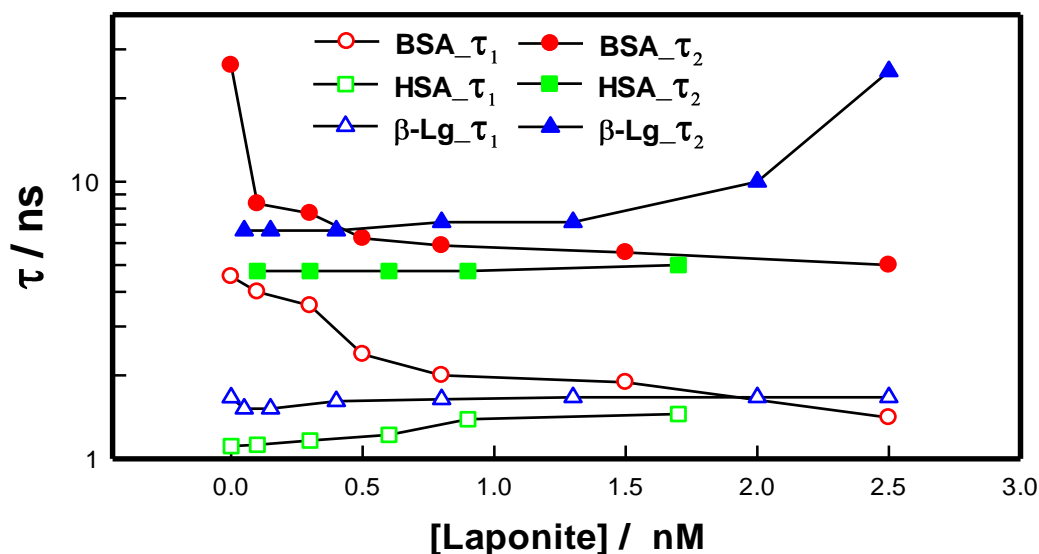


Figure 5.14: Two characteristic decay times τ_1 and τ_2 of various proteins in the absence and presence of various concentration of MMT and Laponite determined at excitation wavelengths of 375 nm.

It may be noted that interaction of proteins with clay also affects the exciton lifetime. Thus, the observed fluorescence quenching in protein–clay complexes have both static and some dynamic nature (due to diffusion etc.). In the case of static quenching, the excited states of the protein form a ground state complex with the quencher (ligand). Hence, there was no decrease in the decay time of the pristine clay (not a fluorophore).

5.6 Nanoclay-Protein interaction: Surface Patch binding

Surface charge of MMT and Laponite are nearly equal (in terms of their zeta potentials), but surface area of MMT is nearly 100 times more than that of Laponite. So the charge density of MMT is 100 times less than Laponite. We did not perform any experiment that can conclude that binding of nanomaterials having identical surface charge density with substrates of different surface area is same or different. It needs to be mentioned that proteins bind to clay platelets through surface patch binding, and not through electrostatic interactions.

Based on the refs. [16, 17],^[16,17] we can claim that proteins and nanoclays are stable at the pH range concerned. BSA is well known to be sensitive to chemical denaturation by pH (sometimes reversible others not). The several structural transitions were seen in BSA with respect to pH change giving rise to different conformations like globular, E and B forms etc. which is well recorded in the literature.^[18,19] Similarly, β -lactoglobulin is also known to undergo variable pH induced structural transformations. In its native state, β -lactoglobulin is a predominantly β -sheet protein containing nine β -strands and

three α -helices.^[20] Thus, the two nanoclays must have caused some conformational changes in the protein structure much more pronounced for the Laponite. Yes, the tryptophan fluorescence quenching and helicity are affected by pH variation, but not like what we observed. The intensity of fluorescence of BSA and its helicity increased with pH in the range 5 to 7, and then decreased with pH increase. However, this change was not so much.^[21] Thus, we can say that the quenching was not due to pH variation alone but was mostly due to the interaction of BSA with clays. HSA should follow the same due to homogeneity with BSA. And for β -lg data was anomalous. The manuscript is revised to show that pH changes alone were not responsible for their changed fluorescence behavior. The presence of nanoclays quenched the fluorescence of Trp residues as shown in experimental results. Fluorescence of Trp residue and conformational changes in proteins are very sensitive to the microenvironment around residues which is well explained in the chapter 16 of the book “Principles of fluorescence spectroscopy”, see refs. 22.^[22] So, we can say that fluorescence of Trp residue is related to the conformation of protein by its microenvironment. As is shown in our results, nanoclays have caused same amount of conformational changes in the proteins (Circular Dichroism data).

Data presented herein pertains to experiments carried out at room temperature (30 °C) and the nanoclay dispersions used were not older than 48 h. In a bid to resolve the issue of differential platelet-protein binding, samples were examined with an array of spectroscopic techniques, and the results were quite revealing. MMT exhibited increased binding affinity as compared to Laponite. Thus, the differential binding owes its origin to protein surface charge anisotropy and difference in surface area of the platelets. The positively charged edges of nanoclay platelets would permit the proteins to adsorb onto the clay surface. The increased favourable interaction first causes the water molecules to redistribute, release counterions and dehydrate the loci of contacts. These effects will finally quench the intrinsic fluorescence of protein. Laponite platelets are associated with high surface charge density compared to MMT. Thus, it effectively causes better binding of protein with MMT compared to L. We have included a schematic to model the clay-protein binding.

Proteins and nanoclays have similar charge polarity at pH > 6 so there should be electrostatic repulsion but there is associative interaction between these due to surface patch binding. And surface patch binding is much dependent on protein surface charge anisotropy. So we can say that if surface charge is of same polarity (responsible for

electrostatic repulsion), the binding interaction depends on surface charge anisotropy. And net surface charge of proteins in our experimental conditions ($\text{pH} > \text{pI}$) are negative. Thus, lesser surface charge density nanoclay (MMT) binds more effectively than higher surface charge density nanoclay (Laponite) by surface patch binding.

Binding constant depends more on the nature of clays, but very less on nature of proteins. The binding constant of proteins with any clay followed the trend that is $\text{HSA} > \beta\text{-Lg} > \text{BSA}$ (same trend as their pI values). The pI values of HSA and $\beta\text{-Lg}$ are nearly equal so was their binding constant values. So one can say that the differential binding owes its origin to protein surface charge not protein surface charge anisotropy and difference in surface area of the platelets.

5.7 Summary

We have studied the aspect ratio and concentration dependent protein binding affinity of two clay preparations. The clays of only two aspect ratios were studied because it was difficult to procure water dispersible clays of other aspect ratio. However, for the two clays concerned our study was systematic as it encompassed a variety of physical parameters of proteins (size, surface charge, intrinsic fluorescence life time, helicity etc). The binding parameters wherever possible were determined. The results demonstrated that MMT could cause substantial fluorescence quenching due to its preferential binding with various serum proteins. We believe that the differential charge density and anisotropy associated with the clays is responsible for causing this behaviour. Surprisingly, the high charge density platelet Laponite exhibited poor protein binding affinity with respect to MMT. On the contrary, the low charge density platelet MMT revealed marginal shift in both absorption and emission peaks but shows substantial fluorescence quenching. This was inferred from the anomalous dependence of binding affinity on aspect ratio. Therefore, the data suggest that aspect ratio impact on protein affinity of clays is non-monotonous. This could imply that the binding was largely dominated by available surface area on clay surface rather than charge density.

The results are convincing enough that the proteins bind to the clay platelets, but preferentially to MMT. Remarkably, the clay platelet induced protein denaturation, and the fluorescence quenching due to binding between tryptophan groups of protein with platelets were observed in the case for each protein. The plausible evidences are quenching of static fluorescence intensity, and lifetime of the tryptophan groups. In summary, it can be concluded that nanoclays when bound to proteins considerably alter their biological activity. Here, protein acts as a nanoclay intercalating agent. On binding

to nanoclay discs, the structural rigidity of proteins increases, so their excited state energy gets effectively converted into fluorescence. As structural rigidity restricts the non-radiative losses due to molecular motion. As its molecular motions slow down and non-radiative energy loss due to collision with solvent and other molecules decreases which also lead to increase in fluorescence intensity. Reduction in protein structural flexibility due to its binding with anisotropic clay platelets lead to fluorescence intensity enhancement as the non-radiative relaxation channels are inaccessible after such binding. In addition, increase in fluorescence lifetime and changes in solvent polarity are other reasons that contribute to the aforesaid phenomenon.

The relationship between aspect ratio and protein type (globular or fibrous) needs to be further assessed through carefully designed experimentation. In the present work, we have specifically focused on the aspect ratio dependence. We do not believe the results are either material or experimental condition dependent. These findings will provide basic information about the potential toxicity of natural clays and finally, leading to their sustainable development as personal care products within the permissible safety limits. We believe that the present study may help improving the general understanding of the role of anisotropic nanomaterials in their biomolecular interactions. This calls for deeper understanding of nanomaterial-protein interaction.

5.8 References

- [1] B. Ruzicka, E. Zaccarelli, L. Zulian, R. Angelini, M. Sztucki, A. Moussaid, T. Narayanan, and F. Sciortino, *Nat. Mater.*, **2011**, *10*, 56.
- [2] M. Baek, J. A. Lee, S. J. Choi, *Mol. Cell Toxicol.* **2012**, *8*, 95.
- [3] B. D. Chithrani, W. C. W. Chan, *Nano. Lett.* **2007**, *7*, 1542.
- [4] J. Pathak, K. Rawat, H.B. Bohidar, *Int. J. Biol. Macromol.* **2014**, *63*, 29.
- [5] P. Kandagal, J. Seetharamappa, S. Ashoka, S. M. T. Shaikh, D. H. Manjunatha, *Int. J. Biol. Macromol.* **2006**, *39*, 234.
- [6] N. Glazer, E. L. Smith, *Biol. Chem.* **1961**, *236*, 2942.
- [7] D. H. Hu, H. M. Wu, J. G. Liang, H. Y. Han, *Spectrochim. ActaA.* **2008**, *69*, 830.
- [8] Y. Moriyama, D. Ohta, K. Hachiya, Y. Mitsui, K. Takeda, *J Protein Chem.* **1996**, *15*, 265.

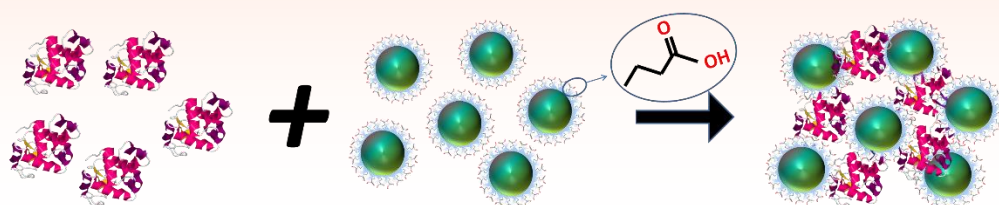
- [9] Y. Katakura, M. Totsuka, A. Ametani, S. Kaminogawa., *Biochim. Biophys. Acta.* **1994**, *1207*, 58.
- [10] K. Kuwata, R. Shastry, H. Cheng, M. Hoshino, C. A. Batt, Y. Goto, H. Roder, *Nature Structural Biology* **2001**, *8*, 151.
- [11] M. Yagi, K. Sakurai, C. Kalidas, C. A. Batt, Y. Goto, *J. Biol. Chem.* **2003**, *278*, 47009.
- [12] Y. J. Hu, Y. Liu, L. X. Zhang, R. M. Zhao, S. S. Qu, *J. Mol. Str.* **2005**, *750*, 174.
- [13] U. Mote, S. Bhattar, S. Patil and G. Kolekar, *Luminescence* **2010**, *25*, 1.
- [14] J.Q. Lu, F. Jin, T.Q. Sun, X.W. Zhou, *Int. J. Biol. Macromol.* **2007**, *40*, 299.
- [15] X. X. Cheng, Y. Lui, B. Zhou, X. H. Xiao, Y. Liu, *Spectrochim. Acta. A.* **2009**, *72*, 922.
- [16] N. Pawar, H. B. Bohidar, *The Journal of chemical physics* **2009**, *131*, 045103.
- [17] P. Chen, L. Zhang, *Biomacromolecules* **2006**, *7*, 1700.
- [18] D. C. Carter, J. X. Ho, *Adv. Protein Chem.* **1994**, *45*, 153.
- [19] J. T. Peters, *Academic Press, Inc., New York* **1996**.
- [20] N. Taulier and T. V. Chalikian, *J. Mol. Biol.*, **2001**, *314*, 873.
- [21] M. Bhattacharya, N. Jain, K. Bhasne, V. Kumari, S. Mukhopadhyay, *J Fluoresc.* **2011**, *21*.
- [22] J.R. Lakowiczed, *Principles of Fluorescence Spectroscopy Springer Science & Business Media*, **2013**.

Chapter 6

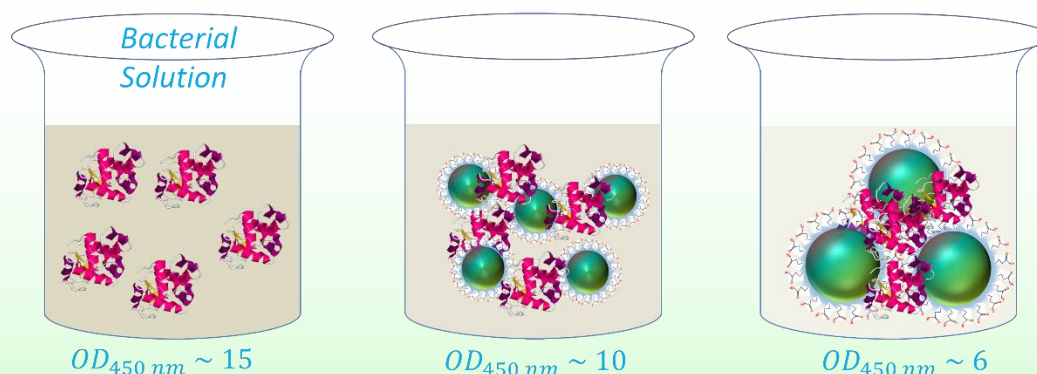
Size Variational Quantum Dot -Lysozyme Interaction and Effect on Enzymatic Activity

Abstract: This chapter discusses the size dependent hydrophobic interaction of CdSe quantum dots with Lysozyme. Binding and thermodynamic parameters, nature of interaction, structural changes in enzyme after binding and enzymatic activity of Lysozyme-QDs complex have been presented and discussed.

Lysozyme – QDs Complex Formation



Enzymatic Activity



Pictorial representation of lysozyme adsorption on CdSe QDs & enzymatic activity of these complexes is shown here.

6.1 Introduction

The protein-QD interactions have become a topic of considerable interest due to its similarity with protein–ligand (antibody opsonization) the interactions in living body.^[1,2] It is crucial to understand how proteins (bioreceptors) interact with these inorganic nanomaterials which are routinely used for application such as drug delivery and targeting and bio-imaging etc. These interactions depend on many factors like protein conformation and orientation. Researchers have investigated applications for the nanocrystalline QDs as agents for cell imaging, and as potential qubits in quantum

computing. Recently, Medintz et al have provided a generalized strategy for determining the orientation of a protein on a QD, or other spherical nanoparticles.^[3] Binding of QDs to proteins and amino acids have altered the secondary structure which affects their functional properties. The unusual optical properties of QDs make them ideal for in vivo and in vitro applications as fluorophores in a range of biological investigations, where use of traditional organic molecules as fluorescent labels inadequately provide long-term stability, with simultaneous detection of multiple signals. The availability of water dispersible QDs have shown important applications in cell, and deep-tissue imaging. Further, these are efficient fluorescence resonance energy transfer (FRET) donors.^[4] Needless, to say, photo-luminescent low-dimensional semiconductor nanocrystals hold considerable promise for in vivo imaging.^[5]

Wu et al have reported a class of designer nanogels prepared by in-situ immobilization of CdSe quantum dots inside the core of temperature and pH responsive hydroxypropyl cellulose (HPC)-poly (acrylic acid) interpenetrating network matrices. The hydroxyl groups of the HPC chains were designed to seclude the precursor Cd²⁺ions into the nanogel networks. Further, these gels stabilized the in-situ formed CdSe QDs. These smart nanogels offered a strong emission at 741 nm for sensing pH-dependent environment, and depicted a visible exciton emission at 592 nm for mouse melanoma (B16F10 cell) imaging. Also, these hybrid nanogels could provide excellent stability as a drug carrier with high drug loading capacity for a model anticancer drug temozolomide.^[6] Savla et al have reported the targeted and controlled delivery of pH-responsive QD-mucin1 aptamer-doxorubicin conjugate for chemotherapy of ovarian tumor. DOX was conjugated to QD through a pH-sensitive hydrazone bond to provide stability of the complex and drug release in acidic environment prevailing inside cancer cells. The results showed that this bond was stable both at neutral, and slightly basic pH. Further, rapid hydrolysis in mildly acidic pH environment was noted. Results demonstrated the high potential of the QD conjugate in treatment of multidrug resistant ovarian cancer.^[7] Functionalization of the surface of a quantum dot (QD) with aptamers can recognize cocaine which was studied in depth by Zhang and Johnson. The single-molecule detection and FRET between QD and Cy5, and Iowa Black RQ was exploited to develop a QD-based aptameric sensor. This sensor was capable of sensing the presence of cocaine in both signal-off and -on modes. In comparison to aptameric sensors, this single-QD-based aptameric sensor had many advantages, such as easy sample preparation, high sensitivity, and extremely low sample requirement.^[8]

Jaiswal and Simon have reviewed the potential of QDs in biological applications. With improved synthesis protocols of water-stable QDs, the development of approaches to label cells efficiently with QDs, and concurrent improvements in conjugation possibility of QDs to selected biomolecules have generated considerable interest in their use in biology. There have been many successful applications of QDs in biology. Regardless, several limitations remain that need to be overcome before these can be used routinely.^[9] Nanoparticle-based imaging and targeting methods using nano core-shell structures, and quantum dots have been studied in depth by Alvisatos et al. Emerging nanoelectronics-based sensing and controlled synthesis protocols on the applications of every nanoparticle system addresses their advantages, and shortcomings in medical research.^[10] Many investigations have illustrated the hidden potential of using quantum dots as new probes in vitro and in vivo. In a review, Alvisatos et al have summarized the recent advances of quantum dot use at the cellular level, in immune-labeling, cell tracking, in situ hybridization, FRET, in vivo imaging, etc.^[11]

Therefore, it is important to understand the protein-QD interactions at molecular level. In particular, the protein enzymatic activity is of concern. In the present study, the steady state and synchronous fluorescence, UV–visible spectroscopy and CD-spectroscopy were used to investigate the binding constant, binding sites and free energy of binding (entropy and enthalpy) and conformational changes induced by QDs in lysozyme. Thus, a complete profiling of enzymatic activity of lysozyme in its bound state with CdSe quantum dots was evaluated, much of which yielded new information.

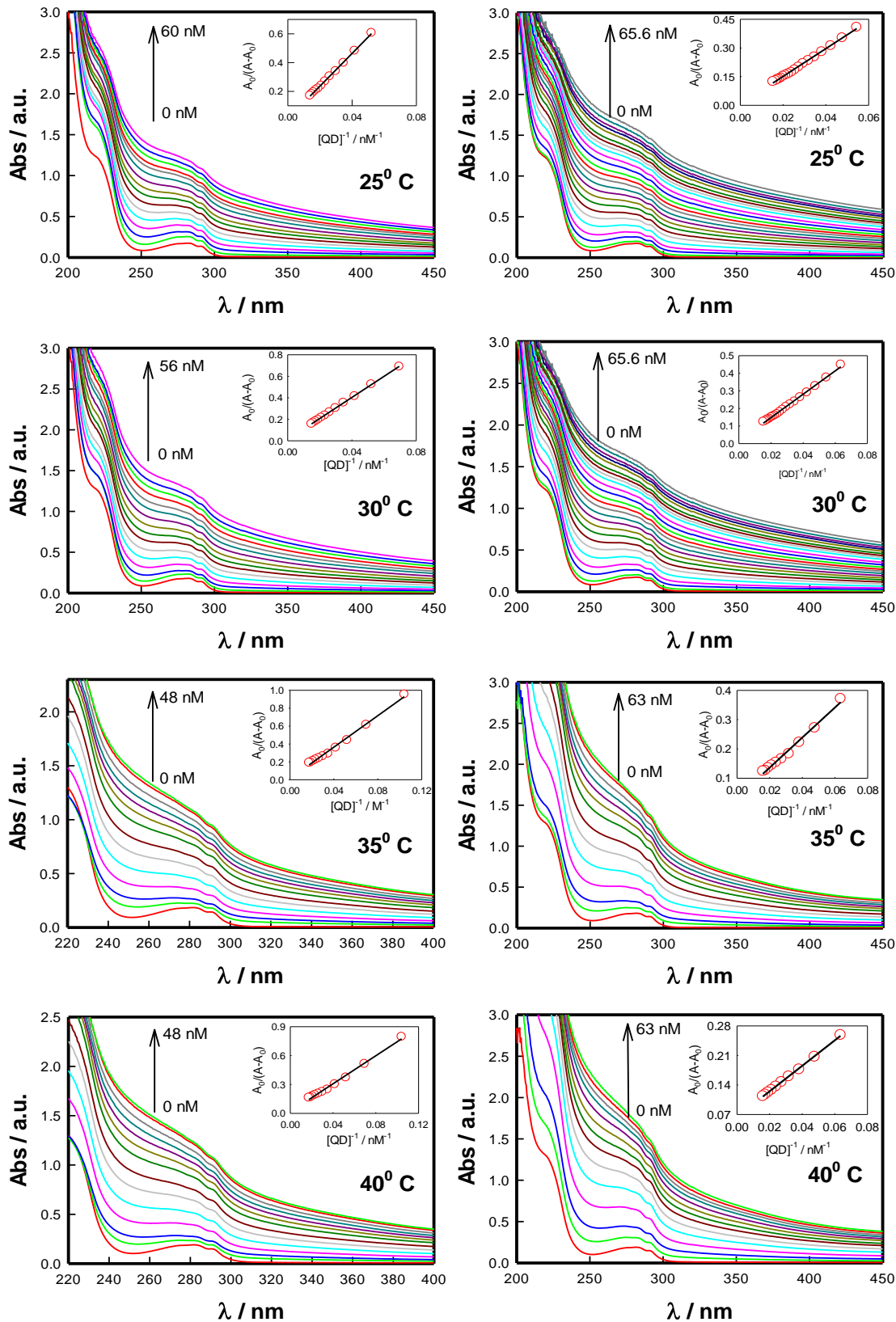
6.2 Sample Preparation

Lysozyme (90%) was purchased from Sigma-Aldrich (Batch no. L6876) and the QDs were synthesized in our laboratory. The 10 mM lysozyme stock solution was prepared in 6.4 pH phosphate buffer solution. The enzyme concentration was quantified as the ratio of absorbance at 280 nm to the molar extinction coefficient of the Lysozyme, $\epsilon_{280}=2.64 \text{ ml mg}^{-1} \text{ cm}^{-1}$.^[12] A stock substrate solution of *Micrococcus lysodeikticus* (Sigma) was prepared in 66 mM potassium phosphate buffer with a concentration of 0.3 mg/mL. All other reagents used were of analytical reagent grade and doubly distilled deionized water was used throughout the experiments.

6.3 UV-Vis absorbance: Complex Formation and Binding Constant

UV–visible absorption spectroscopy has been extensively used in the past to explore the change in physical structure, and to identify the complexation between ligands and

protein molecules^[13]. The absorption spectra of lysozyme (5 μM) with increasing concentration of both size of QD in phosphate buffer at pH 7.0 at five different temperatures are shown in Figures 6.1.



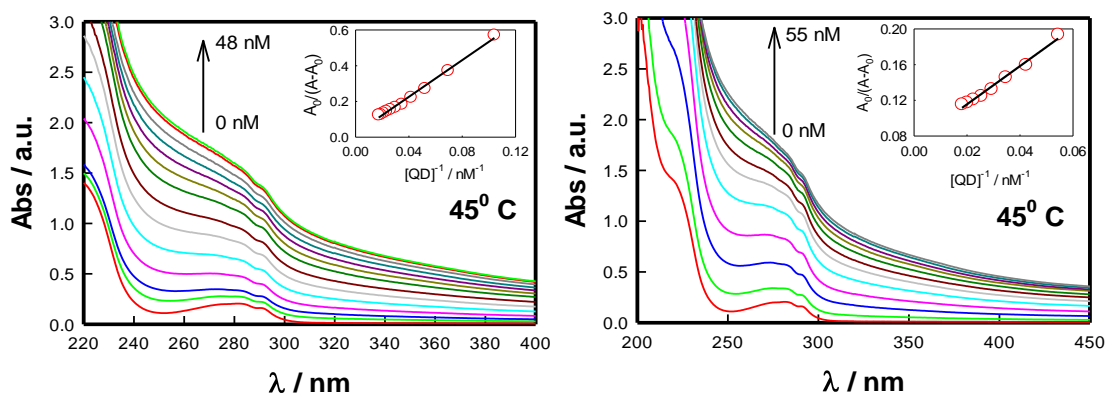


Figure 6.1: Absorption spectra of lysozyme (5 μM) in the absence and presence of 2.5 nm sized QD (left panel) and 6.3 nm sized QD (right panel) with increasing concentration at different temperature.

6.3.1 Strength of the Binding Forces

To determine binding parameters, absorption spectra are expressed according to double reciprocal equation^[14]

$$\frac{A_0}{A - A_0} = \frac{\varepsilon_{Lys}}{\varepsilon_{com}} + \frac{\varepsilon_{Lys}}{\varepsilon_{com}} \frac{1}{K_b} \frac{1}{[QD]} \quad (6.1)$$

where all terms were described in Chapter 2. From the absorption data, the double reciprocal plot for the interaction of lysozyme and different sized QD at different temperatures was obtained as shown in Figure 6.2.

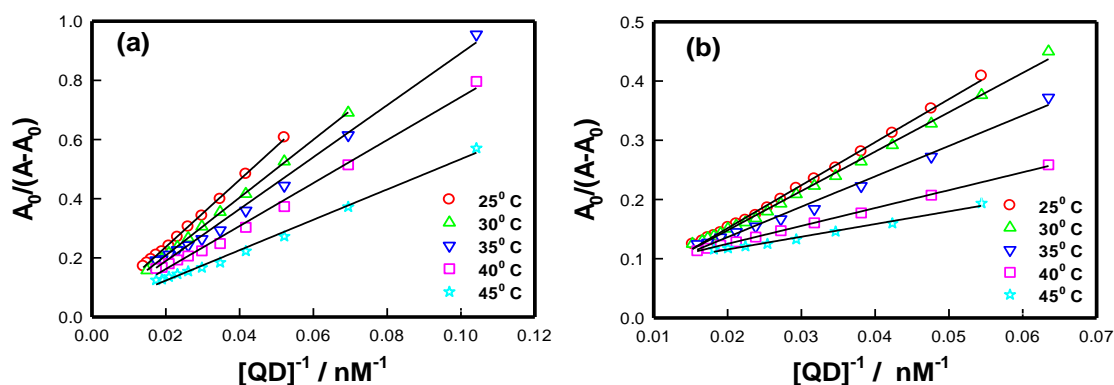


Figure 6.2: Double reciprocal plot for the interaction of lysozyme (5 μM) and (a) 2.5 nm, (b) 6.3 nm sized QD with increasing concentration at different temperature.

Binding constant at different temperature are calculated by the equation 6.1 and tabulated in Table 6.1.

Table 6.1: The binding constant (K_b) for the lysozyme-QD system at five temperatures.

S. No.	Temperature (K)	K_b 2.5nm (10^5L mol^{-1})	K_b 6.3nm (10^5L mol^{-1})
1	298	8.27	8.39
2	303	12.3	22.3
3	308	15.3	65.4
4	313	22.8	214
5	318	39.9	340

Results clearly show the absorbance increasing with the addition of quantum dots. Binding strength are increasing with temperature for both types of complexes. Bigger size QDs were found to bind strongly with lysozyme compared to smaller QDs for all temperature. Normally, the spectral range between 260 and 300 nm indicates change in the microenvironment of the chromophore^[15]. Thus, we conclude that lysozyme-QD interaction leads to the ground state complex formation.

6.3.2 Nature of the Binding Forces: Thermodynamic Parameters

Secondary force interaction, such as hydrophobic forces, hydrogen bonding, van der Waals forces and Coulombic interactions govern binding between ligands and biomolecules^[16]. Thermodynamic parameters like the enthalpy and entropy are indicators of the existence of non-covalent forces. For instance, enthalpy (ΔH), and the entropy change (ΔS) may provide information about nature of binding forces. Ojha and Das^[17] have categorized interactions based on these parameters.

The values of enthalpy (ΔH), and the entropy change (ΔS) were determined from the intercept and slope of the least square fitted straight line to the data points as described by equation 2.26 of Chapter 2.

The values of ΔG (ΔH and ΔS) for the interaction between QD and lysozyme were summarized in Table 6.2. The value of R^2 for linear fitting were more than 0.99. The observed negative value of free energy of binding implied spontaneous and energetically favourable interaction. The more negative value of ΔG and more positive value of ΔS showed that the lysozyme-QDs complexation was more energetically favourable. Data ($\Delta H > 0$ and $\Delta S > 0$) shown in Table 6.2 implies hydrophobic forces were important in the binding between QD and lysozyme.

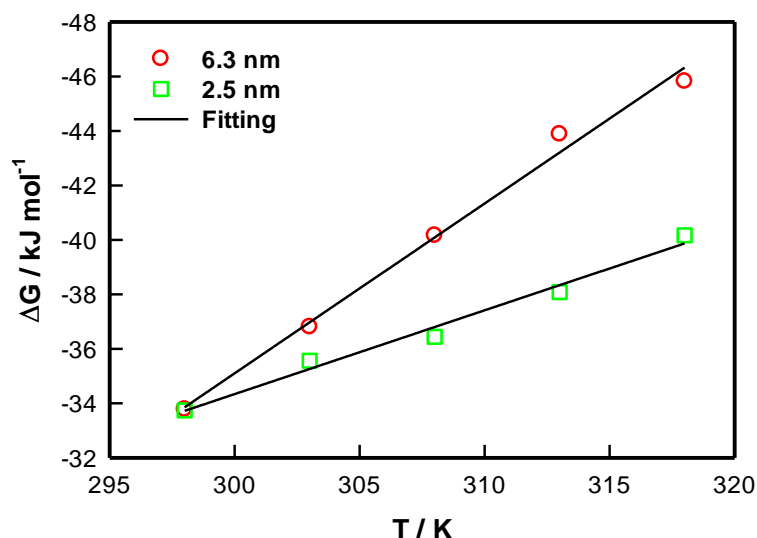


Figure 6.3: Gibbs free energy plot for the interaction of lysozyme (5 μ M) with 2.5 and 6.3 nm sized QD at different temperatures (298, 303, 308, 313 and 318K).

Table 6.2: The binding constant (K_b) and thermodynamic parameters for the lysozyme-QD system at five temperatures.

S. No.	Temperature (K)	$\Delta G_{2.5nm}$ (kJ mol ⁻¹)	$\Delta G_{6.3nm}$ (kJ mol ⁻¹)	ΔH (kJ mol ⁻¹)		ΔS (J mol ⁻¹ K ⁻¹)	
				2.5 nm	6.3 nm	2.5 nm	6.3 nm
1	298	-33.74	-33.77				
2	303	-35.56	-36.81				
3	308	-36.44	-40.17				
4	313	-38.08	-43.88	58	152	307	623
5	318	-40.17	-45.82				

6.4 Fluorescence Spectroscopy: Quenching and Binding Constant

Fluorescence spectroscopy measurements yield considerable information about the binding mechanism in general. Parameters like the binding constant, number of binding sites, and intermolecular distances are parameters easily accessible from this spectroscopy data^[18]. The three distinct intrinsic fluorophore residues, such as Phenylalanine (Phe), Tyrosine (Tyr) and Tryptophan (Trp), when present in proteins may provide information about the conformation, dynamics and intermolecular interactions of the proteins concerned. Out of these residues, Trp and Tyr are mostly used as intrinsic fluorophores. Fluorescence signal arising from Phe is ignored due to its low molar extinction coefficient, and poor quantum yield^[19]. Fluorescence quenching spectra recorded from lysozyme (5 μ M) solutions in the presence of different size QDs at 298 K are shown in Figure 6.4.

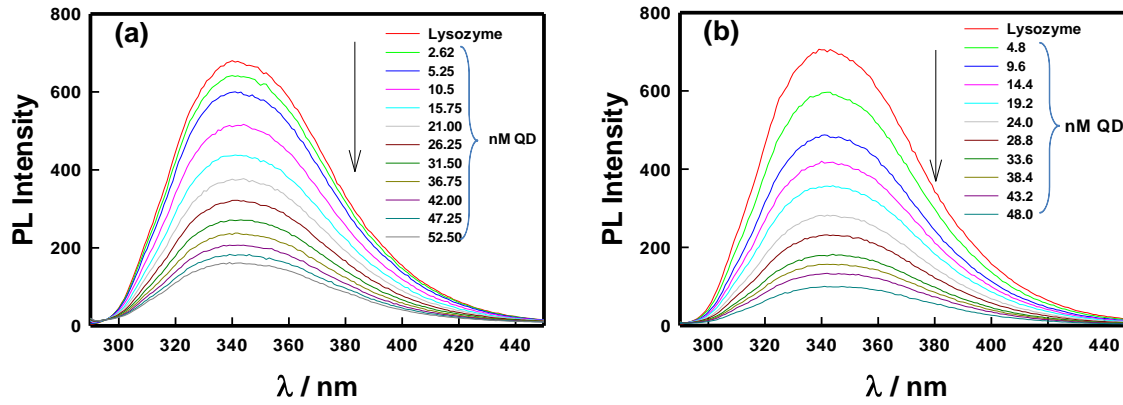


Figure 6.4: Fluorescence quenching spectra of lysozyme (5 μM) in the absence and presence of (a) 2.5 nm, (b) 6.3 nm sized QD at 298 K.

The fluorescence spectral profile revealed lysozyme fluorescence was gradually quenched accompanied by marginal red shifts from 343 to 340 nm with increasing QD concentration for a given lysozyme content. This could be just the error of fluorometer. This clearly indicated lysozyme complexation with QD, and the concomitant fluorophore shift towards more hydrophilic environment^[20]. Fluorescence intensity determined from the lysozyme samples were adequately corrected by evaluating the absorbance of the QD at emission A_2 , and excitation wavelengths A_1 . This was done using the following equation^[21]

$$F_{Cor} = F_{Obsd} 10 (A_1 + A_2)/2 \quad (6.2)$$

Where F_{cor} and F_{obsd} are the corrected and observed fluorescence intensities, respectively.

6.4.1 Binding Constant and Number of Binding Sites

The quenching mechanism was analyzed using the following Stern–Volmer equation^[22]

$$\log \left(\frac{F_0}{F} - 1 \right) = \log K_{SV} + n \log [QD] \quad (6.3)$$

where F_0 and F are the fluorescence intensities in the absence and presence of QD, K_{SV} and n are the Stern–Volmer quenching constant and number of binding sites, respectively, $[QD]$ is the concentration of QD, K_q is the quenching rate constant of biomolecular reaction and τ_0 is the average lifetime of molecules in the absence of QD, and its value is about 10^{-8} s.^[23] Figure 6.5 shows the Stern–Volmer plot of QD-lysozyme system.

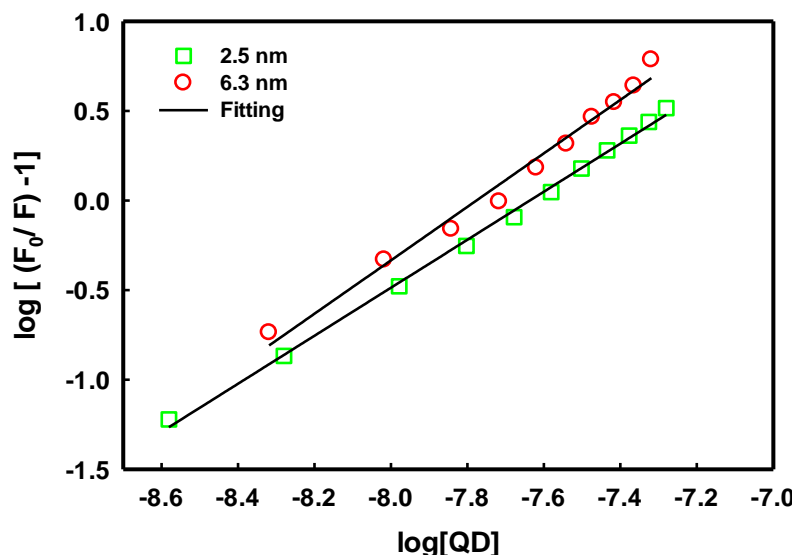


Figure 6.5: Logarithmic plot (Stern–Volmer plots) derived from fluorescence data of lysozyme (5 μ M) as function of concentration of 2.5 and 6.3 nm sized QD (\sim 0 to 60nM) at 298 K.

The binding constant ‘ K_{sv} ’ and number of binding sites ‘ n ’ was determined as described by equation 6.3 and listed in Table 6.3.

Table 6.3: Stern–Volmer quenching constants (K_{sv}) and quenching rate constant (K_q) of lysozyme-QD system.

S. No.	Size of QDs (nm)	Number of binding Sites	K_{sv} ($10^{10}L mol^{-1}$)	K_q ($10^{18}L mol^{-1} s^{-1}$)	R^2
1	2.5	1.34	1.74	1.74	0.99
2	6.3	1.49	40.74	40.74	0.98

6.4.2 Salt Dependent Fluorescence Quenching: Electrostatic Binding Contribution

All the binding experiments were done in a buffer solution, at pH of 6.4, where the lysozyme possesses approximately + 7.5 mV of zeta potential. Also, the zeta potential of the small and big QDs were strongly negative $\zeta = -56$ and -62 mV. Hence, a priori, it is difficult to negate the presence of electrostatic interaction. To confirm this we did perform the binding experiments at different ionic strengths ($I = 0, 0.001, 0.01, 0.1$ N NaCl) as shown in Figure 6.6. The binding constant was found to be marginally screened due the presence of salt (See Figure 6.6, 6.7 and 6.8).

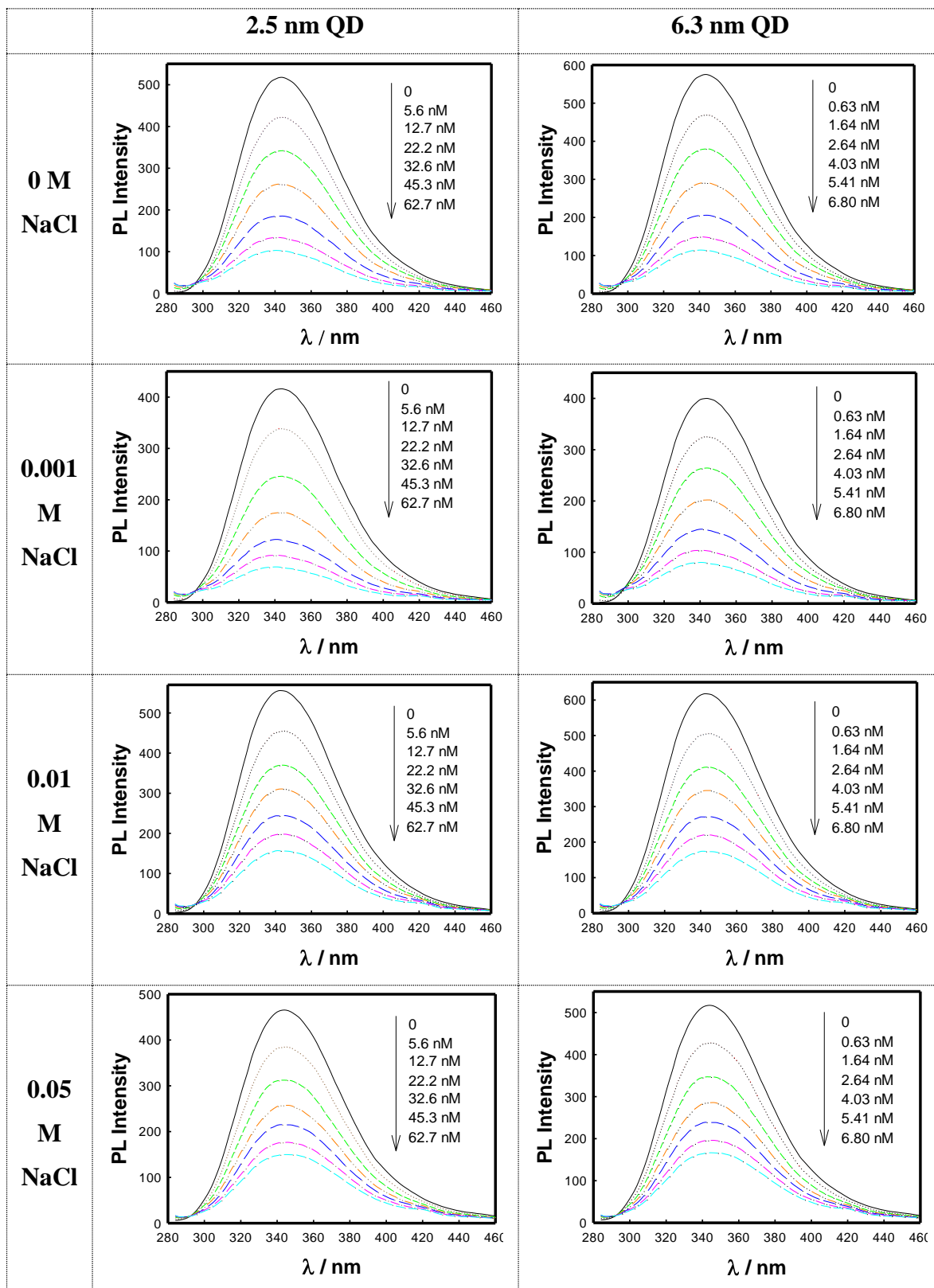


Figure 6.6: Fluorescence quenching spectra of lysozyme (5 μM) in the absence and presence of 2.5 nm and 6.3 nm sized QD at different concentration of NaCl recorded at 298 K.

There was universal quenching of fluorescence caused by QD-protein binding. From Figure 6.6, 6.7 and 6.8, the percentage decrease in the binding constant values was much less than 1% for both QDs implying that there was negligible screening of the interaction due to mobile ions. Therefore, the role of electrostatic interaction was very marginal. We need to differentiate between hydrophobic versus electrostatic binding.

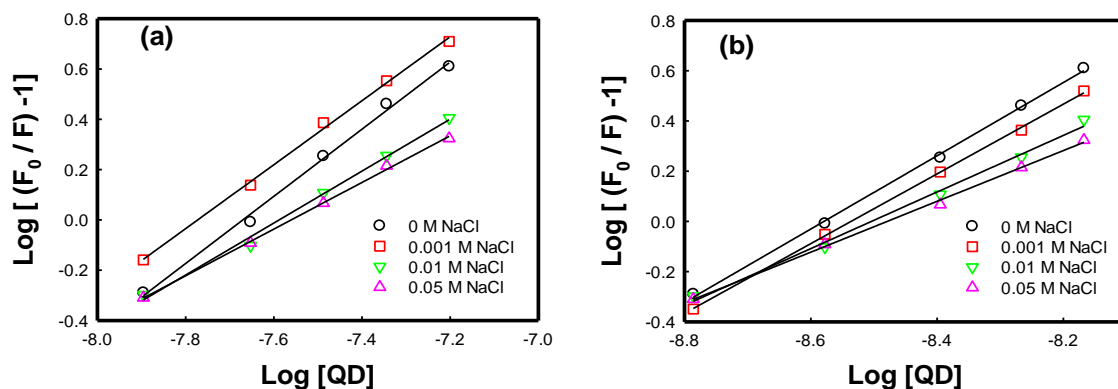


Figure 6.7: Logarithmic plot (Stern–Volmer plots) derived from fluorescence data of lysozyme (5 μM) as function of concentration of (a) 2.5 and (b) 6.3 nm sized QD at different salt concentration.

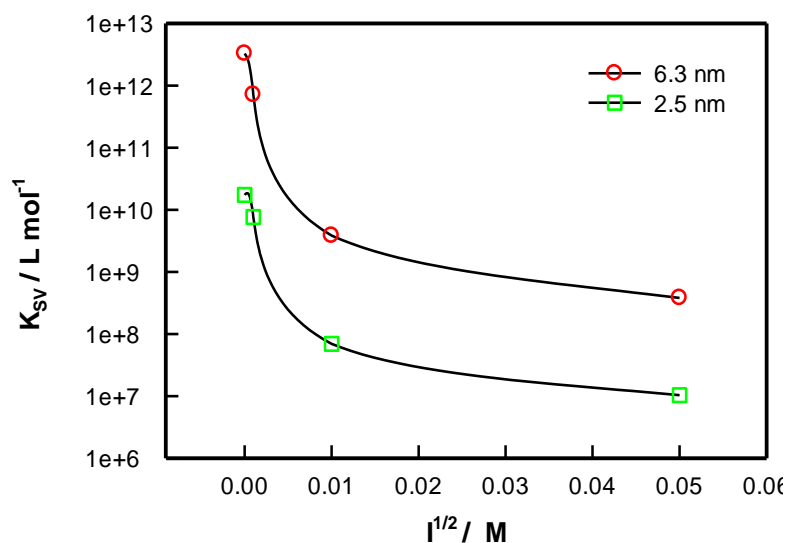


Figure 6.8: Semi-Log plot of binding constant derived from Stern–Volmer plots as function of concentration of NaCl of 2.5 and 6.3 nm sized QD with lysozyme (5 μM).

Based upon energetic considerations, Ross et al (1981) have reviewed the thermodynamics of protein association processes for the examples best characterized in terms of their chemistry and structure. They have accounted for the signs and magnitudes of these thermodynamic parameters (like ΔH , ΔS and ΔG) for protein association (Protein-protein or Protein-ligand) reactions in terms of known molecular forces and the thermochemistry of small molecule interactions^[21]. In an environment of low dielectric

constant, the ΔH_0 should be substantially negative, and ΔS_0 should be substantially negative. But in case of ionic bonding, ΔH_0 should be heavily positive and ΔS_0 should also be positive. Therefore, the electrostatic binding is primarily determined by the positive entropy change accompanying with negative enthalpy change (are predominantly of negative sign)^[21].

Our thermodynamic calculations showed the dominance of the hydrophobic interaction in the QD-Lysozyme binding. Further, the zeta potential of the complex was followed as a function of the QD concentration which again implied absence of electrostatic interaction (no charge inversion, Data not shown).

At this stage it is imperative to compare our results with those of Li et al. (2014) who found strong electrostatic interaction between graphene oxide (negative charged) and lysozyme (from a mixture of binary and ternary proteins) using an array of techniques, i.e. sodium dodecyl sulfate polyacrylamide gel electrophoresis (SDS-PAGE), UV-vis absorption and fluorescence spectroscopy etc^[24]. They have demonstrated how strongly Graphene oxide (GO) interacts with lysozyme. This strong electrostatic interaction also renders the selective adsorption of lysozyme on GO from a mixture of binary and ternary proteins. This was selectivity confirmed by SDS-PAGE, spectroscopy, UV-vis absorption and fluorescence spectroscopy. The adsorbed lysozyme could be released from the surface of GO by adding NaOH solution and then precipitating GO with CaCl_2 . The fast reduction of fluorescence intensity reveals the existence of a strong electrostatic interaction between GO and lysozyme where pH played a central role on the quenching effect. Following, Wetter et al (1951), the pH must be below its isoelectric point (≈ 10.5), to acquire more net positive charge on the protein concerned^[25].

The ionic strength and pH value is extremely important for determining the charge of lysozyme. At a pH ≈ 6.5 , the Lysozyme possess low positive charge which weaken the electrostatic contribution inspite of the high charge density on both the QDs ($\zeta = -56\text{mV}$ (big) and -62 mV (small)). The marginal reduction in quenching at higher ionic strength indicates that the weakly electrostatic nature of the QD-lysozyme interaction. Eliminating the possibility of the π - π stacking interaction, it should be realized that some weak interactions may also exist like van der Waals and hydrogen bonding. Hydrophobic interaction are the major player (from thermodynamic parameter calculations), to probe it further, the ionic strength of NaCl further neutralized the surface charge. The strong quenching of QD on lysozyme is predominantly due to the hydrophobic interaction (not due to electrostatic attraction) between them. This elucidates the difference between our

results vis a vis the Li et al (2014) conclusion.^[24]

6.5 Structural Changes in Lysozyme after Binding

The interaction of lysozyme with QDs may induce conformational changes in their secondary structure, due to hydrophobic binding, which may change the surrounding of its fluorophores hence synchronous fluorescence intensity.

6.5.1 Effect on Microenvironment around Fluorophores

Synchronous fluorescence is a standard technique for the simultaneous determination of multi-component samples without any pre-treatment.^[26,27] One of the major advantages of this technique is, the analysis can be carried out directly under ambient conditions.

Selection of wavelength interval is a major experimental parameter, when synchronous fluorescence technique is used. This selection was made empirically by taking into account the excitation and emission maxima for the three chosen analytes (phenol, resorcinol and hydroquinone), and the scans were recorded from $\Delta\lambda=5$ to 40 nm.^[28] For $\Delta\lambda\leq 5$ nm, the peaks could not be reliably separated while $\Delta\lambda\geq 40$ nm, the fluorescence intensity decreased sharply. For $\Delta\lambda= 15$ nm scan, the peaks revealed good peak shape with a synchronous scanning between $\lambda_{exc}= 230\text{--}360$ nm, and $\lambda_{em}= 245\text{--}375$ nm. This selected spectral region had 130 distinct wavelength values for each sample.

Synchronous fluorescence spectroscopy happens to be a sensitive technique to explore the alteration in the molecular environment of fluorophore residues.^[29] Spectral bandwidth reduction combined with spectral simplification, and perturbation effect noticed in synchronous spectra offer signature information on Tyr and Trp residues, when the $\Delta\lambda$ was fixed at 15 and 60 nm, respectively.^[30] Positional synchronous maxima of these residues are usually manifested on binding, and this yields information about changes in polarity around these fluorophores, and thus on their proximity to the ligand concerned.^[31] The synchronous fluorescence spectra of lysozyme (as function of concentration) in the presence of QDs are illustrated in Figures 6.9.

The results indicated that on increasing the concentration of QD, the fluorescence intensity of Trp decreased more significantly than that of Tyr, as shown in Figure 6.9, which implied that QD quenched the fluorescence spectra of lysozyme mostly by quenching the Trp residue. In addition, a minor red-shift in maximum emission wavelength was noticed revealing that quantum dots changed the hydrophobicity of the microenvironment around the Trp residue, which also changed the physical conformation of lysozyme.^[32]

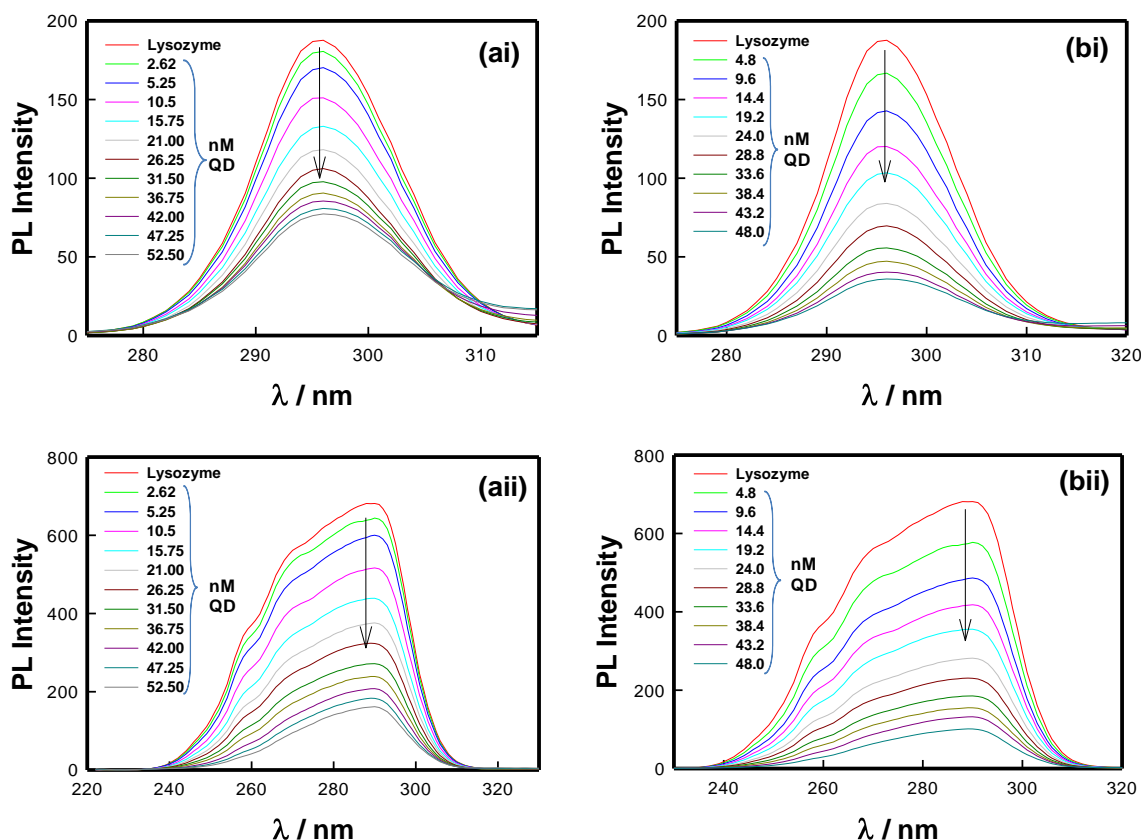


Figure 6.9: The synchronous fluorescence spectra at (i) $\Delta\lambda=15$ nm (Tyrosine) and (ii) $\Delta\lambda=60$ nm (Tryptophan) of Lysozyme ($5 \mu\text{M}$), in the absence and presence of (a) 2.5 nm, (b) 6.3 nm sized QD (2.6 nM to 52.5 nM).

6.5.2 Effect on Secondary Structures

Circular dichroism measurements performed in the far-UV region were used to study the secondary structure change in proteins [33,34] and the change in the ellipticity measured at 222 nm can be used to quantify α -helix content. [35] The CD spectra taken from lysozyme samples in the absence, and presence of QD are shown in Figure 6.10 which exhibits two negative bands at 208 and 218 nm, characteristic of alpha-helix structure of proteins. [36]

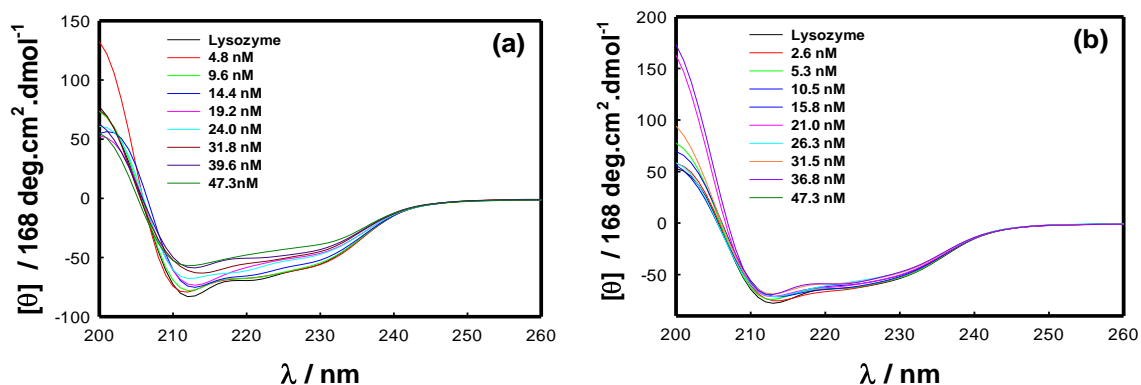


Figure 6.10: The CD spectra of Lysozyme ($5 \mu\text{M}$), in the absence and presence of (a) 2.5 nm, (b) 6.3 nm sized QD.

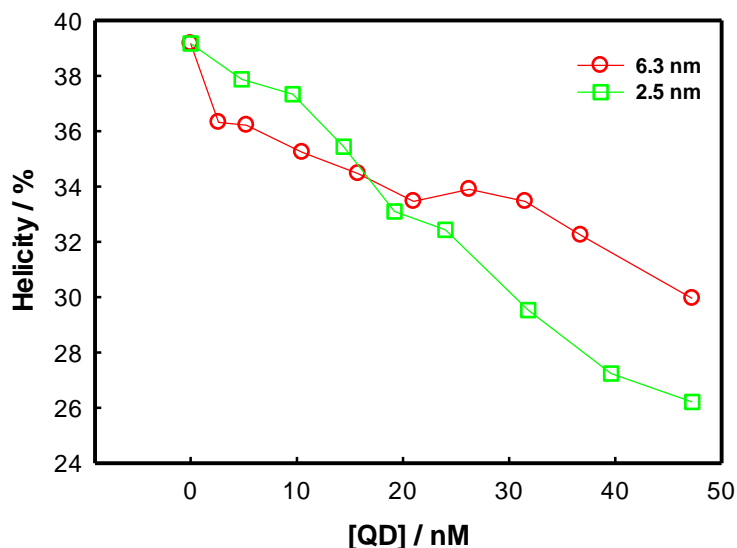


Figure 6.11: Dependence of secondary structure (helicity) of lysozyme ($5 \mu\text{M}$) by 2.5 and 6.3 nm sized QD concentration at 298 K. Note the remarkable loss of secondary structure due to complexation of lysozyme with 2.5 and 6.3 nm sized QD particles.

The helix content was observed to decrease, which reduced from 36.43 % (when untreated) to 32.89 %, 28.53 % and 24.09 % when the QD content was 20, 33 and 50 mM, respectively. At higher the QD concentration, the α -helix content was less (Figure 6.11) which implied secondary structure change in the protein during its interaction with QD. This clearly infers binding of QD to protein surface, which causes protein to reveal its hydrophobic residues. At higher QD concentration, disruption of the α -helix structure of protein was noticed. This results in the appearance of more solvent compatible structures such as β -sheets and random coils.

6.6 Enzymatic Activity of Size Dependent QDs-Lysozyme Complex

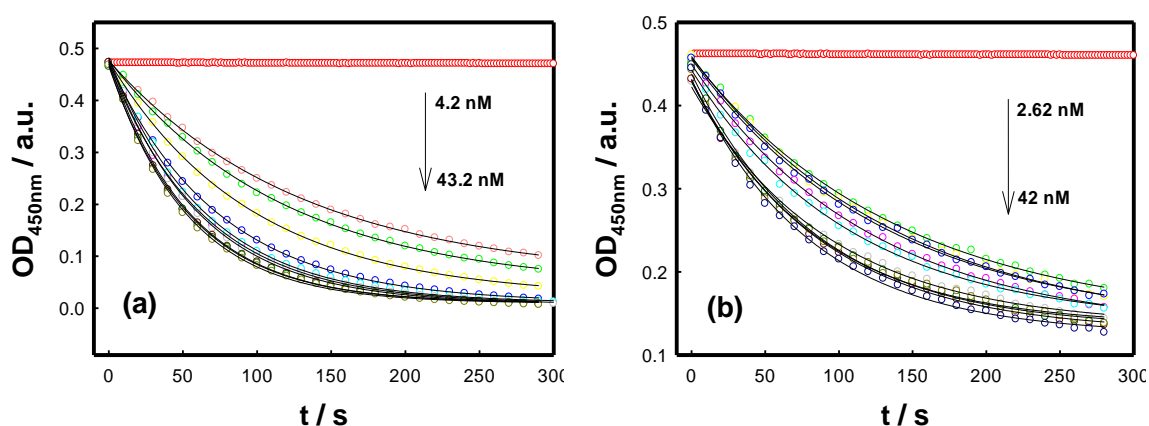


Figure 6.12: Enhancement in the enzymatic activity of lysozyme ($5 \mu\text{M}$) by (a) 2.5 nm, (b) 6.3 nm sized QD. Different amount of QD is used as indicated by the colored lines.

Figure 6.12 shows the effect of the concentration of QD on the enzymatic activity of lysozyme. The normalized reading of optical density (OD), at 450 nm, of micrococcus lysodeikticus was used to indicate the activity of lysozyme.

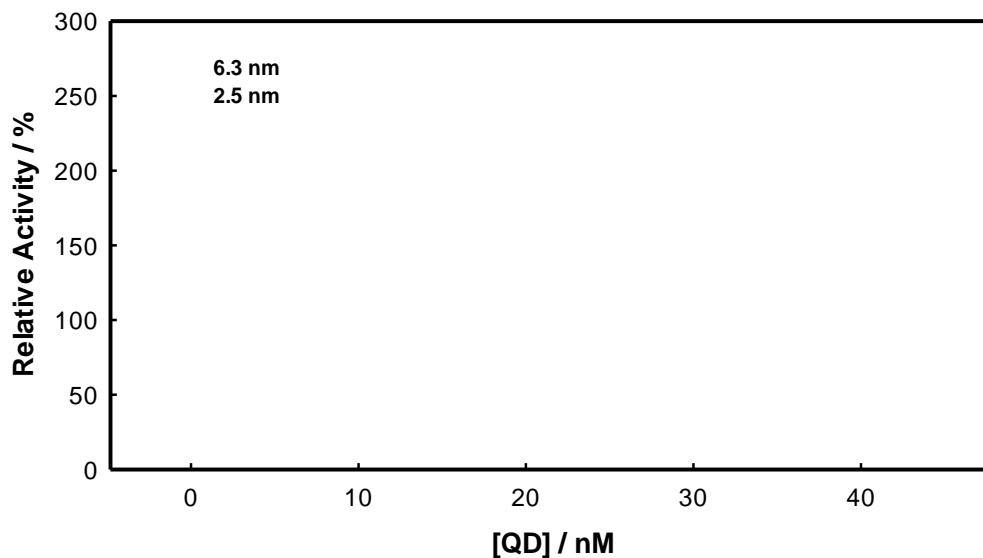


Figure 6.13: Effect of 2.5 and 6.3 nm sized QD concentration on the enzymatic activity of lysozyme (5 μ M).

All data were fitted with exponential decaying with $R^2 > 0.99$. As can be seen, the higher the concentration, the higher is the activity of lysozyme. The enzyme is highly activated (almost 2 times) when the concentration of smaller QD is greater than 19 nM from 2.6 nM. This has been summarized in Figure 6.13.

6.7 Phenomenology of Differential Binding

It was found that smaller size QDs were found to bind poorly to lysozyme, but produced much enhanced enzymatic activity compared to bigger QDs which in turn showed aggressive binding. The thermodynamics of binding of the smaller QD to lysozyme revealed, $\Delta H = 58$ KJ/mol, and $\Delta S = 307$ JK⁻¹mol⁻¹ while for the bigger QDs these values were 152 KJ/mol and 623 JK⁻¹mol⁻¹. The corresponding free-energy of binding was, $\Delta G \approx -34$ KJ/mol for small as well as bigger QDs at 25⁰ C. A pertinent question is did Coulombic interactions play any role in QD-lysozyme binding? The zeta potential of 2.5 and 6.3 nm QDs were -56 and -62 mV respectively. This implied that the smaller size QD had a typical surface charge density that was ~6 times higher than the other QD. On the other hand, lysozyme has a hydrodynamic radius of 20.5 nm^[37], and pI = 11.35. The binding studies were carried out at pH=8, where lysozyme was carrying a net positive charge.^[38] Regardless of the magnitude of this charge, an electrostatic interaction

between the negatively charged QDs and positively charged lysozyme becomes a finite possibility. Since, the surface charge density of smaller QD was about 6-times higher than its competitor, these smaller QDs will preferentially bind to lysozyme surface. This was observed in our experiments. Electrostatic interactions between QD and lysozyme cause local charge neutralization to the lysozyme surface, and this will release counterions into the bulk solvent, thereby increasing its entropy. We did observe this effect. Therefore, possibility of electrostatic interaction between QDs and lysozyme cannot be ruled out, completely. The smaller sized QDs bind more efficiently to lysozyme, but exhibit enhanced enzymatic activity when compared to bigger QDs. This is due to the differential enzymatic behavior activity of the so formed Lysozyme-QD complex. The results showed the individual contribution of QDs towards the enhanced enzymatic activity.

6.8 Summary

The interactions of MPA coated CdSe quantum dots (QDs) with lysozyme was studied by fluorescence, UV–visible, and circular dichroism. The results showed that the QDs quenched the fluorescence of lysozyme. The interactions process (binding) is mostly dominated by hydrophobic forces which induced conformational changes in the protein involved.

The present study provides an important quantitative data of lysozyme binding affinity with QDs by the UV–visible spectroscopy, circular dichroism, steady state and synchronous fluorescence (quenching) measurements. The calculated thermodynamic parameters calculations reveal that apart from electrostatic forces, the hydrophobic interaction plays major role in stabilizing the lysozyme–QD complex. As a result, QD is able to enhance the enzymatic activity of lysozyme and activate the enzyme. Both, synchronous fluorescence and circular dichroism, spectra confirmed that complex formation between the QDs and lysozyme caused conformational changes in protein structure. It was concluded that smaller size QDs were found to bind poorly to lysozyme, but produced much enhanced enzymatic activity compared to bigger QDs. Comprehensive physical characterization, and stability of lysozyme-QD complexes is an important step in their potential use as imaging agents and intracellular delivery vectors. In summary, smaller sized QD were found to bind poorly to lysozyme, but produced much enhanced enzymatic activity compared to bigger QDs.

6.9 References

- [1] M. Wellington, J. M. Bliss, C. G. Haidaris, *Infect. Immun.* **2003**, *71*, 7228.
- [2] J. Hostetter, R. Kagan, E. Steadham, *Clin. Diagn. Lab. Immunol.* **2005**, *12*, 793.
- [3] I. L. Medintz, J. H. Konnert, A. R. Clapp, I. Stanish, M. E. Twigg, H. Mattoussi, J. M. Mauro, J. R. Deschamps, *Proc. Natl. Acad. Sci.* **2004**, *101*, 9612.
- [4] I. L. Medintz, H. T. Uyeda, E. R. Goldman, H. Mattoussi, *Nat. Mater.* **2005**, *4*, 435.
- [5] M.-K. So, C. Xu, A. M. Loening, S. S. Gambhir, J. Rao, *Nat. Biotechnol.* **2006**, *24*, 339.
- [6] W. Wu, M. Aiello, T. Zhou, A. Berliner, P. Banerjee, S. Zhou, *Biomaterials* **2010**, *31*, 3023.
- [7] R. Savla, O. Taratula, O. Garbuzenko, T. Minko, *J. Controlled Release* **2011**, *153*, 16.
- [8] C.-y. Zhang, L. W. Johnson, *Anal. Chem.*, **2009**, *81*, 3051.
- [9] J. K. Jaiswal, S. M. Simon, *Trends Cell Biol.* **2004**, *14*, 497.
- [10] N. G. Portney, M. Ozkan, *Anal. Bioanal. Chem.* **2006**, *384*, 620.
- [11] A. P. Alivisatos, W. Gu, C. Larabell, *Annu. Rev. Biomed. Eng.* **2005**, *7*, 55.
- [12] C. Tanford, K. C. Aune, *Biochemistry (Mosc.)* **1970**, *9*, 206.
- [13] X. Pan, R. Liu, P. Qin, L. Wang, X. Zhao, *J. Lumin.* **2010**, *130*, 611.
- [14] J. K. Maurya, M. U. H. Mir, U. K. Singh, N. Maurya, N. Dohare, S. Patel, A. Ali, R. Patel, *Biopolymers* **n.d.**, *103*, 406.
- [15] X. Guo, X. Han, J. Tong, C. Guo, W. Yang, J. Zhu, B. Fu, *J. Mol. Struct.* **2010**, *966*, 129.
- [16] Z. Chi, R. Liu, H. Zhang, *Biomacromolecules* **2010**, *11*, 2454.
- [17] B. Ojha, G. Das, *J. Phys. Chem. B* **2010**, *114*, 3979.

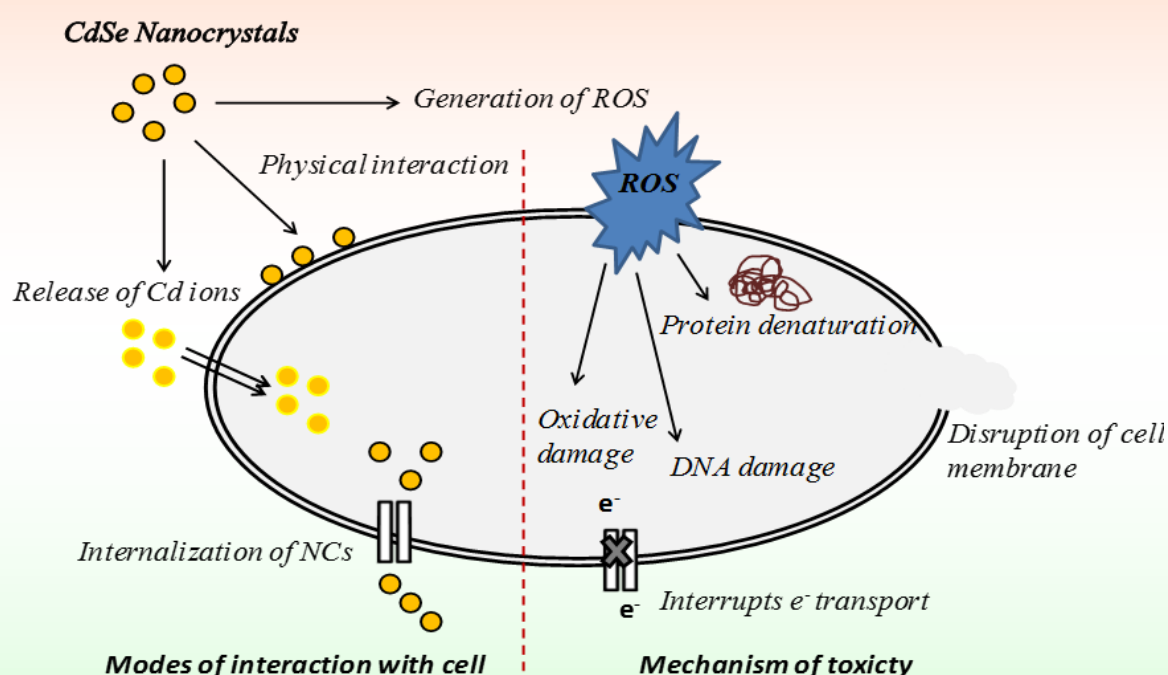
- [18] Y. Shu, M. Liu, S. Chen, X. Chen, J. Wang, *J. Phys. Chem. B* **2011**, *115*, 12306.
- [19] L. He, X. Wang, B. Liu, J. Wang, Y. Sun, E. Gao, S. Xu, *J. Lumin.* **2011**, *131*, 285.
- [20] D. Li, J. Zhu, J. Jin, *J. Photochem. Photobiol. Chem.* **2007**, *189*, 114.
- [21] P. D. Ross, S. Subramanian, *Biochemistry (Mosc.)* **1981**, *20*, 3096.
- [22] Y.-P. Wang, Y. Wei, C. Dong, *J. Photochem. Photobiol. Chem.* **2006**, *177*, 6.
- [23] M. Bihari, T. P. Russell, D. A. Hoagland, *Biomacromolecules* **2010**, *11*, 2944.
- [24] S. Li, J. J. Mulloor, L. Wang, Y. Ji, C. J. Mulloor, M. Micic, J. Orbulescu, R. M. Leblanc, *ACS Appl. Mater. Interfaces* **2014**, *6*, 5704.
- [25] L. R. Wetter, H. F. Deutsch, *J. Biol. Chem.* **1951**, *192*, 237.
- [26] M. del Olmo, C. Díez, A. Molina, I. de Orbe, J. L. Vílchez, *Anal. Chim. Acta* **1996**, *335*, 23.
- [27] A. Espinosa-Mansilla, A. Muñoz de la Peña, F. Salinas, D. González Gómez, *Talanta* **2004**, *62*, 853.
- [28] M. F. Pistonesi, M. S. Di Nezio, M. E. Centurión, M. E. Palomeque, A. G. Lista, B. S. Fernández Band, *Talanta* **2006**, *69*, 1265.
- [29] J.-Q. Lu, F. Jin, T.-Q. Sun, X.-W. Zhou, *Int. J. Biol. Macromol.* **2007**, *40*, 299.
- [30] J. Fan, X. Chen, Y. Wang, C. Fan, Z. Shang, *J. Zhejiang Univ. Sci. B* **2006**, *7*, 452.
- [31] G. Zhang, N. Zhao, L. Wang, *J. Lumin.* **2011**, *131*, 880.
- [32] C. Sun, J. Yang, X. Wu, X. Huang, F. Wang, S. Liu, *Biophys. J.* **2005**, *88*, 3518.
- [33] M. Dockal, D. C. Carter, F. Rüker, *J. Biol. Chem.* **2000**, *275*, 3042.
- [34] Y.-H. Chen, J. T. Yang, H. M. Martinez, *Biochemistry (Mosc.)* **1972**, *11*, 4120.
- [35] J. Corbin, N. Méthot, H. H. Wang, J. E. Baenziger, M. P. Blanton, *J. Biol. Chem.* **1998**, *273*, 771.
-

- [36] S. Zhi-Cai, Y. Ping-Gui, Y. Qing-Sen, L. Rui-Sen, S. Zhi-Cai, Y. Ping-Gui, Y. Qing-Sen, L. Rui-Sen, *Acta Phys.-Chim. Sin.* **2001**, *17*, 48.
- [37] V. Calandrini, D. Fioretto, G. Onori, A. Santucci, *Chem. Phys. Lett.* **2000**, *324*, 344.
- [38] M. Boström, D. R. M. Williams, B. W. Ninham, *Biophys. J.* **2003**, *85*, 686.

Chapter 7

Size Variational Synthesis and Antimicrobial Activity of Core/Shell CdSe/CdS Quantum Dots

Abstract: This chapter presents a simpler route to synthesize CdSe/CdS core/shell QDs with varying core size and shell thickness and discusses their size dependent antifungal activity.



Pictorial representation of the possible ways of cellular interaction of QDs and the different toxicity pathways by QDs against Candida albicans is shown here.

7.1 Introduction

Semiconductor nanocrystals are more fluorescent in terms of their brightness and stability against photo-bleaching compared to organic dyes and fluorescent proteins [1]. Recent progress in nanocrystal synthesis and bioconjugation has opened up a whole new area of nanobio-activity dedicated to nanocrystals, and this is facilitated by the possibility of rendering the NCs water soluble, and therefore amenable to bio-conjugation [2-3]. Regardless, their biological application have not been explored extensively largely because of problems associated with their surface chemistry. Nonetheless, these materials have come of age in the past decade, due to the inclusion of surface

modification in the bio-conjugation protocols [4].

The size, crystal structure, and surface coatings can dictate the cellular uptake and cytotoxicity of a given nanoparticle [5-6]. The smaller size nanoparticles have shown enhanced toxicity over their larger counterparts [5-6]. The nanoparticle cores containing heavy metals are toxic due to free radical generation resulting in producing oxidative stress [7-13]. Any biological application of a nanomaterial requires prior screening of its cellular uptake and cytotoxicity profile. These two signature parameters are indeed dependent on nanoparticle size and surface morphology. Derfus et al have shown that cytotoxicity of CdSe nanocrystal was conditioned by the processing parameter during synthesis. This toxicity arose from the leaching of Cd²⁺ ions from the CdSe lattice over a period of time [14]. Hild et al have described the ideal features that a nanoparticle must possess for biological applications and cellular imaging [15]. Cytotoxicity of CdSe and ZnS nanocrystals synthesized using various stabilizing agents such as 3-mercaptopropionic acid (MPA), silanization and polymer was extensively evaluated by Kirchner et al [16]. These studies suggested that nanoparticle aggregation; in addition to release of Cd²⁺ ions played a key role in deciding cytotoxic effects. The effect of surface chemistry and particle size on the cellular and cytotoxicity in murine macrophage cell lines was extensively studied by Cliff et al [17].

The literature reveals that the CdSe water soluble NCs have gained considerable acceptance from biologists as a promising bio-conjugation and cell imaging agent. Therefore, its size and shell thickness dependent antimicrobial activity must be evaluated precisely to suitably modify their synthesis protocol. Herein, we have performed this analysis for CdSe nanoparticles, for core-only and core-shell structures, where the CdS forms the shell (corona). The outbreak of multi-drug resistant pathogenicity is one of the major global health issues being faced today that has become a matter of concern in medical science [18]. Resistance to antibiotics develop due to enzymatic and genetic mutations in pathogenic organisms. Therefore, development of new and efficient antimicrobial agents to control these pathogens has been a prime focus recently. Amongst the pathogenic organisms, *Candida albicans*, an opportunistic fungus is known to cause serious fungal infections.

The antifungal ability of noble metal nanoparticles has been widely investigated [19-21]. Though, there has been significant interest in research using CdSe nanoparticles for bioimaging and pharmaceutical applications, not much or little studies focus on the potential antimicrobial ability of these nanoparticles. Antimicrobial property of

nanoparticle is known to depend on the composition, surface functional groups, size and shape [20]. CdSe nanoparticles possess superior fluorescent properties that make them potential candidates in biosensing, cell imaging and in vivo tracking. There have been numerous studies on the varied applications of CdSe nanoparticles; however studies are yet to uncover the toxicity and examine their potential for antifungal applications.

In the current study, we evaluated the antifungal activity of well-defined and size-controlled CdSe/CdS core/shell QDs synthesized by very simple route, against *Candida albicans* CAF2-1. The uniqueness of the work is the simpler method to synthesize core/shell structure with varying core size and shell thickness and based on the fact that it examines the effect of size of CdSe QDs synthesized with a very narrow size distribution and the effect of shell thickness on the antifungal property. We compared the toxicity of CdSe QDs relative to CdSe/CdS core-shell structure. The results provide the qualitative assessment of size-dependent antifungal property of CdSe nanoparticles and effect of shell thickness on this property.

7.2 Sample Preparation

7.2.1 Synthesis of CdSe QDs of Different Size

The synthesis of these QDs is discussed in chapter 2 which follows a kinetic growth process. Reaction temperature was 200, 230 and 260 °C for three sized QDs and time interval for synthesis was kept 120 seconds for each. We could successfully prepare these QDs with three different size which was ascertained from the UV-vis spectroscopy, dynamic light scattering and TEM (Table 7.2) data.

Briefly, a mixture of CdO (26 mg), OA (0.6 mL), and ODE (10 mL) was heated to a temperature 220 °C in a 100 mL three-neck round-bottom flask without any special condition. When the temperature reached 220 °C, the reacting solution turned colourless due to the formation of cadmium oleate. The CdSe QDs made from a selenium solution which was 5 mmol of Se prepared in 0.4 ml of TOP diluted with 2.6 ml of ODE. This was rapidly injected into the reaction flask maintained at a temperature of 220 °C. Then the reaction temperature was reduced to 200 °C, and the structures were grown until the required size was achieved which took 2 min. In this way we prepared 3 sized CdSe QDs one by one by keeping reaction temperature at 200 °C, 230 °C and 260 °C.

7.2.2 Synthesis of CdSe/CdS Core /Shell QDs with varying Shell Thickness

The protocol for the synthesis CdSe/CdS core/shell nanostructures was already discussed in synthesis sections of Chapter 1 and 2. For the synthesis of core-shell structures, a

solution of CdO (0.76 g), OA (6 ml), and ODE (24 ml) was heated to 220 °C till it turned colourless. Sulphur shell precursor was made as sulphur powder (0.16 g) with 4 ml TOP was dissolved in 11 ml ODE. These solutions were then added drop-wise one by one to the CdSe reaction vessel, starting immediately the shell growth on CdSe QDs. The quantity of shell precursor was chosen in such a way that suitable thick thickness could be achieved. After synthesis, the aliquots were isolated and extracted as described in chapter 2. We noticed that excess of ODE, and OA adsorbed to the nanocrystals. So, these samples were washed at least eight times with extraction solution prior to their characterization. Ligand exchange was used for the transfer of oil-dispersed quantum dots to aqueous phase using 3-MPA. The synthesized QDs were named as shown in Table 7.1.

Table 7.1: Naming of synthesized QDs is described.

Reaction Temperature Structure	200 °C	230 °C	260 °C
Core Only	1A	2A	3A
Core / thinner Shell	1B	2B	3B
Core / thicker Shell	1C	2C	3C

7.3 Physical Characterization

The physical size of these nanostructures were measured from the TEM, DLS and UV-vis absorbance data (Figures 7.1, 7.2 and 7.3). While DLS and TEM directly yielded the values for mean particle size, we used the empirical relation 2.19 of Chapter 2 to derive size parameter from UV-vis spectral data. Crystalline phase, surface charge and optical properties were also measured.

7.3.1 Structural Characterization

It must be noted that size, D values determined by UV-vis for CdSe and CdSe/CdS QDs were underestimate of the particle size. The DLS method produced higher size because of the hydration mediated clustering of the QDs but gave the information of uniformity exactly. Single and narrow size distribution correspond to uniform sized QDs. The size derived from the TEM reflected the true physical dimensions of the QDs.

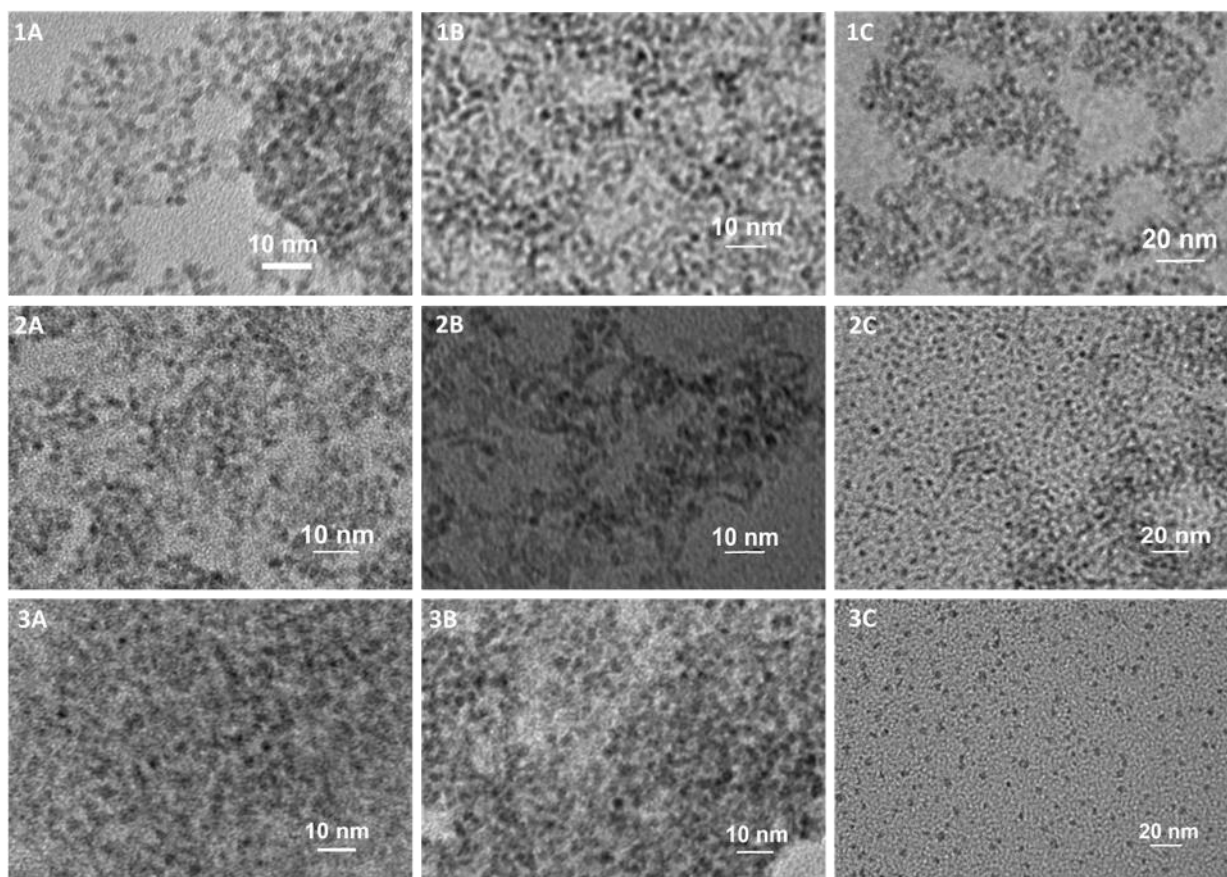


Figure 7.1: TEM images of synthesized core CdSe and Core/shell CdSe/CdS QDs.

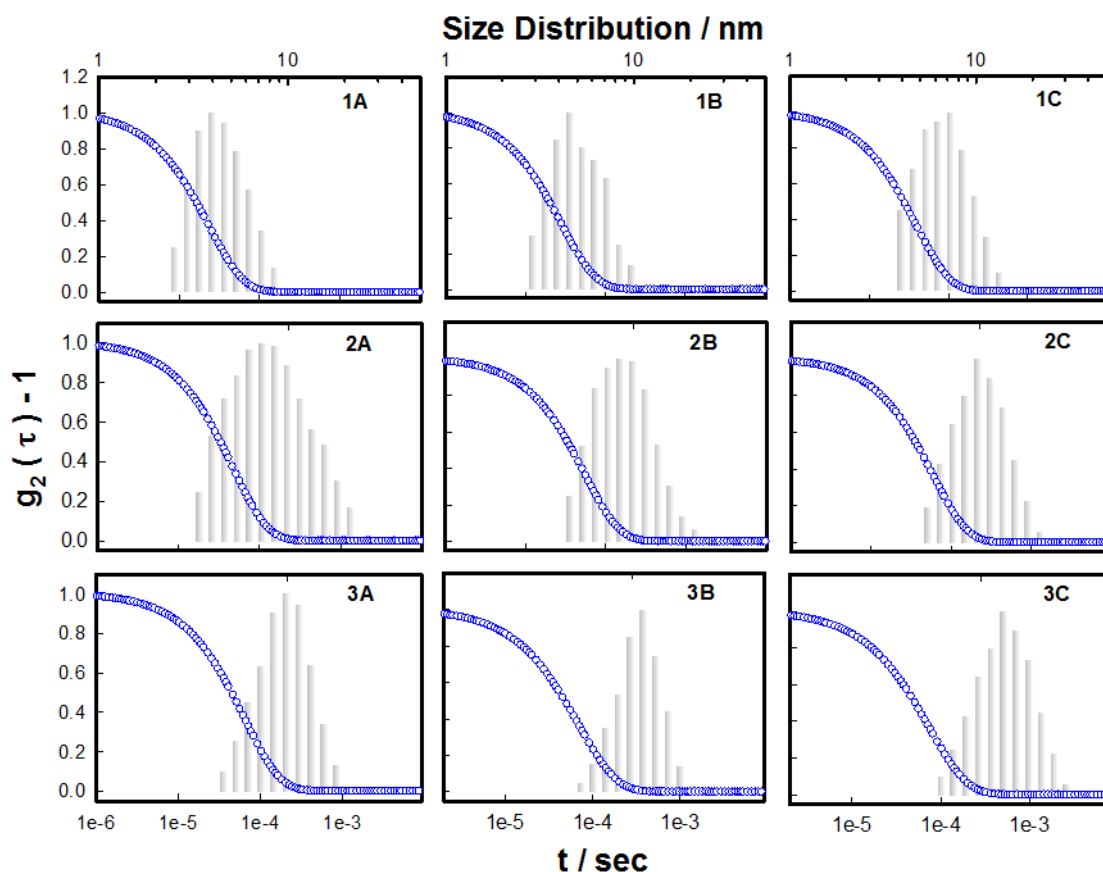


Figure 7.2: DLS plot of synthesized core CdSe and Core/shell CdSe/CdS QDs.

7.3.2 Surface Charge

Aqueous dispersions of the colloidal nanocrystals were subjected to electrophoresis studies to evaluate their zeta potentials, which is the potential at the hydrodynamic slipping plane. It is a direct measure of the colloid surface charge [22]. We found that the core-shell nanocrystals had a zeta potential that was about 35% more than that of the core-only structures (Table 7.2). A more relevant parameter is the surface charge density which was estimated to be 0.9 mV/nm² for CdSe and 0.4 mV/nm² for CdSe/CdS particles. Thus, the core-only NCs were associated with higher charge density, and thus electrostatically more active. The zeta potential histograms are shown in Figure 7.3.

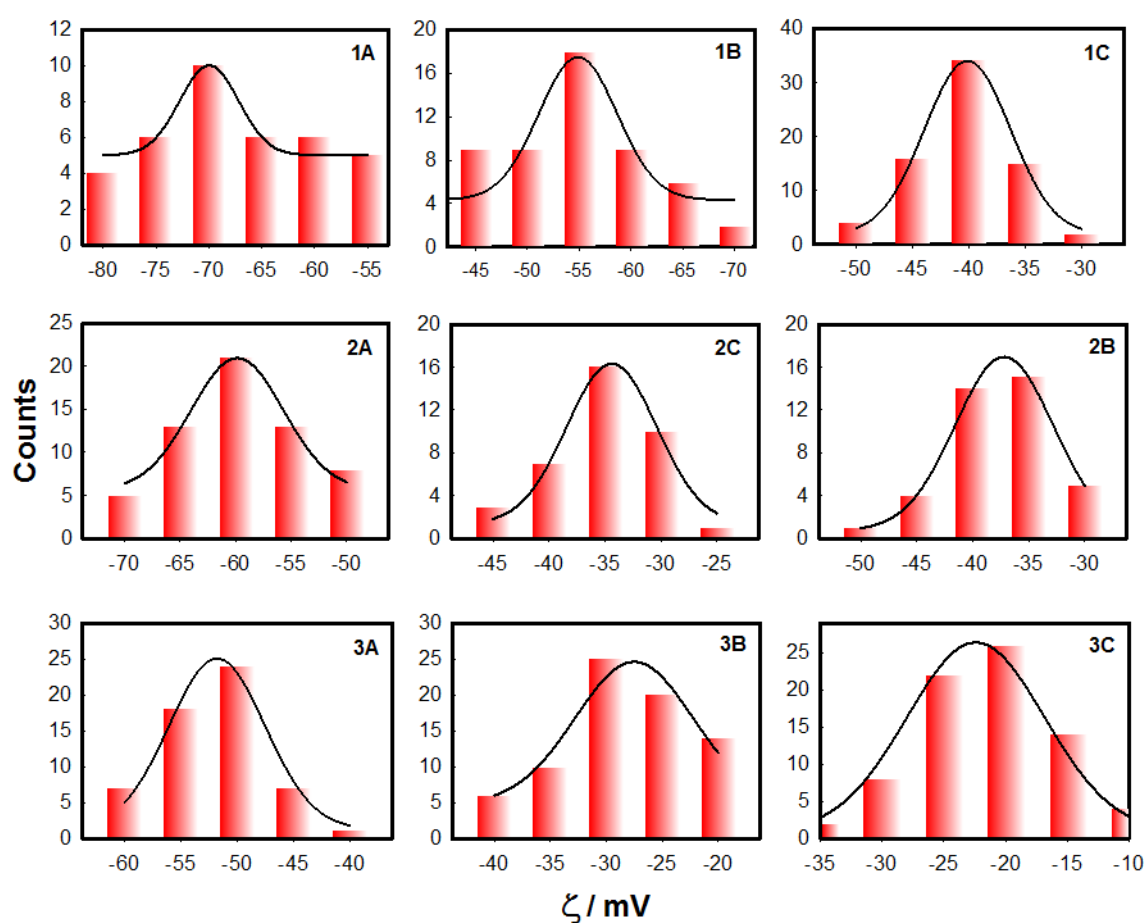


Figure 7.3: Zeta potential plot of synthesized core CdSe and Core/shell CdSe/CdS QDs.

The average surface charge of these QDs (Figure 7.4) are tabulated in Table 7.2. Two observations could be readily made from the data presented in Table 7.2. These are: (i) the core-shell structure was associated with a lower negative surface charge and (ii) the thickness of CdS layer on the CdSe core-only QD was on the order of nm (Figure 7.1 and Table 7.2).

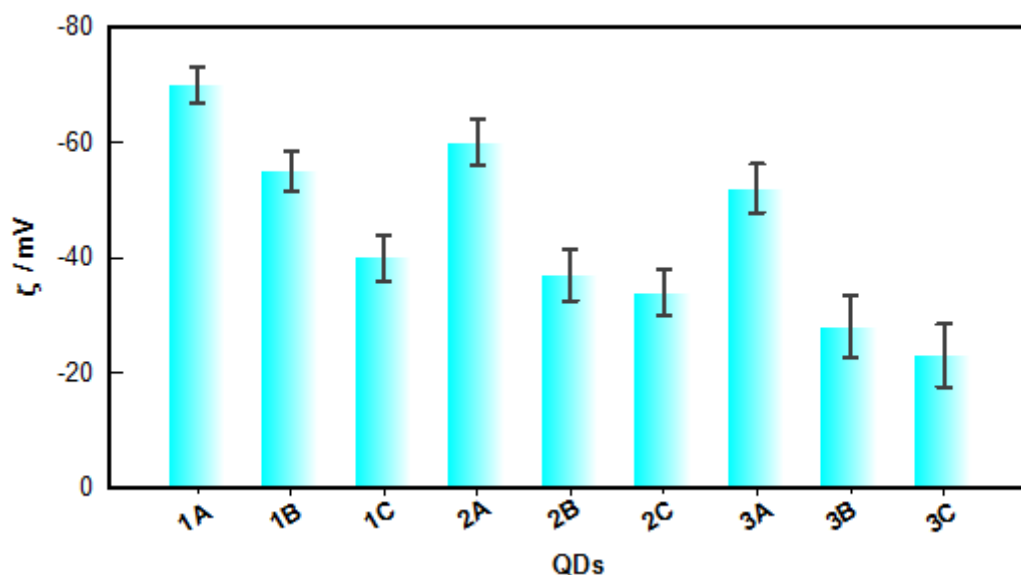


Figure 7.4: The average surface charge of synthesized core CdSe and Core/shell CdSe/CdS QDs.

Table 7.2: Physical characteristics of the nanocrystals used in this study measured at room temperature.

Sample IDs	Absorbance (λ_{ab})/nm	Emission (λ_{em})/ nm	Size/ nm			Zeta potential/mV
			UV	TEM	DLS	
1A	475±2	512±2	2.14	2.2±0.2	4.0±0.4	-70±3
1B	482±2	519±2	2.19	2.8±0.3	4.8±0.5	-55±2
1C	485±2	519±2	2.21	3.3±0.3	6.7±0.6	-40±2
2A	499±2	535±2	2.34	2.4±0.2	8.0±0.7	-60±2
2B	507±2	543±2	2.41	3.1±0.3	9.4±0.8	-37±1
2C	511±2	543±2	2.46	3.6±0.3	10.1±0.9	-34±1
3A	543±2	578±2	2.91	2.9±0.3	10.9±0.9	-52±2
3B	549±2	586±2	3.02	3.4±0.3	11.9±1.0	-28±1
3C	553±2	586±2	3.11	3.9±0.4	12.6±1.1	-23±1

7.3.3 Optical Characterization

Absorbance was measured for all the QDs which showed sharp peak and these peaks were red-shifted with size but effect of shell on absorption peaks were not significant (Figure 7.5 a). It can be understood by the fact that the absorption and fluorescence are caused by core only not by shell. And core size was nearly fixed for fixed reaction temperature. So fluorescence peak wavelengths are also not so much different by shelling the QDs and that was confirmed by the emission spectra (Figure 7.5 b).

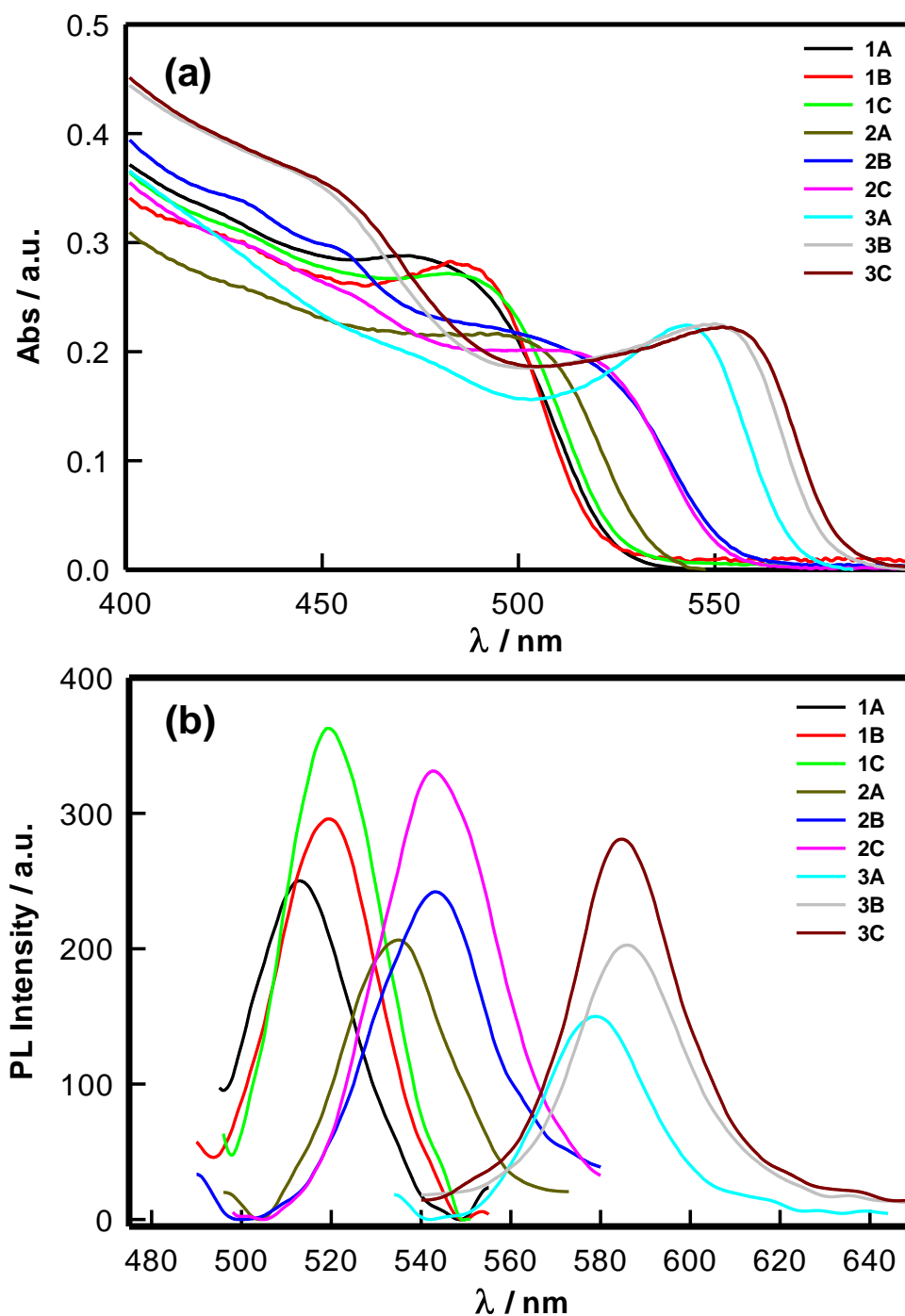


Figure 7.5: (a) UV-vis and (b) fluorescence emission spectra of CdSe and CdSe@CdS core-shell QDs (excitation wavelength \approx 450 nm).

One of the main objectives was to enhance the fluorescence by cladding the QDs with CdS. Fluorescence emission was measured by exciting all the samples at 450 nm. We observed that core-shell QDs had a higher fluorescence emission peak intensity compared to core-only QDs. Enhancement in fluorescence of core CdSe QDs was because of the presence of CdS shell. The emission peak was recorded (Figure 7.5 b) and tabulated in Table 7.2 for all nanostructures. The CdSe/CdS QDs were observed to be associated with red shift compared to core only.

7.3.4 Crystalline Structure

The morphology and crystallite size of CdSe and CdSe/CdS QDs were evaluated from the X-ray diffraction data collected in the 2θ range of $20-60^\circ$. The X-Ray diffractograms are shown in Figure 7.6 and are indexed based on the cubic system. The interplanar spacings determined from the prominent peaks in diffractograms corresponded to reflections arising from (111), (220) and (311) planes of CdSe QDs are consistent with JCPDS Card No. 32-0483). Thus, QDs had face centered cubic (FCC) structure with the interplanar d-spacing determined from the (111) reflection peak was 3.54 \AA , 3.48 \AA and 3.50 \AA for CdSe and CdSe/CdS QDs, respectively. The broadness of the peaks correspond to nanocrystalline size. Core structure with shell showed peak shifting that is due to CdS shelling structure and peak broadening also due to lattice mismatch of CdSe core & CdS shell. Increasing the shell thickness enhanced crystallinity of CdS hence the peak of thicker shell XRD was less broad than that of thinner shell XRD.

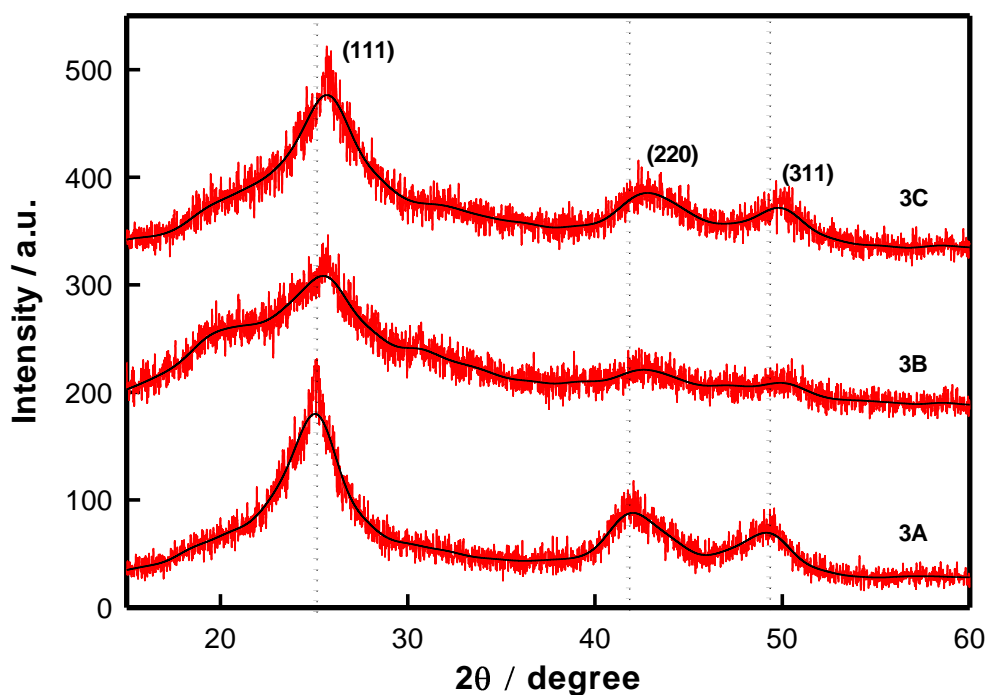


Figure 765: XRD pattern with plain indexed of CdSe core and CdSe/CdS core /shell QDs of third group (3A, 3B and 3C).

7.4 Antifungal Activity of Synthesized QDs

The antifungal properties of synthesized CdSe and CdSe/CdS QDs were tested against *Candida albicans* CAF2-1. MIC is defined as the minimum concentration of drug that inhibits the visible microbial growth [23]. MIC was evaluated for all types of CdSe particles synthesized. A lower MIC corresponds to higher antifungal ability. Comparative analysis of the core-only and core-shell QDs suggested that the CdSe

particles (core-only) were most toxic towards *Candida albicans* CAF2-1. The shell thickness dependent antifungal property was observed to be in the following order, CdSe > CdSe/thicker CdS > CdSe/thinner CdS. Their MIC₈₀ values were 25 µg/mL, 78 µg/mL and 150 µg/mL respectively (Figure 7.7). These results suggest that the core-only QDs in comparison to the core-shells QDs were more toxic to this fungal strain, which may be because of their smaller particle size and higher charge density, that favoured easier penetration of the microbial membrane, and was not only caused by the leaching of heavy (Cd²⁺) metal ions [24]. The difference in inhibition between the core-only and core-shell QDs synthesized could be attributed to their differential diffusion tendency which in turned arise from their differential mobility. It is well established that cadmium ions exhibit broad spectrum biocidal activity against various microorganisms [25]. This justifies the fact that CdSe particles (core-only) show higher antifungal activity compared to its core-shell counterpart.

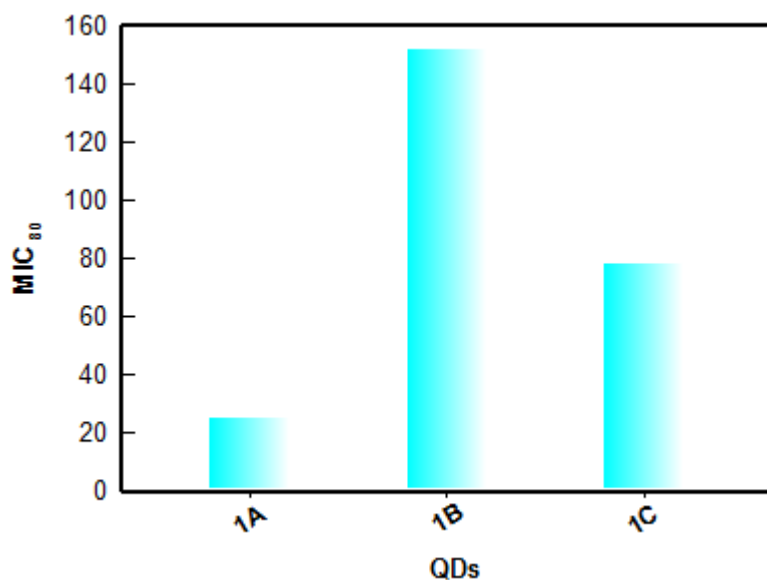


Figure 7.7: Graph showing the MIC₈₀ value of synthesized particles (1a) and (1b and 1c) represents CdSe and CdSe@ CdS core-shell nanocrystals of nearly same core size. For more details see Figure 7.6.

We further analysed the effect of particle size on the antifungal properties. For this, three different size (1A, 2A and 3A) of core-only, three (1B, 2B and 3B) core-thinner shell and three (1C, 2C and 3C) core-thicker shell particles were used. The MIC for all the three series of QDs was determined. Figure 7.8 showed the MIC₈₀ values of the QDs. For the core-shell QDs of different size (1B, 2B and 3B), MIC₈₀ obtained \approx 150 µg/mL. In the case of core-only (CdSe) QDs, the MIC₈₀ values were \approx 25 µg/mL, 33 µg/mL and 38 µg/mL for 1A, 2A and 3A samples, respectively, clearly suggesting the higher toxicity for smaller particles.

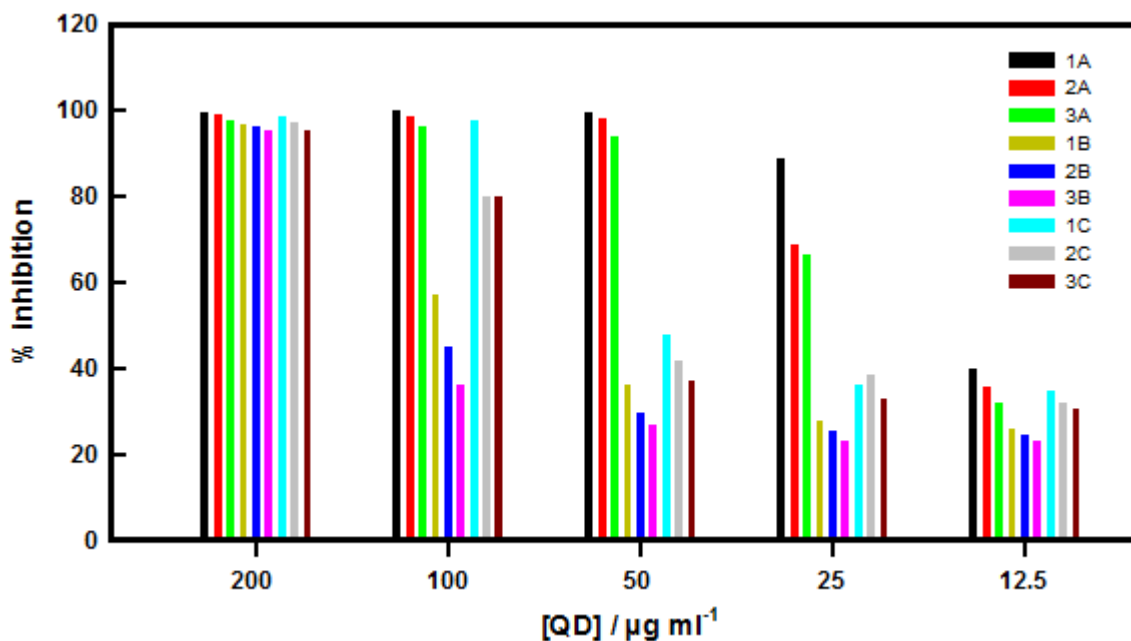


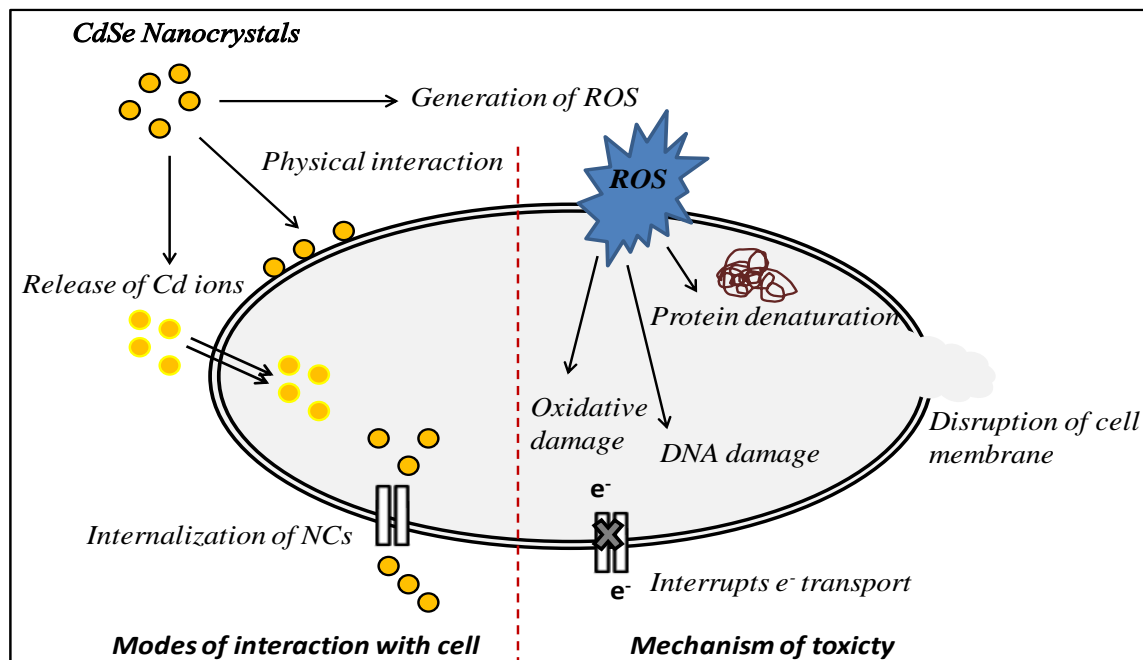
Figure 7.8: Graph showing the inhibition percentage of the different size of CdSe core-only (1a-3a) and CdSe/CdS core-shells (1b-3b and 1c-3c) against *Candida albicans*.

We observed that the antifungal property of the QDs against *Candida albicans* had a size dependent effect, with the smallest size particles being more toxic (1A) compared to others (Figure 7.8). As can be seen in the graph the core-only particles (1A, 2A, 3A) showed high inhibition percentage compared to their core-shell series samples (1B, 2B, 3B). While 1A particles (core-only CdSe of smallest size) showed complete inhibition (100 %) of fungus at a low concentration of 50 µg/mL, for core-shell NCs complete inhibition was found at a much higher concentration of 200 µg/mL. This variation in toxicity was because of the size of QDs and presence of a surface coating that increased the surface (shell) thickness of QDs. Particles of small size easily penetrated the fungal cells, thereby interacting more effectively with the cellular structure that induced possible cell damage.

7.5 Summary

We have successfully synthesized core/shell QDs with much simpler way with no special condition and characterized them. And also systematically and comprehensively probed the impact of core (CdSe) and core-shell (CdSe/CdS) QDs on *Candida albicans*. It was observed that core-shell QDs showed reduced inhabitation compared to core-only QDs. Particle size difference and presence of a shell had significant implications on the antifungal activity of QDs. The observed antifungal activity of CdSe QDs warranted deeper understanding of interaction of these materials with opportunistic fungal cells. Scheme 7.1 depicts an overview of the different pathways that caused toxicity to these

fungi. QDs and their ions (e.g., cadmium and selenium) can produce free radicals which induce oxidative stress (ROS) leading to irreversibly damage to cell constituents (e.g., their membrane, DNA, and mitochondria). This can be the possible mechanism for the fungi cell death.



Scheme 7.1: Schematic overview of the possible ways of cellular interaction of QDs and the different toxicity pathways by CdSe QDs against *Candida albicans*.

7.6 References

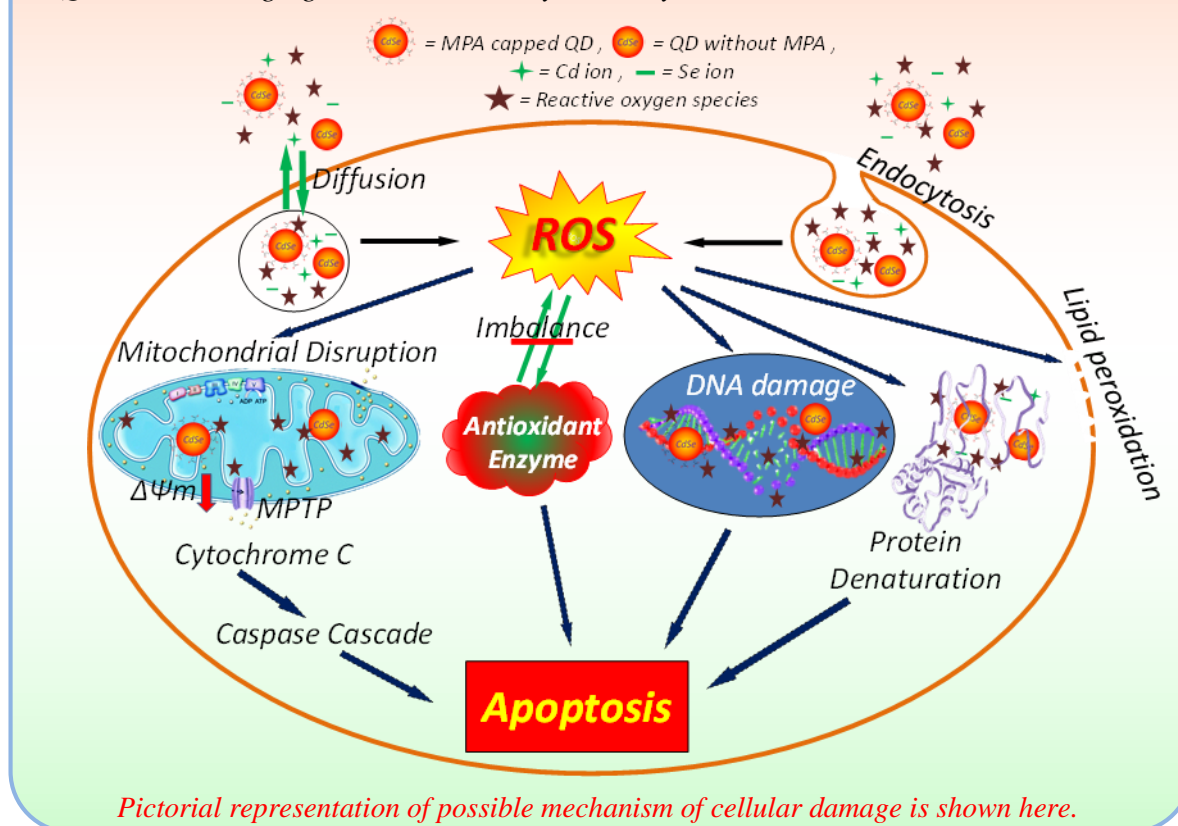
- [1] A. M. Smith, X. Gao, S. Nie, *Photochemistry and Photobiology* **2004**, *80*, 377.
- [2] W. C. W. Chan, S. M. Nie, *Science* **1998**, *281*, 2016.
- [3] M. Bruchez, M. Moronne, P. Gin, S. Weiss, A. P. Alivisatos, *Science* **1998**, *281*, 2013.
- [4] T. M. Jovin, *Nat. Biotechnol.* **2003**, *21*, 32.
- [5] A. Tyagi, K. Rawat, A. K. Verma, H. B. Bohidar, *Analytical Methods* **2016**, *8*, 1060.
- [6] S. Sanwlani, K. Rawat, M. Pal, H. B. Bohidar, A. K. Verma, *J. Nanopart. Res.* **2014**, *16*, 2382.
- [7] S. J. Cho, D. Maysinger, M. Jain, B. Röder, S. Hackbarth, F.M. Winnik, *Langmuir* **2007**, *23*, 1974.

- [8] B. I. Ipe, M. Lehnig, C. M. Niemeyer, *Small* **2005**, *1*, 706.
- [9] M. Green, E. Howman, *Chemical Communications*. **2005**, 121.
- [10] J. Ma, J. Y. Chen, J. Guo, C. C. Wang, W. L. Yang, L. Xu, P. N. Wang, *Nanotechnology*, **2006**, *17*, 2083.
- [11] J. Lovric, S. J. Cho, F. M. Winnik, D. Maysinger, *Chem. Biol.* **2005**, *12*, 1227.
- [12] W. W. Yu, X. G. Peng, *Angew. Chem. Int. Ed.* **2002**, *41*, 2368.
- [13] L. Liu, X. Guo, Y. Li, X. Zhong, *Inorg. Chem.* **2010**, *49*, 3768.
- [14] A. M. Derfus, W. C. W. Chan, S. N. Bhatia, *NanoLett.* **2004**, *4*, 11.
- [15] W.A. Hild, M. Breunig, A. Goepferich, *European Journal of Pharmaceutics and Biopharmaceutics* **2008**, *68*, 153.
- [16] C. Kirchner, T. Liedl, S. Kudera, T. Pellegrino, A. Muñoz Javier, H.E. Gaub, S. Stölzle, N. Fertig, W.J. Parak, *Nano letters* **2005**, *5*, 331.
- [17] M. J. Clift, B. Rothen-Rutishauser, D. M. Brown, R. Duffin, K. Donaldson, L. Proudfoot, K. Guy, V. Stone, *Toxicology and applied pharmacology*, **2008**, *232*, 418.
- [18] T. Sibanda, A. I. Okoh, *African Journal of Biotechnology* **2007**, *6*, 2886.
- [19] T. Ahmad, I. A. Wani, N. Manzoor, J. Ahmed, A. M. Asiri, *Colloids Surf B Biointerfaces* **2013**, *107*, 227.
- [20] J. A. Lemire, J. J. Harrison, R. J. Turner, *Nat Rev Microbiol.* **2013**, *11*, 371.
- [21] M. Gnanadesigan, M. Anand, S. Ravikumar, M. Maruthupandy, M.S. Ali, V. Vijayakumar, A. K. Kumaraguru, *Appl Nanosci.* **2012**, *2*, 143.
- [22] H. Ohshima, *Adv. Colloid Interface Sci.* **1995**, *62*, 189.
- [23] L. Qi, Z. Xu, X. Jiang, C. Hu, X. Zou, *Carbohydr. Res.* **2004**, *339*, 2693.
- [24] J.R. Morones J. L. Elechiguerra, A. Camacho, K. Holt, J. B. Kouri, J. T. Ramirez, M. J. Yacaman, *Nanotechnology* **2005**, *16*, 2346.
- [25] J. A. Kloepper, R. E. Mielke, J. L. Nadeau, *Appl. Environ. Microb.* **2005**, *71*, 2548.
-

Chapter 8

Size Variational Cellular Uptake and Cytotoxicity of Quantum Dots

Abstract: This chapter presents a detail study of size and shell thickness dependent fluorescence behaviour of hydrophilic CdSe (core-only) and CdSe/CdS (core/shell) QDs in cell imaging as well as their cytotoxicity mechanism.



8.1 Introduction

Quantum dots (QDs) are nanoparticles with remarkable photochemical and photo-physical properties. The huge interest in QDs research owes its origin to the size dependent optical and electronic properties arising from quantum confinement effects [1,2]. Semiconductor QDs are more fluorescent in terms of brightness and stability against photo-bleaching compared to organic dyes and fluorescent proteins [3]. Recent progress in QDs synthesis and bio-conjugation has opened up a whole new area of nanobio-activity dedicated to QDs, and this can be facilitated by the possibility of rendering the QDs water soluble, and therefore amenable to bio-conjugation [4,5]. Regardless, their

biological application have not been explored extensively largely because of problems associated with their surface chemistry. Nonetheless, these materials have come of age in the past decade, due to remarkable surface modification in the bio-conjugation protocols [6].

Any biological application of a nanomaterial requires a prior screening of its cellular uptake and cytotoxicity profile. These two signature parameters are indeed dependent on nanoparticle size and surface morphology. Derfus et al [7] have shown that cytotoxicity of CdSe nanocrystal was conditioned by the processing parameter during synthesis. This toxicity arose from the leaching of Cd²⁺ ions from the CdSe lattice over a period of time. Su et al [8] have evaluated the cytotoxicity of multi-layer core shell QDs and shown that CdTe QDs were highly toxic to K562 and HEK293T cell lines due to the leaching of cadmium ions. The core shell structures were relatively more bio-compatible [9]. Delivery of these QDs from the circulation to the target cells is an important step that involves cellular uptake, receptor trafficking and intracellular delivery. Hild et al have described the ideal features that a nanoparticle must possess for biological applications and cellular imaging [10]. Cytotoxicity of CdSe and ZnS QDs with different surface modifications coating such as 3-mercaptopropionic acid (MPA), silanization and polymer was extensively evaluated by Kirchner et al [11]. These studies suggested that nanoparticle aggregation in addition to the release of Cd²⁺ ions played a key role for cytotoxic effects. Chan et al [12] have shown that CdSe core QDs induced apoptotic biochemical changes, loss of mitochondrial membrane-potential and release of Cytochrome-C in the IMR-32 human neuroblastoma cell lines. However, these biochemical changes were not seen when the QDs were surface coated with ZnS. The size dependent activation of autophagy caused by QDs was studied by Sleverstov et al [13]. The effect of surface chemistry and particles size on the cellular and cytotoxicity in a murine macrophage cell lines was extensively studied by Cliff et al [14].

Fluorescent proteins and organic fluorophores are comprehensively used in many bioimaging and biosensing investigations. Nonetheless, traditional fluorophores such as organic dyes and fluorescent proteins suffer from several intrinsic problems including rapid photobleaching, spectral cross-talking, narrow excitation profiles, and limited brightness/signal intensity. In contrast, QDs possess the novel optical properties which have overcome many of the problems and offer new applications which are either difficult or impossible with traditional fluorophores. For instance, because of their extraordinary properties i.e. broad excitation profiles and narrow/symmetric emission

spectra, high-quality QDs are well suited for multiplexed tagging or encoding, in which multiple colours and intensities are combined to encode thousands of genes, proteins, or small-molecule compounds ^[15].

QDs can be used to specifically and effectively label molecular targets at the subcellular level ^[16]. In many studies, bio-functionized QDs which was encapsulated within a polymer-shell with molecules (streptavidin and immunoglobulin) were used and applied to target cell surface receptor, cytoskeletal components (actin and microtubules) and nuclear antigen (in both fixed and living cells). Two different colours of QDs (630 nm and 535 nm) were used simultaneously and found QDs were substantially photostable. However, toxicity is the limiting factor for their broad range of application ^[17-19]. In brief, QDs toxicity may depend on different factors that are composition, the chemistry of the capping material, and their size. However, along with an ever-increasing number of reports on QDs toxicity ^[20-24], there is widespread research intended at obtaining nontoxic and safe QDs ^[25-27], which can be safely used for various biomedical applications. Mainly, two reasons suggest that bare core QDs use is impractical Firstly, the crystalline structure of the nanoparticle lends itself to imperfections ^[28], which effects in emission irregularities, mainly blinking, in which single QDs switch between fluorescent and non-fluorescent states despite continuous illumination ^[29]. Secondly, the cores, due to their large surface area: volume ratio, are highly reactive ^[15] resulting in a very unstable structure and prone to photochemical degradation.

Desorption of free Cd (QD core degradation) ^[30,31], free radical formation, and interaction of QDs with intracellular components are some responsible mechanism for QDs cytotoxicity. Studies observed QD toxicity in a hepatocyte culture model which revealed that exposure of core CdSe to an oxidative environment causes decomposition and desorption of Cd ions. Such exposure during synthesis and processing played an important role in subsequent toxicity. Reduction of oxidation can be achieved by the addition of a different shell ^[32]. Free radicals production, is an important factor which is found to contribute to toxicity ^[33-35]. Studies observed that, CdSe core QDs induced apoptosis in neuroblastoma cells through the activation of a number of apoptotic pathways, and down regulation of survival signalling molecules ^[36].

Other factors are, the composition of the core, and the colour of the QD (a reflection of core size) which are found to influence toxicity ^[33]. Previous studies reported that addition of a shell results the free radical generation reduction. Oxidation of the nanoparticle surface, induced by exposure to air before solubilisation or catalysed by UV

light can cause oxidation of selenium and/or sulphur and expose-free cadmium [37]. Coatings add the additional layer which not only act as a physical barrier to the core but also preventing access therefore have been found to reduce cytotoxicity, with different coatings having varying levels of passivation [38].

Increase stability and performance has been achieved with capping core QDs, by producing QDs with improved luminescence, higher photochemical stability and higher quantum yields at room temperature [39,40]. Though, QD synthesis can be tailored to specific requirements, with core, shell and coating characteristics all affecting photochemical properties. Choice of shell and coating are the two aspects which are important to be considered while producing, as the shell stabilises the nanocrystal and to some extent alters the photophysical properties.

In this work we used two different size QDs which were CdSe core QDs and CdSe/CdS core/shell QDs for investigating their size dependent cellular uptake and cytotoxicity.

8.2 Sample Preparation

8.2.1 Synthesis of CdSe QDs

The synthesis of these QDs is discussed in Chapter 2 which follows a kinetic growth process. Reaction temperature was 300 °C for synthesizing CdSe QDs and time interval for synthesis was kept 240 seconds. By this we could successfully prepare CdSe QDs.

8.2.2 Synthesis of CdSe/CdS Core /Shell QDs

The protocol for the synthesis CdSe/CdS core/shell nanostructures was already discussed in synthesis sections of Chapter 1 and 2. Reaction temperature was 300 °C for synthesizing core CdSe QDs and time interval for synthesis was kept 240 seconds. Then after shell structure was grown on it. After synthesis, washing with extraction were done prior to their characterization.

8.3 Physical Characterization

The physical size of these core CdSe and CdSe/CdS core/shell were measured from the TEM and DLS (Figures 8.1 and 8.2). While DLS and TEM directly yielded the values for mean particle size. Crystalline phase, surface charge and optical properties were also measured.

8.3.1 Structural Characterization

The DLS method produced higher size due to the hydration mediated clustering of the QDs but gave the information of uniformity exactly. Single and narrow size distribution

correspond to uniform sized QDs. The size derived from the TEM reflected the true physical dimensions of the QDs.

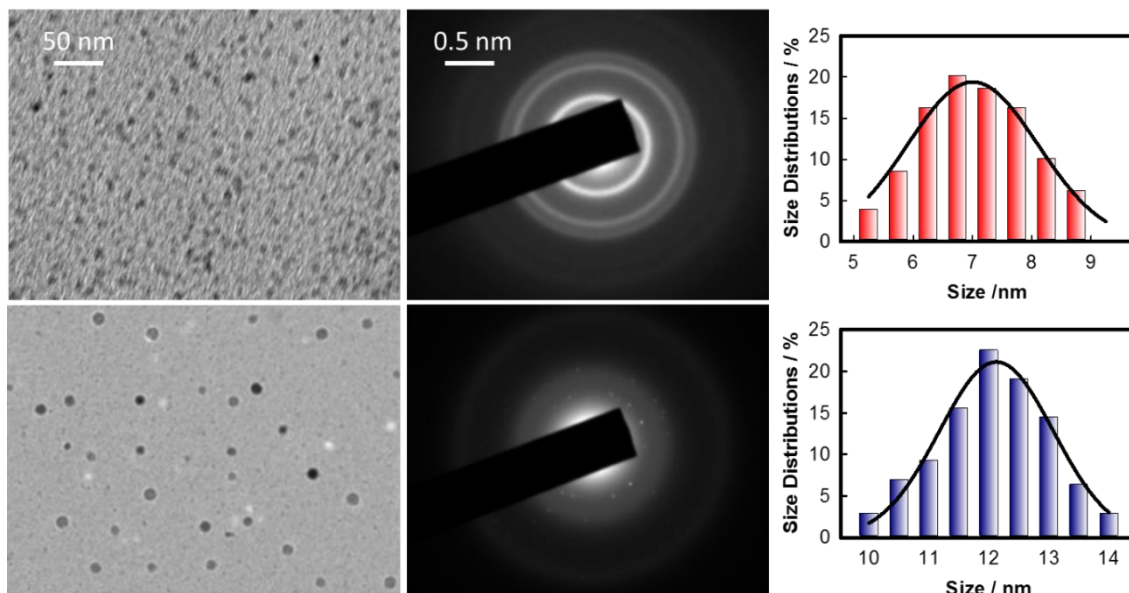


Figure 8.1: TEM images of synthesized core CdSe and Core/shell CdSe/CdS QDs.

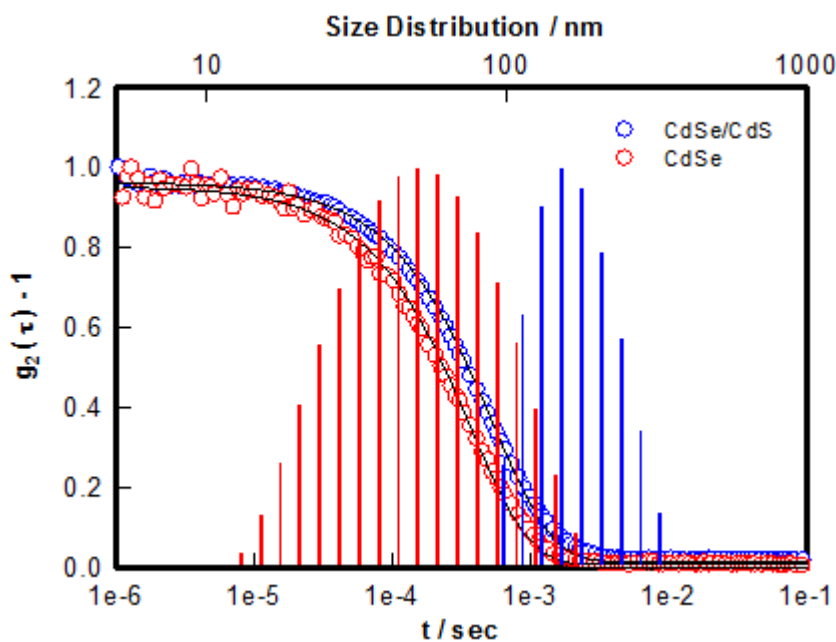


Figure 8.2: Time autocorrelation function, size distribution of hydrodynamic size of core CdSe [(51±5) nm] and Core/shell CdSe/CdS core/shell [(60±7) nm] QDs.

8.3.2 Surface Charge

Aqueous dispersions of the colloidal QDs were subjected to electrophoresis studies to evaluate their zeta potentials. We found that the core-shell QDs had a zeta potential that was about 35% more than that of the core-only structures (Table 8.1). A more relevant parameter is the surface charge density which was estimated to be 0.9 mV/nm² for CdSe and 0.4 mV/nm² for CdSe/CdS particles. Thus, the core-only QDs were associated with

higher charge density, and thus electrostatically more active. The zeta potential histograms are shown in Figure 8.3. The average surface charge of these QDs (Figure 8.3) are tabulated in Table 8.1.

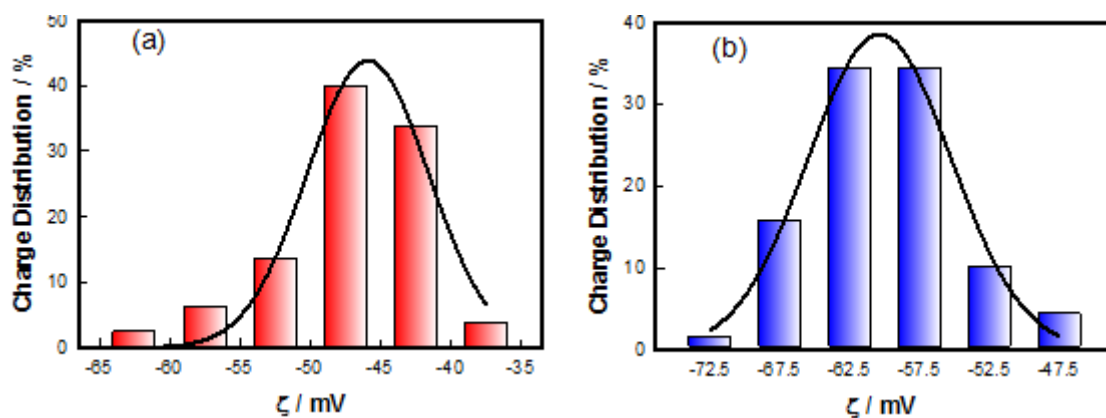


Figure 8.3: Zeta potential of (a) CdSe (-45 ± 4) mV and (b) CdSe/CdS core/shell (-60 ± 5) mV QDs.

8.3.3 Crystalline Structure

The morphology and crystallite size of CdSe and CdSe/CdS QDs were evaluated from the X-ray diffraction data collected in the 2θ range of 20 - 60° . The X-Ray diffractograms are shown in Figure 8.4 and are indexed based on the cubic system. The interplanar spacings determined from the prominent peaks in diffractograms corresponded to reflections arising from (111), (220) and (311) planes of CdSe QDs are consistent with JCPDS Card No. 32-0483). Thus, QDs had face centered cubic (FCC) structure with the

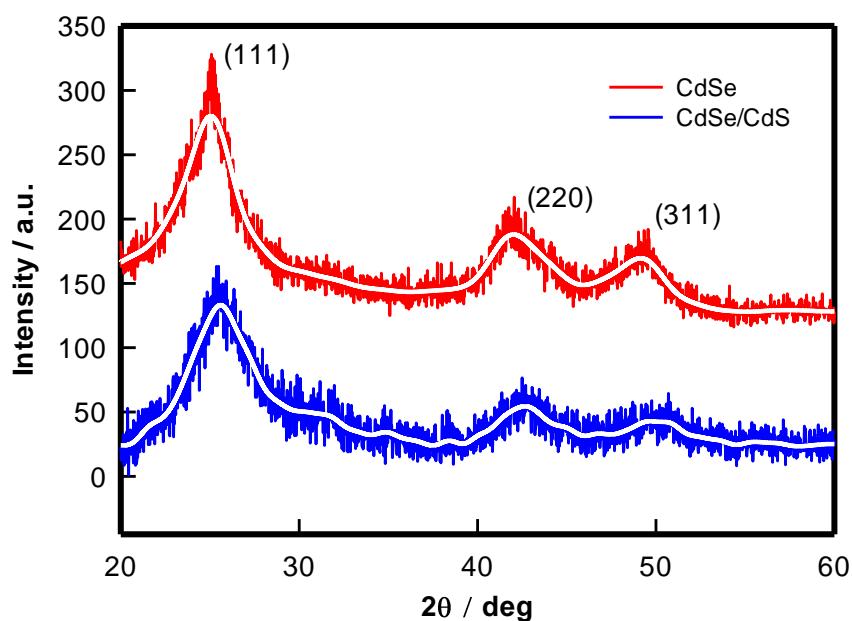


Figure 8.4: XRD pattern with plain indexed of CdSe core and CdSe/CdS core /shell QDs.

interplanar d-spacing determined from the (111) reflection peak was 3.54, 3.48 and 3.50 Å for CdSe and CdSe/CdS QDs, respectively. The broadness of the peaks correspond to nanocrystalline size. Core structure with shell showed peak shifting that is due to CdS shelling structure and peak broadening also due to lattice mismatch of CdSe core & CdS shell. Increasing the shell thickness enhanced crystallinity of CdS hence the peak of thicker shell XRD was less broad than that of thinner shell XRD.

Table 8.1: Different parameters calculated from XRD data for CdSe and CdSe/CdS QDs.

Sample	Planes (hkl)	2θ ($^\circ$)	FWHM ($^\circ$)	Relative Intensity	d-spacing (Å)	Lattice vector a(Å)	Lattice Strain	Crystallite size (nm)
CdSe	(111)	25.2	2.83	0.579	3.54	6.13	0.0553	3.01
	(220)	42.1	3.00	0.253	2.15	6.08	0.0340	2.96
	(311)	49.4	2.75	0.154	1.84	6.10	0.0261	3.32
CdSe / CdS	(111)	25.3	3.86	0.996	3.52	6.10	0.0751	2.20
	(220)	42.3	3.04	0.404	2.14	6.05	0.0343	2.93
	(311)	49.7	3.00	0.320	1.83	6.07	0.0283	3.05

8.3.4 Optical Characterization

Absorbance was measured for both the QDs which showed sharp peak at 505 ± 5 nm. The effect of shell on absorption peaks were not significant (Figure 8.5 a). One of the main objectives was to make the CdSe QDs fluorescent by cladding it with CdS. Fluorescence emission was measured by exciting both the sample at 470 nm.

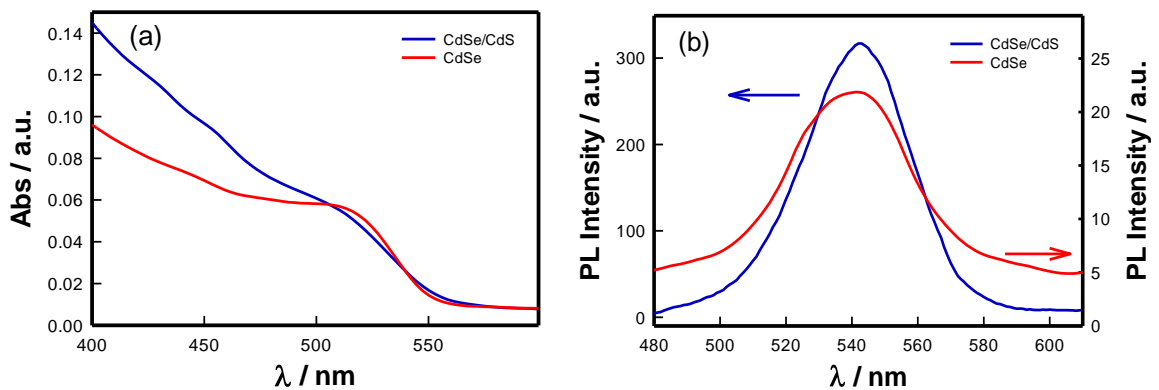


Figure 8.5: (a) UV-vis and (b) fluorescence emission spectra of CdSe and CdSe@CdS core-shell QDs (excitation wavelength ≈ 470 nm).

The fluorescence emission peaks for core/shell QDs were much higher than bare QDs. The fluorescence peak wavelengths are also not so much different by shelling the QDs and that was confirmed by the emission spectra (Figure 8.5 b). The presence of CdS cladding was definitely responsible for enhancing fluorescence of the core CdSe nanoparticles.

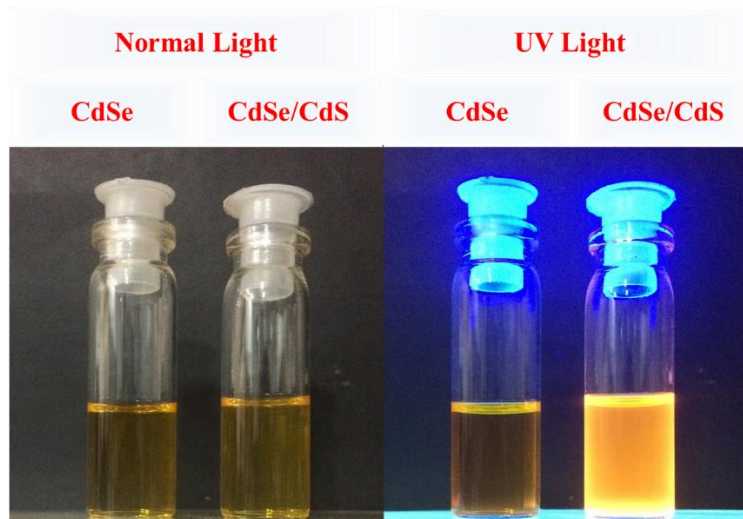


Figure 8.6: CdSe QDs and CdSe@CdS core-shell QDs under bright light and UV illumination.

Table 8.2: Physical characteristics of the QDs used in this study measured at room temperature.

Sample IDs	Absorbance (λ_{ab})/nm	Emission (λ_{em})/ nm	Size/ nm		Average crystallite size/nm	Zeta potential/ mV
			TEM	DLS		
CdSe	505	548	7 \pm 1	51 \pm 5	3.10 \pm 0.5	-45 \pm 4
CdSe/CdS	500	542	12 \pm 1	60 \pm 7	2.70 \pm 0.5	-60 \pm 5

8.4 Cytotoxicity Analysis for Biocompatibility Screening

The MTT assay is one of the most simple, fast, relatively cheaper methods for screening cell viability. The viability of all studied cells (MCF-7, HEK-293 and HeLa) decreased as a function of time and dose for both CdSe and CdSe/CdS QDs, but the cytotoxicity rate was higher for CdSe treated cells as compared to CdSe/CdS treated cells. Meanwhile the cancerous cell lines (MCF-7 and HeLa) treated with CdSe showed ~85-90% cytotoxicity at a dose of 12 pM, but for HEK-293 cells it was ~70 %, whereas in CdSe/CdS treated cells cytotoxicity rate was ~75, 70 and 55 % in MCF-7, HeLa and HEK-293 cells, respectively (Figure 8.7).

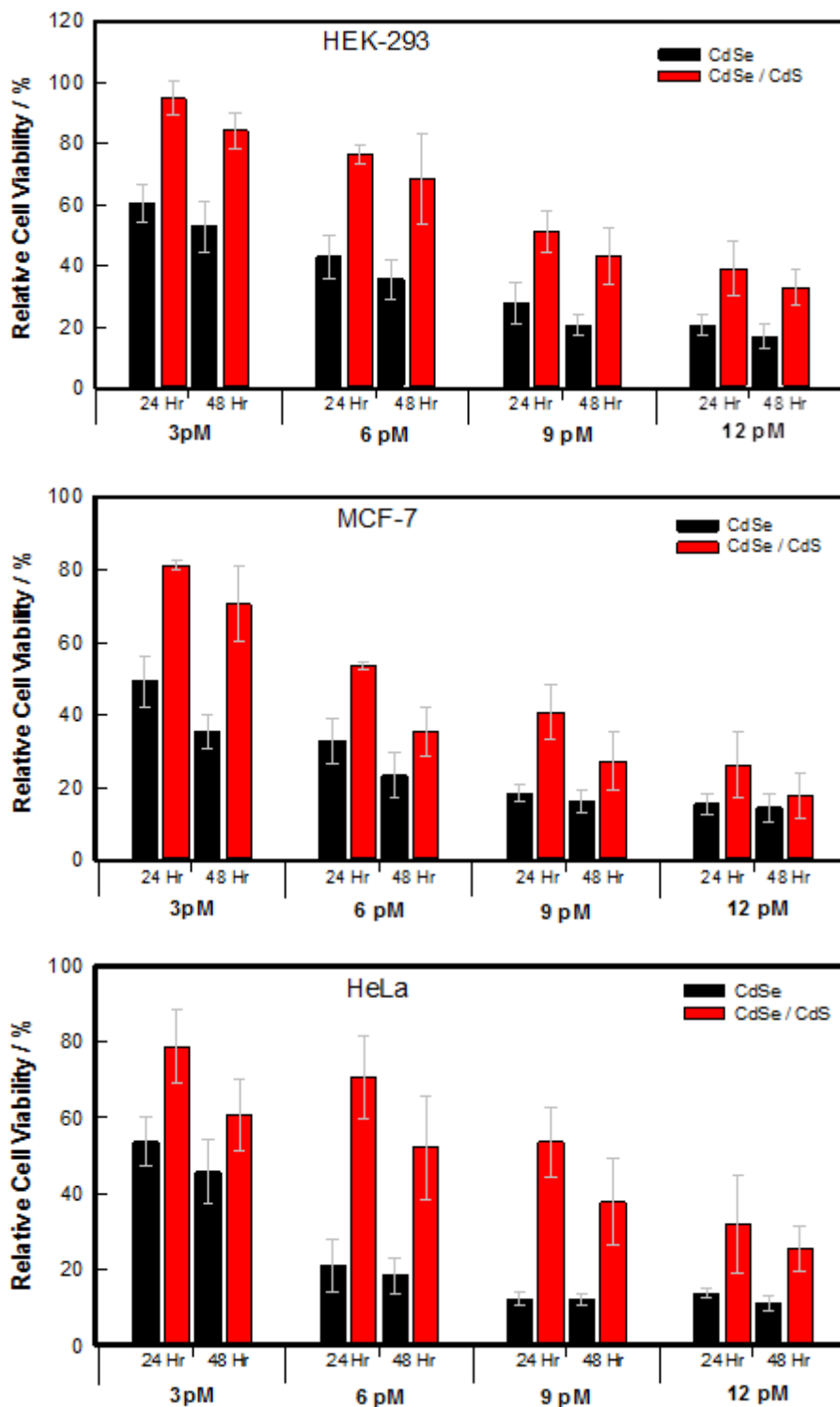


Figure 8.7: Comparative cell viability of CdSe and CdSe/CdS nanoparticles on human kidney embryo (HEK-293, a), Human breast cancer (MCF-7, b), and human epitheloid cervix carcinoma (HeLa, c) at 24 and 48 assessed by MTT assay.

It was evident that the cytotoxicity in the case of both CdSe and CdSe/CdS QDs was more in cancerous cells compared to normal cell lines. Due to large membrane pore size, cancerous cells uptake more nanoparticles that may be the caused the observed cytotoxicity. We have tested the efficacy of these nanoparticles in p53 HeLa, and p53

mutated breast cancer cell line MCF-7 which clearly yielded differential results. The LC_{50} value of CdSe nanoparticles in MCF-7 and HeLa was 3.09 and 2.79 μM respectively, which were enhanced to 7.17 and 9.15 μM in CdSe/CdS treated cells. In normal cells (HEK-293) LC_{50} of CdSe/CdS nanoparticles was 10.02 μM , which was significantly higher than the same for CdSe treated cells (4.5 μM). It indicated that surface modification reduced the toxicity of CdSe QDs. The aforesaid observations demand wider investigation to understand the pathway of cell death.

8.5 QDs induced Reactive Oxygen Species (ROS) Production

DCF (Dichlorofluorescein) fluorescence intensity, an indicator of oxidative stress (OS) was measured in the cells after 24-h treatment of CdSe and CdSe/CdS QDs. Reactive oxygen species level of CdSe treated cells was higher as compared to CdSe/CdS QDs treated cells at same concentration (Figure 8.8). The fluorescence intensity of DCF positive cells increased significantly in a dose dependent manner of CdSe QDs, whereas for the cells treated with CdSe/CdS QDs, the DCF intensity did not enhance significantly. These results indicate that surface coating of CdS reduced the release of free radicals, which may be the reason for lower oxidative stress in CdSe/CdS QDs treated cells.

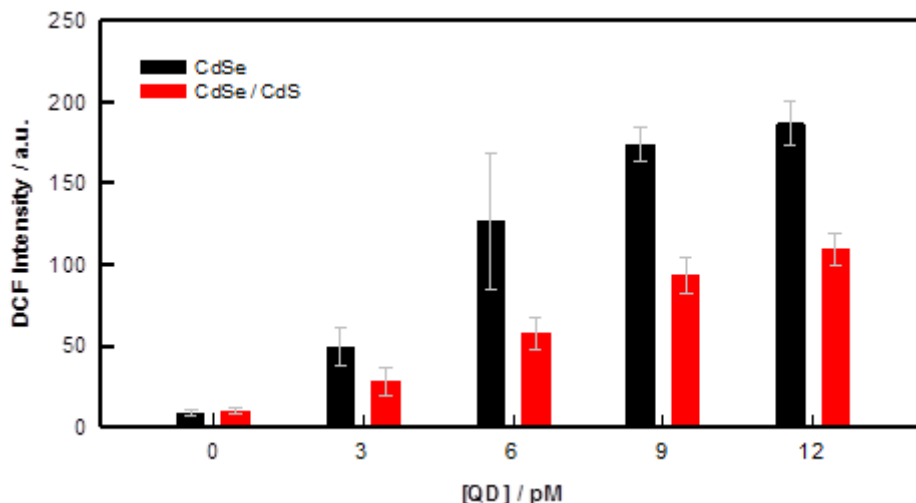


Figure 8.8: ROS level in the HeLa cells after 12-h exposure to QDs at different concentrations measured by DCFDA staining.

Detection of free radicals by EPR

Despite of the size and surface charge, free radicals generated by nanomaterials is also the prominent reason for cytotoxicity. The direct detection of free radicals was done by EPR spectroscopy using 5, 5 –Dimethyl-1-pyrroline N-oxide (DMPO) spin trap. Relative generation of free radicals inside the cells can be quantified by comparing peak intensity

in treated cells with that in untreated one i.e. control. As shown in EPR spectra (Figure 8.9), the intensity of peaks for CdSe treated cells was higher than that of CdSe/CdS treated cells that confirmed the greater amount of generation of free radicals in CdSe treated cells. The prominent peak in all three spectra with g value 2.006 is corresponds to the DMPO-OH adduct.

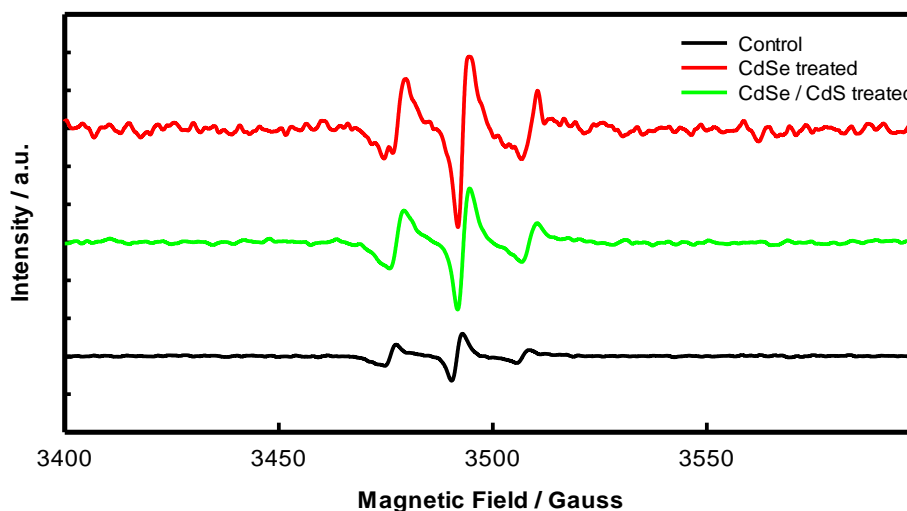


Figure 8.9: EPR spectrum of HeLa cells after exposure of 12 pM QDs.

8.6 QDs induced Apoptosis Mechanism

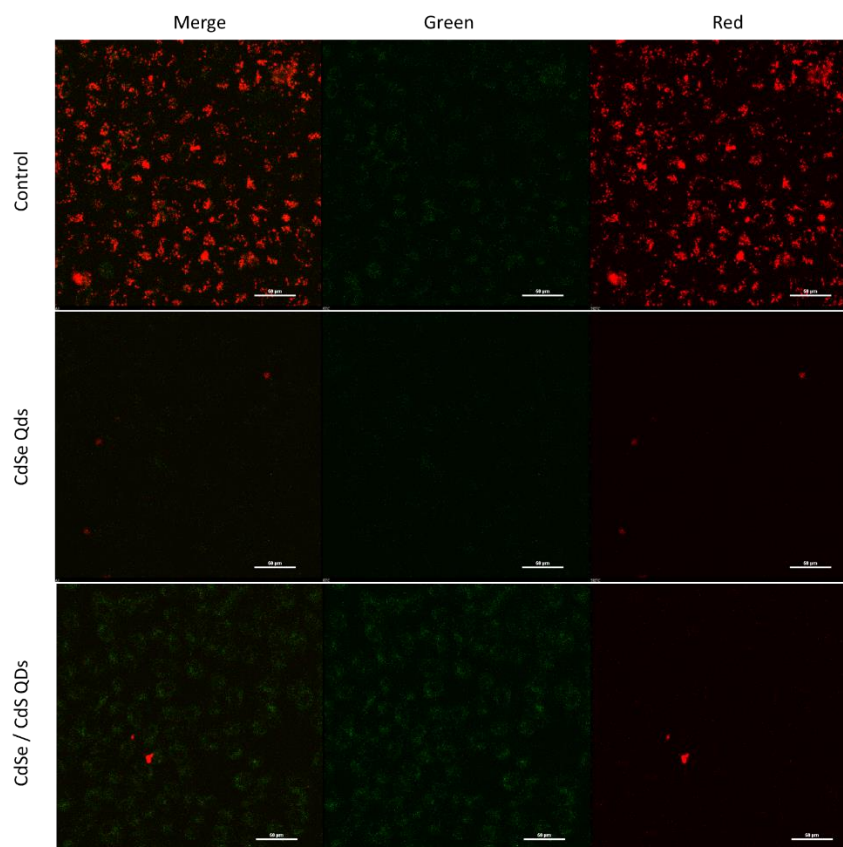


Figure 8.10: Mitochondrial membrane depolarization of HeLa cells exposed to 12 pM QDs for 12 h measured by JC-1 staining.

Since reactive oxygen species (ROS) regulates mitochondrial permeability and also has dominating role in initiating apoptosis, to find out the role of ROS in mitochondrial mediated apoptosis pathway, one should have to measure the mitochondrial membrane potential ($\Delta\Psi_m$) and we also have done it. The results from (Figure 8.10) showed the decrease in percentage of $\Delta\Psi_m$ from 100% (control) to 55% and 35% at 12pM of CdSe and CdSe/CdS QDs respectively. These results suggest that mitochondrial pathway was possibly playing a significant role in regulating induced apoptosis caused by these QDs but the intensity of damage was more in core-only as compared to core-shell QDs.

In this study, both core-only and core-shell QDs increased ROS production in HeLa cells in a dose-dependent manner. To investigate that these QDs can trigger intrinsic apoptotic cascade, we examined the expression of p53, Bax, Bcl-2 and caspase-3 proteins in the treated cells as well as in control using Western blot analysis.

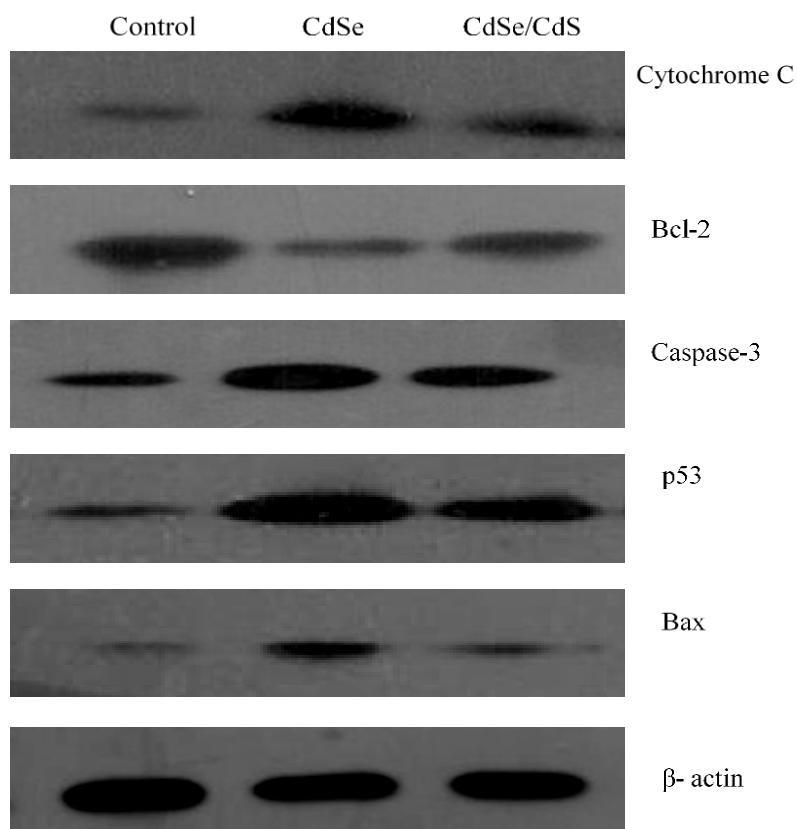


Figure 8.11: Changes in the expression of apoptosis regulatory proteins in response to treatment with 12pM CdSe and CdSe/CdS QDs in HeLa cells after 12h exposure.

The results demonstrated that expression of pro-apoptotic markers like p53, Bax and caspase-3 was significantly elevated in CdSe and CdSe/CdS QDs treated cells while Bcl-2 decreased in both QDs treated cells (Figure 8.11 & 8.12). Meanwhile the release of Cytochrome-C was found more in Core-only as compared to Core-shell QDs treated cells.

The intensity of alteration was more in CdSe treated cells in comparison to CdSe/CdS QDs treated cells.

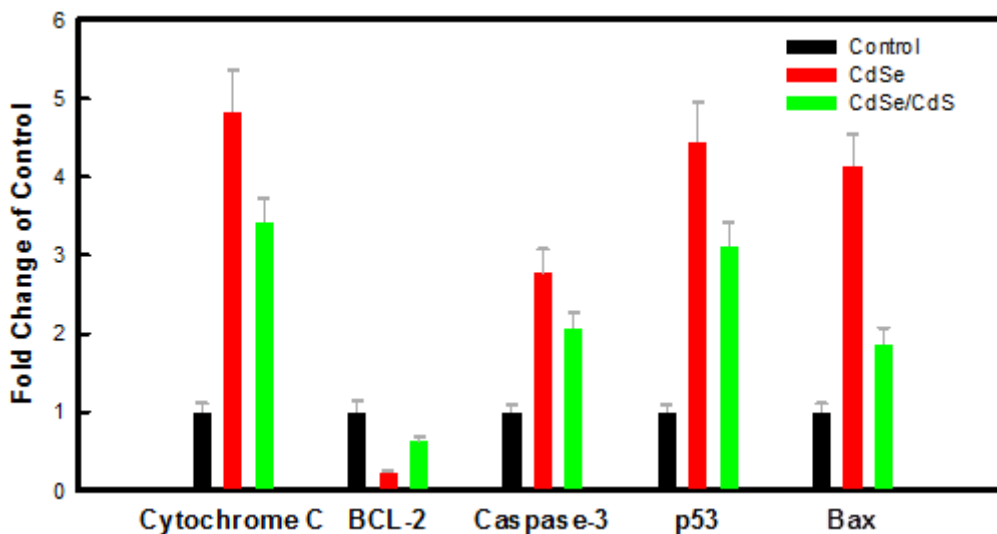


Figure 8.11: Bar diagram represents the mean change in band intensity (protein level / β -actin value normalized with untreated control).

These results suggesting that both QDs induces apoptosis through intrinsic pathway. CdSe and CdSe/CdS both increased apoptotic cell population in a dose dependent manner. There was significant increase in apoptosis rate in CdSe treated groups as compared to control group (Figure 8.13). The cells treated with lower concentration of CdSe/CdS did not show any significant change in apoptosis with respect to control groups, but higher concentration of CdSe/CdS caused significant increase in cell apoptosis in dose dependent manner.

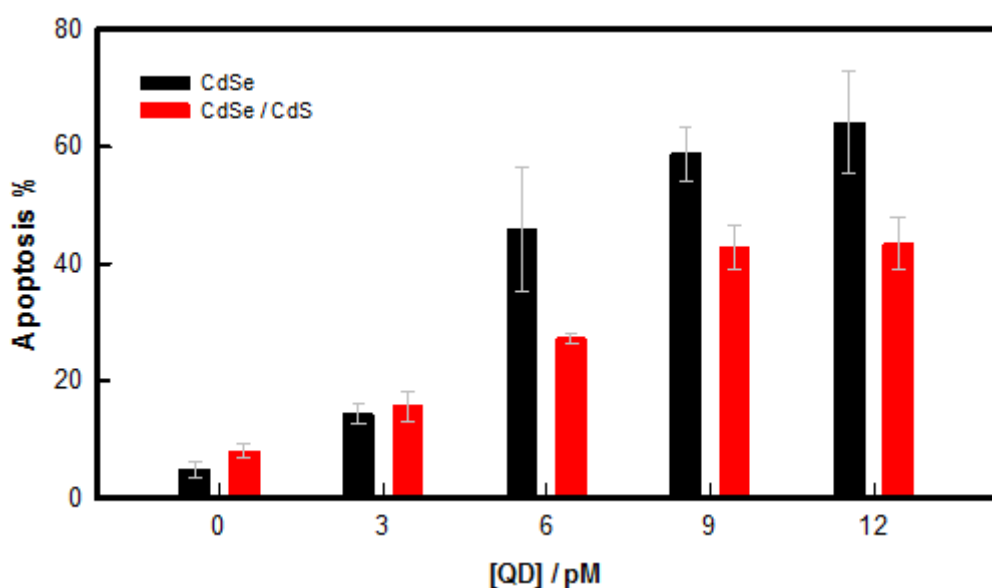


Figure 8.13: Apoptosis percentage of HeLa cells after 12h exposure to different NCs (with and without CdS coating) at different concentrations.

Excessive generation of ROS is the main reason for apoptosis. In this study, we found more ROS production in cells treated with CdSe QDs as compared to CdSe/CdS treated cells. Surface coating is one of the possible reasons for lesser ROS generation in CdSe/CdS treated cells as size, crystal structure, and surface coatings influence cellular uptake and cytotoxicity of a given nanoparticle. ROS generated by nanoparticles favours pore formation in mitochondria, mitochondrial permeability transition (MPT) that induces further ROS formation which result in impairing of mitochondrial function [41].

In this section, the caspase-3 was found to be increased when the cells were treated with CdSe QDs. This data clearly signifies that QDs induces apoptosis in HeLa cells through mitochondrial dysfunction and caspase-3 mediated pathway. In similar study, the CdSe core nanocrystal was found to induce apoptotic biochemical changes, loss of mitochondrial membrane-potential and release of Cytochrome-C in IMR-32 human neuroblastoma cell lines [12].

8.7 Effect of QDs Treatment to Cells on Cellular Morphology

In this work, morphological changes were observed by using phase contrast microscope and significant dose dependent morphological changes were observed which was similar to apoptotic cell structure (Figure 8.14). Cells were found to show apoptosis features i.e cell shrinkage in CdSe treated groups. CdSe QDs were found to induce apoptosis in cells whereas CdSe/CdS did not induce any significant change in the cell integrity when treated with identical dose. The characteristic features of apoptosis like cell shrinkage, babbings and size alteration was found. However changes were more significant in CdSe QDs treated cells as compared to CdSe/CdS QDs at similar doses.

The ultra-structural results show that control cells were large and round, with intact nuclear membrane and low density of nuclear chromatin. However, the cells treated with CdSe QDs exhibited characteristics of apoptosis including shrinkage of cell membrane, vacuolization in mitochondria, condensation and fragmentation of nuclear chromatin adjacent to the nuclear membrane, whereas the cells treated with CdSe/CdS showed no significant alteration. These results show that CdSe/CdS caused no significant damage, whereas CdSe QDs induced cell apoptosis. It indicated that coating of CdS shell on core CdSe reduced the release of free radical, which may have caused cytotoxicity (Figure 8.15). TEM (Figure 8.15) was used to study ultra-structural changes in cells.

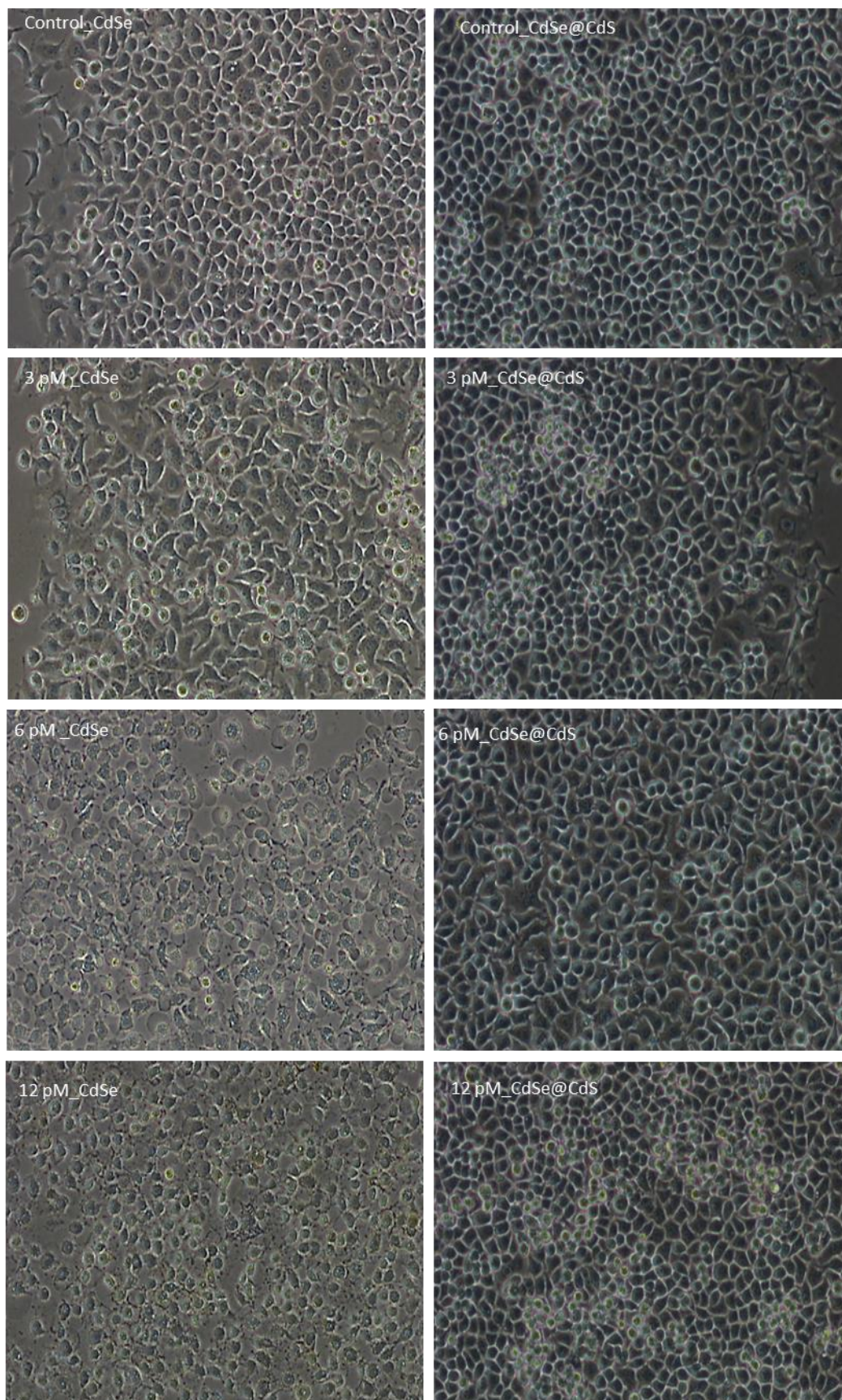


Figure 8.14: Morphological changes in HeLa cell after treatment with QDs. Growth of HeLa cells without and with treatment of different dose of CdSe and CdSe/CdS QDs, for 12 h are shown.

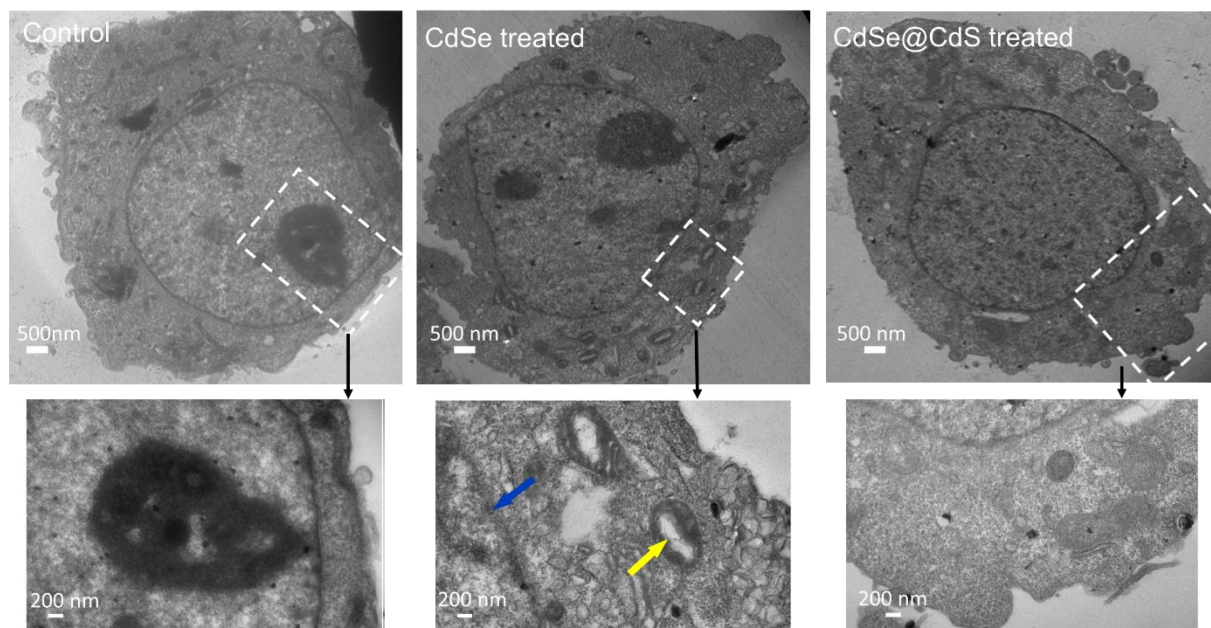


Figure 8.15: TEM images of HeLa cells exposed to different QDs (with and without CdS coating) for 24 h. Control HeLa cells without treatment, HeLa cells treated with 6 pM CdSe, and HeLa cells treated with 6 pM CdSe/CdS are shown. Blue arrow shows deterioration of nuclear membrane due to particle-interaction. Yellow arrow indicates vacuolization in mitochondria.

8.8 Cellular Uptake

Confocal laser microscopy is a widely used technique for high resolution imaging of cells. Fluorescent CdSe quantum dots are ideal probes for imaging of cells. Remarkably, we noticed that fluorescent CdSe QDs were internalized by HeLa and HEK-293 cells, and were also adsorbed onto the cell membrane, but the fluorescence intensity was low at only 2 times of the control. When these specific cells were treated with the same concentration (12 pM) of CdSe/CdS QDs the fluorescence intensity increased by ≈ 4 times.

No fluorescence was noticed in the control samples when the cells were treated with CdSe/CdS and CdSe (12 pM) which appeared blue and green under UV and blue excitation, respectively (Figures 8.16 and 8.17). This clearly implied the cellular internalization of these QDs. At higher dosage of CdSe QDs, cell membranes were found to be ruptured due generation of reactive oxygen species. The comparative imaging revealed distinctive features of normal cell lines HEK-293 and cancerous cell lines (HeLa). It was clearly observed that the adsorption of CdSe/CdS (and CdSe) was higher in HeLa cells compared to HEK-293 cells treated with same dosage of QDs (Figures 8.16 and 8.17).

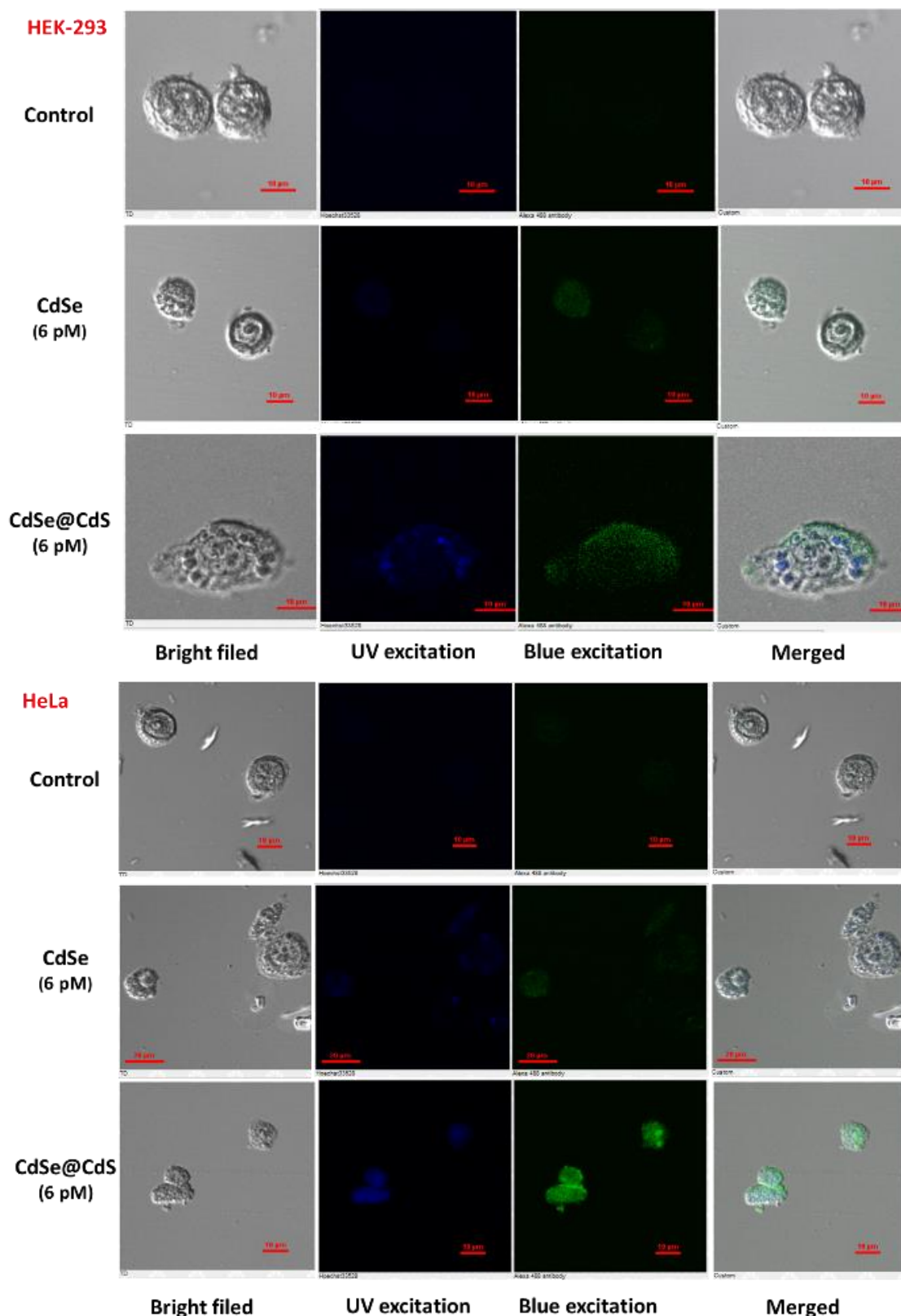


Figure 8.16: Localization of QDs in the HEK- 293 and MCF-7 cells. In all three panels, the left side column represents the phase contrast image, while the central left column represents the fluorescence image by UV light excitation and the central right column represents the fluorescence image by blue light excitation. The right column is an overlay of all columns. In all cases, QDs which are more localized inside the cells, reveal finer structures.

This difference in internalization between cancer and normal cell lines could be assigned to different degree of cell surface charge, thickness of membrane, and higher turnover rate of cancer cells compared to normal cells. This study clearly revealed that the enhanced fluorescent intensity and biocompatibility of the core-shell structures of CdSe/CdS retains the potential to be used for cell imaging applications.

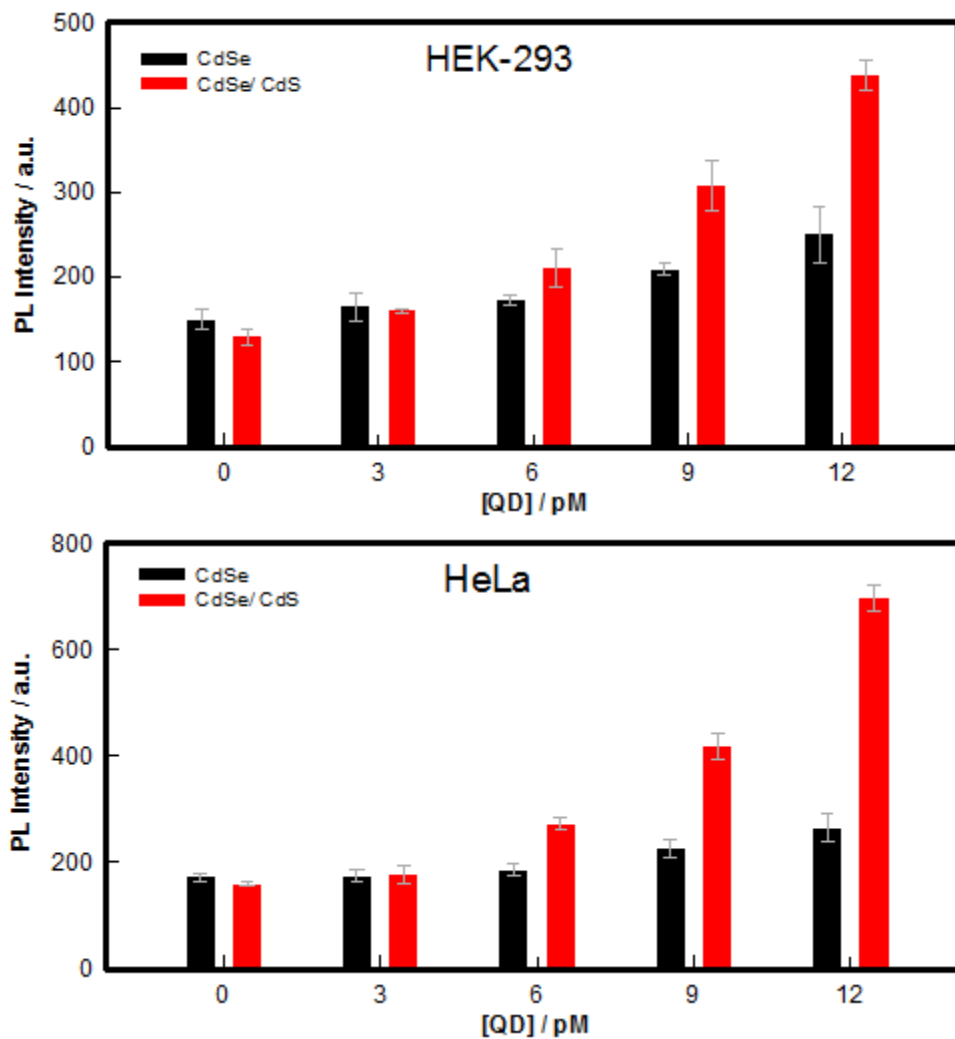


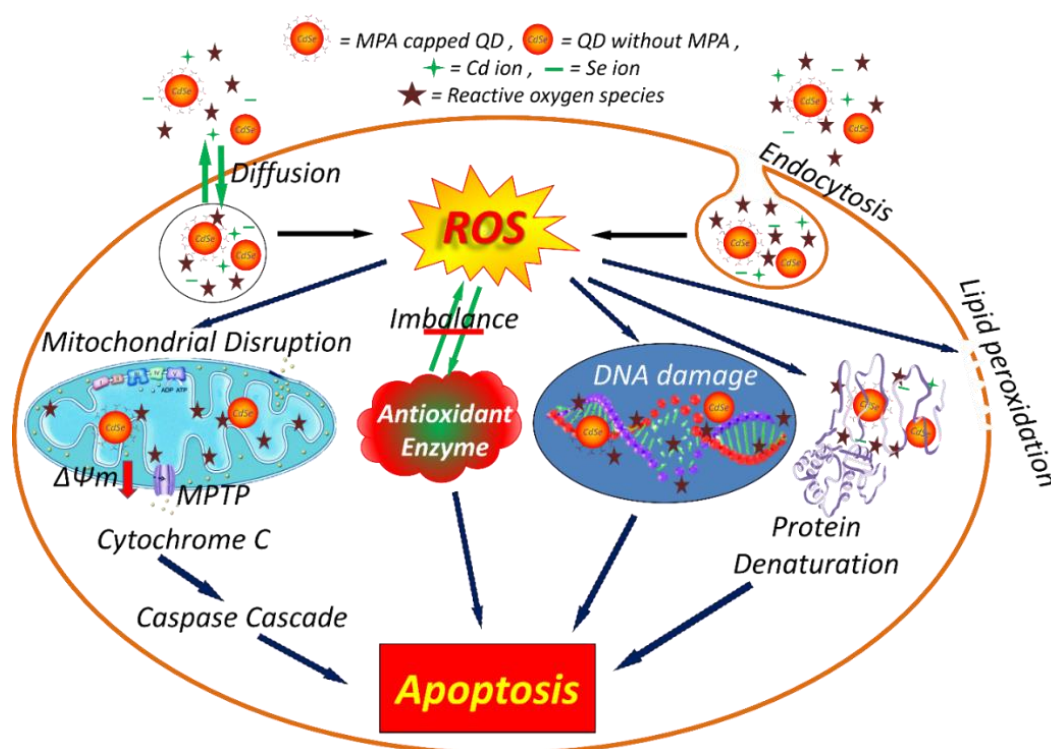
Figure 8.17: The histogram shows the fluorescence intensity of QDs inside the cells HEK-293 and MCF-7.

8.9 Summary

We have systematically and comprehensively probed the impact of core (CdSe) and core/shell (CdSe/CdS) QDs on two cancer cell lines, using HEK normal cell line as reference. These different QDs exhibited distinct cellular uptake and distribution, cytotoxicity and apoptosis. Moreover, it was further observed that core/shell structures showed reduced cytotoxicity in different cell lines compared to core QDs. The larger size QDs (core/shell) were phagocytised efficiently by all cell lines as was evident from the

cellular uptake indicating reduced cytotoxicity of core/shell QDs compared to core QDs. Marginal particle size difference and different cell lines had significant implications on their cellular uptake. The observed cellular-imaging and anticancer properties of CdSe QDs warrants deeper understanding of interaction of QDs with the cells.

We have clearly demonstrated the collective impact of surface modification of QDs. Enhanced uptake of core/shell QDs was observed compared to bare QDs and the uptake was found to depend on the incubation time because internalization is a complex diffusion process. The QDs initially got adhered onto the cell membrane which defined the first stage of interaction with the cells, and in the next step these diffused into the cells and got distributed inside the cytoplasm. These may in some cases, be delivered into cell nuclei if their size are small [42].



Scheme 8.1: Schematic overview of the possible mechanisms of cellular toxicity by different pathways by CdSe and CdSe/CdS QDs.

Control cells were found to have intact cell membrane structure, round shape and clear nuclear membrane with more chromatin region whereas CdSe QDs treated cells were found to contain degenerative and shrinkage in mitochondria, fragmented chromatin, ruptured cell membrane, vacuolization cytoplasm of cells which is features of apoptosis while CdSe/CdS did not show similar alteration in the cell structure. This event suggests

that coating may have reduced the generation of free radicals and eventually saved the cells from oxidative stress dependent apoptosis.

Scheme 1 depicts an overview of the possible mechanisms of cellular toxicity by different pathways followed by core-only and core-shell QDs. The heavy metal ions (e.g., cadmium and selenium) can produce free radicals which induce oxidative stress (ROS) leading to irreversible damage to cell constituents (e.g., their membrane, DNA, and mitochondria). This can be the possible mechanism for cell death. This definitely calls for more extensive exploration of this problem.

8.10 References

- [1] A. L. Efros, A. L. Efros, *Sov. Phys. Semicond.* **1982**, *16*, 772.
- [2] A. I. Ekimov, A. A. Onushchenko, *Sov. Phys. Semicond.* **1982**, *16*, 775.
- [3] A. M. Smith, X. Gao, S. Nie, *Photochemistry and Photobiology* **2004**, *80*, 377.
- [4] W. C. W. Chan, S. M. Nie, *Science* **1998**, *281*, 2016.
- [5] M. Bruchez, M. Moronne, P. Gin, S. Weiss, A. P. Alivisatos, *Science* **1998**, *281*, 2013.
- [6] T. M. Jovin, *Nat. Biotechnol.* **2003**, *21*, 32.
- [7] A. M. Derfus, W. C. W. Chan, S. N. Bhatia, *NanoLett.* **2004**, *4*, 11.
- [8] Y. Su, Y. He, H. Lu, L. Sai, Q. Li, W. Li, L. Wang, P. Shen, Q. Huang, C. Fan, *Biomaterials* **2009**, *30*, 19.
- [9] N. Chen, Y. He, Y. Su, X. Li, Q. Huang, H. Wang, X. Zhang, R. Tai, C. Fan, *Biomaterials*, **2012**, *33*, 1238.
- [10] W.A. Hild, M. Breunig, A. Goepferich, *European Journal of Pharmaceutics and Biopharmaceutics*, **2008**, *68*, 153.
- [11] C. Kirchner, T. Liedl, S. Kudera, T. Pellegrino, A. M. Javier, H. E. Gaub, S. Stollzle, N. Fertig, W. J. Parak, *NanoLett.* **2005**, *5*, 331.
- [12] W. H. Chan, N. H. Shiao, P. Z. Lu, *Toxicology Letters*, **2006**, *167*, 191.

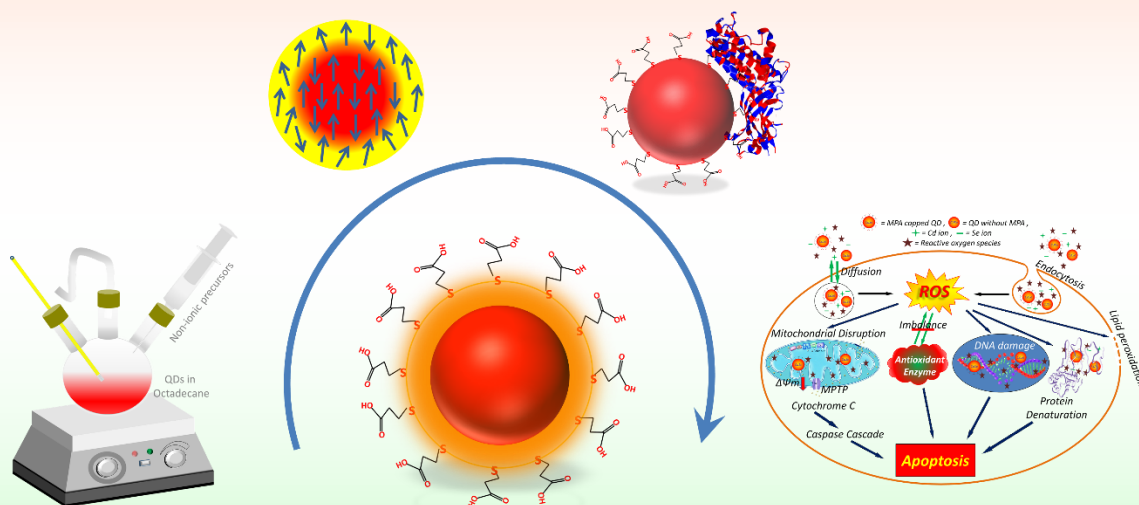
- [13] O. Seleverstov, O. Zahirnyk, M. Zscharnack, L. Bulavina, M. Nowicki, J. M. Heinrich, M., Yezhelyev, F. O'Regan Emmrich, R. Bader, *NanoLett.* **2006**, *6*, 2826.
- [14] M. J. D. Clift, B. Rothen-Rutishauser, D. M. Brown, R. Duffin, K. Donaldson, L. Proudfoot, K. Guy, V. Stone, *Toxicology and Applied Pharmacology* **2008**, *232*, 418.
- [15] R. L. Ehman, W. R. Hendee, M. J. Welch, N. R. Dunnick, L.B. Bresolin, R. L. Arenson, S. Baum, H. Hricak, J. H. Thrall *Radiology* **2007**, *244*, 12.
- [16] S. Santra, D. Dutta, G. A. Walter, B. M. Moudgil, *Technol Cancer Res Treat.* **2005**, *4*, 593.
- [17] L. Ye, K. T. Yong, L. Liu, I. Roy, R. Hu, J. Zhu, H. Cai, W. C. Law, J. Liu, K. Wang, *Nat. Nanotechnol.* **2012**, *7*, 453.
- [18] F. Erogbogbo, K. T. Yong, I. Roy, R. Hu, W. C. Law, W. Zhao, H. Ding, F. Wu, R. Kumar, M. T. Swihart, *ACS Nano* **2012**, *5*, 413.
- [19] J. Liu, F. Erogbogbo, K. T. Yong, L. Ye, J. Liu, R. Hu, H. Chen, Y. Hu, Y. Yang, J. Yang, *ACS Nano* **2013**, *7*, 7303.
- [20] R. Hardman, *Environ. Health Perspect.* **2006**, *114*, 165.
- [21] X., Wu, F. Tian, J. X. Zhao, M. Wu, *Expert Opin. Drug Metab. Toxicol.* **2013**, *9*, 1265.
- [22] K. T. Yong, W. C. Law, R. Hu, L. Ye, L. Liu, M. T. Swihart, P. N. Prasad, *Chem. Soc. Rev.* **2013**, *42*, 1236.
- [23] A. Hoshino, S. Hanada, K. Yamamoto, *Arch. Toxicol.* **2011**, *85*, 707.
- [24] S. Ghaderi, B. Ramesh, A. M. Seifalian, *J. Drug Targeting* **2011**, *19*, 475.
- [25] S. T. Yang, X. Wang, H. Wang, F. Lu, P. G. Luo, L. Cao, M. J. Mezziani, J. H. Liu, Y. Liu, M. Chen, *J. Phys. Chem. C* **2009**, *113*, 18110.
- [26] T. Pons, E. Pic, N. Lequeux, E. Cassette, L. Bezdetsnaya, F., Guillemin, F. Marchal, B. Dubertret, *ACS Nano* **2010**, *4*, 2531.
- [27] A. R. Maity, S. Palmal, S. K. Basiruddin, N. S. Karan, S. Sarkar, N. Pradhan, N. R. Jana, *Nanoscale* **2013**, *5*, 5506.

- [28] R. M. Raab, G. Stephanopoulos, *Biotechnol. Bioeng.* **2004**, 88, 121.
- [29] M. Kuno, D. P. Fromm, S. T. Johnson, A. Gallagher, D. J. Nesbitt, *Phys. Rev. B* **2003**, 67.
- [30] I. L. Medintz, H. T. Uyeda, E. R. Goldman, H. Mattoussi, *Nat. Mater.* **2005**, 4, 435.
- [31] A. M. Derfus, W. C. W. Chan, S. N. Bhatia, *NanoLett.* **2004**, 4, 11.
- [32] S. T. Selvan, T. T. Tan, J. Y. Ying, *Adv. Mater.* **2005**, 17, 1620.
- [33] S. J. Clarke, C. A. Hollmann, Z. Zhang, D. Suffern, S. E. Bradforth, N. M. Dimitrijevic, *Nat. Mater.* **2006**, 5, 409.
- [34] P. H. Hoet, I. Bruske-Hohlfeld, O. V. Salata, *J. Nanobiotechnol.* **2004**, 2, 12.
- [35] G. Oberdorster, A. Maynard, K. Donaldson, V. Castranova, J. Fitzpatrick, K. Ausman, *Part Fibre Toxicol.* **2005**, 2, 8.
- [36] W. H. Chan, N. H. Shiao, P. Z. Lu, *Toxicol. Lett.* **2006**, 167, 191.
- [37] A. P. Alivisatos, *J. Phys. Chem.* **1996**, 100, 13226.
- [38] A. Hoshino, K. Fujioka, T. Oku, M. Suga, Y. F. Sasaki, T. Ohta, M. Yasuhara, K. Suzuki, K. Yamamoto, *NanoLett.* **2004**, 4, 2163.
- [39] L. Manna, E. C. Scher, L. S. Li, A. P. Alivisatos, *J. Am. Chem. Soc.* **2002**, 124, 7136.
- [40] M. A. Hines, P. Guyot-Sionnest, *J. Phys. Chem.* **1996**, 100, 468.
- [41] R. J. Sokol, M. S. Straka, R. Dahl, M. W. Devereaux, B. Yerushalmi, E. Gumprich, G. Everson, *Pediatr. Res.* **2001**, 49, 519.
- [42] D. Maysinger, *Org. Biomol. Chem.* **2007**, 5, 2335.

Chapter 9

Conclusions and Perspectives

Abstract: This chapter concludes the work that has been presented and discussed in this thesis. The thesis emphasizes on the simpler way to synthesis the QDs with no special condition and their biophysical characterization with bioactivity.



Pictorial representation of works in this thesis on QDs is shown here.

9.1 Conclusions

Colloidal QDs are very much different due to their unique size-dependent properties from corresponding bulk materials and that unique properties make them very attractive in scientific and technological world. It is still a big challenge to synthesize in simpler way which yield high-quality and stable QDs at large scale and our knowledge on these QDs are also quite limited. The objectives in this thesis were to synthesize high-quality QDs with simpler approaches as well as to obtain greater understanding of these QDs. Here is the summary of thesis presented chapter wise.

In **Chapter 3**, I present a study on the differential structural and optical properties of CdSe quantum dots (QDs) (size 2.5 and 3.5 nm) which were synthesized with four different surfactant coatings using simpler hot-injection method. The surface functionalization led to change in the morphology of agglomerated QDs that generated

structures such as *tetrapods*, *clusters* and *networks*. Steady state fluorescence showed capping dependent changes in the quantum yield. In particular, QDs formed with TX-100 (Triton X-100) coating, revealed highest quantum yield, compared to QDs synthesized with oleic acid (OA), and three other surfactants (CTAB, DTAB and SDS). The ability to use surface ligands to control the passivation of surface states and non-radiative energy loss pathways can prescribe a route to enhancement of photocurrent enabling tailored design of nanocrystal-based light emitting and photovoltaic devices with improved efficiency. When used in vivo, these nanoparticles are immediately exposed to plasma proteins which motivated our second part of this work. It was noticed that the binding had QD size selectivity and this caused loss in the secondary structure of the plasma protein BSA. These functionalized QDs were interacted with model plasma protein BSA which revealed the protein-QD binding order: BSA-QD₁ (2.5 nm) < BSA-QD₂ (3.5 nm). Maximum binding occurred with DTAB coated QDs. Clearly, more work in this topic needs to be done to develop better understanding of the nanoparticles-protein interaction.

In **Chapter 4**, I present a facile controlled synthesis of non-iron based cubic phase MnSe magnetic nanocrystals with well-defined spherical shape of different size (7-16 nm, TEM data) by hot injection method without need for special conditions. It was found that the size and its polydispersity could be easily controlled by controlling the reaction temperature. The highly crystalline (confirmed by XRD) synthesized nanoparticles showed blue-violet fluorescence emission and were antiferromagnet in nature. Absorption and emission wavelengths were red shifted with size. Neel temperature and Curie constants increased with size whereas coercivity and remanence values decreased. Antiferromagnetic behaviour was found to get stronger with size. Surface effects that were dominant in smaller size, gave weak ferromagnetism to antiferromagnet nanocrystals. Therefore hysteresis loops are more pronounced in smaller size NCs. Blue-violet photoluminescence with magnetic properties create applications in short wavelength optoelectronics and magneto-optical devices.

In **Chapter 5**, I discuss on the morphology dependent interaction of model anisotropic nanoparticles (Laponite, diameter=25 nm and thickness=1 nm, and Montmorillonite MMT, diameter = 300 nm and thickness =1 nm) with three globular plasma proteins namely, bovine serum albumin (BSA), human serum albumin (HSA), and β -lactoglobulin (β -Lg). Acidic residues of these proteins were found to adsorb onto the

platelet surfaces through electrostatic interaction which was evidenced from static fluorescence intensity and lifetime quenching data. The binding pattern followed the hierarchy HSA > β -Lg > BSA, indicating lower binding affinity for protein molecules with lower pI value. Larger platelet surface area offered preferential binding leading to substantial conformational changes in the protein secondary structure.

In **Chapter 6**, I explore the size dependent interaction of CdSe QDs (2.5 and 6.3 nm) with lysozyme is reported comprehensively. The interaction of MPA capped water soluble quantum dots, with lysozyme was investigated, and an array of techniques such as static fluorescence spectroscopy and synchronous fluorescence spectroscopy, to quantify QD–lysozyme binding isotherms, exchange rates, critical flocculation concentrations, and the composition of mixed QD–lysozyme complexes. The results demonstrated that the binding of QDs with lysozyme induced conformational changes in lysozyme. QD was able to enhance the enzymatic activity of lysozyme in a highly efficient dose-dependent manner. It was concluded that smaller size QDs were found to bind poorly to lysozyme, but produced much enhanced enzymatic activity compared to bigger QDs. In summary, comprehensive characterization of stability of lysozyme-bound QDs is a necessary step in their potential use as intracellular delivery vectors and imaging agents.

In **Chapter 7**, I present a detail study on the simpler route to synthesize CdSe/CdS core/shell QDs with varying core size and shell thickness by one pot synthesis and discusses about their antifungal activity. The core-shell structure exhibited enhanced fluorescence compared to the core-only structure. We specifically evaluated for their comparative cytotoxicity on an opportunistic pathogen, *Candida albicans*. The CdSe (QDs) showed more cytotoxicity in these cells compared to core-shell QDs. Results obtained from these assays suggested that the cellular response was a distinct function of the physical size and surface coating (corona) thickness of these QDs. In summary, the CdSe QDs were found to be toxic at higher dosage of $200 \mu\text{g mL}^{-1}$, but CdS coating reduced their toxicity significantly. The CdS corona reduced the release of free radicals that helped cell viability.

In **Chapter 8**, I present a detail study of fluorescence behaviour of hydrophilic CdSe (core-only) and CdSe/CdS (core/shell) QDs in cancer cell imaging as well as their cytotoxicity mechanism. The core/shell structure exhibited ten-fold enhanced fluorescence intensity compared to the core-only structure. The cellular uptake of these

QDs yielded excellent results for cell imaging in MCF-7 and HEK-293 cells, where the fluorescence intensity was higher in cancerous cells as compared to normal cells and the coating of CdS on CdSe enhanced the fluorescence intensity by two fold after cellular uptake. The comparative cytotoxicity results showed that CdSe nanocrystals (QDs) have more cytotoxicity in HEK-293, MCF-7 and HeLa cell lines as compared to core/shell QDs. In addition, generation of intracellular ROS along with the decrease in mitochondrial membrane potential supported that QDs caused oxidative stress resulting in apoptosis through mitochondria mediated pathway. Elevation in the level of cytochrome c, upregulation the expression of pro-apoptotic genes like p53, Bax and caspase-3 and downregulation of Bcl-2 clearly indicated the involvement of the intrinsic pathway of programmed cell death. It was found that the core-only QDs induced more oxidative stress their led to increased apoptosis at same dose of core/shell QDs. These results concluded that surface coating of CdS reduced the release of free radicals that improve cell viability, and in addition, enhanced their fluorescence paving the way for better cell imaging.

9.2 Perspectives

Bare QDs are more toxic than core-shell one. We can use them in biological application after modifying their surface. Bio-conjugation of these QDs are possible as these QDs are interacted with biopolymers (proteins) very strongly as presented in this work. Biopolymers are very biocompatible so coating of QDs with biopolymers make them more biocompatible. Next work we can do is the cytotoxicity assessment of these biopolymeric coated QDs. Real applications of QDs can be understand by their *in vivo* study. Magnetic QDs also have their applications in biomedical field as MRI agent. In vitro and in vivo studies of these magnetic QDs can be done for anti-cancerous activity with the help of magnetic field.

Appendix 1

Fractal Dimension

The ratio that measures the statistical index of complexity of a pattern by comparing the changes of parameter in that pattern with the measured scale of parameter is fractal dimension^[1].

To get the relation of the number of pieces 'n'(parameter) with length of piece 's'(measured scale) and dimension 'd', we generalized that from line, square and cube to 'd' dimension object.

	S	1/1	1/2	1/3	s
D					
line	1	1	2	3	1/s
square	2	1	4	9	(1/s) ²
cube	3	1	8	27	(1/s) ³
d- dimensional object	d	1 ^d	2 ^d	3 ^d	n = (1/s)^d

The relation is

$$n = (1/s)^d$$

Taking log of both side

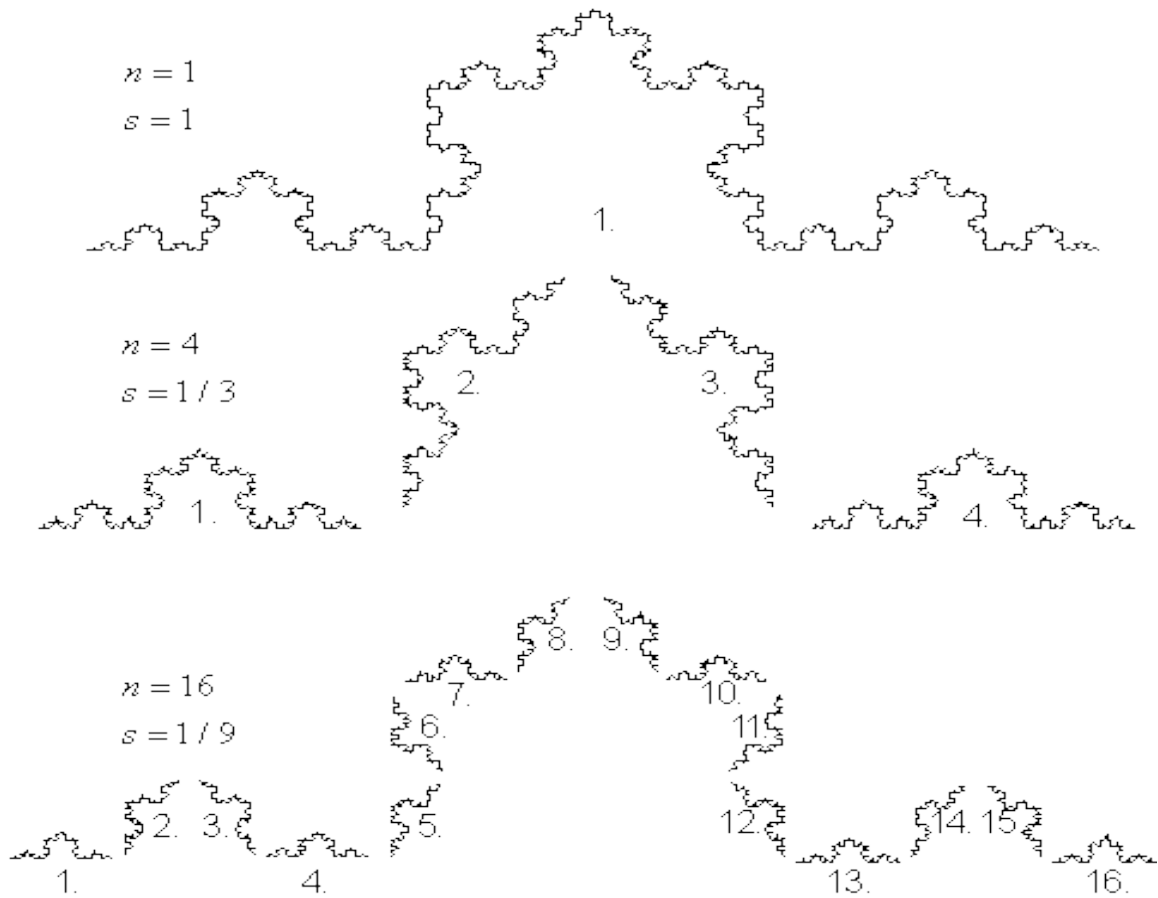
$$\log n = d \log (1/s)$$

So dimension

$$d = \log n / \log (1/s)$$

Although there is no rule that dimension has to have an integer value, this has been the convention in traditional geometry. It can be 'fractional' or 'partial' dimension but it is always positive.

The Koch curve's segments and scale.



For the above structure

$$4 = (1/3)^d = 1/3^d$$

$$d = \log 4 / \log 3 = 1.25$$

References

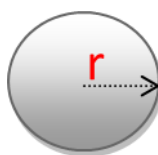
[1] Falconer, Kenneth, *Fractal Geometry*. New York: Wiley. **2003**, 308.

Appendix 2

Conversion from Mass to Number of Particle

For getting the number of nanoparticles from mass of nanoparticles, we use simple mathematics calculation.

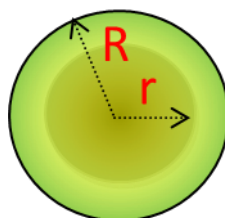
For spherical nanoparticles with radius 'r'



$$\text{number of QDs} = \frac{M}{\rho_{\text{CdSe}} * \text{Volume of QD}} = \frac{M}{\rho_{\text{CdSe}} * \frac{4}{3} \pi r^3}$$

In above equation 'M' is taken mass of QDs, ' ρ ' is density of bulk material of QDs.

For core (CdSe) / shell(CdS) nanoparticle of radius 'R' with core of radius 'r'



$$\begin{aligned} \text{number of QDs} &= \frac{M}{\rho_{\text{CdSe}} * \text{Volume of Core} + \rho_{\text{CdS}} * \text{Volume of Shell}} \\ &= \frac{M}{\rho_{\text{CdSe}} * \frac{4}{3} \pi r^3 + \rho_{\text{CdS}} * \frac{4}{3} \pi (R^3 - r^3)} \end{aligned}$$

ρ_{CdSe} is bulk density of Cadmium Selenide that is 5.816 g / cm³ and ρ_{CdS} is bulk density of Cadmium Sulfide that is 4.82g / cm³.

And core / shell QDs used in *in vitro* studies, we have the value of 'R' and 'r' from TEM which are 6 nm and 3.5 nm respectively. Therefore, for core CdSe QDs, the number of QDs is 1.9013x10¹⁷ in 1g of core QDs and for core/shell CdSe/CdS QDs, there is 1.6327x10¹⁷ QDs in 1g of core/shell QDs.
